Karlsruher Institut für Technologie

Active Shielding for Future Large-Scale Dark Matter Experiments

Zur Erlangung des akademischen Grades eines
DOKTORS DER NATURWISSENSCHAFTEN
der Fakultät für Physik
des Karlsruher Instituts für Technologie
genehmigte

DISSERTATION

von

Dipl.-Phys.

Geertje Heuermann

aus Leer (Ostfriesland)

Tag der mündlichen Prüfung:	29.01.2016
Referent:	Prof. Dr. Dr. h.c. Johannes Blümer
Korreferent:	Prof. Dr. Hans Kraus (University of Oxford)

I declare that I have developed and written the enclosed thesis completely by myself, and have not used sources or means without declaration in the text.

Karlsruhe, 31.12.2015

. . . . . .

(**Geertje Heuermann**)

Zusammenfassung

Aus kosmologischen Beobachtungen geht hervor, dass circa 84 % der Materie unseres Universums aus einer bisher unbekannten Form von Materie besteht, sogenannter Dunkler Materie (DM), welche bislang nur über ihre gravitative Wechselwirkung wahrgenommen werden konnte. Die Natur und der Ursprung der DM sind bis heute ungeklärt. Astroteilchenphysikalische Experimente weltweit suchen mit großem Aufwand und hochsensitiven und hochreinen Detektoren nach ihrem direkten Nachweis. Um die Sensitivität der Experimente zu erhöhen, planen Astroteilchenphysiker die sensitive Detektormasse bis auf ein Tonne zu erhöhen. Da die Wechselwirkungsrate von DM sehr gering ist, ist es von großer Bedeutung jeglichen Untergrund zu reduzieren oder gänzlich zu unterdrücken. Um ein DM-Signal in zukünftigen Experimenten eindeutig identifiziert zu können, erfordert dies unausweichlich eine Verringerung der Untergrundrate auf unter 1 Ereignis/Tonne/Jahr.

Im Rahmen dieser Arbeit wurden zwei aktive Abschirmungstechnologien für zukünftige kryogene DM-Experimente entwickelt, welche es erlauben Myon-induzierte Neutronen und Umgebungsneutronen mit hoher Effizienz zu reduzieren: ein Wassercherenkovdetektor (WCD) und ein Gd-geladener Szintillator. Neutronen stellen eine kritische irreduzible Untergrundkomponente in DM-Experimenten dar, da das Signal eines einzelnen Neutronenrückstoßes (SNR) nicht von einem DM-Signal zu unterscheiden ist. Der hier entwickelte WCD ermöglicht es, das Myon, welches mit dem Myon-induzierten Neutron assoziiert wird, aktiv zu taggen. Myonen produzieren im Wasser des WCD Cherenkovlicht, welches mit PhotoMultiplierTubes (PMTs) detektiert wird. Untergrundneutronen werden in dem hier entwickelte Gd-geladener Szintillator durch die Produktion von Szintillationslicht identifiziert, welches durch den Neutroneneinfang an Gd, H oder C oder durch Neutronstöße am H des Szintillators entsteht. In dem hier entwickelten Konzept wird der Szintillator erstmalig von den PMTs des Myonvetos ausgelesen. Beide Vetosysteme wurden in Hinblick auf hohe Vetoeffizienzen und eine geringe Totzeit konzipiert und mit Hilfe versierter GEANT4 Monte-Carlo (MC)-Simulationen optimiert. In diesem Zusammenhang wurde ein akkurates optisches Model des WCD entwickelt und mit Hilfe von Prototypmessungen am KIT validiert. Somit ermöglichen beide Vetosysteme die geforderte Unterdrückung des Untergrundes auf unter 1 Ereignis/Tonne/Jahr. Gleichzeitig verringert das Konzept aus ultra-reinem Wasser und kombinierter PMT-Auslese den externen Untergrund in der Umgebung der DM-Detektoren.

Der optimierte Trigger des Myonvetos erlaubt es, Myonen mit einer Effizienz von

$$\epsilon_{\mu}^{\text{veto}} > 99,9\,\% \tag{1}$$

zu identifizieren und dabei eine Rate zufälliger Koinzidenzen von $\mathcal{O}(10^{-3}\,\text{Hz})$ zu gewährleisten. In 12 Jahren simulierter Messzeit in einer Tonne kryogener DM-Detektoren im Untergrund Labor in Modane (LSM) wurde kein irreduziebles Myon-induziertes Neutronsignal in Anti-Koinzidenz mit dem Myonveto gemessen.

Daraus ergibt sich ein oberes Limit für die Myon-induzierte Untergrundrate von

$$\Gamma^{\text{veto}}_{\mu\text{–n–bg}} \leq 0,18\,^{+0,02}_{-0,03}\,\text{events/tonne/year at } 90\,\%\,\text{CL } (1\,\text{Tonne}). \tag{2}$$

Die obere Grenze der Rate hängt allein von der MC-statistik des simulierten Myonenflusses ab, welcher wiederum durch die CPU intensive optische Simulation limitiert ist. Der optimierte Trigger des Neutronvetos ermöglicht es ebenfalls, den irreduziblen Untergrund aus Umgebungsneutronen in kryogenen DM-Experimenten mit (ohne) passiver Polyethylenabschirmung im Kryostaten effizient zu taggen:

$$\epsilon^{\text{veto}}_{\text{n}}(\text{SNR}) > 78\,\%\ (91\,\%). \tag{3}$$

Der optimierte Trigger des Neutonvetos ist ein Kompromiss aus hoher Vetoeffizienz und einer geringen Rate zufälliger Koinzidenzen. Die Rate zufälliger Koinzidenzen des Vetos wird durch die hohen Neutroneinfangzeiten an Gd bestimmt und ist $\mathcal{O}(20\,\text{Hz})$.

Das hier entwickelte aktive Abschirmungskonzept zeigt zum ersten Mal, dass ein kombiniertes System aus WCD und Gd-geladenen Szintillator effizient gegen den sonst irreduzible Untergrund Myon-induzierter Neutronen und Umgebungsneutronen in kryogenen DM-Experimenten eingesetzt werden kann. Die Effizienzen der jeweiligen Vetos sind kompetetiv mit anderen DM-Abschirmungskonzepten und ermöglichen es, eine Untergrundrate unter 1 Ereignis/Tonne/Jahr zu gewährleisten. Obwohl das System für zukünftige kryogene DM-Experimente entwickelt wurde, kann es ohne weiteres in jeglichen Experimenten, die nach seltenen Ereignissen suchen, eingesetzt werden.

Abstract

Only about 16 % of the matter in our Universe consists of ordinary visible matter. About 84 % is attributed to non-luminous gravitating matter, so-called dark matter. Dark matter (DM) is one of the great puzzles in modern cosmology. Great efforts are made to shed light on the nature of DM through its direct detection with highly sensitive, ultra clean and radio-pure experiments. As DM interaction cross-sections are expected to be small, it is of great importance to understand and minimize background sources. So far, no convincing DM signal has been detected and astroparticle physicists are eager to improve sensitivities of direct dark matter experiments by increasing the target mass of the detector to the tonne-scale. The suppression of background is crucial to reach the envisaged sensitivities and requires an unprecedented reduction in background rates below 1 event/tonne/year.

Focusing on large scale cryogenic dark matter searches, two active shielding technologies were designed, which allow to efficiently reduce muon-induced and ambient neutron background sources in dark matter experiments below 1 event/tonne/year: a water Cherenkov detector (WCD) and a Gd-loaded liquid scintillator. Neutrons are the most critical background source in dark matter experiments as the single nuclear recoil (SNR) of a neutron scattering in the detector produces the same signal as expected from a dark matter interaction. The proposed WCD allows to actively tag muons, which are associated with muon-induced neutrons. The muons produce Cherenkov radiation in the water of the WCD, which is subsequently detected with photomultiplier tubes (PMTs). Ambient neutrons are tagged through the Gd-doped liquid scintillator via the production of scintillation light from prompt proton-neutron scattering or delayed neutron captures on Gd, H or C. In our proposal of the neutron veto, the scintillation light is for the first time detected with the same PMTs that are used for the muon veto system. Both veto systems were designed in view of high veto efficiencies and a low dead time and were optimized through elaborate and extensive optical GEANT Monte Carlo (MC) simulations. In this context, an accurate model of the light collection in WCDs was implemented which was validated through dedicated prototype measurements at KIT. Both veto systems thus allow to keep residual ambient and muon-induced neutron background rates in large scale cryogenic dark matter experiments below 1 event/tonne/year. The usage of ultra-pure water as a passive and active shield and the shared optical readout system keep external background levels in the vicinity of the target at a minimum.

The optimized trigger condition of the water Cherenkov muon veto system allows for muon tagging efficiencies of

$$\epsilon_{\mu}^{\text{veto}} > 99.9\,\% \tag{4}$$

while keeping an accidental rate of $\mathcal{O}(10^{-3}\,\text{Hz})$. Not a single muon-induced neutron signal was recorded in anti-coincidence with the muon veto in the favored region of interest (ROI) for dark matter search in more than 12 years of simulated data taking.

The resulting upper limit for the rate of the irreducible muon-induced neutron background rate in one tonne of target material is

$$\Gamma^{\text{veto}}_{\mu\text{–n–bg}} \leq 0.18\,^{+0.02}_{-0.03}\,\text{events/tonne/year at } 90\,\%\,\text{CL}. \tag{5}$$

The rate is purely limited by the MC-statistics of the simulated muon flux at LSM. In regard to current developments in cryogenic dark matter searches, we also estimated an upper limit for low mass dark matter searches in a Ge-target with reduced target mass of 43.2 kg. Again, no muon induced neutron signal is recorded in anti-coincidence with the muon veto in 12 years of simulated data taking. The optimized trigger of the Gd-loaded scintillator allows to tag single nuclear recoils induced by ambient neutrons with (without) internal passive polyethylene-shielding with an efficiency of

$$\epsilon_{\text{n}}^{\text{veto}}(\text{SNR}) > 78\,\%\,(91\,\%). \tag{6}$$

The optimal trigger of the neutron veto is a trade-off between high efficiencies and a low accidental trigger rate of the veto system. The accidental trigger rate of the veto system is dominated by the large capture times on Gd and is of the order of 20 Hz.

For the first time, this work shows that a combined active shielding concept of a WCD and a Gd-loaded scintillator can be used efficiently against ambient and muon induced neutrons in large scale cryogenic dark matter experiments. The respective veto efficiencies of the muon and neutron veto are competitive with similar proposed systems and allow to reduce background from ambient and cosmogenic neutrons below 1 event/tonne/year. Even though the two active veto systems were designed for cryogenic dark matter experiments, the concept can be easily applied to any rare event search experiment and help to increase their sensitivity to discover new physics.

„Es gibt Wunder,
die müssen im Dunkeln geschehen“.

Prof. Dr. Abdul Nachtigaller

Contents

1. Search for Dark Matter

The rapid developments in observational and theoretical cosmology and particle physics in the last century has led to a deep understanding of the structure and composition of our Universe. The working models of cosmology and particle physics, the Standard Model of particle physics and the ΛCDM model of cosmology, allow to understand the Universe's particles and their interaction as well as the evolution of the Universe since 10^{-43} s after the so called "hot Big Bang", roughly 14 billion years ago. From cosmological observation, we nowadays know that only about 16 % of the matter content of our Universe consists of ordinary visible matter. About 84 % is attributed to non-luminous gravitating matter, so-called dark matter. Dark matter is one of the great puzzles in modern cosmology as of today the nature of dark matter remains unknown. Though the evidence of dark matter is found on cosmological scales, the constituent of dark matter can only be found in modern particle physics. To identify the nature of dark matter, different experimental approaches are pursued with state-of-the-art technology. The search for dark matter is a prime example for the interplay between particle physics, astrophysics and cosmology.

In the following, we will focus on the direct detection of dark matter. Before detailing the current search for dark matter, we will motivate its existence through cosmological observations (Sec. 1.1) and present particle candidates along with its features (Sec. 1.2). To start with, we will give a short introduction to the Standard Model of particle physics and the ΛCDM model of cosmology which are the cornerstones of modern particle physics and cosmology.

Standard Model of Particle Physics

The Standard Model of Particle Physics (SM) allows to describe the fundamental particles and their interactions through three of the four known fundamental forces: the strong, the electromagnetic and the weak force. The gravitational force is not included in the SM.

A fundamental particle is characterized by its mass, spin, electrical charge, flavor and color charge. Matter consists of fermions (spin 1/2-particles) – namely leptons and quarks [1]. The (six) quarks and the (six) leptons are divided into three generations or families by increasing mass (see Fig. 1.1).

The interactions between particles are mediated by gauge bosons (integer spin particles).

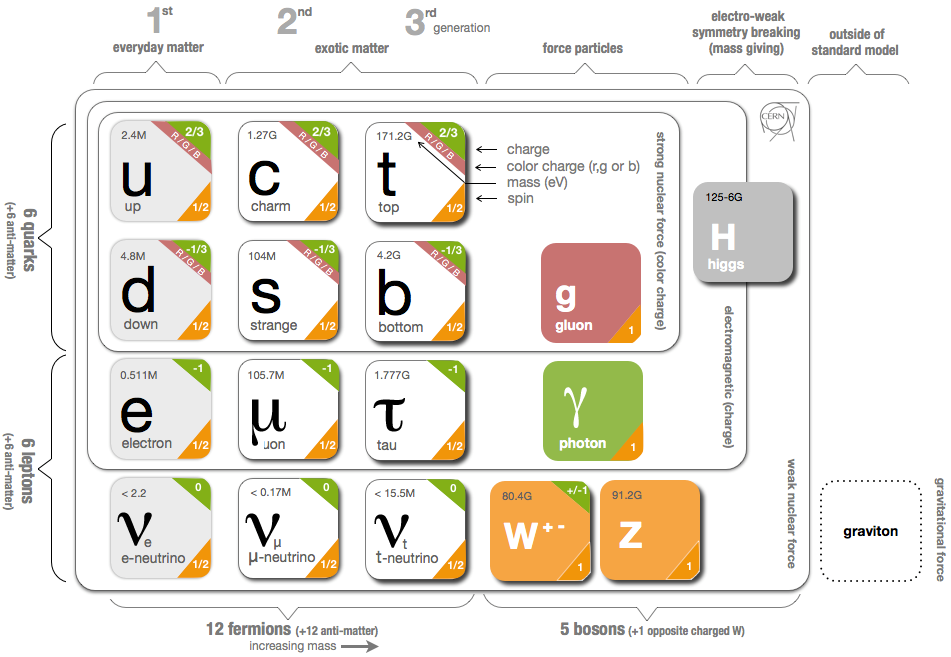

Figure 1.1.: Fundamental particles and force carriers in the Standard Model of particle physics. The (six) quarks and the (six) leptons are divided into three generations or families by increasing mass. Fig. from [2].

The strong (color) interaction between quarks is mediated by eight gluons. Electromagnetic interaction between charged leptons and/or quarks is mediated by the massless photon. Weak interactions between leptons and/or quarks are mediated by the massive $W^{\pm}$, Z^0 and the H^0-boson [3]. Quarks do not exist as free particles but are bound through confinement into color neutral objects, so called hadrons that are sub-divided into baryons (three-quark system) and mesons (quark anti-quark system). The matter observable in our Universe consists for the most part only of the first generation of leptons and baryons: electrons, neutrons (udd) and protons (uud).

The SM unites the strong, the electromagnetic and the weak force in a unified relativistic quantum field theory, where observable particles are excitations of the quantum fields. The kinematics of the particles can be derived from the Lagrangian of the SM. The theory of the SM is based on the gauge invariance of the SM quantum fields under transformations of the SM symmetry group: $SU(3)_C \times SU(2)_L \times U(1)_Y$ which underwent spontaneous symmetry breakdown in the early Universe $SU(3)_C \times U(1)_Q$. $SU(3)_C$ describes the strong interactions, also known as quantum chromodynamics (QCD). $SU(2)_L \times U(1)_Y$ is the gauge group of the electroweak interaction. Y and Q are the hyper charge and electric charge generators respectively. The spontaneous symmetry breaking generated the masses of the charged fermions and the masses of the weak bosons $W^{\pm}$, Z^0 as well as the scalar Higgs field H^0 [4]. For further and in depth information, the reader is referred to e.g. [5].

In the following and through-out this thesis, physical units are chosen such that $\hbar = c = 1$, with the speed of light c and the Planck constant $\hbar$.

Standard Model of cosmology (ΛCDM)

The standard model of cosmology (ΛCDM) describes the evolution of the Universe since 10^{-43} s after the so called "hot Big Bang", roughly 13 billion years ago. The model relies on observations of the cosmic microwave background (CMB), the cosmological principle, the present expansion of the Universe, the present relative abundance of light elements and the existence of cold dark matter and energy. The ΛCDM model assumes that the Universe and its particle content were created in a hot ($> 10^{19}$ GeV) Big Bang. Until temperatures of about 10^{16} GeV, all forces of the SM of particle physics were most likely united in a single Grand Unified Theory (GUT). The particle content of the early Universe, including dark matter, was in thermal equilibrium, i.e. particles were continuously created and annihilated. Thermal equilibrium was maintained as long as the interaction rate[1] was larger than the expansion of the Universe. Diverse observations, e.g. from the CMB suggest that the early Universe underwent an exponential expansion possibly generated by the vacuum energy of some fields at about 10^{-36} s after the Big Bang (inflation). Quantum fluctuations during inflation acted as seeds for density perturbations which in turn resulted in the large scale structures of today's Universe. Inflation and the following expansion forced the Universe to cool down. As the Universe cooled down, the forces of the SM decoupled. Particle species successively fell out of thermal equilibrium and their number density was "frozen". The electroweak force decoupled at the temperature of about 100 GeV and quarks, leptons and gauge bosons acquired mass via the spontaneous symmetry breaking of the Higgs field. At about 0.3 GeV hadronization occurred and quarks and gluons were bound into hadrons. At a temperature of about 1 MeV the neutron freeze-out occurred. Ten to twenty seconds after the Big Bang and at a temperature of 100 keV, He and small fractions of D, Li and Be were created in fusion processes (Big Bang Nucleosysnthesis (BBN)). After the freeze-out of the electrons and positrons, an excess of electrons remained. Several thousand years later ($z = 1000$), the formation of neutral hydrogen and helium gas from H and He atomic nuclei and electrons (*recombination*) occurred after the Big Bang and the Universe became transparent to photons. As a consequence, photons have been propagating freely in all directions through-out the Universe, only effected by the expansion of the Universe. Since Recombination, the photon wavelength has been shifted to the microwave region and can nowadays be observed as the CMB.

Due to a yet unknown matter anti-matter asymmetry in the early Universe, the Universe is completely dominated by matter. The origin of the matter anti-matter asymmetry is assumed to be caused by CP[2] and baryon violating processes as well as departure from thermal equilibrium (Sakharov Conditions). Figure 1.2 depicts the time evolution of our Universe.

The standard model of cosmology relies on Einsteins equations of general relativity which connect the geometry of the Universe to its energy, radiation and matter content, and on the cosmological principle, which assumes that the universe is isotropic and homogeneous. Einstein's equations of general relativity rely on the strong equivalence principle and can be written as:

$$R_{\mu\nu} - \frac{1}{2} g_{\mu\nu} R + \Lambda g_{\mu\nu} = 8\pi \mathrm{G_N} T_{\mu\nu} \tag{1.1}$$

$R_{\mu\nu}$ is the Ricci curvature tensor[3], and gives a measure for the curvature of space-time.

[1] The interaction rate of the particles depends on its number density (n), its relative velocity (v) and its interaction cross section (σ): $\Gamma = n \cdot v \cdot \sigma$.

[2] *c*harge-*p*arity (CP) transformation: left handed particles are transformed into right handed antiparticles

[3] The Ricci-tensor is the contracted Riemann-tensor which gives the change of direction of a vector after parallel transport around a closed curved [7]

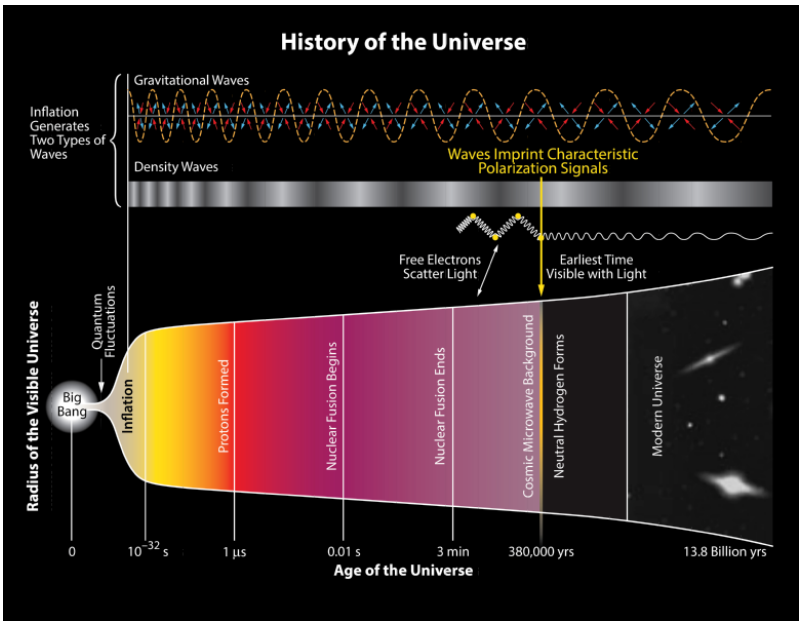

Figure 1.2.: Time evolution of the Universe from inflation, decoupling of the strong and electroweak forces, annihilation of matter and antimatter, big bang nucleosynthesis to the decoupling of photons and the formation of the cosmic microwave background. Fig. from [6].

$T_{\mu\nu}$ corresponds to the (symmetric) energy-momentum tensor. The metric $g_{\mu\nu}$ allows to compute the distance between two points in space-time.[4] G_N is Newtons constant. The cosmological constant Λ in Einsteins equations (i.e. a gravitational field in the absence of matter) is interpreted as the vacuum density or dark energy of the Universe. The energy, radiation and matter density of the early Universe after the hot Big Bang can be described as a perfect fluid using the equations of hydrodynamics. By this, and under the assumption of the cosmological principle, Einstein's equations reduce to the Friedmann equation [1]:

$$\left(\frac{\dot{a}}{a}\right)^2 + \frac{k}{a^2} = \frac{8\pi G_N}{3}\rho_{tot} \tag{1.2}$$

$\rho_{tot} = \rho_m + \rho_{rad} + \rho_{vac}$ is the total energy density as a sum of matter density, vacuum density and radiation density of the Universe. The curvature of the Universe is given by k: $k = 0$ defines a flat Universe, $k =$ -1 gives an open Universe and $k = 1$ results in a closed Universe. The scale factor of the Universe is defined by a. Observations imply that the Universe is expanding and consequently that the scale factor is time depended. Hubble was the first to discover that the Universe is expanding, by detecting the redshift of light from distant galaxies. The redshift is defined via the ratio of the emitted and the observed wavelength of the light: $1 + z = \lambda_{obs}/\lambda_{emit}$. The redshift results from the change of scale factor $a(t)$: $1 + z = a(t_{obs})/a(t_{emit})$. The change of scale factor or rate of expansion is often defined as the Hubble parameter:

$$H(t) = \frac{\dot{a}(t)}{a(t)} \tag{1.3}$$

The current rate of expansion of the Universe is $H_0 = 67.80 \pm 0.77\,\mathrm{km/s/Mpc}$ [8]. If the mass density in Einstein's equations (Eqn. 1.2) is equal to the critical mass-energy density $\rho_c = 3H^2/8\pi G_N$ one finds that $k = 0$, i.e. the Universe is flat as is assumed of as of today.

[4] $g_{\mu\nu}$ reduces to the metric of special relativity (Minkowski space) in local free fall.

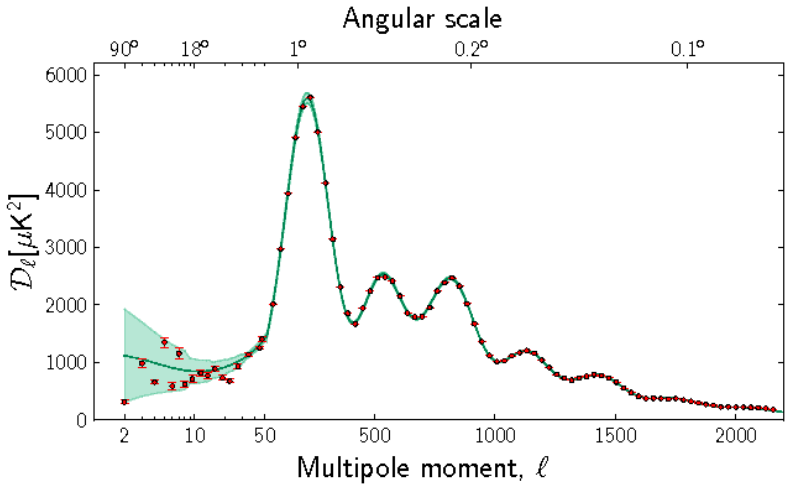

Figure 1.3.: The angular power spectrum of the CMB temperature fluctuations as meaured by Planck [14].

Since their postulation, the Standard Model of particle physics and the ΛCDM model of cosmology have been tested in diverse experiments. Recent achievements are the discovery of the Higgs boson by the ATLAS and CMS experiments [9] [10] and the precision measurement of the Cosmic Microwave Background by the Planck experiment[8]. Nevertheless, outstanding questions remain and the answers can only be found with theories beyond the Standard Models of particle physics. Open questions are, to name a few, the particle nature of neutrinos (Majorana or Dirac) and their mass and hierarchy, the origin of matter-antimatter asymmetry, the strong CP problem in QCD, the hierarchy problem, quantum gravity, the origin of cosmic rays (gamma/neutrino) at highest energies and the existence and nature of dark matter and dark energy.

1.1. Evidence for Dark Matter

Anomalies at all scales of astrophysical systems point towards the existence of non-luminous (dark) matter or a deviation from the known laws of gravity[5]. In 1933, Zwicky [13] discovered that the galaxies in the Coma cluster were moving faster than could be explained by visible mass alone and concluded that additional "invisible" matter - which he called dark (cold) matter - was needed to explain the discrepancy. Since then, the existence of dark matter has been established on all astronomical scales.

The most compelling evidence for dark matter is given at the *scale of the Universe* by the temperature anisotropies in the the cosmic microwave background (CMB), the thermal relic radiation of the Big Bang. The CMB is a perfect black body radiator ($T = 2.725\,\mathrm{K}$) with temperature anisotropies of the order of 10^{-5}. These temperature anisotropies result from gravitational wells in the photon-baryon fluid of the early Universe before recombination. The temperature anisotropies of the CMB can be expanded in spherical harmonics and expressed as a power spectrum (see Fig. 1.3). The parameters (6 to 7) of the cosmological model (ΛCDM), including the total and baryonic mass content, can be extracted by the best fit to the power spectrum of the CMB. The first acoustic peak in the power spectrum of the CMB allows to determine the baryonic mass content, higher order peaks give insights on the non-baryonic mass content. The Planck experiment has measured the temperature

[5]Theories of modified Newtonian dynamics or such as MOND [11], TeVeS [12] are discussed in the community, but beyond the scope of this work.

Figure 1.4.: The collision of two galaxy clusters in the bullet cluster (1E 0657-558) hints, that the gravitational center of the two colliding clusters (blue), which is determined via gravitational lensing, and the visible (pink) center observed through X-rays are clearly separated [16].

anisotropies of the CMB with a angular resolution of ∼10 arcmin. The best fit to the angular power spectrum of the CMB indicates that the Universe is flat, i.e. $\rho_c = 3H^2/8\pi G_N \approx 1$ and that it consists of 5 % visible (baryonic) matter, 26 % dark matter and 69 % dark energy [8]. The prediction of the baryon content of the Universe from the CMB is consistent with predictions from the primordial element synthesis in the early Universe (Big Bang nucleosynthesis) and the observed abundance of light elements. As of today, it is assumed that quantum fluctuations in the early Universe during inflation acted as seeds for density perturbations which in turn resulted in the large scale structures of today's Universe. After thermal freeze-out and the recombination of electrons with H and He, the Universe became transparent to photons around 380 000 years after the Big Bang. Density perturbations of the early Universe were imprinted via temperature anisotropies in the photon spectrum. The structure formation in the early Universe depends on the type and interactions of particles. The interplay between photon pressure and gravitational attraction due to density fluctuations caused the photon-baryon fluid to oscillate within the horizon volume (acoustic oscillation) and density perturbations grew linearly. Baryonic matter alone cannot account for the small-scale structure of today's Universe. Density perturbations from dark matter on the other hand could grow undisturbed before Recombination and by this provide gravitational wells for the photon-baryon fluid which allow to reproduce the small-scale structures which are observed in today's Universe. This is supported by N-body simulations of structure formation with non-relativistic dark matter[6].

At the *scale of galaxy clusters*, the anomalous mass to light ratio as discovered by Zwicky in the Coma cluster is nowadays considered as first evidence for dark matter. Zwicky determined the mass of the Coma cluster by applying the Virial theorem to the observed distribution of the radial velocities with a mean velocity $\langle v \rangle = 1000\,\mathrm{km/s}$ and discovered that the total mass (M) within a cluster radius R exceeds that of the stars by about 400

[6] Though structure formation supports the hypothesis of cold dark matter, caveats such as missing satellite problem remain, i.e. the number of observed dwarf galaxies in Milky Way-like galaxies is smaller than predicted by N-body simulations [15].

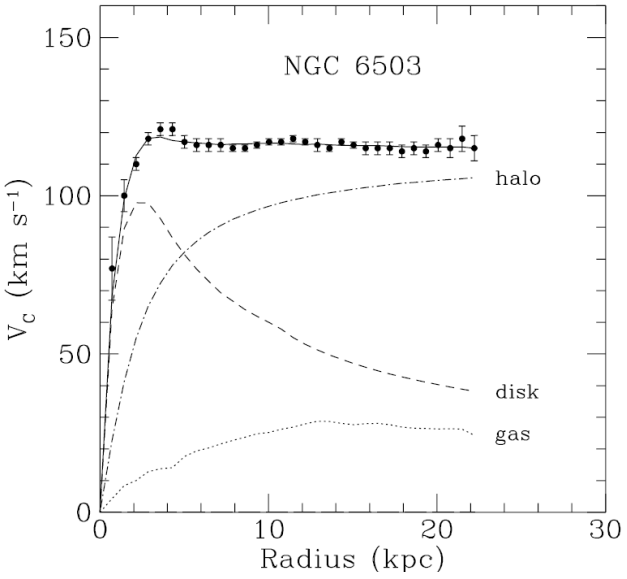

Figure 1.5.: Rotation curve of the galaxy NGC 6503 [20] as measured (markers).The dashed line and the dotted line correspond to the contribution of the disk and gas respectively, the dashed dotted line gives the contribution of the dark matter halo.

times.

$$M = \frac{5\,R}{3\,\mathrm{G_N}}\langle v^2 \rangle \tag{1.4}$$

He attributed the discrepancy to (dark) non-luminous matter. Further evidence of an anomalous mass to light ratio in galaxy clusters is given by gravitational lensing. Gravitational lensing allows to reconstruct the gravitational potential of massive object. The curvature of space-time by the gravitational potential of galaxy clusters, e.g. the galaxy cluster Abell 2218 [17] deflects light rays of observable objects. If the galaxy cluster is in the line of sight between the object and the observer, the object appears as (Einstein) rings, multiplied (strong lensing) or statistically distorted (weak lensing). Additionally, the measurement of 72 collisions of galaxy clusters, such as the collision of two galaxy clusters in the bullet cluster (1E 0657-558), hint that the gravitational center of the two colliding clusters, which is determined via gravitational lensing, and the visible center of thermal X-ray emission are clearly separated [18] (see Fig. 1.4). The gravitational lensing as well as the mass to light ratio imply that galaxy clusters contain five times more mass than visible (baryonic) mass.

At the *galactic scale*, evidence for dark matter is given by anomalous orbital velocities of stars around the galactic center which was first discovered by Very C. Rubin [19]. According to Kepler, a stable orbit requires the centrifugal and the attractive gravitational force to balance out. Thus, the velocities of stars around the galactic center should fall $\propto 1/\sqrt{r}$ outside the visible mass distribution, where r is the distance of a star to the center of the galaxy. Instead, a constant velocity well beyond the optical disc is measured in a multitude of galaxies including our Milky Way [19, 20] pointing towards the existence of a dark matter halo with a mass density profile $\rho_{\mathrm{DM}} \propto 1/r^2$ (see Fig. 1.5).

1.2. Dark Matter Candidates

Though one finds strong evidence for the existence of non-luminous dark matter, the nature and constituents of dark matter is yet to be revealed. Based on astrophysical and experimental particle physics observations, it is assumed that the majority of dark matter is made of non-baryonic and non-Standard Model particles, which are electrically neutral, weakly interacting, stable on a cosmological time scale with a weak self-interaction cross-section and highly collisionless. A fraction of dark matter could be explained by baryonic massive, compact non-luminous objects (MACHOs) such as neutron stars, black holes or brown dwarfs. Current estimates using microlensing of the Large Magellanic Cloud constrain the possible amount of MACHOs in our galactic dark matter halo though to 20 % or less [21].

The structure formation in galaxies gives information about the velocity (temperature) of the dark matter particle. The temperature of dark matter particles influences structure formation in the early universe. The free-streaming of relativistic hot particles – such as neutrinos – would smear out primordial density fluctuations at small scales while cold non-relativistic particles would facilitate growth at small-scales. N-body simulations from seed inhomogeneities have shown dark matter to be cold limiting the lower mass of such particles to $\mathcal{O}(10\,\mathrm{keV})$ [22].

If dark matter was produced in thermal equilibriumin the early Universe, the particle number density (n_{DM}) at freeze-out gives information about the expected (self-)interaction cross section of the dark matter particle. The evolution of the dark matter density can be described by the Boltzmann equation. When the temperature of the Universe (T) dropped below the mass of the dark matter particle ($T \ll m_{\mathrm{DM}}$), the thermal equilibrium distribution became exponentially suppressed: $n_{\mathrm{DM}} \sim \mathrm{e}^{-m_{\mathrm{DM}}/T}$. When its (self-)interaction rate dropped below the expansion rate of the Universe, the dark matter number density was frozen:

$$\langle \sigma_{\mathrm{ann}} v \rangle n_{\mathrm{DM}}^{\mathrm{fo}} < H(T^{\mathrm{fo}}), \tag{1.5}$$

where $H(T^{\mathrm{fo}})$ denotes the Hubble rate at freeze-out temperature T^{fo} and $\langle \sigma_{\mathrm{ann}} v \rangle$ is product of the thermally averaged velocity and the (self)-interaction cross section of dark matter. By using the Friedmann-equations for *H(T)*, and assuming that dark matter is non-relativistic ($n_{\mathrm{DM}} \propto T^3$) one can deduce

$$\Omega_{\mathrm{CDM}} h^2 \approx \frac{10^{-37}\,\mathrm{cm}^2}{\langle \sigma_{\mathrm{ann}} v \rangle} \tag{1.6}$$

i.e. for a flat Universe with $\Omega_{\mathrm{CDM}} h^2 = 0.11$, the interaction cross section of dark matter particles is at the order of the weak scale $\langle \sigma_{\mathrm{ann}} v \rangle \approx 3 \cdot 10^{-26}\,\mathrm{cm}^3/\mathrm{s}$ with a resulting mass scale $\mathcal{O}(100\,\mathrm{GeV})$ [23](see figure 1.6).

Dark matter candidates produced in the thermal equilibrium via the above stated mechanism are classified as weakly interacting massive particles (WIMPs). The most compelling candidates for WIMPs are the lightest stable supersymmetric particles (LSPs) with $m_{\mathrm{LSP}} \sim$ GeV – TeV. Supersymmetry (SUSY) has been proposed as an extension of the Standard Model, amongst other reasons to solve the hierarchy problem (fine tuning of loop corrections) in particle physics. SUSY relates fermions and bosons via comprehensive symmetries (Poincare-group) [24]. To each of the Standard Model bosons there is a corresponding SUSY fermion and vice versa. For example, the superpartner of the spin 1 gluon is a spin 1/2 gluino. In some of its simpler formulations such as the minimal supersymmetric model (MSSM) a new quantum number is introduced: R-parity, which implies that single

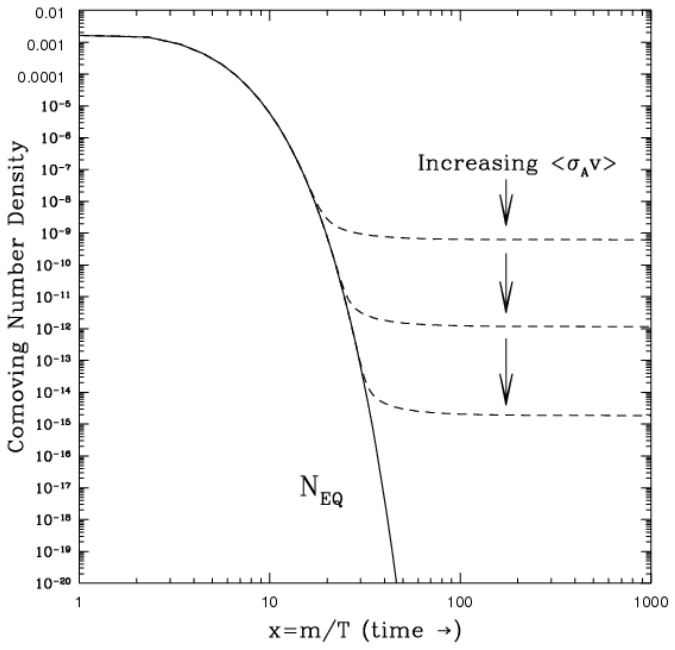

Figure 1.6.: The comoving number density as a function of the temperature where freeze-out occurs: $x = m/T$, where m = dark matter mass and T = temperature of the Universe. Dark matter drops out of thermal-equilibrium when its (self-) interaction rate drops below the expansion rate of the Universe. The number density is frozen. Fig. from [23].

supersymmetric particles cannot decay into SM particles. As a consequence, the LSP such as the Neutralino, which is the superposition of electrically neutral supersymmetric fermions, is a stable particle and an attractive dark matter candidate.

Non-thermal dark matter candidates are a valid alternative to WIMPS and result from phase transitions or decays. Axion like particles (ALPs) are a popular non-thermal dark matter candidates. ALPs are a by product of the attempt to solve the strong CP problem in particle physics and are the Goldstone bosons of a spontaneously broken global U(1) symmetry, which is introduced to the Lagrangian of the QCD in theories beyond the Standard Model. The strong CP problem is associated to the question why the strong force (QCD) in contrast to the electroweak force does not break the CP-symmetry. ALPs can be as light as $m_{\mathrm{ALP}} \geq 10^{-9}$ eV and are non-relativistic.

A large variety dark matter candidates are proposed in theories beyond the Standard model. We refer the reader to [4] and references therein for a detailed account on particle dark matter candidates.

1.3. Direct Detection of Dark Matter

It is commonly assumed that dark matter is a new type of particle (beyond the SM of particle physics), that is electrically neutral and only weakly interacting, stable on a cosmological time scale and highly collisionless. If dark matter is a particle, then there are three handles on how to detect it: indirectly via its annihilation products[7], through its (pair) production at collider experiments, for which the signature would be e.g. missing

[7] Requiring the dark matter particle to be a Majorana-particle

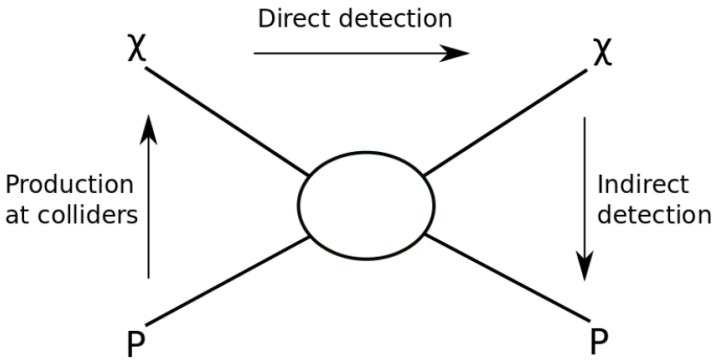

Figure 1.7.: Sketch of a Feynman diagram showing the three possible detection channels of dark matter (χ) from Standard Model particles (P) [25]. The direction of time is indicated by the direction of the arrows.

transverse energy or directly via the elastic scattering of a dark matter particle off a given detector nucleus in a laboratory detector (see Fig. 1.7).

Collider search

At collider experiments such as the Large Hadron Collider (LHC) at CERN, dark matter particles could be produced in the head-on collision of two protons at a centre of mass energy of up to 13 TeV. The multi-purpose particle detectors ATLAS [26] and CMS [27] at the LHC search for characteristic signatures from the direct production of dark matter particles or cascade decays into dark matter particles. The production of dark matter particles would result in an excess of missing transverse energy[8]. Typically, signatures from initial state radiation, so called mono-objects (hadron jet, bosons (γ, W, Z)) of the initial state [28] are used to tag the event:

$$\mathrm{p} + \mathrm{p} \rightarrow \chi\overline{\chi} + \mathrm{X}, \mathrm{X} = \mathrm{jet}\,\gamma,\ \mathrm{Z},\ \mathrm{W} \tag{1.7}$$

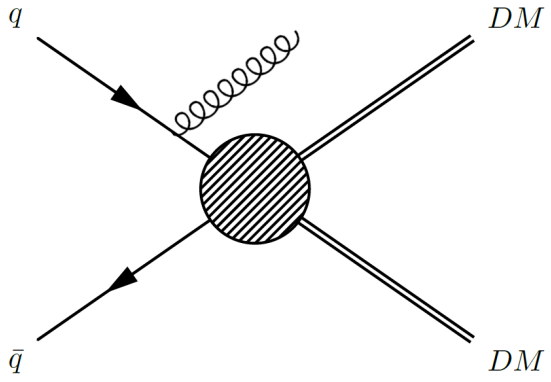

Figure 1.8.: Pair production mechanism of dark matter at the LHC. If the mediator mass is at least a few TeV, the process can be described with the help of an effective field theory [28].

[8] The longitudinal component of the parton momentum is unknown in collider experiments.

Dark matter searches at collider experiments are per se model dependent. If the mass of the mediator for dark matter production is large (> few TeV), the process can be described via a model-independent effective field theory (contact interaction) which depends on the scale of the interaction and the dark matter-nucleon scattering cross-section. Fig. reffig:DMcollider shows the pair production mechanism of dark matter via contact interaction. Collider searches for dark matter are most competitive at low dark matter masses ($\sim 4\,\mathrm{GeV}$) as high mass searches are limited by discrimination power of forward boosted jets. The dominant standard model background processes are Z and W-bosons decaying into one or two neutrinos and associated jets.

Indirect search

Indirect dark matter experiments search for the products of dark matter self-annihilation[9], scattering or decay with terrestrial or space-based particle detectors in regions with high dark matter density:

$$\chi\overline{\chi} \rightarrow \gamma\gamma,\ \gamma\mathrm{Z},\ \gamma\mathrm{H},\ \mathrm{q\overline{q}},\ \mathrm{W^{-}W^{+}},\ \mathrm{ZZ} \tag{1.8}$$

The dark matter annihilation products would give rise to a measurable flux of cosmic γ-rays, secondary charged particles such as positrons as well as neutrinos. The energy of the annihilation products could be as high as the mass of the dark matter particle. As γ-rays and neutrinos travel through space undeflected, indirect dark matter experiments could provide information about the (small-scale) distribution of dark matter. As the dark matter annihilation cross section scales with its density square, indirect searches are generally constrained to regions with high dark matter density such as the galactic centre or dwarf galaxies where annihilation, scattering or decay is more likely to occur.

Most commonly, the detectors which are used for indirect dark matter searches are motivated by other astrophysics topics and in most cases, backgrounds are foregrounds. Consequently, dark matter is identified in indirect searches either through known feature in the dark matter spectrum or through the known type of target [29]. The separation of conventional astrophysical contributions from possible dark matter signal is one of the challenges in indirect dark matter searches. Furthermore, indirect searches rely on the specific knowledge of the dark matter distribution as well as the (model dependent) dark matter coupling to standard model particles.

Earth-bound indirect dark matter experiments such as IceCube [30], SuperKamiokande [31], MAGIC [32], HESS [33] [34] or VERITAS [35] are searching for dark matter annihilation with neutrinos or with γ-rays. So far, no convincing dark matter signal has been detected in a mass range of $20\,\mathrm{MeV} - 300\,\mathrm{GeV}$. A possible γ-ray dark matter signal in the energy region $0.1 - 10\,\mathrm{keV}$ was found by the Chandra satellite and XMM-Newton [36] [37] which could be interpreted as a decay of dark matter candidates e.g. from axions [38]. The origin of the signal is still discussed controversially in the community. Space born experiments such as AMS2 [39] or Pamela [40] have detected an excess in the positron fraction in the energy range of $10 - 250\,\mathrm{GeV}$. The signal could be interpreted as a possible indirect dark matter signal, though it might also be explained by known astrophysical objects such as pulsars.

The following sections will focus on the terrestrial direct detection of dark matter (DM) particles. A detailed account on collider and indirect searches for dark matter can be found e.g. in [41] or [42] and references therein.

[9] Self-annihilation implies that dark matter was produced in the early universe in thermal equilibrium and subsequent freeze-out.

Direct detection

Dark matter particles from the local galactic dark matter halo of the Milky Way could, at an unknown rate, interact with earthbound detectors, leaving a measurable signal. Dark matter particles with a mass of 10 – 1000 GeV would scatter elastically off a nucleus of the target material of the detector. In the following, the direct dark matter detection is detailed for the well motivated WIMP as dark matter candidate. The differential recoil spectrum depends on WIMP-nucleon cross section σ, the WIMP mass (m_{W}), the local dark matter density (ρ_0) and WIMP velocity distribution ($f(v,t)$) as well as the the mass of the target nucleus (m_{t}) in the rest frame of the detector [43]:

$$\frac{dR}{dE}(E,t) = \frac{\rho_0}{m_{\mathrm{DM}} \cdot m_{\mathrm{t}}} \int_{v_{\mathrm{min}}}^{v_{\mathrm{max}}} dv^3 f(v,t) v \frac{d\sigma}{dE} \tag{1.9}$$

A detailed account on WIMP-nuclear interactions can be found in [43]. The WIMP-nucleon cross section depends on the particle-physics model and nuclear-physics processes. The recoil amplitude is given by the coherent sum of individual nucleons. For spin independent (SI) interactions, the protons and neutrons of the target nucleus contribute equally to the coherent sum, while for spin-dependent (SD) interactions, contributions are only given by odd-numbered nucleons:

$$\frac{d\sigma}{dE} = \frac{m_{\mathrm{t}}}{2\mu_{\mathrm{t}}^2} \cdot (\sigma_0^{\mathrm{SI}} \cdot F_{\mathrm{SI}}^2(E) + \sigma_0^{\mathrm{SD}} \cdot F_{\mathrm{SD}}^2(E)) \tag{1.10}$$

where μ_{t} is the reduced WIMP-nucleon mass and $\mathrm{F_{SI}}$ and $\mathrm{F_{SD}}$ are the spin-independent and spin-dependent form factors of the nucleus respectively. The spin-independent cross section is proportional to the square of the number of nucleons A ($\sigma_0^{\mathrm{SI}} \propto A^2$), if the coupling strength to protons (f_{p}) and neutrons (f_{n}) is the same:

$$\sigma_0^{\mathrm{SI}} = \frac{\mu_{\mathrm{t}}^2}{\mu_{\mathrm{p}}^2} \cdot (Z \cdot f_{\mathrm{p}} + (A - Z) \cdot f_{\mathrm{n}})^2 \tag{1.11}$$

where μ_{p} is the reduced WIMP-proton mass and Z the number of protons. The spin-dependent cross section depends on the effective coupling strength to protons and neutrons ($a_{\mathrm{p,n}}$) as well as the expectation value of the proton and neutron spin $\langle S_{\mathrm{p,n}} \rangle$:

$$\sigma_0^{\mathrm{SD}} = \frac{32}{\pi} \mu_{\mathrm{t}}^2 \cdot \mathrm{G_F^2} \cdot (a_{\mathrm{p}} \cdot \langle S_{\mathrm{p}} \rangle + a_{\mathrm{n}} \cdot \langle S_{\mathrm{n}} \rangle)^2 \frac{J+1}{J} \tag{1.12}$$

where J is the total nuclear spin and $\mathrm{G_F}$ is the Fermi coupling constant. The differential event rate for different target nuclei for a WIMP with $m_{\mathrm{W}} = 100\,\mathrm{GeV}$ and a cross-section of $\sigma_{\mathrm{SI}} \sim 10^{-45}\,\mathrm{cm}^2$.

The density profile of the local dark matter halo and its clumping at small scales are to the greatest extent unknown and under ongoing discussion. While N-body simulations of structure formation based on cold dark matter particles predict a cuspy density profile in the inner region of the halo, observations, e.g. in dwarf galaxies point towards a shallow, core like density profile. A commonly used density profiles which is adapted to N-body simulation is given by Navarro-Frank-White (NFW) [44]:

$$\rho_{\mathrm{NFW}}(r) = \frac{\rho_{\mathrm{s}} r_{\mathrm{s}}}{r \left(1 + \frac{r}{r_{\mathrm{s}}}\right)^2} \tag{1.13}$$

Dedicated measurements of radial velocities in the Milky Way and the local group by the GAIA satellite will give more insight on the nature of our dark matter halo. For

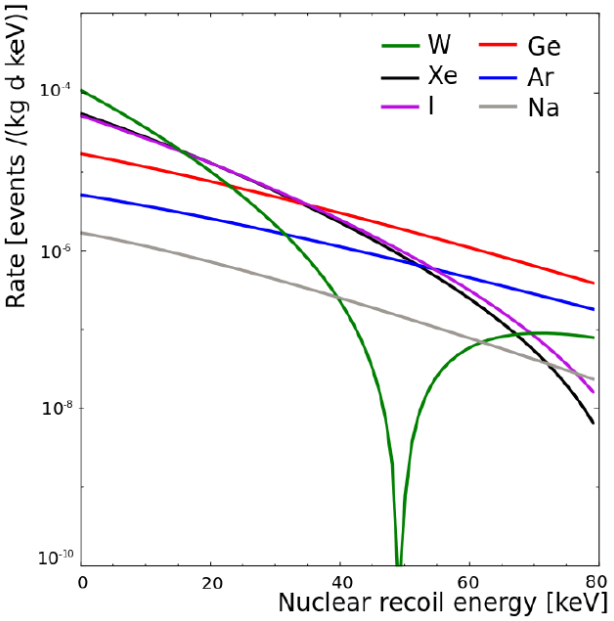

Figure 1.9.: Differential event rate as a function of recoil energy for a WIMP with $m_W = 100\,\text{GeV}$ and a cross-section of $\sigma_{SI} \sim 10^{-45}\,\text{cm}^2$ for different target nuclei (W, Xe, I, Ge, Ar, Na) [25].

the time being, the standard halo model (SHM) has been adapted by most dark matter experiments. The SHM assumes a local dark matter density according to $\rho_{DM} \propto 1/r^2$, assuming an isotropic and isothermal sphere of collisionless particles [45]. The local dark matter density is estimated to be $\rho_{loc} = 0.39 \pm 0.03\,\text{GeV/cm}^3$ [46]. The velocity distribution in the galactic rest frame of dark matter is presumed to be Maxwellian with a local escape velocity for gravitationally bound dark matter particles of $v_{esc} \approx 544\,\text{km/s}$. The Earth's velocity through the WIMP halo is then $v_E \approx 220\,\text{km/s}$. An annual modulation due to the Earth's movement in the galactic rest frame results in a variation of the expected WIMP event rate with a phase of 150 days. The amplitude is expected to be small [47].

The recoil energy in the center of mass system is given by:

$$E_R = \frac{|\boldsymbol{q}^2|}{2m_t} = \frac{\mu_t v^2}{m_t}(1 - \cos(\theta)) \tag{1.14}$$

where θ refers to the scattering angle, $\boldsymbol{q}$ refers to the momentum transfer, μ_t is the reduced WIMP-nucleon mass, m_t is the mass of the target nucleon and v the WIMP velocity relative to the target.

The measured signal of the recoil energy is convoluted by the energy resolution of the dark matter detector. The quenching factor Q

$$Q = E_{\text{measured}}/E_{\text{rec}}. \tag{1.15}$$

accounts for the probability that only a fraction of the real recoil energy is experimentally measured [42]. Quenching factors in different detector materials (Ge, Xe, Ar, I) are determined via gamma and neutron calibration sources and are typically in the order of 0.1–0.3 (a detailed account on the quenching in Ge-crystals will be given in Sec. 3.2.3).

1.4. State of the Art in Direct Detection of Dark Matter

The sensitivity of a dark matter experiment depends on its threshold, its target nucleus and mass as well as its background rate. Target masses of the same order as WIMP masses yield highest sensitivities [47]. The recoil energy from dark matter-nucleon elastic scattering is currently measured in state of the art dark matter detectors via three major signals: phonons, scintillation and ionization. Most experiments use two of those three signals to allow for particle identification or more precisely nuclear and electronic recoil discrimination.

The calorimetric measurement of the recoil energy at temperatures of a few mK is used by experiments such as CRESST, CDMS and EDELWEISS (see Fig. 1.10(a), 1.10(b) and 1.10(c)). CDMS [48] (Si- and Ge-target) and EDELWEISS (Ge-target) [49] [50] use high purity semi-conducting crystals[10] to measure the recoil energy (nuclear collisions) via a-thermal (CDMS) or thermal (EDELWEISS) phonons as well as the ionization signal of the interacting particle. The EDELWEISS-III detector, for example, is a high purity Ge mono crystal (HPGe) equipped with sputtered aluminum ring electrodes and two glued Ge-NTD (neutron transmutation doped) heat sensors which are in thermal contact with the crystal. The CDMS-type detectors use JFETs (junction gate field-effect transistor) and TESs (transition edge sensors) as charge and phonon sensors. The CRESST experiment [52] uses scintillating $CaWO_4$-crystals for the simultaneous measurement of heat and scintillation, both read out by W-TES. The temperature rise $\Delta T = \Delta Q / c_{\mathrm{sp}} \cdot m_{\mathrm{det}}$, where ΔQ is the energy transferred, c_{sp} the specific heat and m_{det} the mass of the detector is of the order of $\mathcal{O}(0.1\,\mu\mathrm{K})$ at recoil energies of $\mathcal{O}(\mathrm{keV})$ and thus challenging to measure. Both, TESs and NTDs measure the temperature rise via a change of resistance ($1\,\mathrm{M}\Omega$ at $17\,\mathrm{mK}$ for an NTD).

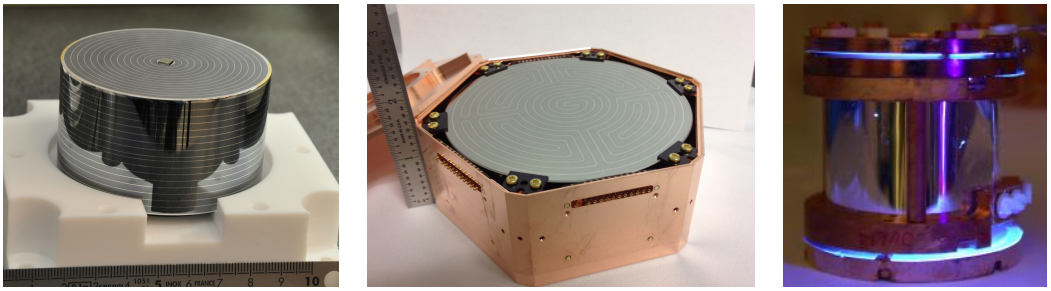

(a) (b) (c)

Figure 1.10.: State of the art cryogenic dark matter detectors. (a) EDELWEISS FID detector [53], (b) SCDMS-Soudan iZip detector [54], (c) CRESST detector module [55].

Noble liquid detectors are the world leading technology in spin-independent dark matter search. The experiment XENON100 [56], LUX [57] as well as PandaX [58] (Xenon target) and the DarkSide [59] (Argon target) measure the ratio as well as the pulse shape of the scintillation and ionization signal of interacting particles in dual phase time projection chambers (TPC). The prompt scintillation light (S1) is produced in the liquid phase of the detector and is detected via photo-detectors at the top and bottom of the TPC. The delayed scintillation light (S2) is produced in the gas phase of the detector and is proportional to the charge carriers produced by ionization.

[10] If a voltage is supplied to the crystal, Ge or Si acts as a semiconductor; the energy needed to create an electron-hole pair is roughly 3 eV in Ge or 3.6 eV in Si [51]. Electron-hole pairs are drifted to the electrodes, their number N is proportional to the measured ionization signal.

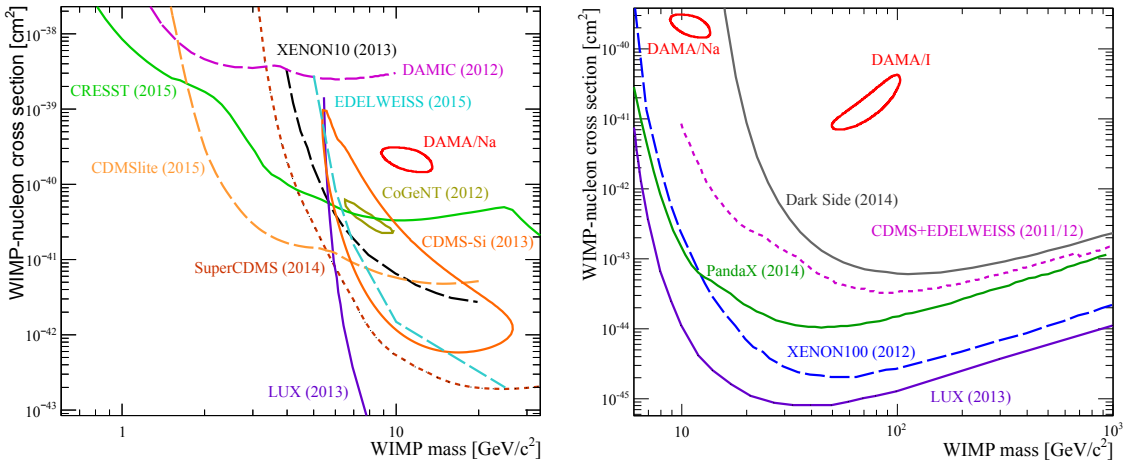

Figure 1.11.: Exclusion limits and signal indications of spin-independent WIMP-nucleon scattering cross sections for current direct dark matter experiments (right figure) [25]. Low mass WIMP exclusion limits are shown in the left figure.

Solid scintillators read out by photomultiplier tubes with scintillation-only signal are employed by DAMA/LIBRA [60] (NaI) or KIMS [61] (CsI). Further example of dark matter technologies use the metastability of superheated liquids (carbon or fluorine) (COUPP [62] and PICASSO [63] now merged to PICO [64]) or the directional detection of dark matter with using gas time projection detectors such as DRIFT [65].

The current limits and (conflicting) claims of a dark matter signal of spin-independent-WIMP-nucleon interactions are shown in Fig. 1.11. Possible dark matter signals are found by the DAMA/LIBRA experiment [60] at Gran Sasso via annual modulation at 9.3 σ and 14 annual cycles at an exposure of 1.33 tonne/years, as well as by CoGent [66] (Ge-Detector at liquid N_2 temperatures) with 2 σ and annual modulation, and the CDMS-II experiment [67] (three excess events at low energy in Si-detectors). All other experiments exclude a signal from dark matter in this region and signal claims are discussed controversially[11]. World leading current limits for spin independent WIMP-nucleon cross-sections are set by the LUX(2013) [68] experiment for high WIMP masses ($m_{\mathrm{DM}} > 10\,\mathrm{MeV}$) and CRESST(2015) [69] for low WIMP masses ($m_{\mathrm{DM}} < 10\,\mathrm{MeV}$).

Dark matter searches in mono-jet signatures at the LHC at a centre of mass energy of 8 TeV give complimentary exclusion limits and constrain WIMP masses below 4 GeV [42].

1.5. Future Dark Matter Experiments

During the last decade, technologies and sensitivities in rare event searches have improved significantly. Since the beginning of direct dark matter searches in the 1990s the sensitivities on WIMP dark matter has been improved by 3 orders of magnitude. Though tremendous efforts and improvements have been made by means of detector development as well as low background techniques to detect a dark matter particle, no convincing evidence has been found so far.

As of today, dark matter experiments are exploring the parameter space of 20 – 200 GeV dark matter at the order of $\sigma_{\mathrm{SI}} \sim 10^{-45}\,\mathrm{cm}^2$. Current experiments are limited by their detector mass, detector threshold as well as their background levels. To improve the

[11] Efforts are made to explain the conflicting dark matter signals by improved background models, detector thresholds and data reanalysis.

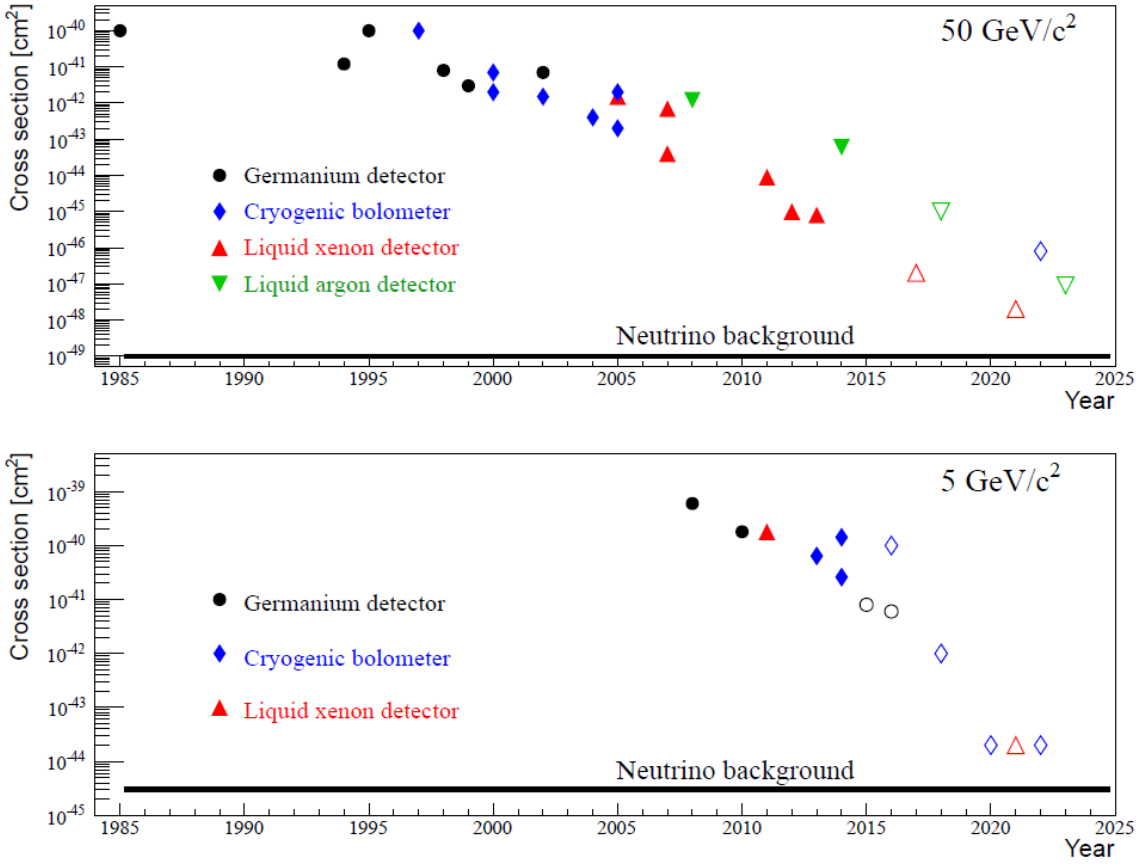

Figure 1.12.: Past, present (solid markers) and expected (empty markers) event rates in current and future dark matter searches for high mass (top) and low mass (bottom) spin-independent WIMP-nucleon scattering [25]. Black round markers represent p-type point Ge-detectors at liquid N temperatures, blue square markers represent cryogenic bolometers ($CaWO_4$, Ge, Si), red upwards pointing triangular markers represent liquid xenon detectors and green downwards pointing triangular markers represent liquid argon detectors.

sensitivity of future dark matter detectors one has to increase the mass and the exposure time of the experiment or decrease the detector energy threshold while at the same time reducing background levels drastically. Future dark matter experiments are being planned to explore the parameter space of spin-independent WIMP-nucleon elastic scattering down to WIMP masses of the order of 0.1 GeV and WIMP-nucleon cross-sections down to the neutrino floor $\sigma_{SI} \sim 10^{-48}\,\mathrm{cm}^2$. Fig. 1.12 shows typical event rates for future rare event searches.

There are two common trends to be observed in future dark matter experiments:

1. Standard WIMP searches
2. Low mass WIMP searches

Noble liquid experiments such as XENON1T/nT [70] (successor of the XENON100-experiment) and LZ [71] (successor of the LUX/Zeplin experiment) will explore the standard (MSSM) WIMP space down to cross-sections of $10^{-49}\,\mathrm{cm}^2$ by means of increasing their fiducial masses to n-tonne experiments. In the near future, the XENON collaboration will increase its detector mass by a factor of 10 to 1 tonne of fiducial mass of xenon aiming at a cross-section of $\sigma_{SI} = 1.2 \cdot 10^{-47}\,\mathrm{cm}^2$ after 2 tonne $\cdot$ years and a background reduction by

two orders of magnitude [72]. The LZ experiment will be set in the current LUX setup at the Sanford Underground Research Facility (SURF). It will run with a fiducial mass of Xenon of 5.6 tonnes and a sensitivity of $\sigma_{\mathrm{SI}} = 2 \times 10^{-48}\,\mathrm{cm}^2$ [73].

1.5.1. Future Cryogenic Dark Matter Experiments

In the last few years, low mass dark matter ($< 10\,\mathrm{GeV}$) searches have gained momentum. The small value of the Higgs mass ($m_{\mathrm{H}^0} = 126\,\mathrm{GeV}$ [10]) as well as constraints from collider experiments hint that the mass scale of SUSY is large and by this looses its "naturalness". This in turn has lead to a paradigm shift towards extended models of SUSY which allow for lighter dark matter masses [74]. Another well motivated alternative to standard WIMPs and a well suited candidate for low mass dark matter is proposed in models of Asymmetric Dark Matter (ADM). ADM is motivated by the observed similarity of the densities of dark and visible matter ($\rho_{\mathrm{DM}}/\rho_{\mathrm{vis}} \sim 5$). ADM-models postulate an asymmetry between dark matter particles and anti-particles similar to the known baryonic matter and antimatter asymmetry [75]. Calorimetric solid state experiments such as EURECA [76](successor of EDELWEISS/CRESST) and SuperCDMS SNOLAB [77] (successor of CMDS) will make use of excellent detector energy thresholds, pushing the limits towards lower dark matter masses of the order of $m_{\mathrm{DM}} = 0.3\,\mathrm{GeV}$ with sensitivities to cross-sections of $\sim 10^{-43}\mathrm{cm}^2$. Both experiments will use a multi-target approach (SuperCDMS will make use of Ge and Si crystals, EURCECA will make use Ge and $CaWO_4$ crystals) to detect low mass dark matter with masses $m_{\mathrm{DM}} < 15\,\mathrm{GeV}$. Each experiment will have a payload of about 50 kg of target mass and employ low threshold heat and ionization detectors (Ge, Si) or heat and scintillation detectors ($CaWO_4$) of roughly 1 kg each, all cooled to around 15 mK by a dilution refrigerator.

In this context, the EDELWEISS-collaboration is focusing on detector R&D e.g. in Neganov-Luke amplification of the signal of the Ge-bolometer, which would allow to decrease detector thresholds down to 100 eV and achieve sensitivity to dark matter masses as low as $0.7 - 5\,\mathrm{GeV}$.

The CRESST collaboration recently demonstrated with one of the CRESST-II detector modules a sub-keV energy threshold (0.3 keV). In 52 kg·days of data taking, masses down to 0.5 GeV were explored [78]. In the near future, the CRESST-III collaboration will decrease the energy threshold of their detector modules by reducing the size of the absorber crystal [69]. By this, recoil energies of the order of 100 eV will be detectable. In-house grown crystals with improved radiopurity and an upgraded holding scheme will allow to reduce background from intrinsic contaminations.

The same trend can be observed for other calorimetric solid-state dark matter experiments such as SuperCDMS. CDMSlite (CDMS low ionization threshold experiment), a sub-experiment within the SuperCDMS cryostat at Soudan underground laboratory, uses Neganov-Luke amplification of the phonon signal. If an electric field is applied (–70 V in the case of CDMSlite) to the crystal, the heat signal increases due to the Joule heating of the detector (see Sec. 3.2.3 for a detailed account on the heat and ionizations signal in Ge dark matter detectors). CDMSlite was able to achieve an energy threshold for electron recoils of 56 eV and exclude light dark matter particles with masses between 1.6 GeV and 5.5 GeV in 70 kg·days of data taking [79] (see Fig. 1.11).

In their first proposals, the EURECA-collaboration planned to build a dark matter detector containing up to 1 tonne of cryogenic detectors (see Sec. 1.5). Recently, the strategy of

the collaboration has changed towards the detection of low mass WIMP search with a reduced detector mass of about 50 kg of EDELWEISS-III and CRESST-like detectors. If, however, tonne scale noble liquid technologies will find a convincing signal for a standard (10 – 1000 GeV) WIMP-nucleon scattering it will be essential for calorimetric experiments to confirm the signal with a complimentary technology. Even though the original 1 tonne design of the EURECA-experiment will not be realized in the near future, it is still an interesting raw model for the development of future shielding technologies for rare event searches. In the following studies, the EURECA 1 tonne design will be used to develop an active shielding concept for muon-induced and ambient neutrons in dark matter searches.

2. Shielding Concepts for Dark Matter Searches

Background is one of the major limiting factors in direct dark matter experiments. It is thus of great importance to understand and to minimize background sources and to provide a low background environment. This chapter will detail the various background sources in direct dark matter experiments together with the technologies and challenges related to the shielding techniques for current (Sec. 2.1) and future dark matter experiments (Sec. 1.5).

2.1. Background Sources and Shielding Techniques in Dark Matter Searches

Dark matter experiments commonly distinguish between three major kinds of background sources: cosmogenic, i.e. backgrounds caused directly or indirectly by cosmic rays, environmental radioactivity including Rn and its progenies, as well as radio-impurities in the detector and shielding components. The predominant *irreducible* background source in the search for dark matter are neutrons from local radioactivity, natural fission, (α, n)-reactions and cosmic-ray induced radiation. The neutrons are electrically neutral particles. Thus, a *single* elastic scattering of a neutron ($E_{\mathrm{n}} \sim \mathcal{O}(\mathrm{MeV})$) off the target can mimic a nuclear recoil equivalent to that of a WIMP elastic scatter.

The major part of rare event and dark matter experimental setups is dedicated to passively and actively reduce background sources. In the following, a short overview of the background sources is given and a standard shielding concept against each component is outlined using the example of the EDELWEISS experiment.

2.1.1. Cosmogenic Radiation

The primary source of cosmogenic radiation are secondary cosmic ray particles such as muons and hadrons. The muon rate at sea level is of the order of: $\phi_{\mu} \sim 12 \times 10^6\,\mathrm{muons/m^2/s}$. Most dark matter experiments are operated in deep underground laboratories such as the Modande underground laboratory (LSM), Gran Sasso or Soudan to reduce cosmic ray induced background sources.The EDELWEISS-III experiment, for example, is located at

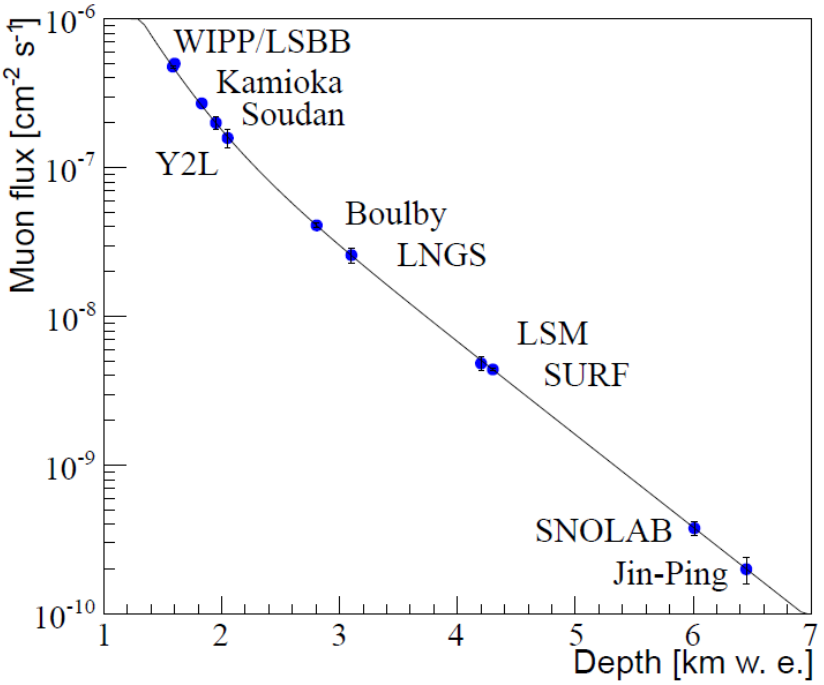

Figure 2.1.: Muon flux at various underground laboratories [25]. The Sanford underground research facility (SURF) at 1.5 km below surface houses the world leading dark matter experiment LUX. The two deepest underground laboratories are CJPL at Jin-Ping in Sichaun (China) and SNOLAB in Canada. Both laboratories specialize on neutrino and dark matter physics and are located 2 km and 2.4 km underground and by they reduce the muon-flux down to $\phi_\mu \sim 0.2\,\text{muons/m}^2\text{/day}$.

LSM under the Fréjus mountain, reducing the muon flux by 6 orders of magnitude[1] to $\phi_\mu \sim 5\,\text{muons/m}^2\text{/day}$ [80]. An overview of the muon flux in underground laboratories world wide is shown in Fig. 2.1. Section 3.2.1 in Chap. 3 will give a detailed account on the parametrization of the muon flux at sea level and underground as an ingredient for modeling muon-induced background.

The second and major source of background from cosmic radiation are (tertiary) neutrons produced via muon-, photon- or hadron-induced spallation on nuclei of the surrounding rock or detector components. Muon-induced neutrons are produced with energies up to several GeV, which are subsequently moderated by surrounding materials down energies of the order of MeV [25]. Most experiments use an active veto to tag any neutron event (i.e. nuclear recoil event) in coincidence with a muon event. In EDELWEISS, the detector is surrounded by a modular setup of plastic scintillator panels. This allows to veto muon events with an efficiency of 98 % [80] and at the same time reconstruct the muon tracks e.g. with regard to its distance to the Ge-detectors.

A third source of cosmogenic induced background is the activation of radioisotopes in detector materials – notably at sea level and even more so in air transportation. Consequently, materials in the vicinity of the detector as well as the detector material itself should be stored and even manufactured underground if possible.

[1] When reducing the muon flux by going underground, the energy spectrum gets shifted to higher energies.

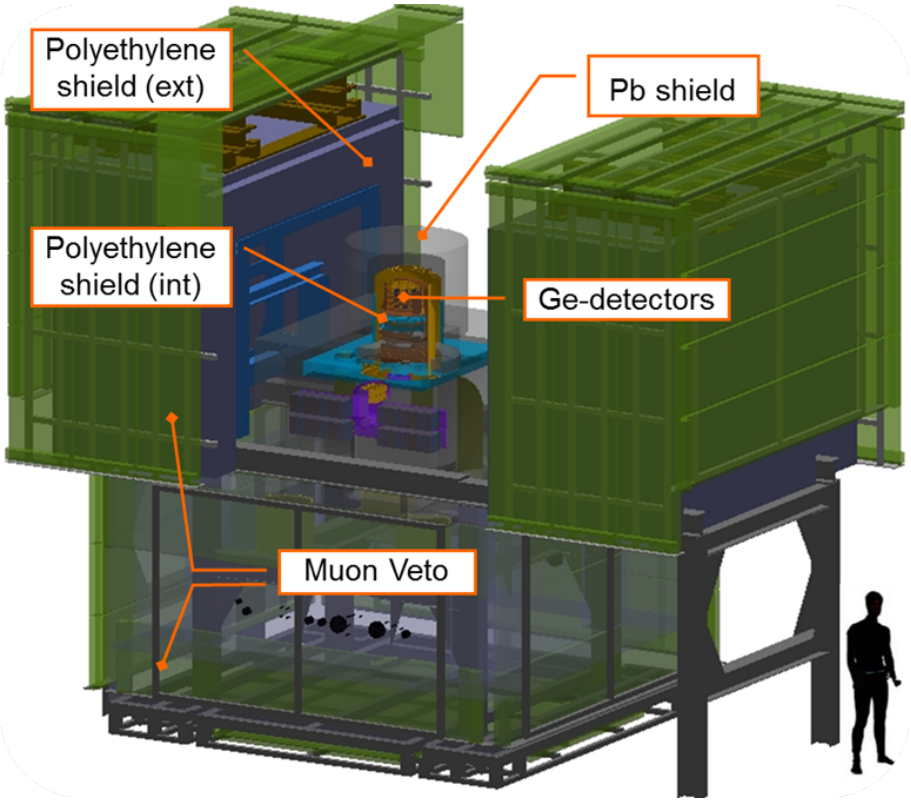

Figure 2.2.: Multilayer shielding concept of the EDELWEISS-III experiment to reduce ambient and radiogenic background. The Ge-detectors are set in a Cu cryostat which is surrounded by passive shields of 2 cm of Roman Pb and 18 cm of Pb against ambient gamma radiation and 50 cm of polyethylene against ambient neutrons. In order to reduce muon-induced backgrounds, the experiment is located in the underground laboratory (LSM) at 4200 mwe depth which reduces the muon flux to $\phi_\mu \sim 5\,\text{muons/m}^2\text{/day}$. A modular setup of plastic scintillators (muon veto) actively tags remaining muon events.

2.1.2. Environmental Radioactivity

The major source of environmental radioactivity is the rock and concrete surrounding the detector: concrete is mostly contaminated with ^{238}U, ^{232}Th, their daughter isotopes as well as ^{40}K. A typical contamination level of concrete and rock in underground laboratories is shown in table 2.1.

^{238}U and ^{232}Th successively decay via α-, β- and gamma-decay into the stable isotope ^{208}Pb. In secular equilibrium, the Th-decay chain yields 6 α's and the U decay chain 8 α's with energies of 5 – 8 MeV. The most prominent gamma emission results from the decay of ^{208}Tl with an energy of 2.6 MeV (Th-chain) or 0.8 MeV (U-chain). The U- and Th-decay chains are shown in Appendix D.7 and D.6. ^{40}K is a naturally occurring beta emitter with an endpoint energy of 1311 keV (90 % BR). The excited nucleus emits a

Table 2.1.: Contamination levels of rock and concrete at LSM [81].

Element	U (ppm)	Th (ppm)	K (ppm)
Rock	0.84 ± 0.2	2.45 ± 0.2	$(6.8 \pm 0.8) \times 10^3$
Concrete	1.9 ± 0.2	1.4 ± 0.2	$(2.5 \pm 0.4) \times 10^3$

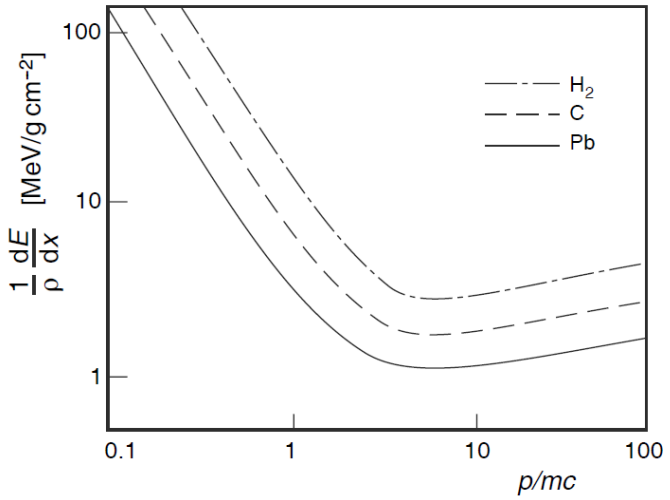

Figure 2.3.: Mean energy loss of charged particles normalized to the density of the material as a function of p/mc through ionization in H_2O, C and Pb [3].

gamma with an energy of 1460 keV. Alpha particles (He-nucleus) and β-particles (e^+,e^-) are highly ionizing when passing through matter and loose their energy continuously through Coulomb interactions with shell electrons of the medium. They are attenuated within the first few 10^{-6} to 10^{-3} m and pose a threat to mimic a rare event signal only if they are implanted within or at the surface of the target material. The stopping power due to the interaction of the charged particle with matter can be derived from the energy loss in the medium. The energy loss dE/dX of charged particles in matter through ionization can be approximated by the Bethe formula which depends on the velocity and charge of the particle as well as the medium (see Fig. 2.3). For non-relativistic particles, $dE/dX \approx 1/v^2$. For relativistic particles, $dE/dX \approx 2\,\mathrm{MeV/g/cm^2}$ [82]. For light charged particles such as electrons with energies above $E_c \approx 600\,\mathrm{MeV}/Z$, ($Z$ = atomic charge) energy loss is mainly through radiative processes (bremsstrahlung) and the energy loss depends on the radiation length (X_0) of the given material according to $-dE/dX = E/X_0$.

Neutrons from spontaneous fission of ^{238}U and (α, n)-reactions as well as the afore mentioned gamma-radiation have a penetration depth of the order of a 10^{-2} to 10^{0} m and present the dominant background from environmental radioactivity. Gamma flux from ^{40}K and ^{208}Tl is at the order of $\phi_\gamma(\mathrm{K}) \approx 0.1\,1/\mathrm{cm^2/s}$ and $\phi_\gamma(\mathrm{Tl}) \approx 0.04\,1/\mathrm{cm^2/s}$ at LSM [83]. Neutron flux from spontaneous fission of ^{238}U and (α, n)-reactions through Th- and U-decays are of the order of 10^{-6} neutrons/cm^2/s for neutron energies > 1 MeV [84].

A powerful way to reduce environmental radioactive sources is a multilayer passive shielding concept of different shielding materials around the detector setup. Gamma-rays loose their energy in matter mainly via Compton-scattering, the photoelectric effect or pair production with subsequent emission of an electron. The photoelectric effect dominates at low gamma-ray energies ($E_\gamma \lesssim 500$ keV), pair production dominates above $E_\gamma \sim 5$ MeV and Compton scattering dominates in between. The exponential attenuation of the intensity I of gamma-rays: $I = I_0 \cdot \mathrm{e}^{-al}$ depends on the thickness l, attenuation coefficient a and the density of the medium (see Fig. 2.4). High Z (atomic charge) materials with a low intrinsic activity are well suited for the suppression of gamma radiation. A common *gamma shield* in dark matter experiments is Pb due to its high Z, low n-capture and low activation. Downsides of Pb is its high intrinsic activity due to ^{210}Pb. The use of Roman Pb in the vicinity of the sensitive detectors reduces the intrinsic activity of ^{210}Pb from 2500 Bq/kg

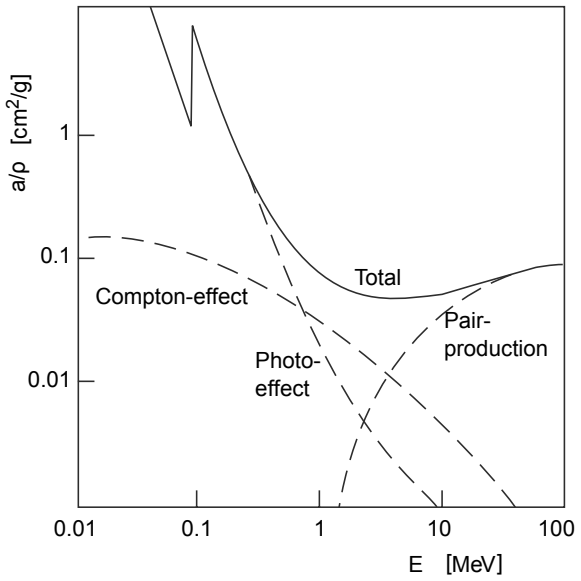

Figure 2.4.: Gamma attenuation coefficient a in Pb (normalized to density) as a function of gamma energy (E_γ) [3].

to 20 mBq/kg. The EDELWEISS-III experiment uses 18 cm of Pb and 2 cm of Roman Pb as can be seen in Fig. 2.5 and Fig. 2.2.

Neutrons loose their energy mainly via elastic and inelastic scattering with the nuclei of the medium or neutron-induced nuclear reactions such as radiative capture. In case of inelastic scattering, the nucleus gets excited and subsequently decays via gamma-ray emission. Efficient *neutron shields* are characterized by low A (atomic mass) - with favorably high H contents such as polyethylene or water. EDELWEISS-III uses 50 cm of polyethylene to shield against the external neutron flux.

One of the more critical decay products of the decay chains is Rn. As a gas, Rn is steadily released into the atmosphere ($\mathcal{O}(40\,\mathrm{Bq/m^3})$), it is then attached to surfaces where it decays via β- and α-decay into ^{210}Bi or via α-decay into ^{210}Pb, ^{210}Bi,^{210}Po and ^{206}Pb. As a consequence, most experiments are set in radon 'free' environments e.g. with the help of radon traps. The EDELWEISS-III cryostat is set in an environment with a Rn level of about 30 mBq/m^3.

2.1.3. Radioimpurities

Most materials are contaminated with natural U, Th as well as K. In the vicinity of the detector, where it is not possible to shield against radiation, it is of great importance to screen and select clean materials. Screening facilities use high purity germanium crystals (HPGe) to determine contamination levels of detector components. Typical contamination levels of materials used by dark matter experiments are shown in table 2.2. Cu is generally used in the proximity of the dark matter detectors as it can be electro formed [86] and thus produced at high radiopurity. Furthermore, it has a high neutron capture cross-section. Downsides of Cu are its low Z and cosmogenic production of radioactive nuclei. Capacitors, resistors, transistors need special attention if placed close to detectors (ceramics are carriers of U, Th and K).

Next to the selection of materials, surface contamination can be suppressed using data analysis together with the fiducialization of the dark matter detector volume.

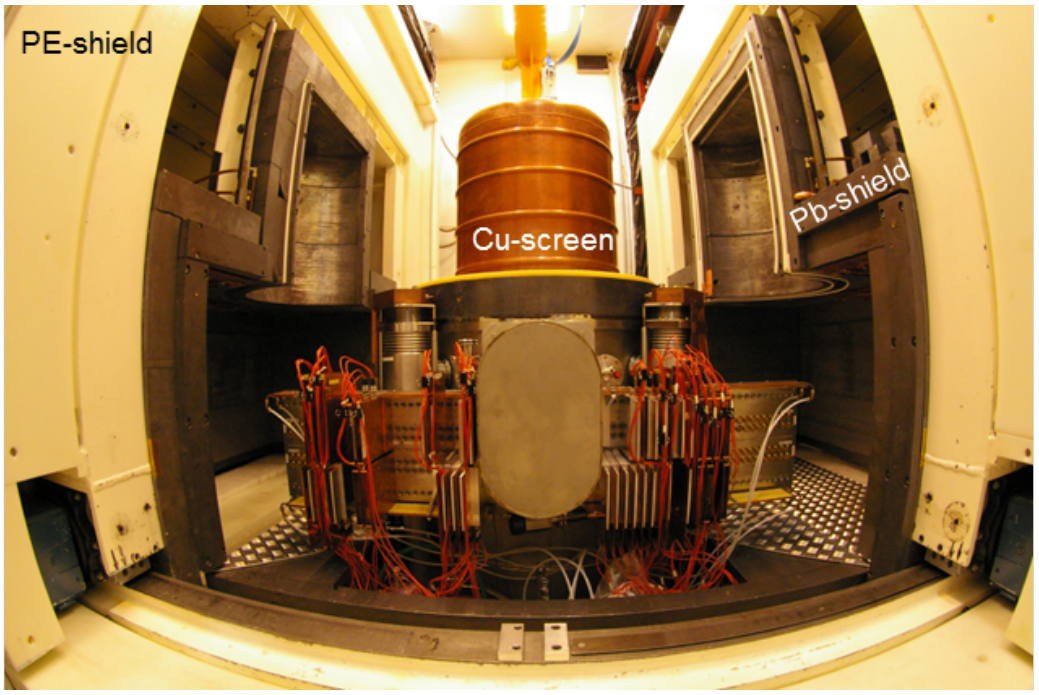

Figure 2.5.: Multilayer shielding concept of the EDELWEISS-II experiment to reduce ambient background. The Ge-detectors are set in a Cu cryostat which is surrounded by 2 cm of Roman Pb, 18 cm of Pb and 50 cm of polyethylene.

Characteristic event features:
Finally, most experiments make use of particle identification to discriminate between nuclear and electronic recoils, i.e. electronic and gamma versus neutron interactions. EDELWEISS Ge-detectors use the ratio of total energy deposit in the detector given by the heat signal, and the ionization signal where the ratio for electron recoils is set to one. The discrimination between single and multiple nuclear scattering via segmentation of the crystals is a powerful technique to reduce nuclear recoil backgrounds. As WIMPs are expected to interact only once within the target material, all multiple scatters can be dismissed as background. Noble liquid experiments such as XENON1T use the ratio of total energy deposit in the detector given by the prompt scintillation signal, and the ionization signal (delayed scintillation) as well as a 3D position reconstruction to dismiss multiple nuclear recoils.

Table 2.2.: Contamination levels in mBq/kg of shielding and detector components. Data taken from dedicated HpGe measurements for EDELWEISS in 2011.

Element	U	Th	K	210 Pb	Co	Cs
Cu	<3	<2	25	-	2	-
NOSV Cu	< 0.016	0.012	<0.11	-	-	-
Stainless steel	< 1	< 1	-	<10 [85]		
Pb	1	1	-	-	-	-
Polyethylene	0.65 ± 0.08	0.3 ± 0.07	< 1	< 3	< 0.06	< 0.06
Kapton connectors	14 ± 7	187	67 ± 31	150 ± 98	-	-
Axon cables(1)	182 ± 70	13.0 ± 2.5		-	-	-
Axon cables(2)	$4\pm <3$	5 ± 2	177 ± 22	138 ± 53	<5	<2
Brass screws	-	3.5 ± 0.9	<19	620 ± 254	<3	2.6 ± 1.5

With current shielding techniques, EDELWEISS-III estimates a gamma background of 70 events/kg/day in an energy region $E \in [20, 200]$ keV, which is the favored region of interest (ROI) for a signature from WIMP-nucleon interactions in Ge. An irreducible neutron background from ambient radiation of is of the order of 0.2×10^{-3} events/kg/day and arises mostly from connectors and electronics close to the bolometers [87]. The irreducible muon-induced neutron background is estimated as 0.53×10^{-3} events/kg/day [88].

2.2. Background Sources and Shielding Techniques in Future Dark Matter Searches

The reduction of background levels by one to three orders of magnitude in future rare event searches is crucial to achieve proposed sensitivities. Sensitivities to cross-sections of $10^{-48}\,\mathrm{cm}^2$ (or less) require a background reduction below one event per tonne and year to stay background free. Limiting background sources at these sensitivities are the radio-purity of materials, muon-induced neutrons as well as the "neutrino floor". The following summarizes an extract of new measures (complementary as well as improvements to the ones listed in Sec. 2.1) on how to reduce intrinsic as well as muon-induced background sources.

2.2.1. Intrinsic Material Contaminations

Neutrons from fission and (α,n)-reactions from natural U and Th are the dominating source of intrinsic backgrounds. Two future trends can be observed:

1. Improvement in radiopurity of materials
2. Active tagging of ambient neutrons

Improvements with respect to radio-purity are investigated primarily for Cu, front end electronics as well as the target itself. Most experiments refrain from using Pb in their shielding entirely, even though it is a very efficient gamma shield, due to its high contamination with ^{210}Pb. Instead, water shields are used as a clean alternative. As a result, the size of the experimental setup increases significantly as a reduction of roughly six orders of magnitude of gamma (neutron)-flux requires about 3 m (1 m) of water (see Fig. 2.6).

Next to Pb, front-end electronics, cabling and connectors are the dirtiest parts in a detector, with room for improvement. In-house production of clean electronics and cables of less mass and higher radiopurity(e.g. Majorana Demonstrator [89]) or an extra internal polyethylene shield against electronics closest to detectors (e.g. EURECA) are new measures to reduce intrinsic contaminations. Most dark matter experiments use Cu in the vicinity of the target material. Though Cu is already very radio-pure (NOSV < 0.01 mBg/kg in U/Th), Cu surface treatment such as etching (e.g. CUORE [90]) can reduce surface contamination further. Next to surface treatments, surface backgrounds from ^{210}Pb, Bi and Po which are implanted at the target surface can be reduced effectively if the fiducial volume of the detector is increased. This will result in a better self-shielding and is realized in most detector upgrades (e.g. XENON1T, SuperCDMS).

Furthermore, the storage and processing of materials in a clean (Rn free) and underground environment helps to reduce surface contamination and cosmogenic activation of material sources (e.g. SuperCDMS, CUORE). Efforts are made with respect to the prediction of activation and productions rates. As for now, production rates are only available for a few

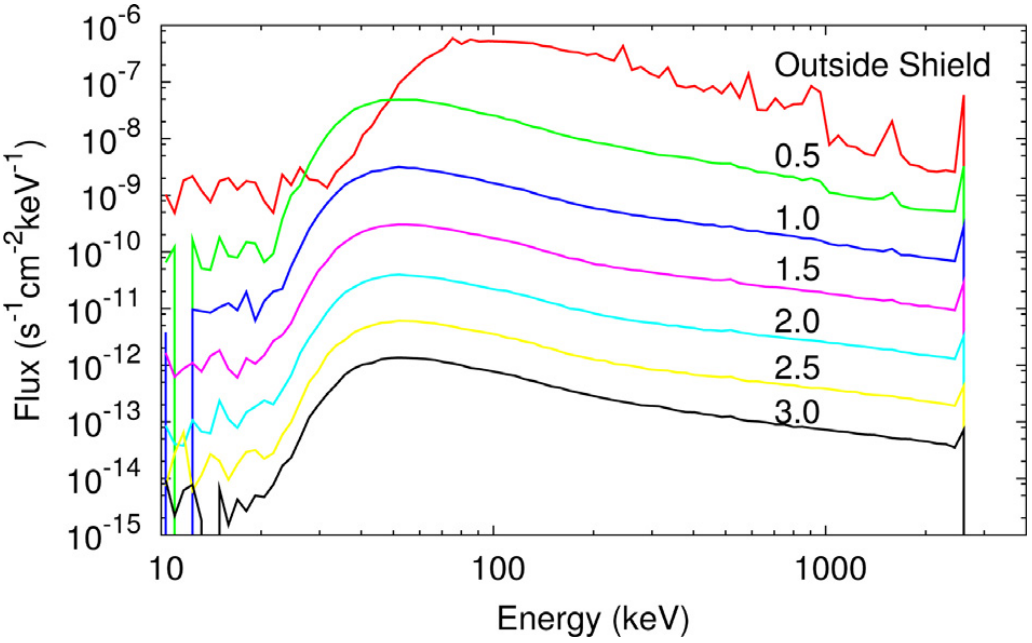

Figure 2.6.: Gamma-flux from Th-contaminations in concrete at LSM before (red) and after 0.5 – 3 m of water shielding [76].

materials such as Ge and Cu [91]. Contaminations which are intrinsic to the target materials such as are especially a problem in future noble liquid detectors. As Xe is extracted from the atmosphere, it is contaminated with Kr at a ppm level [92]. For tonne-scale experiments, contaminations though need to be of the order of and 1 ppt in Kr. To reduce intrinsic contaminations of the target itself, e.g. XENON1T uses a Kr distillation plant.

A new trend in current and future ambient shielding techniques is the active tagging of neutrons. Doped scintillators will act as an active neutron veto in the vicinity of the detector (e.g. LZ, DarkSide, SuperCDMS) and will tag and monitor ambient neutrons from contaminated materials. A detailed description of doped scintillators as neutron vetos will be given in Chap. 4.

2.2.2. Muon Induced Neutrons

Residual high-energy neutrons from deep-inelastic muon-nucleus scattering need to be tagged actively by muon vetos. To be able to reduce muon-induced neutron events to rates < 1 event/tonne/year or less highest possible muon tagging efficiencies are required. High muon veto efficiencies and a good geometrical coverage can be achieved with water Cherenkov detectors (e.g. XENON1T [93], LZ, EURECA(CDR) [76]). The water of the water Cherenkov detector also acts as an efficient passive shield against gamma and neutron radiation and can be used as an alternative to Pb (as proposed above). Furthermore, the use of water instead of Pb reduces the neutron yield from muon-induced processes. The neutron yield from muon-induced processes underground ($E_\mu \approx 280$ GeV) depends on the atomic number A according to $Y_n = a \cdot A^b$ with $b = 0.76 - 0.82$ (a is a numerical fitting coefficient) [94] [95]. A detailed account of water Cherenkov detectors as active muon vetos will be given in Chap. 3.

An additional reduction of muon-induced neutron background can be achieved when going deeper underground into laboratories such as SNOLAB (e.g. SuperCDMS) or Jin-Ping and by this reducing the muon flux and hence the neutron flux by one or two orders of magnitude.

2.2.3. Neutrino Floor

Ultimately, the limiting background of future dark matter experiments will be the "neutrino floor", the irreducible flux of solar, atmospheric and diffuse supernova neutrinos (DSNB). Future dark matter experiment will be sensitive to the coherent nuclear and electronic neutrino scattering. The coherent[2] neutrino-scattering (CNNS) is event-by-event indistinguishable from WIMP-nuclear scattering. Fig. 2.7 shows the neutrino fluxes which are backgrounds for dark matter experiments. Dark matter experiments which are sensitive to CNNS will mostly be limited by solar neutrino interactions. The dominant CNNS

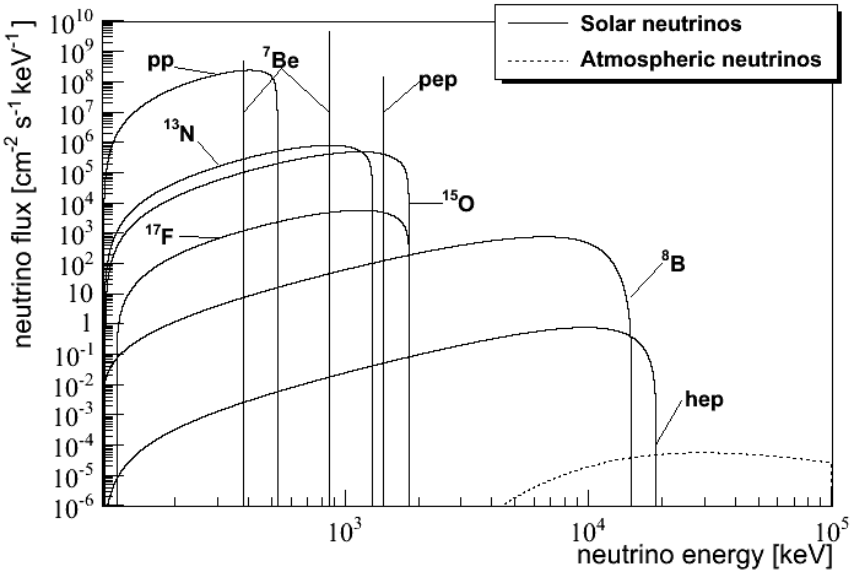

Figure 2.7.: Atmospheric and solar neutrino fluxes as a function of neutrino energy. Fig. from [96]. The dominant CNNS background from solar neutrinos arises from ^{8}B-decays and hep neutrinos.

background from solar neutrinos arises from ^{8}B-decays ($^{8}\mathrm{B} \rightarrow {}^{7}\mathrm{B}^{*} + \mathrm{e}^{+} + \nu_{\mathrm{e}}$) and hep neutrinos ($^{3}\mathrm{He} + \mathrm{p} \rightarrow {}^{4}\mathrm{H} + \mathrm{e}^{+} + \nu_{\mathrm{e}}$) from the proton-proton (pp) fusion process of the sun. For ^{8}B neutrinos, the total flux from neutral current interactions is of the order of $\phi_{\nu} \sim 5 \times 10^{6}\,1/\mathrm{cm}^{2}/\mathrm{s}$. The dominant background from neutrino-electron scattering arises from proton-proton fusion processes in the sun ($\mathrm{p} + \mathrm{p} \rightarrow \mathrm{d} + \mathrm{e}^{+}\nu_{\mathrm{e}}$) and will be the limiting background in low WIMP mass searches if the experiment lacks discrimination power between nuclear and electronic recoils [97]. The solar-neutrino background count rate in dark matter experiments depends on the energy threshold of the detector. Fig. 2.8 shows exemplary the count rate of solar neutrinos as a function of recoil energy in a Ge-target materials. Spin-independent low mass WIMPs searches ($< 10\,\mathrm{GeV}$) are limited by solar neutrino coherent scattering below cross sections of the order of $10^{-45}\,\mathrm{cm}^{2}$ [25]. The electronic recoil background from solar neutrinos is expected to be of the order of $10-25\,$events/tonne/year for low mass WIMP searches. The solar neutrino-induced nuclear recoils are expected to be of the order of 10^{3} events/tonne/year, depending on the detector threshold [91]. Atmospheric and DSNB neutrino coherent scattering will start to limit standard spin-independent WIMP searches ($\mathcal{O}(100\,\mathrm{GeV})$) below a cross section of $10^{-49}\,\mathrm{cm}^{2}$. The atmospheric and DNSB neutrino rate is of the order of $0.01\,$event/tonne/year.

[2] At low scattering energies, the wavelength of the virtual Z exchange in CNNS processes is of the order of the size of the nucleus resulting in a coherent scattering off all nucleons with an enhanced cross section [96]

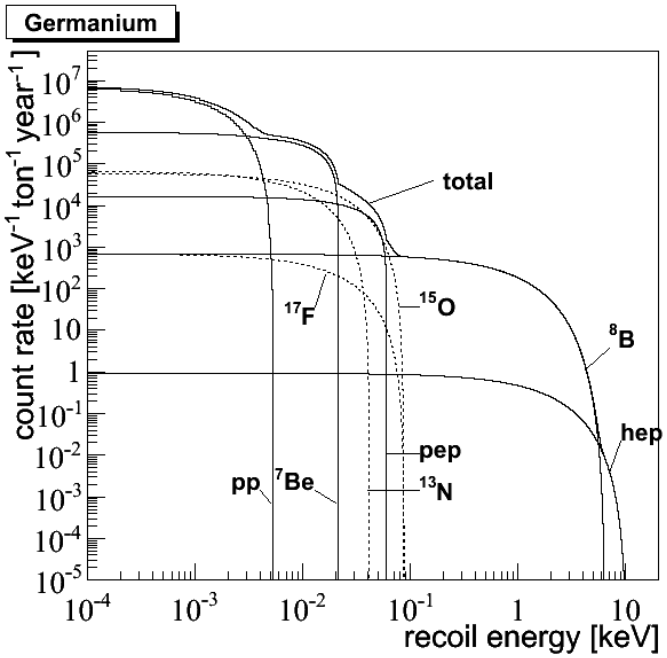

Figure 2.8.: Solar induced count rate of nuclear recoils in a Ge-target as a function of recoil energy. Fig. from [96].

Background from solar neutrinos can be reduced in standard WIMP searches via a sufficiently high energy threshold of the detector. This is not possible for atmospheric neutrinos as their energy spectrum and thus recoil energies are higher. Instead, the measurement of annual modulation might allow to exclude signals from atmospheric as well as solar neutrinos. While the flux of dark matter particles is at its highest in June, the neutrinos flux peaks around January[3] for both solar and atmospheric neutrinos[4] [25].

[3]The solid angle is larger when the Earth is nearest to the sun

[4]A modulation for atmospheric neutrinos is caused by a seasonal variation in atmospheric density

3. Design of an Active Muon Veto System for Future Dark Matter Experiments

Active muon vetos are an important element in shielding concepts of current and future rare event searches. Active muon vetos are designed to tag muon-induced backgrounds. In direct dark matter experiments, one of the dominant background sources are μ-induced neutrons as the single elastic scattering of neutrons can mimic dark matter like signals in the detector. The muon-induced background becomes more and more dominant at increasing sensitivities. Sensitivities of future experiments will increase by two orders of magnitude, down to a cross-section of $\sigma_{\mathrm{SI}} \sim 10^{-48}\,\mathrm{cm}^2$ and this necessitates the cosmogenic background suppression by the same order of magnitude. In the last couple of years, water Cherenkov detectors have found an application as active muon vetos in the context of large scale dark matter and rare event searches such as LUX [98], DarkSide [99] or Xenon1T [93]. The reasons to use a water Cherenkov detector are manifold: water Cherenkov detectors achieve high muon tagging efficiencies (at the order of 99 % or more) and at the same time the 500's of tons of ultra-pure water act as an efficient shield against external radioactivity. What is more, the use of a water shield instead of lead reduces the yield of muon-induced neutron which is roughly proportional to the atomic number of the material.

This chapter determines the key parameters of a water Cherenkov detector muon veto for the one tonne cryogenic solid state experiment EURECA. The emphasis is laid on the development of the optical system of the water Cherenkov detector. Though the water Cherenkov detector model is developed with respect to EURECA specific geometries and muon flux, the model of the water Cherenkov detector (PMT, foil, tank) can be applied to any rare event search. The studied parameters related to the optical veto systems are: the optical setup, muon tagging efficiencies and trigger, the veto dead time and the absolute muon-induced single nuclear recoil rates in one tonne of target material. The parameters are determined via extensive Monte Carlo (MC) simulations and prototype measurements. The simulations are conducted with an elaborate GEANT4 based framework which considers the detailed geometry of the detector setup, all involved physics processes, the muon flux underground as well as optical photon and neutron detection.

The chapter is organized as follows: Sec. 3.1 outlines the layout and the mode of operation of a water Cherenkov detector with the help of the EURECA water Cherenkov detector as proposed in the conceptual design report (CDR). Sec. 3.2 illustrates the implementation of

the Monte Carlo model of the muon veto system. The Monte Carlo model is validated with the help of prototype measurements in Sec. 3.3. Sec. 3.4 concentrates on the optimization of the optical system of the water Cherenkov detector. Sec. 3.5 determines the optimal trigger condition of the muon veto system and Sec. 3.7 the expected muon-induced background rate.

3.1. Concept of a Water Cherenkov Active Muon Veto

This section demonstrates the design and detection principle of a water Cherenkov detector with the help of the water Cherenkov detector muon veto of the EURECA experiment as proposed within the one tonne proposal of the conceptual design report [76]. The EURECA water Cherenkov detector has typical dimensions for a future large scale dark matter water Cherenkov muon veto. It consists of a stainless steel tank of 8 m diameter and 12 m height, filled with 400 m^3 of ultra-pure water and read out by about 100 photo-detectors (see Fig. 3.1). The inner surface of the tank is lined with a highly reflective foil. The detection principle of muons in a water Cherenkov detector is based on two principles: the (muon-induced) production of Cherenkov radiation in water and the subsequent detection with photo-detectors.

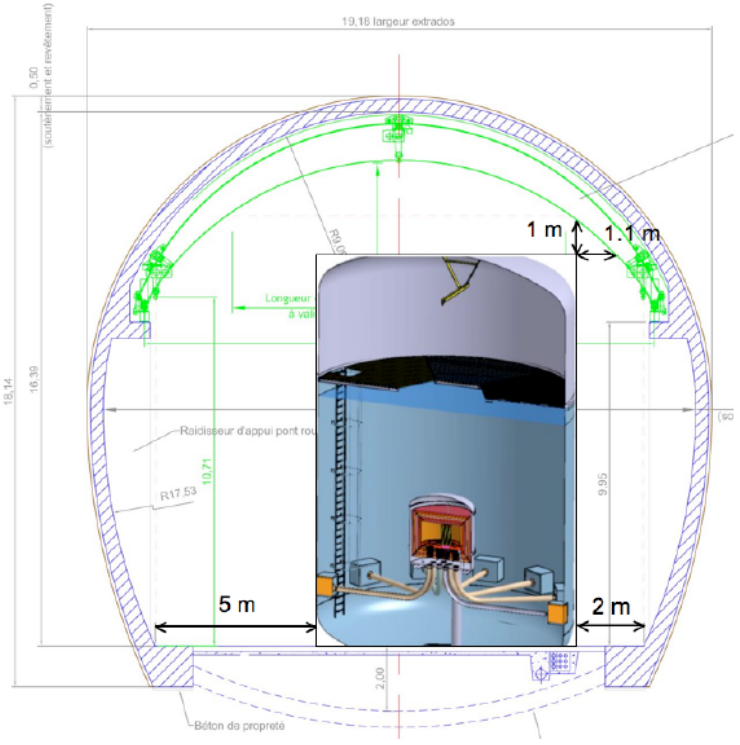

Figure 3.1.: Conceptual design of the EURECA experiment. Up to one tonne of Ge- and $CaWO_4$-detectors are set in a 2 m × 2 m Cu cryostat a 10 mK. The cryostat is surrounded by 8 cm of polyethylene and 3 m of ultra-pure water. The water (400 m^3) is contained within a stainless steel tank of 8 m diameter and 12 m height and will be equipped with roughly 100 8" PMTs. The experiment will ideally be installed at DOMUS, the planned extension of the underground laboratory at Modane (LSM), 1263 m below the Fréjus mountain [76].

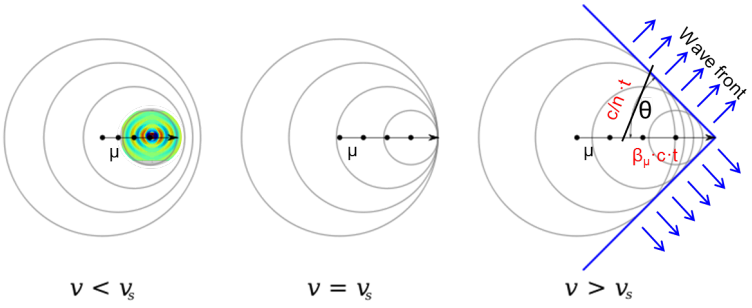

Figure 3.2.: Production mechanism of Cherenkov light: A charged particle moving through a dielectric medium produces net time varying electric dipoles along its track. If $v_s > c/n$, the radiation associated to the local dipoles interfere constructively. The wave front (Cherenkov light) is emitted in the direction of $\cos(\theta) = 1/(\beta n)$.

Cherenkov light

A muon (or any charged particle) produces Cherenkov light, i.e. an electromagnetic shock wave, when travelling through a dielectric medium with $n > 1$ (n = refractive index) and with a speed $v > c/n$ (v = phase velocity in that medium, c = speed of light in vacuum). The number of photons (N) per unit wavelength ($\lambda = 2\pi c/\omega$) and per unit path length (x) depends on the charge of the particle (q), its velocity ($\beta = v/c$) and the refractive index ($n(\omega)$) of the medium [100]:

$$\int \frac{d^2N}{dx\, d\omega} d\omega = \int_{\omega_1}^{\omega_2} \frac{q^2\omega}{c^2} \left(1 - \frac{1}{\beta^2 n(\omega)^2}\right) d\omega \tag{3.1}$$

Eqn. 3.1 defines a threshold velocity and threshold energy for the production of Cherenkov light according to $v_{thr}/c = 1/n$ and $E_{thr} = m_0 c^2 n(\omega)/\sqrt{(n(\omega)^2 - 1)}$ as radiation is emitted only if $n(\omega) \cdot \beta > 1$. The threshold energy for the production of Cherenkov photons by ultra-relativistic muons ($m_\mu = 105.7\,\text{MeV}$ [101]) in water ($n_{water} = 1.33$ [102]) is $E_{thresh} = 182\,\text{MeV}$. The number of photons emitted is [100]:

$$\frac{dN}{dx} = 2\pi q^2 \alpha \left(\frac{1}{\lambda_2} - \frac{1}{\lambda_1} \sin^2(\theta)\right) \tag{3.2}$$

with the fine structure constant $\alpha \approx 1/137$ and the Cherenkov angle θ. An ultra-relativistic muon in water emits roughly

$$\left\langle \frac{N_\gamma}{l_\mu} \right\rangle_{\text{water}} = 175\,\text{photons/cm}, \tag{3.3}$$

number of Cherenkov photons (N_γ) per muon track length (l_μ) assuming that $\lambda \in [350, 500]\,\text{nm}$, $q = 1$, and thus: $dN/dx \approx 390 \sin^2(\theta)\,[\text{photons/cm}]$ [1]. The spectrum of Cherenkov light is dominated by short wavelength within the ultraviolet (UV) to near infrared (IR) range as dispersion[1] is largest for UV-IR. $n(\omega)$ drops below one for X-rays, thus $n(\omega) \cdot \beta < 1$ falls below the condition of Cherenkov light production.

Photon Detection

The detection of Cherenkov radiation or any visible (IR-UV) light with photon detectors relies on three major aspects: the generation of a photoelectron, the amplification of the photoelectron and finally the collection of a detectable electrical signal. Water Cherenkov detectors generally use vacuum photomultiplier tubes (PMTs) as photo-detectors.

[1] The refractive index of a medium depends on the wavelength.

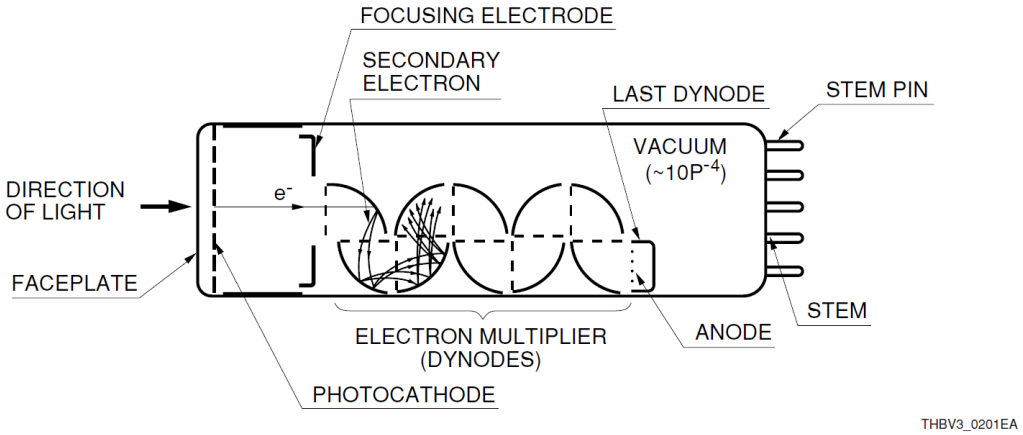

Figure 3.3.: Mode of operation of a photomultiplier tube [103]. A photon produces a primary photoelectron via the photoelectric effect within the photo-cathode which is focused by a focusing electrode and repeatedly accelerated towards several dynodes (~ 10), each time producing an avalanche of secondary electrons. The greatly amplified now measurable signal is collected by the anode.

Photomultiplier Tubes (PMT)

PMTs are a broadly used class of multi-purpose photon detectors. They consist of a vacuum tube, a photo-cathode placed behind a transparent glass window, up to 19 dynodes and a collection anode (see Fig. 3.3). A photon which passes through the glass window produces a primary photoelectron via the photoelectric effect within the photo-cathode. The material of the photo-cathode has generally a low work function, i.e. the energy needed to extract an electron from the material is low. The electron will then be focused by a focusing electrode and repeatedly accelerated towards several dynodes (~ 10), each time producing an avalanche of secondary electrons. Finally, the greatly amplified, now measurable signal is collected by the anode. The choice of glass and photo-cathode depends on the photon spectrum one wishes to detect. A typical glass material for IR to near UV range is borosilicate glass. Photo-cathode materials are generally made of compound semi-conductors based on Cs and/or Sb such as bi-alkali (SbRbCs). PMT characteristics are defined by its photo-cathode material (work function), supply voltage, dynode number and material [103]. Important characteristics are:

- Quantum efficiency (QE): probability that a photoelectron is emitted from the photo cathode when hit by an incident photon. The QE depends on the choice of cathode material.
- Collection efficiency (CE): probability that photoelectrons will land on the surface of the first dynode (effect less important with increasing number of dynodes).The CE depends on the voltage between cathode and first dynode.
- Gain (G): current amplification $G = A \cdot V^{(kn)}$. Depends on the number of interstage dynodes (n), the supply voltage (V) and the structure and material of the dynode (k), with $V \cdot k = 0.7 - 0.8$. $A = a^n/(n+1)^{(kn)}$ where a is a constant.
- Dark current: measurable current with no incident light. Main causes are thermionic emission[2] and its temperature and leakage current.

[2]The dark current from thermionic emission depends mainly on the work function of the cathode

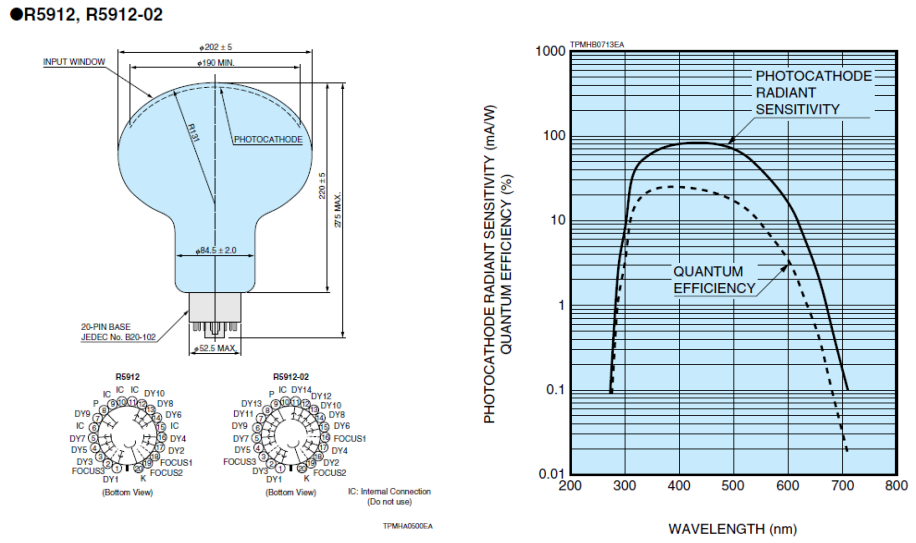

Figure 3.4.: Left: Schematic drawing and arrangement of dynodes of PMT R5912. Right: Photocathode quantum efficiency of the PMT R5912 [104].

For the EURECA water Cherenkov detector, a potentially viable PMT could be PMTs supplied by Hamamatsu Photonics [104] which are encapsulated to prevent water ingress (type R5912 ASSY). PMT R5912 is commonly used for other active muon veto systems [93], [93]. The PMT tubes have an 8" diameter, with a borosilicate window, bialkali photo-cathode and 10 box-and-linear-focussed dynodes (see Fig. 3.4 (left)). The peak quantum efficiency of the PMT R5912 lies at $\epsilon_p \approx 30\,\%$ for a wavelength of $\lambda_p = 425\,\text{nm}$ and it covers a spectral range of 300 nm to 650 nm (see Fig. 3.4 (right)). The photocathode consists of bi-alkali and covers an effective area of 190 mm. The PMT window is made of Borosilicate glass. The gain of this PMT lies typically around 10^7 with a voltage of 1500 V [104]. The high voltage would be supplied to each of the 100 PMTs individually to allow to adjust PMT response. The response of the PMTs will be calibrated and monitored with an in-house built LED diffuser light bulb. A likely choice of reflective film is the DF-2000 foil by 3M [105]. The DF2000MA specular foil is metal free, non-corroding, non-conducting and provides a reflectivity of more than 99 % in the visible spectral range (400 – 775 nm). Light above 775 nm is transmitted. Light below 400 nm is absorbed.

Water:

Ultra-pure water is required for water transparency and the provision of a low background environment. Water purity will be maintained via a water purification plant, and will be recirculated at $2\,\text{m}^3/\text{h}$. Intrinsic background from U, Th, K, Pb contaminations within the water tank will be kept at levels of the order of ppt [76]. Water recirculation together with a membrane degassing unit will keep radon levels in the water at less than $100\,\text{mBq}/\text{m}^3$.

3.2. Monte Carlo Model of a Water Cherenkov Active Muon Veto

In the context of this thesis, a GEANT4 (version Geant4.10.00.p02) [106] based Monte Carlo (MC) simulation software was developed to model the response of future water Cherenkov systems used for rare event searches – using the example of the EURECA water Cherenkov detector as described in Sec. 3.1.

The MC-package allowed to evaluate key parameters of the water Cherenkov detector system, which can only be estimated with MC simulations:

- optimize the geometry of the EURECA PMT setup (Sec. 3.4)
- study ambient background sources within the PMTs (Sec. 3.6)
- deduce most effective trigger conditions for muon-induced signals (Sec. 3.7)
- estimate the muon-induced background rate for the EURECA experiment in one tonne of germanium and an exposure time of 10 years (Sec.3.7)

This section illustrates the implementation of the MC model of the muon veto system. It is subdivided into the implementation of the water Cherenkov detector and the implementation of a one tonne cryogenic dark matter experiment (EURECA).

The main ingredients of the water Cherenkov detector simulation tool-kit are the underground muon flux, a detailed detector geometry of the tank and PMTs (including material and optical properties), muon interaction with the surrounding rock, laboratory and detector (Sec. 3.2.1), the production, tracking and detection of Cherenkov light (Sec. 3.2.2) and the data output.

The main ingredients of the dark matter experiment are a detailed detector geometry of the dark matter detectors (Ge-crystals) and cryogenic system, rare event physics processes, the production, tracking and detection of muon-induced neutrons (Sec. 3.2.3, Sec.3.2.4)) in Ge-crystals and the data output. The GEANT4 framework handles all of the above features apart from the generation of the underground muon flux (due to computation time).

GEANT4

GEANT4 is a powerful C++ based object oriented framework, the primary goal of which is to model and track the interaction of fundamental particles with matter. Initially designed to simulate high energy physics processes at particle colliders, it now incorporates a wide range of energies and physics applications such as nuclear physics, space or medical sciences. Important sub-categories of physics processes in GEANT4 are: electromagnetic, hadronic, radioactive decay and optical physics. GEANT4 assigns physics processes and models to particles, with each particle subject to several competing processes and models. In this context, a model defines the production of secondary particles whereas a process defines initial and final state of the particle in question. Each process provides the particle with a survival probability $P(l)$ for a given distance l within the detector material via its mean free path X_0. For decays, the mean free path depends on the mean life time τ: $X_0 = \gamma v \tau$, where v corresponds to the velocity of the particle.

$$P(l) = \mathrm{e}^{-\int_0^l dl/X_0(l)} \tag{3.4}$$

Materials of individual detector components are defined via their composition of elements and isotopes as well as their density ρ_{comp} and mass m_{comp}. The mean free path in the given detector material that has a fraction x_{i} by mass of the material is then given by $1/X_0 = \rho_{\mathrm{comp}} \Sigma x_{\mathrm{i}} \sigma_{\mathrm{i}} / m_{\mathrm{comp,i}}$ for a given interaction cross section σ_{i} [106]. The material composition of the EURECA and water Cherenkov detector components can be found in Appendix C. Along this chapter, we will refer to libraries of GEANT4 code which have been used for the simulations.

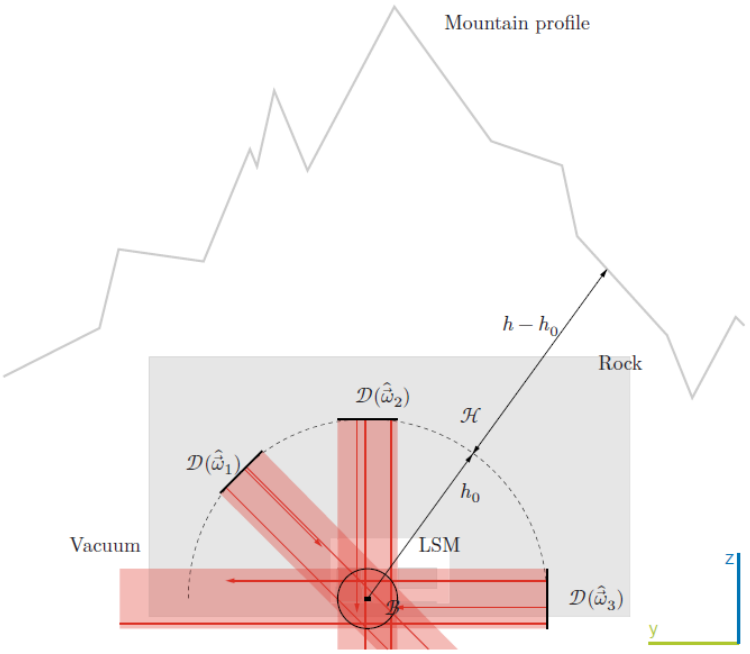

Figure 3.5.: Illustration of the muon generator as implemented for the EDELWEISS detector at LSM. The muon generator provides GEANT4 with start energy, angular information and position of the primary muon which are started on a plane disk $\mathcal{D}$ in direction $\vec{\hat{\omega}}_i$. GEANT4 propagates the primary muons in a hemisphere $\mathcal{H}$ of radius $h_0 = 30\,\text{m}$ through the rock (light gray area). The primary muons illuminate a sphere $\mathcal{B}$ of 10 m radius around LSM homogeneously. Fig. from [107].

3.2.1. Modelling the Muon Flux and Muon Interactions at LSM

Dark matter experiments are operated in deep underground laboratories to reduce cosmic rays including muon-induced background sources (see Sec.2.1). The deepest of these sites in Europe and a potential location of future rare event experiments such as EURECA is the Laboratoire Souterrain de Modane (LSM) underneath the Fréjus mountain on the French-Italian border. A Monte Carlo driven muon generator [107], which was developed for the EDELWEISS collaboration,allows to model the local muon flux at LSM based on the muon flux at sea level and the subsequent muon energy loss in rock according to the rock composition and mountain profile of Fréjus.

The major source of muons in the Earth's atmosphere is the leptonic decay of charged pions $\pi^{\pm} \rightarrow \mu^{\pm} + \nu_{\mu}/\overline{\nu}_{\mu}$ ($\tau_{\pi} \approx 26\,\text{ns}$). Charged pions in turn are produced when charged primary cosmic radiation: (about 90 % of which are protons) interacts with the atomic nuclei of the Earth's atmosphere [1]. The muon flux of atmospheric muons at sea level follows a power law of the primary particle and is approximately given by the Gaisser parametrization [108]:

$$\frac{d\phi_{\mu,0}}{dE_{\mu,0}\mathrm{d}\Omega_0} = \frac{0.14}{\text{cm}^2\ \text{s}\ \text{sr}} \left(\frac{E_{\mu,0}}{\text{GeV}}\right)^{-2.7} \left(\frac{1}{1 + \frac{1.1 E_{\mu,0} \cos\theta_0}{115\,\text{GeV}}} + \frac{0.054}{1 + \frac{1.1 E_{\mu,0} \cos\theta_0}{850\,\text{GeV}}}\right) \tag{3.5}$$

The energy loss of atmospheric muons in the rock can be parametrized according to

$$\frac{-dE}{dx} = a(E) + b(E) \cdot E \tag{3.6}$$

where $a(E)$ gives the energy loss due to ionization processes and $b(E) \cdot E$ gives energy loss due to radiative processes such as muon bremsstrahlung, electron pair creation and nuclear interaction. The energy loss depends on the rock composition as well as the energy of the muon [1]. The electronic and radiative contributions for the Fréjus mountain are approximately $a = 217\,\text{MeV}$ per meter water equivalent (m.w.e) and $b = 4.38 \times 10^{-4}$ per mwe [107]. Mwe is a measure of cosmic ray attenuation in underground laboratories and defined as the slant interaction depth according to the density of water: $1\,\text{m.w.e} = 1\,\text{g/cm}^3$. The profile of the LSM rock overburden is provided by the Wei-Rhode map [109] with a resolution of $1\,\text{deg} \times 1\,\text{deg}$ and average depth of 4850 mwe. The expected charge ratio of muons at LSM is $\mu^+/\mu^- \approx 1.37$ [101]. The differential muon flux at LSM as a function of zenith angle and as a function of muon energy is shown in Fig. 3.6 and Fig. 3.7 respectively. The single muon flux at LSM was measured by the EDELWEISS-II experiment and found to be $\phi_\mu = 5.4\,\text{muons/cm/day}$ with an average muon energy of $\langle E_\mu \rangle = 255\,\text{GeV}$ [80].

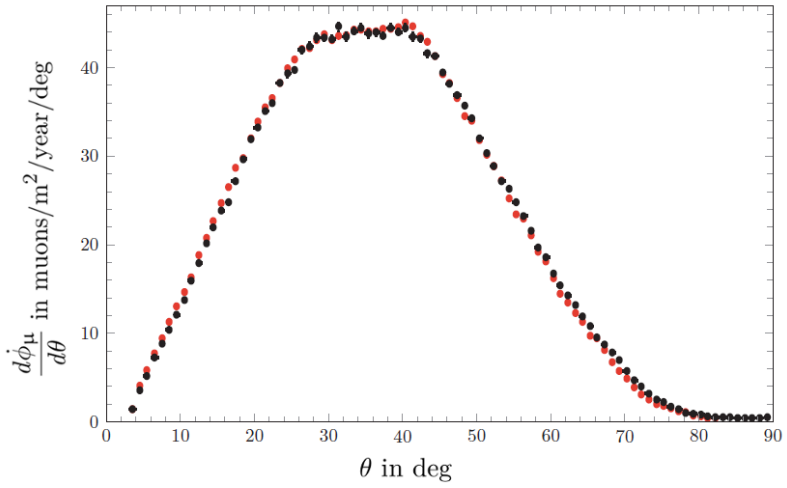

Figure 3.6.: Differential muon flux at LSM as a function of zenith angle as simulated (red) and measured in the Fréjus experiment (black) [107].

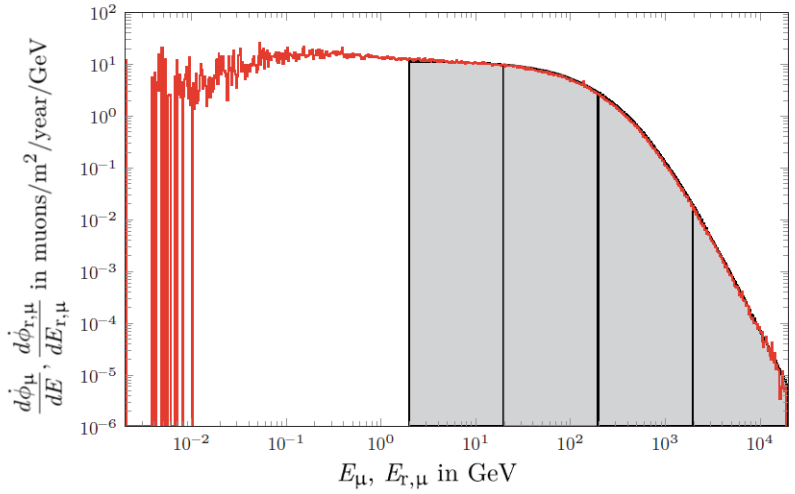

Figure 3.7.: Primary muon energy spectrum at LSM. The shaded area indicates the energy range of muons as started on a sphere of 30 m radius around the laboratory [107]. The average muon energy is $\langle E_\mu \rangle = 255\,\text{GeV}$.

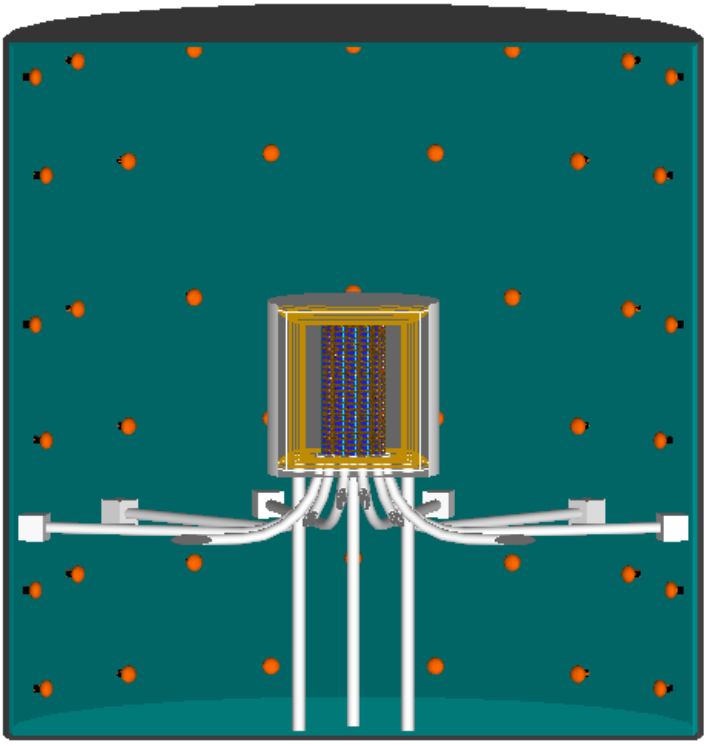

Figure 3.8.: The water Cherenkov detector as implemented in GEANT4. The water Cherenkov detector consists of a stainless steel tank of 8 m diameter and 12 m height, it is equipped with 72 8" PMTs and filled with 400 m^3 of ultra-pure water. The water Cherenkov detector is built around a 2 m × 2 m Cu cryostat which contains 1254 800 g germanium crystals. See text for details.

The muon generator provides GEANT4 with the start position, direction and energy of the primary muon[3] within a rock shell of 30 m around LSM. GEANT4 subsequently handles muon propagation, tracking and production of secondary particles within the rock shell (see Fig. 3.5).

In GEANT4 (version g4.10), nuclear interaction of muons with the production of hadrons is handled by the Bertini [110] cascade `(BERT)` based muon absorption model. The Bertini cascade is part of the GEANT4 `Shielding physics list` [111] which is recommended for shielding applications at high energies. The `standard` and `low electromagnetic physics list` handles the electromagnetic interactions of muons such as ionization, scattering and bremsstrahlung. Direct neutron production from spallation and capture is modeled with the help of `G4MuonMinusCaptureAtRest` and `G4MuonVDNuclearModel`, respectively.

3.2.2. Optical Model of a Water Cherenkov Detector

Fig. 3.8). The geometry of the water Cherenkov detector is based on the geometry of the EURECA water Cherenkov detector as described in Sec. 3.1. The water Cherenkov detector is set inside an LSM like experimental hall within the Fréjus mountain at a depth of 4000 mwe. The laboratory hall with a width of 10.60 m, length of 19.80 m and height of 10.80 m is secured by a concrete wall of 30 cm thickness and filled with air. The detector consists of a stainless steel tank of 8 m height and 8 m diameter, filled with 400 m^3 of

[3]The start values are randomly chosen from the probability density function of the local muon flux.

Figure 3.9.: PMT (8") as implemented in GEANT4. The body consists of borosilicate glass filled with vacuum. A 0.1 mm thin photo-cathode is placed behind the glass front. At the back of the PMT, a thin layer of aluminium with high reflectivity is added. A tube of low reflectivity describes the rubber encasing of the PMT.

ultra-pure water (see The tank is internally furnished with up to 100 8-inch PMTs, which can be arranged in alternating rings. The number and position of PMTs is a free parameter within the simulation framework.

Light collection in Cherenkov detectors can only be predicted accurately, if the production and tracking of optical photons is considered in the MC-model. The response of the PMTs is modelled according to the main characteristic parameters of the PMT R5912 as given by Hamamatsu: its quantum efficiency (QE $\approx 15\,\%$ at 350 nm), its collection efficiency (CE $\in [0.8, 1.0]$), its spectral range (300 – 650 nm) and its dark count (3.3 kHz, see Sec. 3.1). A photon is detected according to the probability given by the quantum and collection efficiency which is assigned to a `G4OpticalSurface`.The quantum and collection efficiency are assigned to a 0.1 mm thin photo-cathode (optical surface) which is placed behind a borosilicate glass body filled with vacuum. At the back of the PMT, a thin layer of Aluminium with high reflectivity is added along the lines of the real PMT R5912. A tube of low reflectivity describes the rubber encasing of the PMT (see Fig. 3.9). The collection efficiency (CE $\in [0.8, 1.0]$) is specific to each PMT and will be tuned according to measurements (see Sec. 3.3.7). The quantum efficiency is wavelength dependent and is set according to the data sheet provided by Hamamatsu (see Fig. 3.4).

The GEANT4 package `G4OpticalPhysics` models the production and tracking of Cherenkov light (according to Eqn. 3.1) if a material has been provided with a table of refractive indices. The resulting Cherenkov light (optical photon[4]) is linearly polarized and treated as a homogeneous monochromatic plane wave [112]. Light reflection and refraction at a boundary of two dielectric materials with refractive indices ($n_1(\omega)$, $\mathrm{n}_2(\omega)$) is calculated based on Fresnel's equations. The probability of reflection at the border of two media with refractive index n_1 and n_2 is given by [113]:

$$\mathrm{R} = \frac{1}{2}\left[\frac{\sin^2(\theta_\mathrm{i} - \theta_\mathrm{t})}{\sin^2(\theta_\mathrm{i} + \theta_\mathrm{t})} + \frac{\tan^2(\theta_\mathrm{i} - \theta_\mathrm{t})}{\tan^2(\theta_\mathrm{i} + \theta_\mathrm{t})}\right] \tag{3.7}$$

θ_i , θ_t are the angles of incidence and refraction with respect to a local's microfacet's or average normal with $n_1 \sin\theta_\mathrm{i} = n_2 \sin\theta_\mathrm{t}$. The probability of reflection and absorption at a boundary of a dielectric and a metal can be provided directly via the reflectivity of the material in question. The type of reflection is defined by the surface of a medium. It can be specular spike (perfect mirror), specular lobe and diffuse. Diffuse reflection is modeled by Lambert's cosine law around the average surface normal [113], [114] (see Fig. 3.10). Surface

[4]A photon is treated as an optical photon in GEANT4 if its energy is below 100 eV.

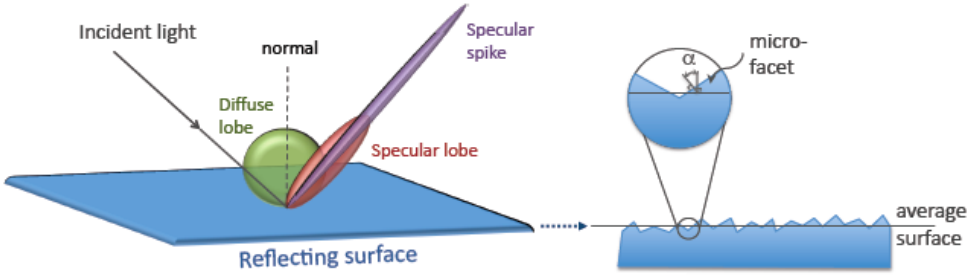

Figure 3.10.: Light reflection types which are implemented in GEANT4: Specular spike (polished surface), specular lobe, diffuse (ground surface). In case of a ground surface, the angle of refraction is given by the surface normal of a micro facet. The orientation of the micro facet is randomly chosen within a set angle (σ_α) around the average surface normal. See [113], [114] for details. Fig. from [115].

models available are - amongst others: polished (perfectly smooth), ground (rough) and front or back painted.

GEANT4 requires the user to provide all optical properties such as refractive index, absorption length and reflectivity according to their wavelength dependence. The optical properties of the water Cherenkov detector can be found in Appendix B. Prototype measurements of the PMT light collection (Sec. 3.3.7) will counter check the optical model of the water Cherenkov detector.

3.2.3. Monte Carlo Model of Cryogenic Germanium Dark Matter Detectors

The EURECA water Cherenkov detector is built around a 2 m high × 2 m of diameter Cu cryostat which can hold up to 1254 germanium or $CaWO_4$ crystals[5]. The cryostat consists of an outer vacuum container (OVC) and 5 thermal shields at 60 K, 1.8 K, 500 mK, 50 mK and 10 mK. An extra layer of polyethlyene at the 50 mK shield acts as a passive shield against ambient neutrons from the cold front-end electronics. The thermal shields are made of NOSV Cu vessel each of 3 mm thickness. The OVC will most likely be made of of PMMA as Cu is known to corrode in deionized water. The crystals – 1254 in total – are arranged in a honeycomb like structure of 22 layers, with 57 crystals in each layer. The crystal height is 4 cm, with a diameter of 7 cm and a total mass of 800 g (see Fig. 3.11).

The geometry of the crystals is implemented based on the FID800 bolometers used in the EDELWEISS-III experiment [116]. EDELWEISS-III uses cryogenic HPGe-crystals to measure the heat and ionization signal created by interacting particles [117]. The simultaneous measurement of the heat and ionization signals allows an event by event discrimination (see Sec. 1.3 in Chap.,2). A particle interacts with matter through ionization (electronic recoil) or nuclear collisions (nuclear recoil). WIMPs or neutrons will lose their energy primarily via nuclear collisions whereas gamma- and β-particles from radioactive decays interact via ionization. The discrimination power between nuclear and electronic recoils is based on the fact that ionizing particles of a given energy (E_{rec}) produce about three times more electron-hole pairs ($N_{\mathrm{e/h}}$) in germanium than WIMPs or neutrons of the same energy. The ionization signal of electronic recoils is proportional to $N_\gamma = E_{\mathrm{rec}}/\epsilon_{\gamma,\,\mathrm{e/h}}$, where $\epsilon_{\gamma,\,\mathrm{e/h}} \approx 3\,\mathrm{eV}$ is the energy needed by a photon to create an electron-hole pair in germanium at cryogenic temperatures. The ionization signal of nuclear recoils on the other

[5] In the context of this thesis only the response of Ge-crystals is studied.

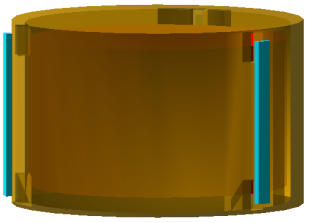

Figure 3.11.: EDW-III type bolometer as implemented in GEANT4. The HPGe-crystals has a height of 4 cm, a diameter of 7 cm and a total mass of 800 g. The crystal is placed inside a Cu encasing of 0.5 cm.

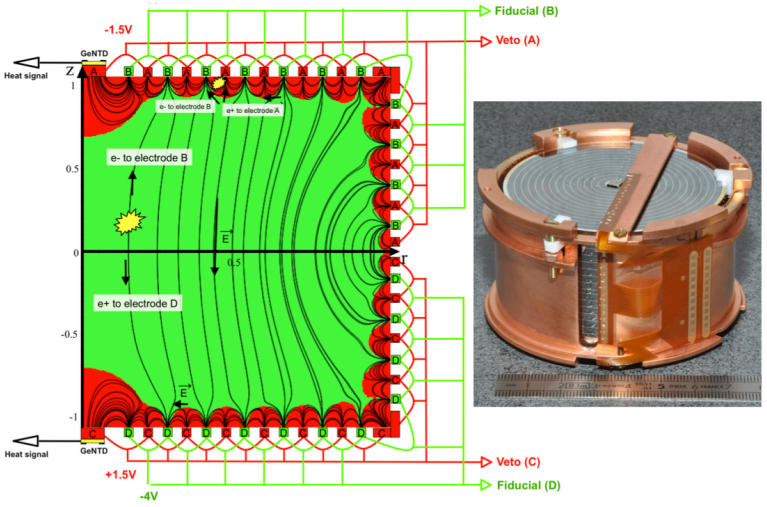

Figure 3.12.: Schematic of InterDigit field configuration of an FID800 detector.

hand is proportional to $N_{\mathrm{n}} = E_{\mathrm{rec}}/\epsilon_{\mathrm{n,\,e/h}}$, where $\epsilon_{\mathrm{n,\,e/h}} \approx 12\,\mathrm{eV}$ is the energy needed for nuclear recoils to create in electron-hole pair in Ge at cryogenic temperatures.

The energy scale of the detector derived from gamma calibrations[6] relates the heat and ionization signal to nuclear and electronic recoil: after calibration, the ionization signal E_{ion} can be expressed in terms of incident energy E_{rec} via: $E^{\gamma}_{\mathrm{ion}} = E_{\mathrm{rec}}$ for electronic recoils and $E^{\mathrm{n}}_{\mathrm{ion}} = Q \cdot E_{\mathrm{rec}}$, for nuclear recoils. The ionization yield Q is energy dependent and accounts for the difference in ionization yield of nuclear and electronic interactions in matter. The Lindhard formula gives a theoretical description of the ionization yield of nuclear and electronic interactions in matter [118]. Experimentally, the energy loss in germanium can be parametrized according to:

$$Q = E^{\mathrm{n}}_{\mathrm{ion}}/E_{\mathrm{rec}} = 0.16 \cdot E^{0.18}_{\mathrm{rec}} \tag{3.8}$$

$$Q = E^{\gamma}_{\mathrm{ion}}/E_{\mathrm{rec}} \equiv 1 \tag{3.9}$$

at recoil energies in the order of 10 keV.

The heat signal in Ge-bolometers is given by the sum of incident energy E_{rec} and the Joule heating of the detector. The Joule heating is a result of electron-hole pairs drifting to the electrodes, also known as Neganov-Luke (NL) effect and depends on the applied voltage. After gamma-calibration of the heat signal in terms of electron-equivalent, the heat signal

[6] given in electron-equivalent (keVee)

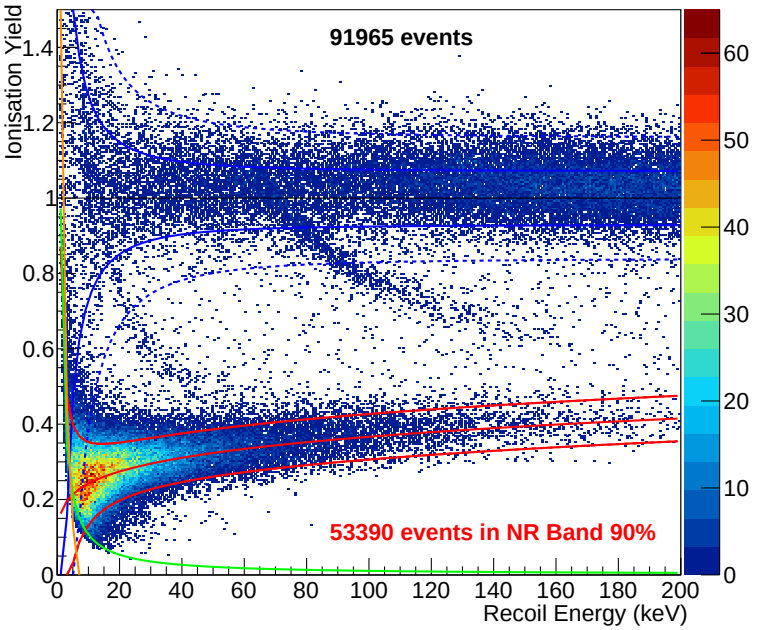

Figure 3.13.: The measured event distribution of ionization yield against recoil energy of a AmBe neutron calibration of a typical EDELWEISS Ge-detector. Electronic recoils can be found in the 90% CL electronic recoil band (blue line) with ionization yield Q = 1 nuclear recoils can be found in the 90% CL nuclear recoil band (red line) with Q < 0.5. The green and yellow line corresponds to the ionization and heat energy threshold of the detector, respectively.

of electronic recoils E_{h} is given by $E_{\mathrm{h},\gamma} = E_{\mathrm{rec}}$. The heat signal of nuclear recoils is then given by:

$$E_{\mathrm{h,n}} = E_{\mathrm{rec}} \frac{\left(1 + Q\frac{V}{\epsilon}\right)}{\left(1 + \frac{V}{\epsilon}\right)}$$

for nuclear recoils. The heat signal increases by $E_{\mathrm{NL}} = V/\epsilon_{\gamma} E_{\mathrm{i,n}}$ caused by the Joule heating. Since EDELWEISS-II, the detector is able to discriminate between bulk and surface events. Surface events have a lower ionization yield due to poor charge collection and can mimic nuclear recoil signals. The definition of an inner fiducial volume suppresses surface events efficiently. The fiducial volume of the detector is realized through a cleverly devised electrical field configuration using inter digit ring electrodes (see Fig. 3.12).

The event distribution of the ionization yield as a function of recoil energy of a gamma (^{60}Co) and neutron (AmBe) calibration typical EDELWEISS ID Ge-detector is shown in Fig. 3.13. The nuclear and electronic recoil band of the detector in question corresponds to the 90 % confidence limit (CL).

The EDELWEISS-III FID800 detector distinguishes between four event categories, based on the ionization yield of the interacting particle as well as its interaction depth: bulk nuclear recoils (WIMPs and neutrons); surface nuclear recoils (recoiling nuclei: α, Rn, Pb, Po); bulk electronic recoils (Compton scattering: gamma); surface electronic recoils (ionization: β). The bolometer response in the simulation is derived from the four aforementioned event categories where GEANT4 provides information about incident energy E_{rec}, particle type and interaction point within the detector. The reconstructed energy is smeared according

Table 3.1.: Energy resolution of the ionization and heat signal of a typical EDW-III FID800.

signal	baseline resolution (keV) FWHM	resolution at 356 keV (keV) FWHM
ionization	0.87	15.0
heat	1.74	12.2

to the gaussian energy resolution of the heat and ionization channel respectively. The energy resolution of the ionization and heat signal is taken from a typical FID800 detector from run 308 [116] (see Tab 3.1).

3.2.4. Rare Event Physics Processes

Rare event physics processes are dominated by decay processes from natural radioactivity, neutron-induced (sub – thermal – (10 MeV)) and cosmic ray induced interactions such as high energy muons and muon-induced hadronic processes. GEANT4 provides a dedicated `Shielding physics list` which handles the interaction and propagation of the afore stated physics processes. The list is used to handle the interaction and propagation of particles through the detector geometry [111].

Standard and Low Energy Hadronic Processes

Elastic, inelastic and capture processes of neutrons from sub – thermal – 2 MeV are provided by the high precision (HP) physics list which uses a data driven approach based on libraries given by G4NDL, ENDF/B-Vii [119]. Radioactive decay processes include α, β, isometric transition and electron capture processes and are modelled by `G4RadioactiveDecay`. Cross section for nuclear reactions are taken from the ENSDF database (Evaluated Nuclear Structure Data File). Hadron-nuclear inelastic scattering at energies between 20 MeV – 100 TeV is modelled by `FRITIOF` and Bertini-style cascade (20 MeV – 100 TeV) and hadron-elastic scattering processes at energies between 20 MeV – 100 TeV are provided by the `CHIPS physics list` [110].

Standard and Low Energy Electromagnetic Processes

The standard and low electromagnetic physics list includes energy loss via ionization, bremsstrahlung, multiple scattering, Compton and Rayleigh scattering, photoelectric effect, pair conversion and annihilation of electrons and positrons (`G4eEnergyLoss`, `G4eIonisation`, $\cdots$). Low energy electron and gamma-processes are based on data libraries provided by EPDL97 [120], EEDL [121] and EADL [122].

3.2.5. Data Output

All necessary simulation data is stored in an elaborate C++ ROOT [123] based event class which is subdivided into event specific properties such as event ID, muon tracks, neutron tracks, optical photon tracks, PMT hits and bolometer hits. The track classes give access to information such as time, position and energy at creation and destruction,and the parent. Further more – if needed – track specific information (such as track length in water) is stored. The hit class provides information about energy, time, hit position, and specific information for each hit type. This includes nuclear and electronic recoil energy in the case of a bolometer hit, and the number of photoelectrons in the case of a PMT hit.

3.3. Prototype Measurements and Simulations

This section will asses the reliability of the afore described water Cherenkov detector MC-model with the help of prototype measurements. The MC-model will then be used in the following sections to design and optimize the full-size detector (see Sec. 3.4 and the following). Prototyping is one of the main pillars in the R&D process of detector development. Next to the assessment of the MC-model, the water Cherenkov prototype helped to evaluate key aspects connected to the light collection of the water Cherenkov detector system, the long term performance of detector components (PMT, calibration light source) and the calibrations of the veto system.

3.3.1. Prototype Setup

The experimental prototype setup is based around a 32 cm diameter × 1.6 m long stainless steel water tank. A calibration source is centrally placed into the tank, with one encapsulated PMT R5912 at each end (PMTs SA1766 and SA1767) [124]. The tank is shown in Fig. 3.14, calibration light source and one PMT are shown in Fig. 3.15(a) and Fig. 3.15(b).

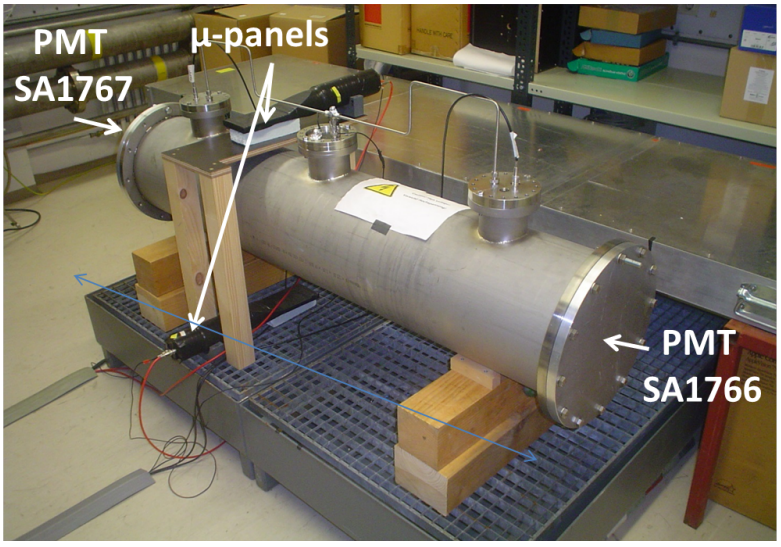

Figure 3.14.: Prototype as set up at the KIT laboratory. The water Cherenkov detector prototype consists of a 0.32 m diameter × 1.6 m long stainless steel tank filled with pure water (1.33μS/cm). Two PMTs are placed opposite of each other at the long end of the tank. PMT SA1767 is mounted to the left endcap in the above photo, PMT SA1766 is mounted to the right. Both PMTs are tilted downwards by 5 deg to make room for cabling. The PMTs are connected to the high voltage through the two outer flanges. The calibration light source is mounted to the central flange and connected to a VME source [125]. The muon panels are placed with an offset of 5 cm with respect to the central flange. Data acquisition is driven by a DRS4 board.

The calibration light source consists of a 1 mm diameter optical fibre embedded into a 50 mm diameter surface-roughened borosilicate round-bottomed flask containing a mixture of 8 % by volume glass bubbles of 65 μm size (supplied by R&G Faserverbundwerkstoffe) and 92 % Wacker SilGel 612 epoxy. The mixture was then sealed into the flask with Masterbond E3520. The remaining end of the fibre is then coupled to a 425 nm light-emitting diode (LED) light source (type 425-6-30 supplied by Roithner Lasertechnik) [126], closely matched to the 420 nm peak response of the R5912 PMTs. During data acquisitions, the LED was pulsed at a frequency of 20 Hz at a variety of voltages via a driver card through

(a) PMT SA1766 (b) Calibration light source

Figure 3.15.: PMT SA1766 of type R5912 WP ASSY-D5 (a) and in-house built calibration source (b). The calibration light source is made of a 1 mm diameter optical fibre embedded into a 50 mm diameter surface-roughened borosilicate round-bottomed flask (see text for details). The PMT tube has an 8" diameter, with a borosilicate window, bialkali photo-cathode, 10 box-and-linear-focused dynodes and is encapsulated against water ingress. The PMT is mounted onto the endcap flange.

a Versa Module Europa (VME) source all mounted within a 19" crate. The driver also provides a coincident Nuclear Instrument Module (NIM) trigger to data acquisition (DAQ). Two muon panels made of scintillating plastic blocks of size 10 cm × 15 cm × 1 cm, each optically coupled to a PMT, are placed above and below the water tank to measure coincident muon signals. The central flange prohibits to place the panels centrally with respect to the long axis of the tank. Instead, the panels are positioned with an offset 5 cm in direction of PMT SA1766.

The interior of the tank was tested under three different conditions: as an untreated surface, lined with aluminum foil with enhanced reflectivity in the blue region of the spectrum [127], and lined with DF2000MA film [105]. The PMTs are supplied by Hamamatsu Photonics [104], a detailed description can be found in Sec. 3.1. The PMTs were biased at voltages between +1800 V for calibration measurements allowing good separation of the single photoelectron (SPE) peak from noise whilst remaining safely below the maximum recommended +2000 V. The gain vs high voltage characteristics were measured at voltages between +1050 V and +1800 V. Measurements of muon signals were taken at voltages between +1500 V and +1800 V to avoid saturation. Within Fig. 3.14, the three ports across the top provide feedthroughs for electrical connections as well as a pressure balancing manifold to allow the tank to receive an overpressure of 1 bar. This is equivalent to 10 m depth of water, which is the maximum foreseen for the EURECA muon veto. The DAQ system consists of a DRS4 (Domino Ring Sampler) evaluation board, a four-channel-input switched capacitor array supplied by the Paul Scherrer Institute (PSI), Switzerland [128]. It has 12-bit resolution with a $+/-0.5$ V full range and maximum sampling at 5.12 GHz. One channel is used for each of the PMTs, one for the trigger and one spare. Software, written in-house but based on that supplied by PSI, enables data acquisition to be run over practically any length of time. The DAQ was run at its maximum sampling rate for all measurements. Attenuators were necessary to reduce PMT amplitude sizes under conditions of high light collection compared with the lower light output of the light source

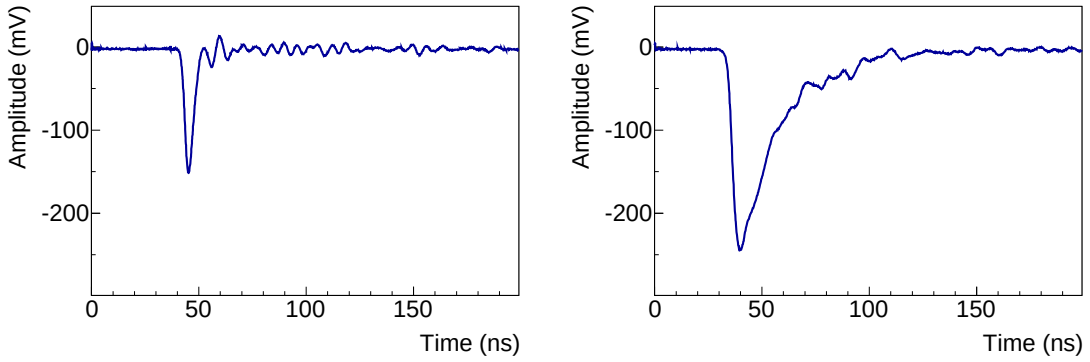

(a) LED pulse, $V_b = +1800\,V$, no attenuator. (b) Muon pulse, $V_b = +1600\,V$, attenuator = 20 dB.

Figure 3.16.: (a) Typical pulse spectrum in PMT SA1766 for an LED flash and (b) a muon event .

during SPE calibrations, due to the limited full scale of the DAQ (DRS4 evaluation board). The attenuators were of values of either 10 dB or 20 dB. The value chosen for a particular tank interior was governed by providing maximum signal without saturation working in conjunction with a reduced PMT bias offering lower gain. SPE calibrations were performed at the fixed bias voltage of $V_b = +1800\,V$ and without attenuators to maximise the peak-to-valley ratio. An additional separate facility exists consisting of an aluminium box internally lined with black film, allowing testing of a single PMT. Capacity exists within the facility to allow light sources of a fibre optic, or calibration ball, as used in the water tank, to be placed and used as a calibration source for the PMT.

3.3.2. Data Analysis

Data from the DAQ software was written directly into a ROOT file [123]. Measurements were separated into two different run types: calibration mode or muon detection mode. A series of routines identify the largest PMT pulse within a time-line, usually occurring within 30 ns of the trigger. In calibration mode, the PMT signal is recorded if in coincidence with the LED flash. In muon detection mode, a PMT signal is recorded if both muon panels were triggered by a thoroughgoing muon. A typical pulse for both run types respectively is shown in Fig. 3.16(a) (LED flash) and Fig. 3.16(b) (muon). The baseline was determined by averaging channels 20 to 100 of the 1024-channel time-line (15.6 ns total) at the start of each pulse acquisition. In order to avoid the unphysical effects (ringing [129]) present in the PMT when determining the pulse area, a semi-Gaussian curve was fitted to each side of the pulse, and the area determined from the parameters of each of these fits [130]. For the pulse rise, the Gaussian was fitted from pulse peak amplitude to 10 % of the pulse above baseline. For pulse decay, less of the pulse could be fitted due to the onset of ringing; therefore from peak amplitude to 1/3 of the pulse above baseline was used. Pulse areas were converted into values of collected charge before being histogrammed. Further fits were then applied to these histograms: noise was fitted by a sum of Gaussian plus exponential, and the single photoelectron (SPE) was fitted by a Gaussian [131]. Multiple photoelectrons were subsequently fitted with multiples of the position of the SPE Gaussian peak with identical sigma values for their widths; only the height of the peak of the multi-PE values were free parameters within these fits. An SPE spectrum for a calibration within a water tank is shown in Fig. 3.17.

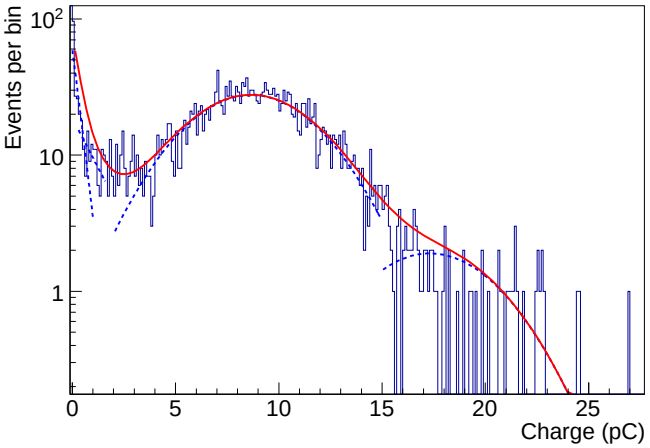

Figure 3.17.: Single photoelectron spectrum for PMT SA1766. The PMT voltage is set to $V_\mathrm{b} = +1800\,\mathrm{V}$, the LED voltage is at 4.55 V. The SPE peak corresponds to a collected charge of 8.66 pC with$P/V = 3.82$.

3.3.3. Determination of the Single Photo Electron Peak

SPE measurements were taken under all three tank interior treatments, each with water and with air [124]. These are of use as a calibration tool during muon Cherenkov light measurements and as a measure of differing light collection. A typical SPE plot is shown in Fig. 3.17 with the light source biased at 4.55 V, and in the instance of the plot with the PMTs biased at $V_\mathrm{b} = +1800\,\mathrm{V}$. The SPE peak is located at 8.66 pC with a peak to valley ratio of $P/V = 3.82$ ($P/V = 3.33$ according to Hamamatsu).

3.3.4. Gain vs Voltage

The gain G of a PMT, is a function of the voltage V_b applied across the photocathode to anode, according to [103]

$$G = A \cdot V_\mathrm{b}^{kn} \tag{3.10}$$

where A is a constant, n is the number of dynodes within the PMT (10 for the R5912 model), and k is determined by the structure and material of the dynodes. With the LED biased at 4.9 V, a number of PE spectra were obtained for both PMTs. The mean SPE as a function of applied voltage is shown in Fig. 3.18, yielding well-fitted values for k of, respectively, 0.78 and 0.75 for PMTs SA1766 and PMT SA1767).

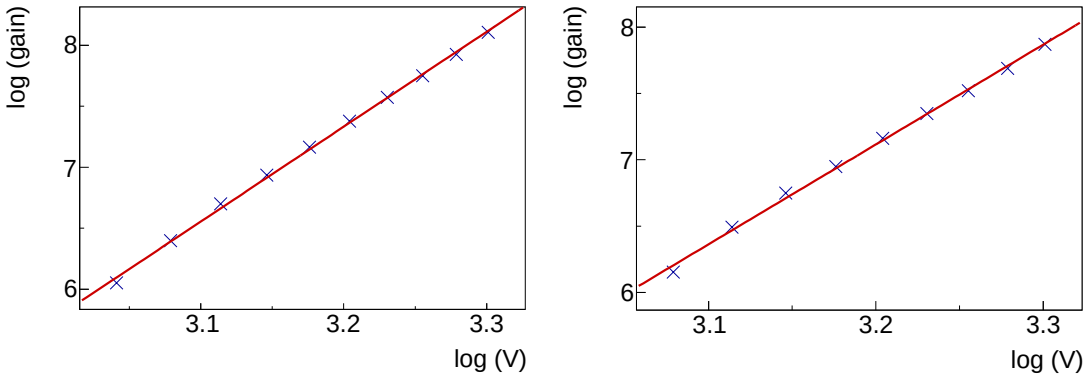

Figure 3.18.: Gain $G = A \cdot V_\mathrm{b}^{kn}$ as a function of bias voltage for PMT SA1766 (left) and PMT SA1767 (right). Fitted values for k are respectively 0.78 and 0.75.

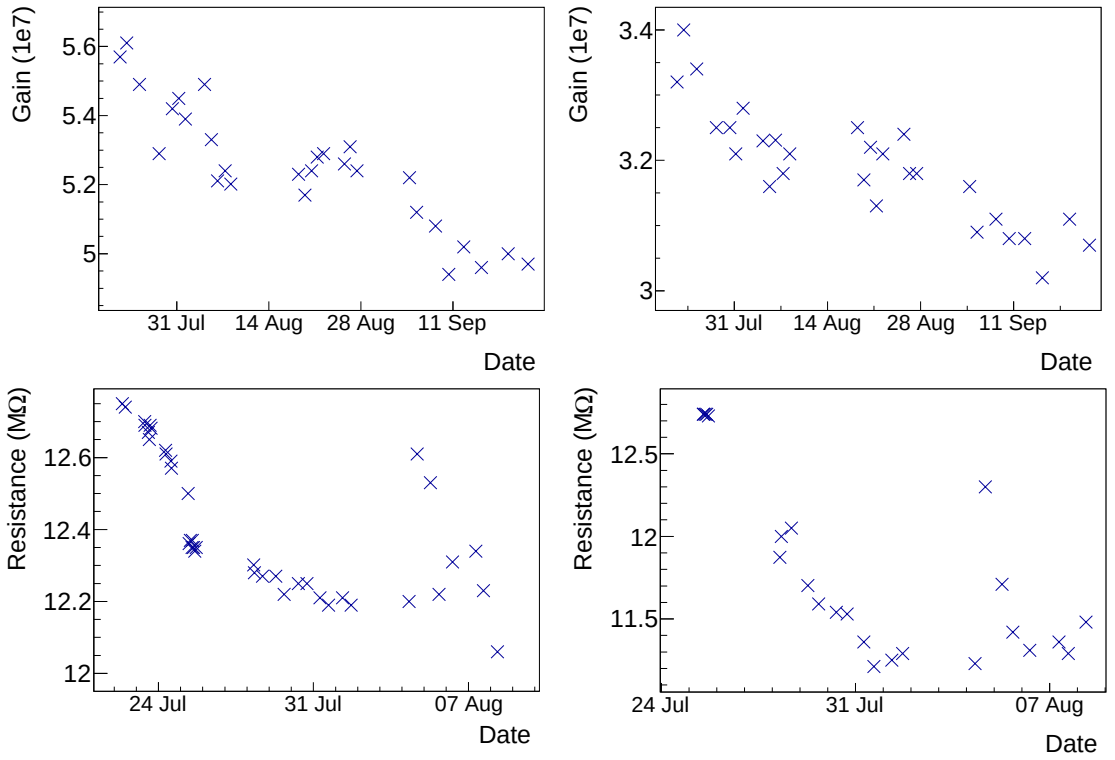

Figure 3.19.: Gain of PMT SA1766 (top left) and PMT SA1767 (top right) as a function of time. Resistance of PMT SA1766 (bottom left) and PMT SA1767 (bottom right) as a function of time.

3.3.5. Long-term Stability of PMTs in Water

Since measurement periods for current and near-future rare-event searches are of the order of years, stability is needed not only for the detectors themselves, but also for the ancillary systems such as the active shielding discussed within this thesis. With this in mind, a testing programme was initialized whereby the long-term stability of two PMTs and of the calibration source was monitored whilst in water [124]. Using the above-mentioned water tank apparatus, PMT SA1766 and PMT SA1767 along with a calibration source were placed within pure water obtained from the water purification plant at KIT. The water purity at the plant is measured periodically, the previous measurement having taken place five months earlier yielding a conductivity of 1.33 µS/cm

Gain and resistance of the VDN (voltage divider network) of the PMTs were monitored during a period of two months between end of July and end of September during which the water tank was filled and emptied several times. The gain of both PMTs fell by 10 % during this period (see Fig. 3.19). Although the resistance of the VDN decreased during this two-month period, no clear correlation can be seen between resistance and gain. Further, the VDN resistance recovered to nominal values for both PMTs once the water had been drained, but then returned close to their previous in-water resistance within about a day [124]. The gain of the two PMTs was again monitored for a period of four month in 2015 between mid July and mid November. The previously visible trend was not re-observed and the gain of both PMTs was stable within 5 % [132].

Table 3.2.: The chosen biases, attenuator and mean SPE values of PMT SA1766.

Lining	voltage (V)	attenuator (dB)	SPE (pC)
No lining	1800	20	8.43
Aluminum	1600	20	3.60
DF-2000MA	1500	20	2.16

Table 3.3.: The chosen biases, attenuator and mean SPE values of PMT SA1767.

Lining	voltage (V)	attenuator (dB)	SPE (pC)
No lining	1800	10	5.11
Aluminum	1700	20	3.44
DF-2000MA	1600	20	2.19

3.3.6. Influence of Reflective Film on Light Collection

The reflective film, and hence the light collection, is a key parameter when designing a water Cherenkov muon veto. Therefore, the cosmic ray muon response of the prototype for three different tank surfaces were measured; bare (unpolished) stainless steel, aluminium foil (blueTec) [127] and DF2000MA foil (3M) [105]. PMT voltages were reduced for the measurement with Al and DF-lining as light collection increased significantly. Each measurement was taken over a time period of 76 hours in total, intermitted every 24 h for SPE calibration measurements. PMT biases and selected attenuators were chosen for each run individually to avoid saturation of the DAQ. The chosen biases, attenuator and mean SPE values for each measurement are given in Tab. 3.2 and Tab. 3.3.

The influence of the tank surface (bare, Al-lining, DF-lining) on the light collection in PMT SA1766 is shown in Fig. 3.20.

The features of the spectrum will be discussed in the context of the MC-modlleing in Sec. 3.3.7. The difference in light collection in PMT SA1767 and SA1766 can be explained by two factors: the muon panel position as well as possible difference in collection efficiency in PMT SA1767 and PMT SA1766. The muon panel position is arbitrary. For the above measurements, the panels were positioned with an offset of 5 cm to the tank center in direction of PMT SA1766 (see Fig. 3.21). The positions influences the number of reflection a photon needs to reach PMT SA1767 or PMT SA1766. The difference in light collection will be investigated with the help of the prototype simulations in the following section. The absolute number and spectrum of detected photoelectrons in PMT SA1766 and PMT SA1767 depends on the lining and position of the muon padels and is specific to the prototype setup. The absolute number of photoelectrons will be of no interest when designing the full scale muon veto in the following sections. Instead, the performance with respect to light collection as well as the assessment of the optical MC model in the following

Table 3.4.: The mean number of collected photoelectrons in PMT SA1766 and SA1767 for different tank linings.

Lining	$\langle N_{\mathrm{PE}} \rangle$ in PMT SA1766	$\langle N_{\mathrm{PE}} \rangle$ in PMT SA1767
No lining	25	8
Aluminum	221	168
DF-2000MA	397	296

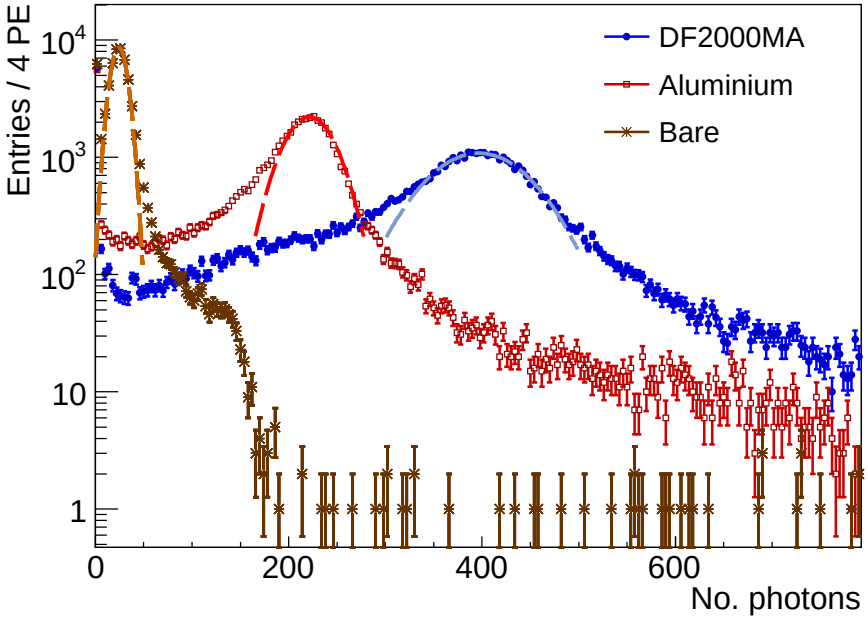

Figure 3.20.: Measured spectrum of photoelectrons in PMT SA1766. Brown markers: no extra lining is added to the tank interior. Red markers: bluetec aluminum-lining. Blue markers: DF-2000MA lining. The brown, red and blue dashed line shows the respective gauss-fit which allows to determine the PE peak of each spectrum. The fitted mean number of photoelectrons are $\langle N_{\mathrm{PE}}^{\mathrm{bare}} \rangle = 24.6$, $\langle N_{\mathrm{PE}}^{\mathrm{Al}} \rangle = 220.8$ and $\langle N_{\mathrm{PE}}^{\mathrm{DF}} \rangle = 396.7$ respectively. In total, $Evts_{\mathrm{bare}} = 57121$, $Evts_{\mathrm{Al}} = 57648$ and $Evts_{\mathrm{DF}} = 57933$ muon events were recorded.

section is of importance. In order to estimate the performance of each foil, the mean number of collected photoelectrons is determined via a Gauss-fit around $2\,\sigma$ of the peak (see Tab. 3.4), and the relative increase is studied. An increase in light collection with increasing surface reflectivity can be observed. The DF-2000-lining by 3M shows the best performance with regard to light collection. An overall increase of 15 % in reflectivity between the Al- and DF-lining leads to an increase of 55 % in number of detected photoelectrons. The observed increase by a factor of two is due to the fact that the number of surviving photons N_{ph} after reflection can be described as $N_{\mathrm{ph}} \propto r^n$, with the reflectivity r and n denoting the number of reflections. In the case of the prototype geometry, the average number of reflections on the tank surface is $n\mathrm{ref} \approx 10$ (as determined from simulations in Sec. 3.3.7), and consequently $N_{\mathrm{ph}}^{\mathrm{Al}}/N_{\mathrm{ph}}^{\mathrm{DF}} = 0.9^{10}/0.95^{10} \approx 0.58$.

3.3.7. Prototype Simulations

The water Cherenkov detector muon veto design as well as the veto performance and background estimations will be evaluated by GEANT4 based detector simulations in Sec. 3.4, 3.5, 3.6 and 3.7. In order to have confidence in the GEANT4 based model of the water Cherenkov detector, the model was verified with the help of the prototype measurements conducted in the previous sections. For this purpose, the prototype geometry is implemented within the simulation framework (see Sec. 3.2.2) as realistically as possible, and the outcome of the simulation is compared to the measurements. Key elements to the prototype simulation are: the cosmic muon flux at sea level and its interaction with the surrounding laboratory and prototype, and the production and reflection of Cherenkov light as well as the detection of photoelectrons in the PMTs (see 3.2.2).

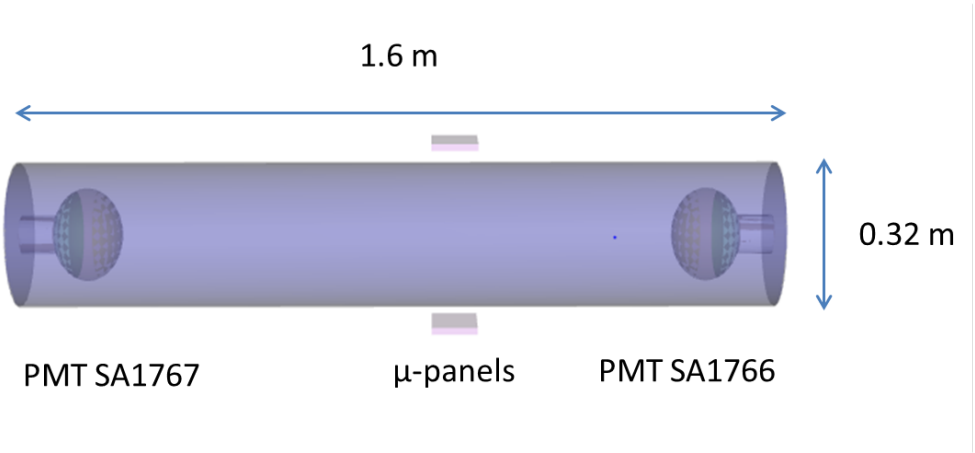

Figure 3.21.: Prototype geometry as implemented in GEANT4. It consists of a steel tank volume, a cylinder of 0.32 m diameter and 1.6 m of length, filled with ultra pure water. Two plastic scintillator volumes are placed above and below the tank. PMT SA1766 and SA1767 are positioned at ±50 cm respectively. All material and optical properties of the tank detector components can be found in Appendix C and B

Prototype Geometry

The prototype geometry as implemented in GEANT4 is shown in Fig. 3.21. It consists of a steel tank volume, a cylinder of 32 cm diameter and 1.6 m of length, filled with ultra pure water. Two plastic scintillator volumes are placed above and below the tank. PMT SA1766 and SA1767 are positioned at $z = \pm 53$ cm respectively and tilted downwards by 5 %. Initial simulations showed that we have to place the prototype setup into a simplified laboratory, a 3 m × 3 m × 3 m air volume surrounded by a concrete wall of 50 cm thickness. The concrete is an important source of secondary particles, which in turn are an important trigger source of the low photoelectron part of the spectrum. The response of PMT SA1767 and PMT SA1766 is implemented according to the data sheet of PMT R5912 provided by Hamamatsu [104] (see Sec. 3.2.2). The peak quantum efficiency is QE ≈ 23 % at $\lambda_{\mathrm{PMT_{max}}} = 420$ nm. The DF2000MA lining is modeled via the wavelength dependent reflectivity as provided by 3M [105]. The reflectivity is of the order of $R_{\mathrm{f}}^{\mathrm{DF}} > 99\,\%$ for $\lambda_{\mathrm{PMT_{max}}} = 420$ nm (see Fig. 3.22).

After extensive simulations with different optical models and polish types, the unified model is selected, assuming a perfectly polished, i.e. mirror-like, surface. Next to the unified model, which was developed by Detect at Triumf [113], the influence of light collection was studied using the glisur model, as well as different degrees of polishes. We found that the glisur model (the former optical model of choice in GEANT3) does not reproduce the shape of the afore measured spectrum. It showed a broader distribution in comparison to the unified model. The same influence could be seen when decreasing the degree of

Table 3.5.: Table of optical properties: refractive index n and absorption length a at $\lambda_{\mathrm{PMT_{max}}} = 420\,\mathrm{nm} \triangleq 2.95\,\mathrm{eV}$

Material	n	a (m)	reference
Air	1.00	∞	[133]
Borosilicate glass	1.52	13.4	[134]
Water	1.33	220	[135]

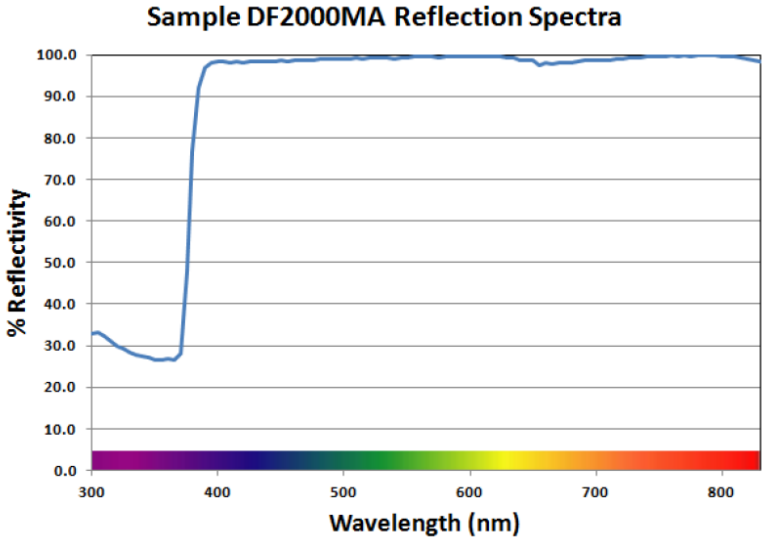

Figure 3.22.: Reflectivity of the DF-2000 foil as a function of wavelength. The foil exhibits a reflectivity of more than 99 % in the visible spectral range (400 – 775 nm) and drops below 30 % in the UV-region (< 400 nm) [105].

polish of the foil. Since the foil is a pure specular reflector, a perfectly polished surface is a reasonable assumption[7]. Key optical informations can be found in Tab. 3.5.

Muon Flux at Sea Level

Prototype measurements of the water Cherenkov detector were conducted at the KIT laboratory at sea level [124]. The muon flux at sea level is generated using a dedicated muon generator as developed by [107] see Sec. 3.2.1. The muon generator for the atmospheric muon flux at sea level is derived from the Gaisser parametrization according to [136]. The Gaisser formula (see Eqn. 3.5 is corrected for muon energy loss in a standard US atmosphere as well as the muon decay probability. The final muon energy E_f at sea level is given by some mean initial muon energy at point of production $\langle E_\mathrm{i} \rangle = E_\mathrm{f} + \Delta E$ [107]. Interaction of atmospheric muons with the atmosphere, assuming a standard US-atmosphere, can be approximated by $-dE/dx = a(E) + b(E)E$, which yields a final muon energy at sea level of:

$$E_\mathrm{i} = -\frac{a}{b} + \mathrm{e}^{b\,\delta X}\left(\frac{a}{b} + E\right) \tag{3.11}$$

with $a = 0.262\,\mathrm{GeV}$, $b = 3.5 \cdot 10^{-4}$ and a thickness of the atmosphere as seen by the muon of $\delta X = X_\mathrm{tot}(\theta) - X_0$. δX (in mwe) depends on the point of first interaction $X_0 = 100\mathrm{g/cm}^2$ and the total mass overburden $X_\mathrm{tot}(\theta)$ which is a function of zenith angle and can be parametrized according to:

$$X_\mathrm{tot}(\theta) = \frac{1\,\mathrm{mwe}}{p_1 + p_2 \cos^{p_3}(\theta) + \mathrm{p}_4(1 - \cos^2(\theta))^{p_5}} \tag{3.12}$$

with best fit parameters $\mathrm{p}_1 = -0.017326$, $\mathrm{p}_2 = 0.114236$, $\mathrm{p}_3 = 1.15043$, $\mathrm{p}_4 = 0.0200854$, $\mathrm{p}_5 = 1.16714$ [136]. The decay probability of a muon depends on the decay length λ and is given by $P_\mu = \mathrm{e}^{-1/\lambda_\mu}$ with $\lambda_\mu = E_\mu/(m_\mu \cdot \mathrm{c} \cdot \tau_\mu)$. The muon decay length and depends on the muon mass m_μ and finite muon lifetime τ_μ. The resulting muon energy spectrum is shown in Fig. 3.23.

[7] Beside the glisur and unified optics models, which are based on the reflectivity and Snell's law, detailed look up tables (LUT) for specific foils are provided by GEANT4, including the DF2000MA. Unfortunately, at the time of writing this thesis, the model did not support cylindrical geometries (`G4TUBS`).

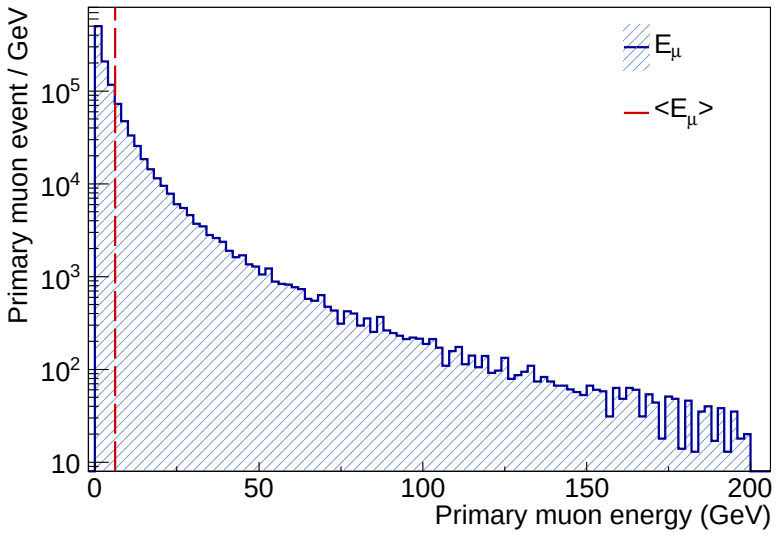

Figure 3.23.: Muon energy spectrum at sea level for $E_\mu \in [0.2, 200]$ GeV. The mean muon energy is $\langle E_\mu \rangle = 6.6$ GeV. Energy contributions for $E_\mu \in [0, 0.2]$ GeV are not considered in the simulation to save computing time as muons with $E_\mu < 200$ GeV are stopped in the 60 cm of concrete.

The need to adjust the Gaisser muon spectrum (Eqn. 3.5 in Sec. 3.2.1) to include the muon interaction with the atmosphere as well as the muon decay probability, arises from the need to correctly model the high photoelectron end of the light collection spectrum. The energy of the interacting muon plays an important factor in the production of secondary particles in water as well as in the concrete, which in turn can produce Cherenkov light in the water of the prototype. In order to mimic the aforementioned prototype measurements, 10000 atmospheric muons are initialised within a sphere of 10 m around the laboratory. A muon event is recorded if there is a coincident energy deposit in both scintillator volumes. An event can be triggered by a primary muon as well as muon-induced secondary particles. The corresponding photoelectron spectrum in PMT SA1766 can be seen in Fig. 3.24.

The spectrum is composed of three parts:

1. a Gaussian-like peak around 370 photonelectrons (328 PE in PMT SA1767) resulting from Cherenkov photons from primary muons in the water volume. The number of photons is directly related to the track length of muons in water.

2. a high PE tail resulting from the sum of secondary particles produced in the water and concrete. The tail is sensitive to the muon energy as it directly relates to the number of secondary particles produced.

3. low photoelectron distribution triggered and produced by secondary particles.

The offset between SA1767 and SA1766 can be explained by the offset of the scintillators panels by 5 cm in direction of PMT SA1766. In order to reach PMT SA1767, a photon has to be reflected on average 12 times while a photon reaching PMT SA1766 is only reflected 10 times[8].

The outcome of the simulation does not ab initio match the measurements in Sec. 3.3.6.

[8] At a reflectivity of 93 % we expect a difference of 14 % light collection assuming that photons need to be reflected 10 or 12 times respectively to reach PMT SA1766 or SA1767. However, the observed 23 % is hinting that PMT SA1767 has a lower collection efficiency.

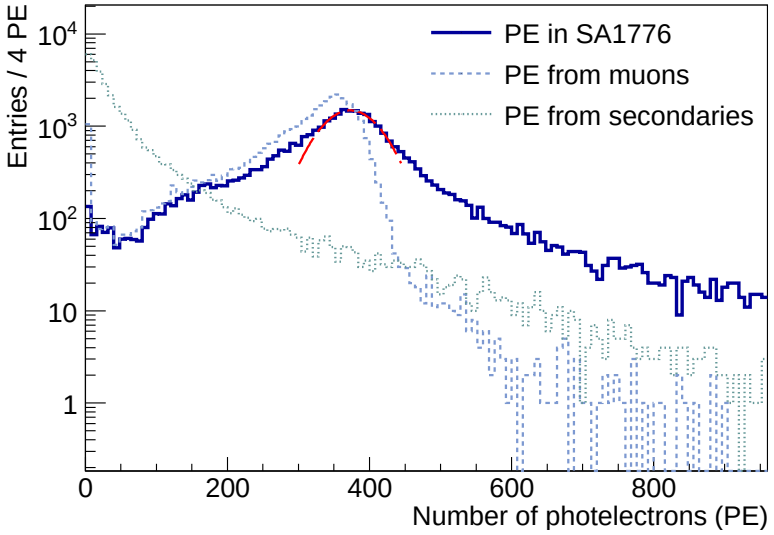

Figure 3.24.: Blue Line: The simulated photoelectron spectrum in PMT SA1766 with DF2000MA lining. The dashed line shows the contribution to the total spectrum from photoelectrons produced by the primary muon track in water. The peak of the spectrum corresponds to a track length of 0.32 m, i.e. the diameter of the tank. The dotted line shows the contribution to the total spectrum from photoelectrons produced by secondary particles. The red line shows the gauss-fit which allows to determine the PE peak the spectrum. The fitted mean number of photoelectrons is $\langle N_{PE} \rangle = 370$.

Key parameter to reproduce with MC-simulations is the Gaussian like photoelectron peak, as this is directly correlated to the primary muon track length in water. In this context, the absolute number of photoelectron is not of interest but rather the match between measured and simulated photoelectron peaks. We will see in the following section, that the muon track length and corresponding number of photoelectrons per muon track length is an important feature for large scale water Cherenkov detectors. To match the simulations, we tuned the collection efficiency of the PMT. The collection efficiency is a free parameter in the range between 0.8 and 1 and depends on the PMT bias as well as the PMT itself (see Sec. 3.1). Assuming a collection efficiency (CE) of CE = 1.06 in PMT SA1766 and CE = 0.9 in PMT SA1767 a good agreement between the simulated and the measured spectrum can be achieved (see Fig. 3.25). In order to estimate the agreement between the measured and simulated data, a χ^2 test of the two normalized histograms is performed. We test the hypothesis, that both histograms represent the same Gaussian distribution of the photoelectron peak:

$$\chi^2 = \frac{1}{M \cdot S} \sum_i \frac{(M \cdot s_i - S \cdot m_i)^2}{s_i + m_i} \tag{3.13}$$

The total number of measured (simulated) events $M = \sum_i m_i$ ($S = \sum_i s_i$) is given by the sum of the number of events m_i (s_i) per bin i [137]. If the number of events per bin is sufficiently large, the number of bins equals the number of degrees of freedom (NDF) of the χ^2 probability density function. A reasonable match between the two histograms can be assumed, if the mean of the χ^2-distribution $\approx$ NDF. To perform the test, we limit the two histograms to a range of PE $\in [350, 450]$ to ensures a sufficient number of entries per bin. The test gives a χ^2/NDF of $106/100 \approx 1.06$, pointing to a very good agreement between the measured and simulated spectra.

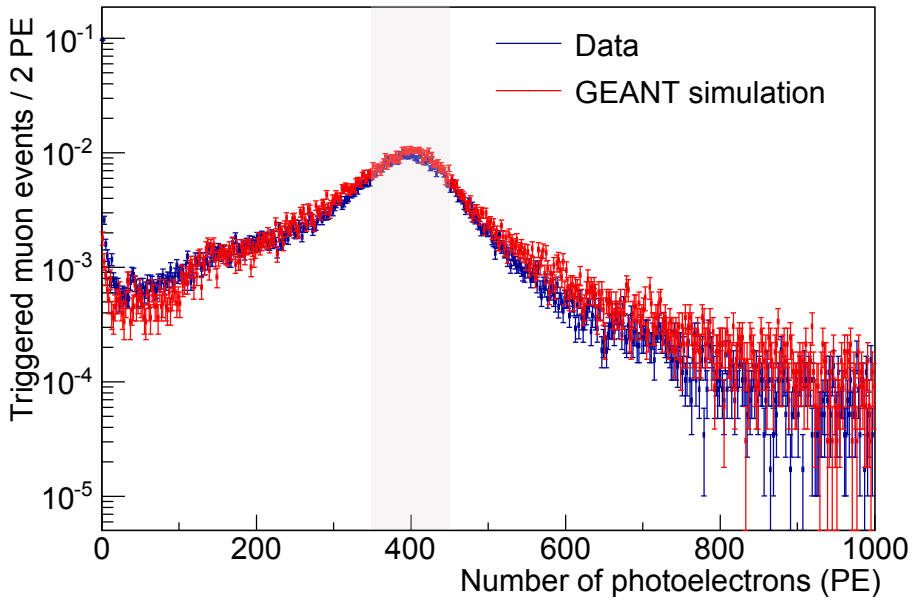

Figure 3.25.: The measured photoelectron spectrum in PMT SA1766 with DF2000MA lining (blue) and the adjusted simulated spectrum (red).

To conclude: The prototype water Cherenkov detector components, including the 8" PMT of type R5912 and the DF2000MA, are common detector components in current and future rare event muon vetos. An understanding of the optical parameters of such muon vetos will help to reliably design and optimize a full scale detector. The optical model of the water Cherenkov detector prototype with DF2000MA lining reproduces the measured photoelectron spectrum including the Gaussian like peak around 370 PE (328 PE) in PMT SA1766 (SA1767), the high PE tail as well as the low photoelectron distribution, if a collection efficiency of CE = 1.06 in PMT SA1766 and CE = 0.9 is assumed. Around the PE peak, the measured and simulated data follow the same distribution with a $\chi^2/\text{NDF} \approx 1.06$.

3.4. Optimization of the PMT Configuration for a Water Cherenkov Muon Veto

The purpose of an active muon veto system in dark matter experiments is to tag single nuclear recoil events in the target material in coincidence with a muon veto signal. Single nuclear recoil events from neutrons are indistinguishable from WIMP signals in dark matter experiments. The veto efficiency is one of the key parameters of active muon veto systems: the higher the veto efficiency, the better the background suppression of single nuclear recoil events. The better the background suppression, the better the sensitivity of the dark matter experiment. This section is dedicated to the study and optimization of the muon detection efficiency. The afore described GEANT MC-model of a water Cherenkov detector is applied in order to optimize the PMT configuration as well as trigger conditions of the EURECA muon veto design at LSM (see Sec. 3.1); aiming at high muon veto efficiencies. We showed in the previous section (Sec. 3.3) that we can describe the prototype measurements of a water Cherenkov detector adequately with our GEANT4 water Cherenkov detector MC-model. The MC-model can thus be reliably used to model the response of the full-scale water Cherenkov detector.

The optimization process is carried out for the muon veto setup of the EURECA experiment as described in Sec. 3.2.2, placing the water Cherenkov detector at the LSM laboratory with the corresponding muon flux (see Sec. 3.2.1). Given the rock profile above LSM, the majority of muons will hit the water tank with zenith angles between 30 deg – 60 deg (see Fig. 3.6) and mean muon energy of $\langle E_\mu \rangle \approx 255\,\mathrm{GeV}$ which will result in long muon track lengths and a considerable amount of light in the water Cherenkov detector. Consequently, the majority of muons at LSM should be easily tagged. A more challenging task on the other hand is the detection of muons with short track lengths or even the detection of muons that do not hit the tank directly but which interact in the vicinity ($< 10\,\mathrm{m}$) of the water Cherenkov detector . It will be seen that muons with short or no track length inside the veto also produce neutrons which can subsequently give a signal in the dark matter detectors. Therefore, our main focus lies on the optimization of the muon veto setup for short or no track length in the veto. The following studies assume that the water tank and cryostat surface are lined with the high reflective specular film DF-2000, which shows good performance with respect to light collection (see Sec. 3.3.6). All studies are performed with the afore developed and verified GEANT4 framework. For a detailed description of the simulation setup is see Sec. 3.2. Each simulation is based on 10^6 primary muons started in a 30 0m sphere around the LSM facility. To optimize computing time, studies are conducted with muon energies $E_\mu^{\mathrm{start}} \in [200, 2000]\,\mathrm{GeV}$, which is the dominant energy window for muon-induced neutron production at LSM [138]. The optimization of the optical setup is performed as follows: as a first reference, the tank illumination at the LSM laboratory from muon-induced processes is studied. Based on the outcome of this study and the experience from similar experiments, such as Xenon1T and Gerda [139] [93], five PMT setups with differing PMT numbers and arrangements are defined. Finally, the performance of each PMT setup is assessed by means of light collection and muon detection efficiency. In this context it makes sense to distinguish between two event classes:

1. The light collection of the water Cherenkov detector in coincidence with a muon inside the water tank volume, as this yields a direct measure of the muon detection efficiency.

2. The light collection of the water Cherenkov detector in coincidence with characteristic properties of muon-induced nuclear recoil events.

Before studying the light collection and the efficiency of the veto, characteristic muon properties of nuclear recoil events shall be defined.

3.4.1. Veto Threshold

The specific requirements of the muon veto performance are dictated by muon events in coincidence with nuclear recoils as *single* nuclear recoils (SNR) constitute the *irreducible* background source of dark matter experiments. Though the muon-induced background is one of the dominant backgrounds in future dark matter experiments, the production rate is low, requiring excessive simulation time (1 nuclear recoil event in $\sim$ 20 000 started muons). Optical simulations are very CPU intensive in GEANT4. The CPU time of a muon event with a track length of 6 m in water takes 50 times longer (84.65 s instead of 1.72 s) if production and tracking of optical photons is turned on. As a consequence, characteristic muon properties in coincidence with nuclear recoil events are studied without optical simulations and subsequently used to define the veto threshold for nuclear recoil events. The characteristic muon properties in coincidence with nuclear recoils in question are:

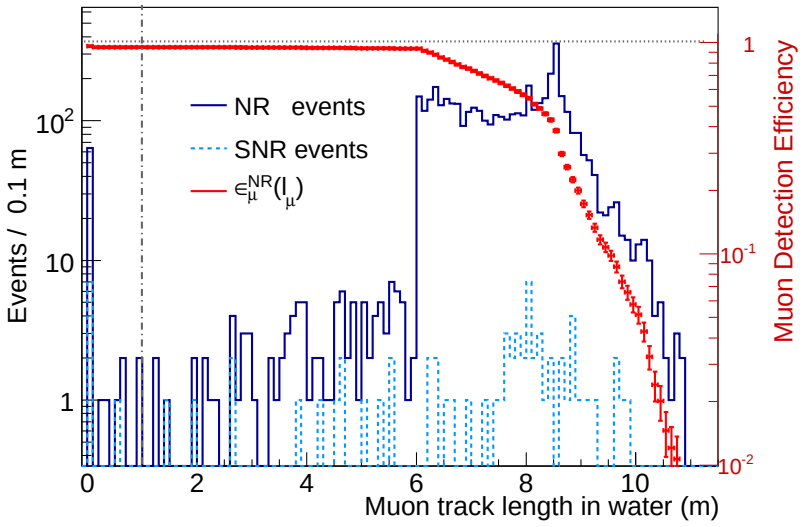

Figure 3.26.: Blue spectra: Distribution of muon track length in the water Cherenkov detector for events with a nuclear recoil signal (blue solid spectrum) or single nuclear recoil signal (ligt blue dashed spectrum) in the bolometer. Red markers: Muon detection efficiency as a function of muon-track length in the water Cherenkov detector . A muon detection efficiency of 99.9 % can be achieved if the threshold is set to $l_\mu^{\text{veto}} = 1\,\text{m}$ (grey line). $E_\mu^{\text{start}} \in [200, 2000]\,\text{GeV}$.

1. l_μ^{veto}: the primary muon track length inside the water tank
2. $E_{\text{dep}}^{\text{veto}}$: the energy deposit of the primary muon and its secondary particles within the water
3. d_l^{out}: the muon track distance to the water tank if the muon was outside the tank and
4. $E_{\text{dep}}^{\text{out}}$: the energy deposit in the veto if the muon was outside the tank.

The muon track length is directly related to the number of Cherenkov photons ($N_\gamma \propto l_\mu$, see Eqn. 3.3) produced and allows to define a threshold in terms of the light collection of the veto (l_μ^{thr}). Particles from muon showers can illuminate the tank even if the muon did not hit the water volume. Therefore, not the track length but the energy deposit (from the primary muon as well as secondary particles) inside the veto is used as a complimentary measure for the veto performance ($E_{\text{dep}}^{\text{thr}}$). To complete and test the limits of the muon veto, nuclear recoil events with muon tracks outside the tank are studied. Due to constraints on the computation time, the nuclear recoil simulations are limited to the muon energy range: $E_\mu^{\text{start}} \in [200, 2000]\,\text{GeV}$ with 2×10^7 primary muons started in a 30 m sphere around the laboratory. About 10 % of the primary muons hit the muon veto system. The muon energy window $E_\mu^{\text{start}} \in [200, 2000]\,\text{GeV}$ contributes $\sim 37\,\%$ to the main muon flux underground but 46 % to the neutron yield[9] [107]. The array of dark matter detectors recorded 4516 nuclear recoils (NR) and 71 single nuclear recoils (SNR) in total. Nuclear recoils are defined according to their Q-value ($Q < 0.5$) (see Sec. 3.2.3) with a detector threshold of 1 keV. Fig. 3.26 shows the distribution of the muon track length inside the water Cherenkov detector and corresponding muon detection efficiency for all events with a (single) nuclear recoils signal in the bolometer. 64 (7) events respectively are recorded

[9] $E_\mu^{\text{start}} \in [20, 200]\,\text{GeV}$ contributes 57 % to the main muon flux but only 10 % to the neutron production yield.

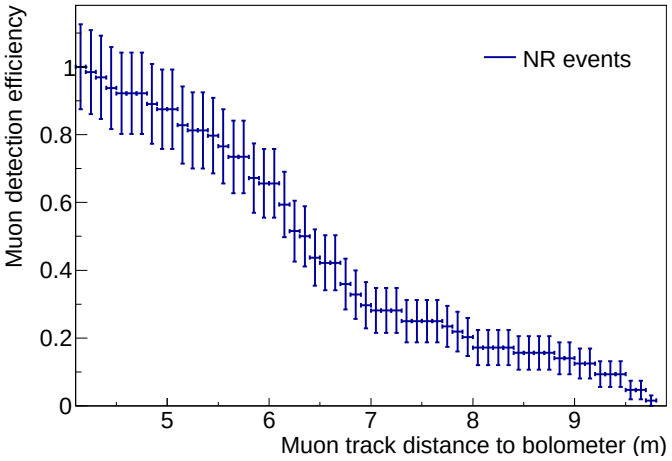

Figure 3.27.: Detection efficiency for events with at least one nuclear recoil signal in the bolometer if the muon did not hit the water Cherenkov detector as a function of muon track distance to the bolometer (d_{μ}^{out}). $E_{\mu}^{\text{start}} \in [200, 2000]$ GeV.

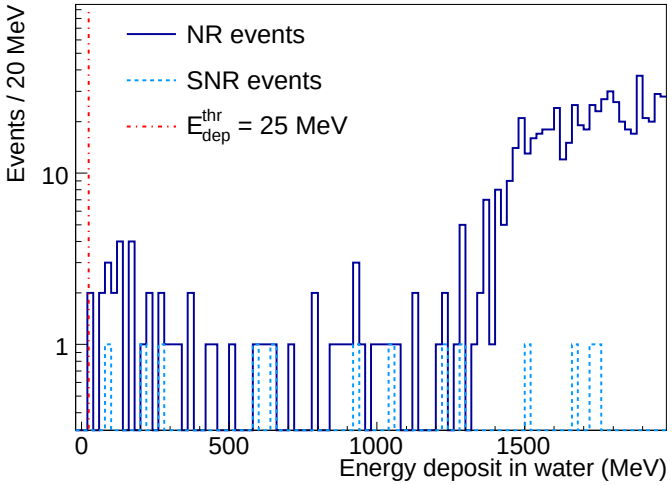

Figure 3.28.: Distribution of total energy deposit in the water Cherenkov detector for events with at least one nuclear recoil signal in the bolometer (blue solid spectrum) or single nuclear recoil signal (light blue dashed spectrum). A muon detection efficiency of 99.9 % can be achieved if the threshold is set to $E_{\text{dep}}^{\text{veto}} = 25$ MeV (grey dashed line). $E_{\mu}^{\text{start}} \in [200, 2000]$ GeV.

with muon tracks outside the water Cherenkov detector. The mean muon track length for nuclear recoil events is $\langle l_{\mu}^{\text{NR}} \rangle = 7.5$ m. The furthest distance to the dark matter detectors is $d_{\mu}^{\text{out}} = 9.8$ m. 99.9 % of the nuclear recoil events can be associated with $l_{\mu}^{\text{veto}} > 1$ m, not counting muons which did not hit the tanl. Fig. 3.27 shows the muon veto efficiency to tag nuclear recoil events if the muon track lies outside of the water tank as a function of muon track distance to the bolometer. A muon detection efficiency of 80 % can be achieved if the muon track distance to the bolometer is $d_{\mu}^{\text{out}} = 5$ m, i.e. the muon track lies about 1 m outside of the tank. In the following, the performance of the veto system in case of small light signals will be tested with $l_{\mu}^{\text{veto}} < 1$ m. Fig. 3.28 shows the total energy deposit in the tank for all events with at least one nuclear recoils signal in the bolometer. 99.9 % of the nuclear recoil events and all of the nuclear recoil events where the muon did not hit the

veto and $d_{\mu}^{\text{veto}} < 10\,\text{m}$ can be associated with $E_{\text{dep}}^{\text{veto}} > 25\,\text{MeV}$. In the following, we set $E_{\text{dep}}^{\text{thr}} = 25\,\text{MeV}$.

To conclude: two muon veto thresholds which allow to tag muon-induced nuclear recoil events with an efficiency of 99.9 % or more are derived based on characteristic muon properties in coincidence with nuclear recoil events from the primary muon track length in water (l_{μ}^{veto}) and the energy deposit of the primary muon and its secondary particles within the water ($E_{\text{dep}}^{\text{veto}}$) respectively. The threshold for $E_{\text{dep}}^{\text{veto}}$ is set to $E_{\text{dep}}^{\text{thr}} = 25\,\text{MeV}$. The threshold for l_{μ}^{veto} is set to $l_{\mu}^{\text{thr}} = 1\,\text{m}$.

3.4.2. Tank Illumination from Underground Muon Flux

The knowledge of the illumination of the tank surface from muons of the underground muon flux is a first measure to deduce sensible PMT arrangements. An efficient way to study the tank illumination as seen by a PMT is to cover the entire inner tank surface with a photo-cathode like foil with the corresponding quantum efficiency of PMT R5912. If the photon is not detected, it is reflected on the highly reflective DF2000MA foil. The study is split into two scenarios: events with a muon in the water volume ($l_{\mu}^{\text{veto}} > 0\,\text{m}$)and events in coincidence with muons with a track length in water of $l_{\mu}^{\text{veto}} < 1\,\text{m}$. Each bin in Fig. 3.29 corresponds to the size of an 8" PMT. The light produced by muons with $l_{\mu}^{\text{veto}} > 0$ and $E_{\mu}^{\text{start}} \in [200, 2000]\,\text{GeV}$ is clearly visible at the surface of the tank (see Fig. 3.29 (top)). The lowest number of photoelectrons detected per PMT bin is 3 photoelectrons. The illumination of the lateral tank surface is not homogeneous. The lower part of the later tank surface sees about a factor two more light than in the upper part (see Fig. 3.29 top left). This is to be expected, as muons enter from the top of the tank and the Cherenkov light is emitted in a forward cone along the track of the muon[10]. Furthermore, one can learn that the lateral surface of the tank detects about a factor two more light than floor surface (see Fig. 3.29 top right) which is shielded from the primary Cherenkov light by the cryostat. As the cryostat is lined with the highly reflective foil DF2000MA, the central part of the floor sees slightly more light than the edge. Muons with $l_{\text{mu}}^{\text{veto}} < 1\,\text{m}$ on the other hand illuminate the tank mainly up to 1 m around the edges and yield at most 5 photoelectrons per PMT bin (see Fig. 3.29 (bottom)).

3.4.3. Arrangement of PMTs

Five different PMT setups with two differing PMT arrangement and differing PMT numbers are defined from the insight of Sec. 3.4.2 and following the example of water Cherenkov detector muon vetos used in other rare event searches (e.g. XENON1T, GERDA). The arrangement of the five seups is shown in Appendix A. Total number of PMTs per setup studied are: 40, 72 and 105. The PMTs are arranged in alternating rings of 8, 12 or 15 PMTs in 5, 6 or 7 rings. The naming of the setup is defined as follows: setup *K-L*, where K = 0, 1 refers to the number of rings on the floor surface and L = 40, 72, 105 refers to the total number of PMTs. Sec. 3.4.2 showed that throughgoing muons are clearly visible on the lateral surface of the muon veto, yielding 3 photoelectrons per PMT bin or more. Also, more photoelectrons are seen at the lateral surface of the tank than at the top or floor surface. The simplest and most cost efficient PMT setup is thus setup 0 (see Fig. A.1 and A.2). Setup 0-40 arranges 40 in alternating rings of 8 PMTs in 5 lateral rings. Setup 0-72 arranges 72 PMTs in alternating rings of 12 PMTs in 6 lateral rings. Additionally, setups with the first ring facing upwards and the last ring facing downwards are studied. In order

[10]This effect will be washed out when the full reflectivity of the foil is used.

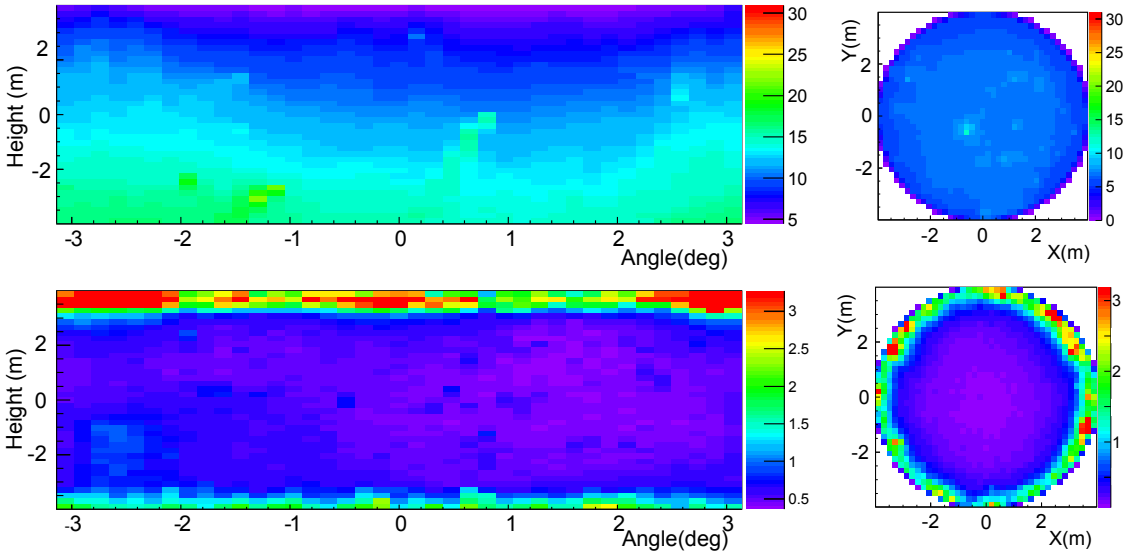

Figure 3.29.: Top: Average tank illumination from throughgoing muons ($l_\mu^{\text{veto}} > 0$). Bottom: Average tank illumination from short muon tracks inside the tank ($l_\mu^{\text{veto}} < 1\,\text{m}$). Left: lateral surface. Right: floor surface.

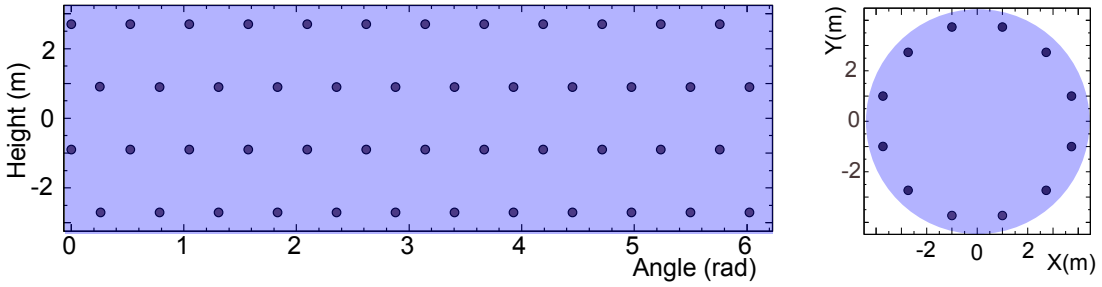

(a) (b)

Figure 3.30.: Setup 1 with 72 PMTs in total: 12 PMTs in 5 lateral rings (a), 12 PMTs in one lower and one upper ring each (b).

to tag $l_\mu^{\text{veto}} < 1\,\text{m}$, it may prove useful to have an extra PMT ring at the bottom and top, close to the edges of the tank. This is realized in setup 1. Setup 1-40 arranges 40 in alternating rings of 8 PMTs in 3 lateral rings and one upper and one lower ring. Setup 1-72 arranges 72 in alternating rings of 12 PMTs in 4 lateral rings and one upper and one lower ring. Due to the reduced illumination of the tank, it might as well be necessary to increase the number of PMTs to increase light collection. This is realized in setup 1-105 which arranges 105 PMTs in alternating rings of 15 PMTs in 5 lateral rings and one upper and one lower ring (see setup 1 in Fig. A.3, 3.30, A.5). Fig. 3.30 exemplary shows the PMT arrangement of setup 1-72. The water tank surface coverage per PMT row in z-direction (height of the tank) is 5 % for setups with three later rings of PMTs, 7 % for setups with four lateral rings and 9 % coverage for setups with five lateral rings of PMTs (2 % gain in coverage per ring). The water tank surface coverage per ring in x- and y-direction is 5 % for rings with 8 PMTs, 7 % for for rings with 12 PMTs and 9 % coverage for rings with 15 PMTs. To conclude: PMT setups with differing PMT arrangement and different numbers of PMTs are deduced. Total number of PMTs studied are: 40 (setup 0 & 1), 72 (setup 0 & 1) and 105 (setup 1 only).

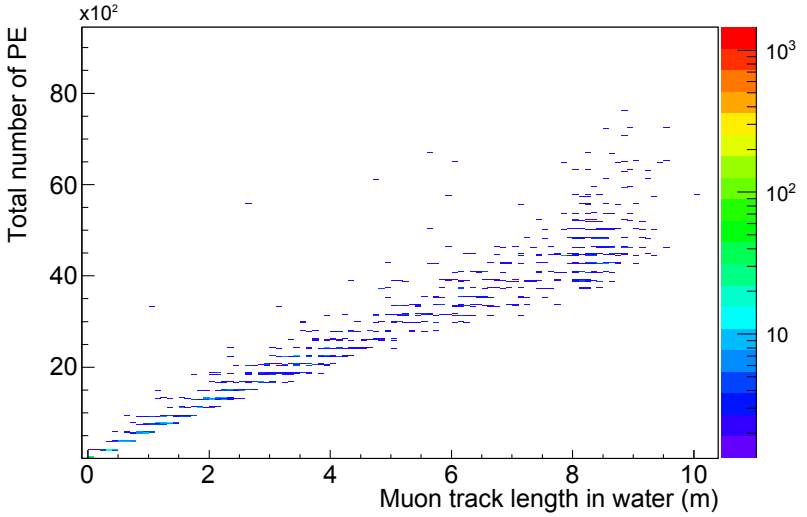

Figure 3.31.: Total number of photoelectrons as a function of muon track length in water for setup 1-72. For a muon with $\langle l_{\mu}^{\text{veto}} \rangle \approx 5.2\,\text{m}$ about $\langle N_{\text{PE}} \rangle = 3483$ photonelectrons are detected.

3.4.4. Water Cherenkov Detector Performance Studies

The performance of five different PMT setups (setup 0-40, setup 0-72, setup 1-40, setup 1-72, setup 1-105, see Sec. 3.4.3 for PMT arrangements) of the EURECA water Cherenkov detector is evaluated based on the light collection and the muon detection efficiency. The water tank is lined with the highly reflective foil DF2000MA. Light collection and detection efficiency are evaluated bearing in mind the afore characteristic muon properties from nuclear recoil studies (see Sec. 3.4.1). For each PMT setup, 10^6 primary muons with $E_{\mu}^{\text{start}} \in [200, 2000]\,\text{GeV}$ are started in a 30 m sphere around the water Cherenkov detector. The GEANT4 framework records amongst other properties the number of detected photoelectrons as well as the muon track length and total energy deposit (primary muon as well as secondaries) in water. On average, a muon event produces 1.54×10^5 Cherenkov photons, with $\langle l_{\mu}^{\text{veto}} \rangle \approx 5.2\,\text{m}$. The total number of reflections per detected photon is on average $\langle N_r \rangle = 14$ for 105 PMTs, $\langle N_r \rangle = 17$ for 72 PMTs and $\langle N_r \rangle = 21$ for 40 PMTs, i.e. in setups with a smaller total number of PMTs, photons have to be reflected more often in order to be detected as the overall photo-sensitive area is smaller. Consequently, the light collection in setups with small number of PMTs will depend stronger on the reflectivity of the tank surface.

Light collection

The light collection is defined as: $L_{\text{l}} = N_{\text{PE}}/l_{\mu}^{\text{veto}}$ or $L_{\text{E, dep}} = N_{\text{PE}}/E_{\text{dep}}^{\text{veto}}$. Exemplary, Fig. 3.31 shows the total number of photoelectrons as a function of muon track length in water for setup 1-72. Tab. 3.6 lists the light collection for all five PMT setups for l_{μ}^{veto} and $l_{\mu}^{\text{veto}} < 1\,\text{m}$. Tab. 3.7 lists the light collection for all five PMT setups for energy ranges of different $E_{\text{dep}}^{\text{veto}}$.

Setup 1-105, the setup with the highest numbers of PMTs, is the best performing setup with respect to light collection as the overall photo-sensitive surface of the tank is highest. It is followed by setup 1-72. A decrease of PMTs by 30 % from 105 to 72 results in a decrease of light collection by 20 %. Overall, a change in PMT arrangement shows little effect ($< 3\,\%$) on the light collection for setup 0 and setup 1 with 72 PMTs when looking at large energy

Table 3.6.: Light collection of 5 different PMT setups in relation to muon $l_\mu^{\text{veto}} > 0$, $l_\mu^{\text{veto}} < 0.5\,\text{m}$ and $l_\mu^{\text{veto}} < 1\,\text{m}$. Statistical error: $< 1\,\%$.

Setup	$l_\mu^{\text{veto}} > 0\,\text{m}$ (PE/m)	$[0-1]\,\text{m}$ (PE/m)	$[0-0.5]\,\text{m}$ (PE/m)
Setup 1-40	2325	354	200
Setup 1-72	3483	485	260
Setup 1-105	4257	572	304
Setup 0-40	2384	327	180
Setup 0-72	3450	423	235

Table 3.7.: Light collection of different PMT setups for different $E_{\text{dep}}^{\text{veto}}$. Statistical error: $< 1\,\%$. Energy ranges are given in MeV.

Setup	$E_{\text{dep}}^{\text{veto}} < 5000$ (PE/MeV)	$[0-25]$ (PE/MeV)	$[0-100]$ (PE/MeV)	$[100-200]$ (PE/MeV)
Setup 1-72	2.24	0.59	2.03	3.79
Setup 1-105	2.89	0.71	2.39	4.45
Setup 0-72	2.22	0.54	1.79	3.20

deposits ($E_{\text{dep}}^{\text{veto}} < 5\,\text{GeV}$) or long muon track lengths ($l_\mu^{\text{veto}} \sim 5\,\text{m}$) muons with long track length completely illuminate the tank. The light collection of short muon track lengths and low energy deposits, on the other hand, increases by 13 % when adding a ring of PMTs at the bottom and top surface of the tank while keeping the number of PMTs the same as muons with $l_\mu < 1\,\text{m}$ illuminate the tank mainly up to 1 m around the edges. An energy deposit of $E_{\text{dep}}^{\text{veto}} = E_{\text{dep}}^{\text{thr}} = 25\,\text{MeV}$ yields on average a total of $N_{\text{PE}} = 25$ in setup 1 with 72 PMTs. To conclude: At low energy thresholds, setup 1 outperforms setup 0 with respect to light collection by 15 %. This can be explained by the fact, that low energy deposits in the veto are a result from near edge events, as has been seen when studying short muon track lengths. With increasing energy deposit, the difference between setup 0 and setup 1 becomes negligible, the number of PMTs is now the only influencing factor on the light collection with a 20 % increase between 72 and 105 PMTs.

Muon Detection Efficiency

The muon detection efficiency determines the quality of a muon veto system and gives a complimentary measure of the performance of the afore defined five setups and will help to deduce an optimal PMT setup of the water Cherenkov detector. The definition of a muon detection efficiency in the context of simulations is not straightforward as the muon itself as well as the secondary particles it produces when passing through the rock may produce a detectable light signal in the tank. Again, the muon detection efficiency is defined along the lines of the event categories defined in Sec. 3.4.1. A global muon detection efficiency of the water Cherenkov detector is defined as the percentage of tagged muon events over all muon events hitting the veto:

$$\epsilon_{\mu^{\text{veto}}} = \frac{N_{\text{tagged}}(l_\mu^{\text{veto}} > 0)}{N(l_\mu^{\text{veto}} > 0)} \tag{3.14}$$

which yields a direct measure of the overall muon detection efficiency. A muon is tagged if the event complies with a given trigger condition. Within the optimization process the

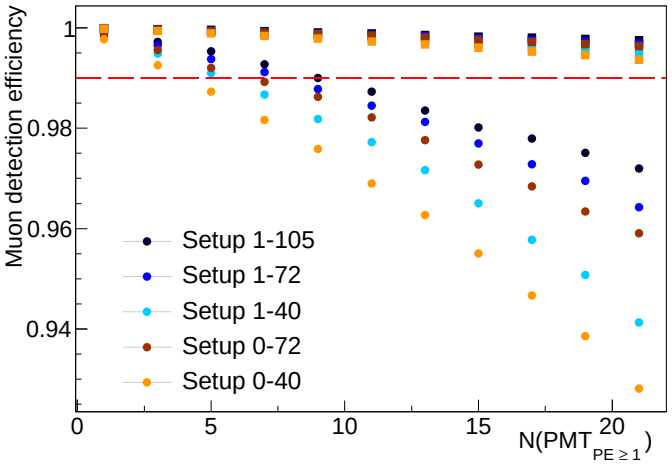

Figure 3.32.: Integral muon detection efficiency as a function of $\mathrm{PMT}_{\mathrm{PE}\geq 1}$: $\epsilon_{\mu}^{\mathrm{veto}}$ (square) as well as $\epsilon_{\mu}^{\mathrm{short}}$ (circle) for setup 0-40 (yellow), setup 0-72 (red), setup 1-40 (light blue), setup 1-72 (blue) and setup 1-105 (dark blue).

trigger condition is defined as a coincident number of PMTs above a given threshold of photoelectrons ($N(\mathrm{PMT}_{\mathrm{PE}>\mathrm{thr}})$) in a given coincidence interval. A second, more stringent muon detection efficiency is defined according to:

$$\epsilon_{\mu^{\mathrm{short}}} = \frac{N_{\mathrm{tagged}}(l_{\mu}^{\mathrm{veto}} < 1\,\mathrm{m})}{N(l_{\mu}^{\mathrm{veto}} < 1\,\mathrm{m})} \tag{3.15}$$

to test the veto in the limit of low light production. Two further detection efficiencies are defined according to:

$$\epsilon_{E_{\mathrm{dep}}} = \frac{N_{\mathrm{tagged}}(E_{\mathrm{dep}}^{\mathrm{veto}} > 25\,\mathrm{MeV})}{N(E_{\mathrm{dep}} > 25\,\mathrm{MeV})} \text{ and} \tag{3.16a}$$

$$\epsilon_{E_{\mathrm{dep}}^{\mathrm{out}}} = \frac{N_{\mathrm{tagged}}(E_{\mathrm{dep}}^{\mathrm{veto}} > 25\,\mathrm{MeV} \wedge d_{\mu}^{\mathrm{out}})}{N(E_{\mathrm{dep}}^{\mathrm{veto}} > 25\,\mathrm{MeV} \wedge d_{\mu}^{\mathrm{out}})} \tag{3.16b}$$

This gives an indirect measure of the veto performance when vetoing nuclear recoil events. In this context, it is interesting to look at events with $E_{\mathrm{dep}}^{\mathrm{veto}} > 25\,\mathrm{MeV} \wedge d_{\mu}^{\mathrm{out}}$, as those events allow to estimate the performance of the veto event if the primary muon does not hit the veto directly. The average muon track distance to the bolometers is $\langle d_{\mu}^{\mathrm{out}} \rangle = 6.16\,\mathrm{m}$ if the muon did not hit the tank but its secondary particles deposited at least 25 MeV inside the tank, i.e. the muon track passes the tank surface at an average distance of $1-2\,\mathrm{m}$. Fig. 3.32 shows $\epsilon_{\mu}^{\mathrm{veto}}$ and $\epsilon_{\mu}^{\mathrm{short}}$ as a function of PMTs above threshold, where the threshold is set to 1 photoelectron ($\mathrm{N}(\mathrm{PMT}_{\mathrm{PE}\geq 1})$). All PMT setups exhibit muon detection efficiencies in the order of 90 % or more. When increasing the number of coincident PMTs above threshold, two trends can be observed: Firstly, the muon detection efficiency is highest for the setup with the highest number of PMTs (i.e. 105 PMTs). Secondly, the PMT arrangement of setup 1 outperforms setup 0 when comparing both setups with same number of $\mathrm{N}(\mathrm{PMT}_{\mathrm{PE}\geq 1})$. The veto is less efficient to detect muons with short track length as less Cherenkov light is produced. As a consequence, the drop in detection efficiency $\epsilon_{\mu}^{\mathrm{short}}$ is more prominent for setups with smaller numbers of PMTs. Complimentary, Fig. 3.33 shows the muon detection efficiency as a function of track length in water for a typical trigger of $\mathrm{N}(\mathrm{PMT}_{\mathrm{PE}\geq 1}) = 6$. If the muon does not hit the tank, the detection efficiency

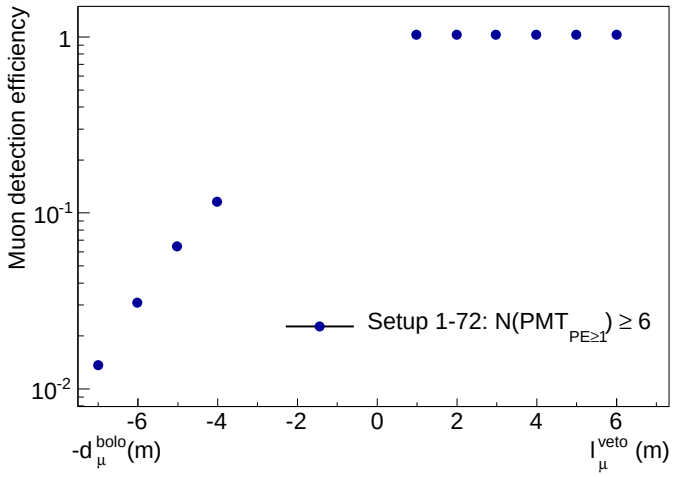

Figure 3.33.: Muon detection efficiency for setup 1-72 as a function of muon track length in water or distance to bolometer if the muon did not hit the tank. The muon trigger is set to $N(PMT_{PE\geq1}) = 6$.

is evaluated as a function of the shortest distance of the muon track to the bolometers. It is interesting to see that even though the muon does not hit the tank, there is still an efficiency of 11 % to tag the muon if it passes in the vicinity of the veto, independent on the energy deposit in the water. The tagging efficiency of muons outside the tank decreases exponentially. At a distance of 8 m to the bolometers, corresponding to a distance of $\geq$ 4 m from the tank, the detection efficiency is a mere 1 %[11].

To conclude: Setups with 40 PMTs or less are not advisable, as they lack the power to detect muons with short track length or no track length efficiently. Setups with one ring at the top and bottom outperform setups with lateral rings only both with respect to light collection and detection efficiency, when detecting muons with short track length or events with low energy deposit in the veto. Though an increase of PMT number increases the light collection and detection efficiency, setups with 72 PMTs achieve veto efficiencies of 99 % or better at sensible trigger conditions. As increasing the number of PMTs increases the cost as well as the work load, setup 1 with 72 PMTs is chosen as the final setup.

3.5. Trigger Conditions for a Water Cherenkov Active Muon Veto

The muon detection efficiency of the water Cherenkov detector depends on the chosen trigger of the system. This section determines the optimal trigger condition, which will be a compromise between high muon detection efficiencies and the dead time of the muon veto system. The trigger is optimized for the optimal PMT setup of the previous section, setup 1-72. The setup arranges 72 PMTs in alternating rings of 12 PMTs in 4 lateral rings and one upper and one lower ring (see setup 1-72 in Fig. 3.30). A possible realization of the muon trigger is the following: each of the 72 PMT signals is digitized at a rate of 10^9 samples per second (see Sec. 3.3.1). The trigger is started for a set time window if the integral of 100 consecutive sampling points (i.e. 100 ns) in one PMT exceeds a predefined

[11] The pure measure of the distance to the bolometers does however not take into account the shower induced in the rock and subsequently inside the veto (i.e. E_{dep}^{veto}). It has been seen in Sec. 3.4.1 that muons which do not hit the tank but induce a NR within the bolometers have a visible energy deposit within the tank which in turn should result in higher detection efficiencies.

threshold (e.g 1, 2, 3 etc. photoelectrons as known from calibration) compared to the baseline. If, within this trigger time window, a predefined number of PMTs exceed the threshold, a muon is tagged.

In the following, the photoelectron threshold, number of coincident PMTs as well as the trigger time window will be derived from simulations with the objective to achieve high muon detection efficiencies while keeping the dead time of the veto at a justifiable rate. In a first step, the performance of different trigger conditions is tested based on the efficiency to tag $l_{\mu}^{\text{veto}} > 0\,\text{m}$ and $l_{\mu}^{\text{veto}} < 1\,\text{m} \equiv l_{\mu}^{\text{short}}$ as well as $E_{\text{dep}}^{\text{veto}} > 25\,\text{MeV}$ and $E_{\text{dep}}^{\text{out}} > 25\,\text{MeV}$. The same event classes are used prior to this in Sec. 3.4.4 to determine the optimal PMT setup. In a second step, the timing information of the photoelectron hit time for individual PMTs as well as the whole system of 72 PMTs is studied to determine the trigger time window of the water Cherenkov detector.
In the last step, the dead time of the muon veto system caused by accidental coincidences is evaluated and used to confine trigger conditions.

Trigger performance

The veto efficiency for 27 different trigger conditions and four different event classes are studied. The trigger conditions investigated are: $N(\text{PMT}_{\text{PE}\geq thr}) = 1\text{–}9$ with $thr = 1\text{–}3\,\text{PE}$. The studied event classes are: l_{μ}^{veto}, $E_{\text{dep}}^{\text{veto}} > 25\,\text{MeV}$, l_{μ}^{short}, $E_{\text{dep}}^{\text{out}} > 25\,\text{MeV}$. The resulting veto efficiencies are shown in (see Fig. 3.34).

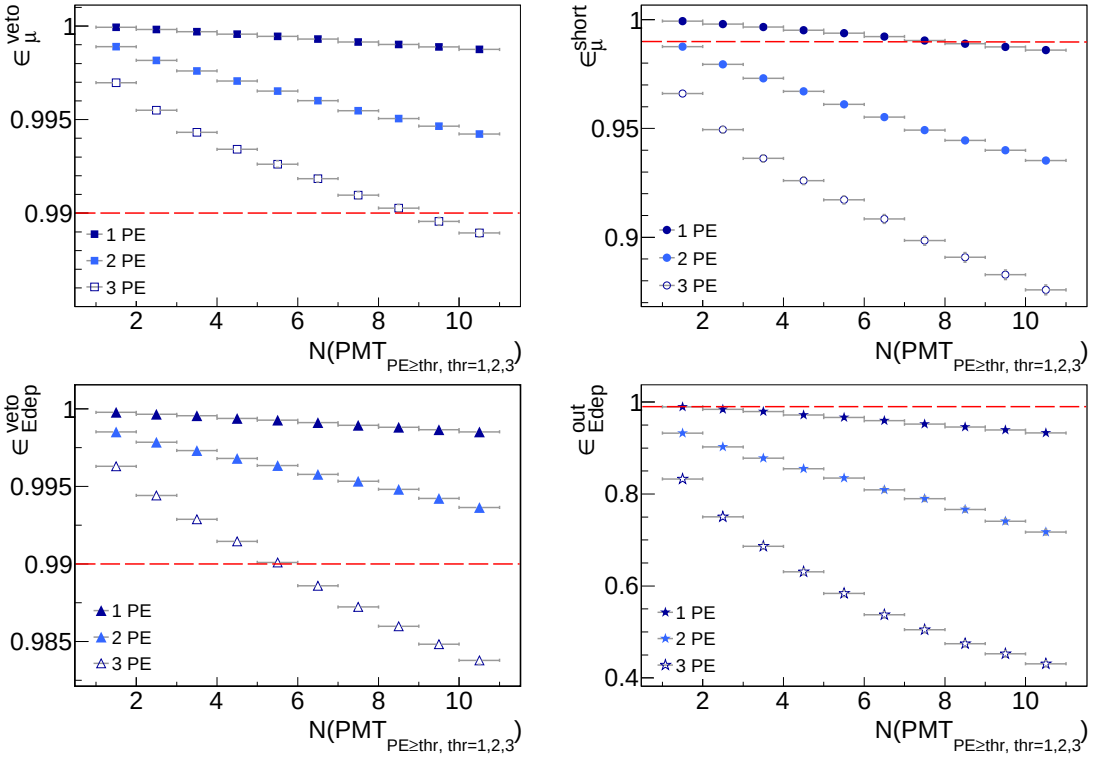

Figure 3.34.: Integral muon detection efficiency as a function of $N(\text{PMT}_{\text{PE}\geq thr})$ with $thr = 1\,\text{PE}$ (dark blue marker), $thr = 2\,\text{PE}$ (light blue marker), $thr = 3\,\text{PE}$ (empty marker) for different classes of events. Top left: $\epsilon_{\mu}^{\text{veto}}$, top right: $\epsilon_{\mu}^{\text{short}}$, bottom left: $\epsilon_{\text{E}_{\text{dep}}}^{\text{veto}}$, bottom right: $\epsilon_{\text{E}_{\text{dep}}}^{\text{out}}$. The red line corresponds to a veto efficiency of 99 %. Statistical uncertainties are determined via Clopper-Pearson and are for most points smaller than the marker.

Table 3.8.: Average time difference between the detection time of the first photoelectron and the detection time of the N^{th} photoelectron of the same PMT: $\langle \Delta t(N^{\text{th}}\text{PE} - 1^{\text{st}}\text{PE}) \rangle$.

$\langle \Delta t \rangle_{N=2}$ (ns)	$\langle \Delta t \rangle_{N=3}$ (ns)	$\langle \Delta t \rangle_{N=5}$ (ns)	$\langle \Delta t \rangle_{N=10}$ (ns)	$\langle \Delta t \rangle_{N=last}$ (ns)
17.3	29.22	49.49	98.33	3300

The following trends can be observed: all 27 trigger conditions allow for high detection efficiencies for muons inside the water tank ($\epsilon_{\mu}^{\text{veto}} \approx 98.6 \pm 0.4\,\%$). Short muon track length can only be detected with high efficiency ($\epsilon_{\mu}^{\text{short}} > 99\,\%$) for single photoelectron trigger conditions as events with short muon track length produce less light. High detection efficiencies of muon events above a veto threshold of $E_{\text{thr}}^{\text{veto}} = 25\,\text{MeV}$ can be achieved for most trigger conditions, though trigger conditions with single or two photoelectron thresholds are favored. Overall, one finds that a more pronounced loss in efficiency is observed when increasing the photoelectron threshold compared to increasing the number of coincident PMTs at constant photoelectron threshold in all four event classes, as higher photoelectron thresolds require more light.

PMT Trigger time window

The PMT trigger time window of the veto defines the time span in which a preassigned PMT trigger condition has to be met. If this preassigned trigger condition is met within this time window, a muon is tagged. The PMT time window will be a compromise between two factors: the veto efficiency and the rate of accidental coincidences. If the trigger window is chosen too small, the efficiency of the veto will decrease. If the trigger time window is chosen too large, the accidental trigger rate will increase. A sensible time span of the trigger window can be determined from the simulation by means of the recorded detection times of the photoelectrons. The timing information of individual PMTs is listed in Tab. 3.8. From Fig. 3.35 it is apparent that a time window of $\Delta t_{\text{PMT}} = 200\,\text{ns}$ is above the time difference between the first photoelectron hit of the first PMT and the first photoelectron hit of the 10th PMT. When setting a time cut after $\Delta t_{\text{PE}} = 100\,\text{ns}$ on the individual PMT recording time, 0.1 % of the signal is lost when requiring a threshold of 2 or 3 photoelectrons.

A final timing study and an important parameter of the trigger system is the time span in which to look for nuclear recoil events after a muon event was triggered. For this purpose, the time difference between the first hit of the first PMT and the first hit of a bolometer if a nuclear recoil event is recorded ($\Delta t_{\text{PMT–Bolo}}$) is investigated. The simulation shows that all nuclear recoil events occur within a time span of 1 µs or less. The average time difference $\langle \Delta t_{\text{PMT–Bolo}} \rangle = 22\,\text{ns}$. Conservatively, the time window to search for nuclear recoil signatures in the bolometers, if a muon event is triggered, is set to $\Delta t_{\text{PMT–Bolo}} = 10\,\mu\text{s}$.

3.6. Veto Dead Time

The dead time of the veto system is determined by the rate of accidental coincidences (R_{acc}), which depends on the number of triggered PMTs, the time window of the trigger as well as the background rate of each PMT. The background rate is determined by the dark count and – in the context of a water Cherenkov detector – by ambient decays in the vicinity of the PMT within the water tank. The rate of dark counts depends on the temperature

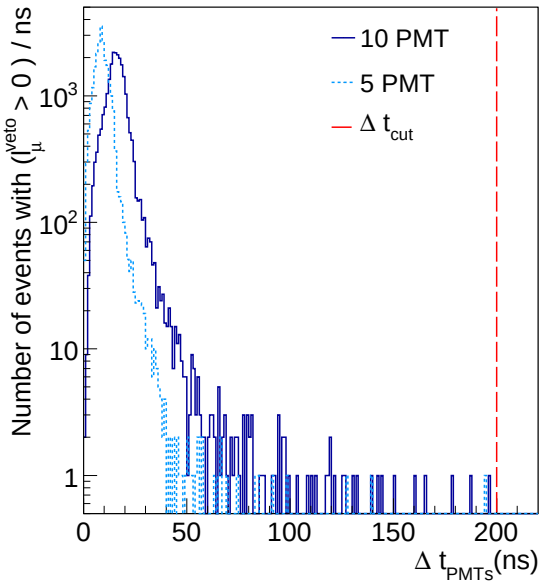

Figure 3.35.: Time difference Δt_{PMTs} between the first hit of the 10th PMT (blue solid) or the 5th PMT (light blue dashed) and the first hit of the first PMT. The red dashed line shows the time cut on the trigger time.

and voltage (see Sec. 3.1). At room temperature and voltages of 1500 V, the dark count rate is dominated by thermionic emission. The dark count of PMT R5912 is 3.3 kHz for single photoelectron signals according to Hamamatsu [104]. Ambient decays in the vicinity of the water Cherenkov detector produce Cherenkov radiation within the water, which in turn produces a photoelectron background count in the PMTs. Before estimating the rate of accidental coincidences, the background rate from ambient decays will be determined via GEANT4 simulations. The photoelectron background count rate is estimated from simulations for three dominating ambient background sources: ^{230}Th and ^{40}K decays from the LSM concrete as well as ^{60}Co decays from the stainless steel of the water tank. Each material is contaminated following typical contamination levels of rare event experiments. The contamination levels of all materials can be found in Tab. 2.2 and Tab. 2.1. In secular equilibrium ^{230}Th yields 6 α-particles with energies between 5–8 MeV. The most prominent gamma- emission results from the decay of ^{208}Tl with an energy of 2.614 MeV. Even though contamination levels of ^{238}U and ^{40}K are higher in concrete than those of ^{230}Th, initial simulation showed that Th decays tend to produce more Cherenkov light in the vicinity of the PMTs than ^{238}U, ^{40}K or ^{60}Co decays. Fig. 3.36 shows the expected integral count rate as a function of photoelectrons per PMT from ^{208}Tl decays. The dark count rate (R_{D}) per PMT drops with increasing number of photoelectrons per PMT from $R_{\mathrm{D}}\mathcal{O}$(kHz) to $R_{\mathrm{D}}\mathcal{O}$(Hz). The count rate of single photoelectrons from ambient decays is of the same order as the SPE dark count of the PMT. Requiring a threshold of $thr = 3$ PE per PMT reduces the count rate to $R_{\mathrm{D}} \approx 1$ Hz. The dead time of the muon veto system due to accidental coincidences can be estimated by means of combinatorial consideration:

$$R_{\mathrm{acc}} = \binom{m}{n} \cdot R_{\mathrm{D}}^{n} \cdot (\Delta t)^{n-1} \text{ with } \binom{m}{n} = \frac{m!}{n!(m-n)!} \tag{3.17}$$

where R_{acc} describes the rate of accidental coincidences with Δt being the time window of accidental coincidences, R_{D} the dark noise rate, m the total number of PMTs, n the number of PMTs in the trigger condition. Fig. 3.37 shows the accidental count rate of the

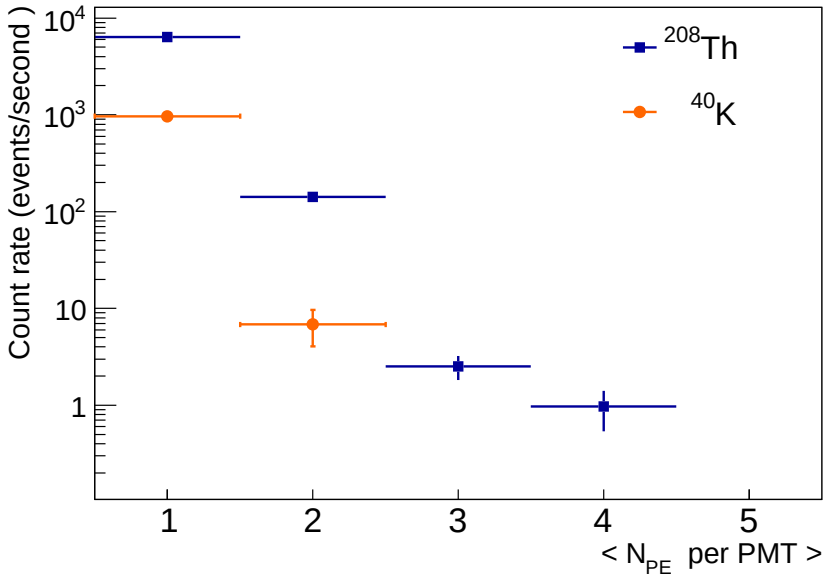

Figure 3.36.: Expected ambient count rate as a function of $\langle N_{\mathrm{PE}} \rangle$ per PMT caused by ambient decays from ^{208}Tl (blue square) and ^{40}K (orange circle) contaminations in LSM concrete.

Table 3.9.: Muon veto trigger conditions to keep accidental coincidences at the same order as the expected muon trigger rate at LSM (i.e. 10^{-3} Hz), assuming a trigger time window of $t_{\mathrm{trig}} = 200$ ns. Accidental coincidences depend on the background count rate R_{D} of the PMT and the number of coincident PMTs $N(\mathrm{PMT}_{\mathrm{PE} \geq thr})$. The background count rate of the PMT in turn depends on its photoelectron threshold *thr*.

Trigger	R_{D} per PMT	$N(\mathrm{PMT}_{\mathrm{PE} \geq thr})$	*thr*
1	6.5 kHz	7	1
2	100 Hz	4	2
3	1 Hz	2	3

muon veto as a function of PMTs above threshold for differing trigger time windows and dark count rates. The trigger rate of muons at LSM is expected to be in the order of: $R_{\mu} \sim 5 \times 10^{-3}$ Hz. An acceptable dead time of the muon veto should be of the same order or less. Tab. 3.9 lists the possible trigger conditions to keep the rate of accidental triggers at the order of 5 mHz. Different trigger time windows imply trigger conditions according to Tab. 3.10 (see also Fig. 3.37). From the stand point of keeping dead time at the order of 10^{-3} Hz, three minimal trigger requirements can be thought of in order to achieve dead time rates to 10^{-3} Hz:

- Trigger 1: $N(\mathrm{PMT}_{\mathrm{PE} \geq 1}) = 7$ within a trigger time window of $\Delta t_{\mathrm{trig}} = 200$ ns.
- Trigger 2: $N(\mathrm{PMT}_{\mathrm{PE} \geq 2}) = 4$ and a trigger time window of $\Delta t_{\mathrm{trig}} = 200$ ns. The photoelectron threshold of $thr = 2$ reduces ambient background rates per PMT to the level of 10^2 Hz.
- Trigger 3: $N(\mathrm{PMT}_{\mathrm{PE} \geq 3}) = 2$ within a trigger time window of $\Delta t_{\mathrm{trig}} = 200$ ns. Here, the photoelectron threshold of $thr = 3$ reduces ambient background rates to the level of 1 Hz per PMT.

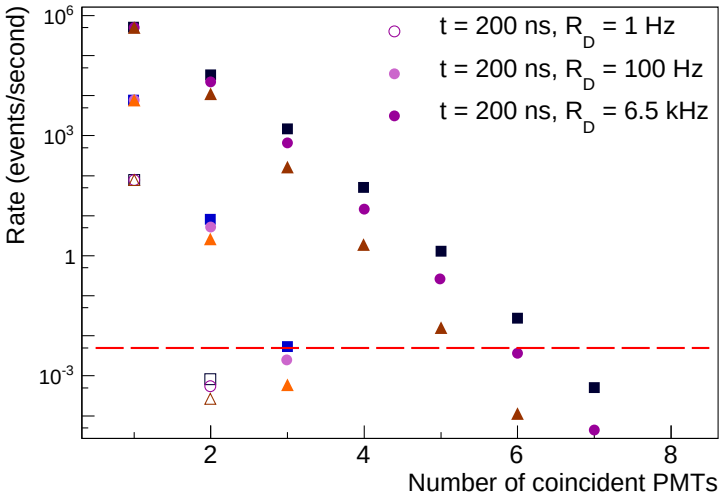

Figure 3.37.: Expected rate of accidental coincidences of the muon veto system as a function of coincident PMTs for varying dark count rates $R_\mathrm{D} = 6.5\,\mathrm{kHz}$ (dark marker), 100 Hz (light marker), 1 Hz (empty marker) and varying trigger time windows $\Delta t = 100\,\mathrm{ns}$ (brown triangle), 200 ns (magenta circle), 300 ns (blue square).

Table 3.10.: Muon veto trigger conditions to keep accidental coincidences at the same order as the expected muon trigger rate at LSM (i.e. 10^{-3} Hz), assuming a dark count rate of $R_\mathrm{D} = 6.5\,\mathrm{kHz}$ for different trigger time windows Δt_trig and different numbers of coincident PMTs $N(\mathrm{PMT}_{\mathrm{PE}\geq thr})$.

Trigger	$N(\mathrm{PMT}_{\mathrm{PE}\geq 1})$	Time window Δt_trig (ns)
4	8	500
5	7	300
6	6	100

To conclude: The timing study of photoelectron arrival times on individual PMTs suggests to use trigger conditions with single photoelectrons as arrival times of several photoelectron per PMT span over 3 orders of magnitude from ns to µs. Single photoelectron trigger conditions are also favoured with regard to muon detection efficiencies. The drop in efficiency is stronger when increasing the number of required photoelectrons compared to the drop in efficiency when increasing the number of PMTs $N(\mathrm{PMT}_{\mathrm{PE}\geq thr=\mathrm{const.}})$. Timing studies of the arrival time of the first photoelectron on the first 10 or 5 PMTs ($\Delta t_{\mathrm{PMT\,1–PMT\,10/5}}$) suggest to set the trigger time window to 200 ns. To keep the dead time of the veto at a rate of a few 10^{-3} Hz, the SPE trigger condition together with a trigger time window of 200 ns requires at least $N(\mathrm{PMT}_{\mathrm{PE}\geq 1}) = 6$ coincident PMTs triggering. The resulting optimal trigger condition for setup 1 with 72 PMTs is thus at least one photoelectron in at least 6 photomultiplier tubes, i.e. $N(\mathrm{PMT}_{\mathrm{PE}\geq 1}) = 6$ in a time window of $\Delta t_\mathrm{trig} = 200\,\mathrm{ns}$. The trigger allows for muon detection efficiencies of $\epsilon_\mu^\mathrm{veto} > 99.9\,\%$. The same trigger allows to tag muons with short tracks ($< 1\,\mathrm{m}$) with an efficiency of $\epsilon_\mu^\mathrm{short} > 99\,\%$.

The muon veto efficiency is comparable to similar proposed concepts of muon veto systems for dark matter experiments. The dark matter experiment XENON1T at the Gran Sasso underground laboratory will employ 84 PMTs 8" PMTs (R5912) inside a water tank of 10 m height and diameter lined with the reflective foil DF2000MA. Tagging efficiencies for

muons inside the veto are stated as $\epsilon_{\mu}^{\text{veto}} = 99.5\,\%$ for a trigger condition of $4-5$ PMTs at SPE threshold [93]. At a comparable muon detection efficiency, XENON1T has to expect higher accidental rates compared to our design. The $0\nu\beta\beta$-experiment GERDA (Gran Sasso) specifies a muon detection efficiency of 98 % [140] at an accidental coincidence rate of $\mathcal{O}(10^{-3}\,\text{Hz})$. The muon veto of GERDA is equipped with 60 PMTs and the tank is lined with the highly reflective VM2000 (which is now called DF2000). The world leading dark matter experiment LUX at Sanford underground laboratory is able to achieve muon tagging efficiencies $\epsilon_{\mu}^{\text{veto}} > 90\,\%$ with 20 10" PMTs [141].

3.7. Application: Muon Induced Background Rate Estimation for EURECA

This section estimates the muon-induced neutron background before and after active muon suppression in a one tonne and 50 kg cryogenic Ge-crystal array at the LSM underground laboratory. The muon-induced neutron rate is estimated with the help of a dedicated GEANT4 simulation toolkit (see Sec. 3.2). 10^7 primary muons ($\mu^+/\mu^- \approx 1.37$) with $E_{\mu}^{\text{start}} \in [2, 20000]\,\text{GeV}$ are started on a 30 m sphere around the LSM site (see Sec. 3.2.1). The muon and muon-induced neutron interactions in rock, the detector material of the muon veto and Ge-crystals are modeled using the `Shielding physics list 2.0` provided by GEANT4 (g4-10.00.p02) (see Sec. 3.2.4). The energy deposit within the Ge-bolometers by hadronic and electromagnetic interactions is translated into electronic and nuclear recoil signals according to Sec. 3.2.3. The detector geometry is shown in Fig. 3.8. The arrangement of Ge-crystals for the 1 tonne and 50 kg scenario are shown in Fig. 3.38.

10^7 primary muons are equivalent to an exposure time of $t_{\text{exp}} = 12.08^{+3.09}_{-1.39}$ years. As measured by EDELWEISS-II [80], the exposure time is derived from the horizontal muon flux at LSM of $\phi_{\mu} = 5.4 \pm 0.2^{+0.5}_{-0.9}\,\text{muons/cm}^2\text{/day}$.

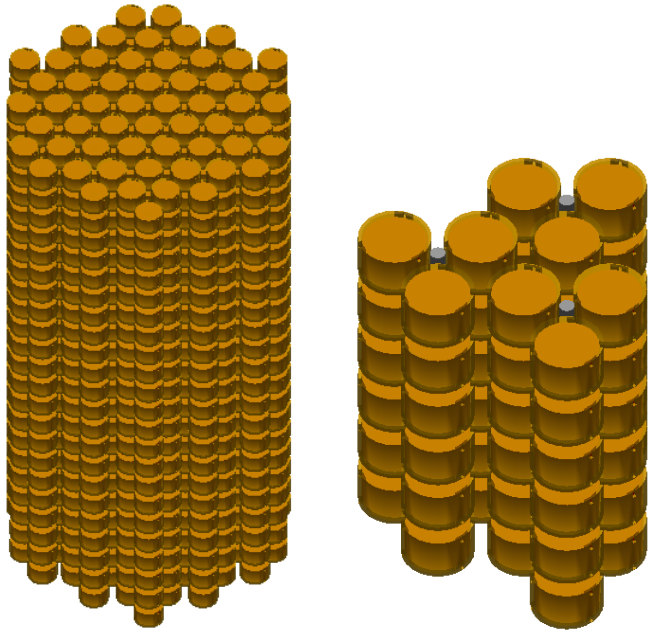

Figure 3.38.: Ge-crystal towers for 1 tonne (left) or 43.2 kg (right) of detector mass.

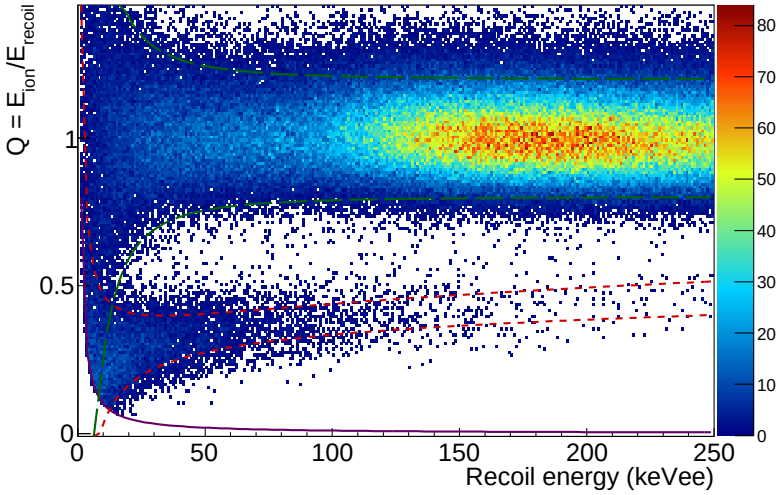

Figure 3.39.: Event distribution of ionization yield $Q = E_{\mathrm{ion}}/E_{\mathrm{rec}}$ against recoil energy in 1 tonne of Ge and in $t_{\mathrm{exp}} \sim 12$ years of exposure time. Electronic recoils can be found in the 90 % CL electronic recoil band (dashed green) with $Q = 1$, nuclear recoils can be found in the 90 % CL nuclear recoil band (red) with $Q < 0.5$.

3.7.1. EURECA 1 Tonne

Fig. 3.39 shows the event distribution of ionization yield against recoil energy in 1254 Ge-bolometers, i.e. one tonne of Ge, and in $12.08^{+1.32}_{-2.42}$ years of data taking. The recoil energy per bolometer for all bolometers and bolometers which recorded nuclear recoils only is given in Fig. 3.40. A nuclear recoil requires the ratio of the recorded ionization and recoil energy ($Q = E_{\mathrm{ion}}/E_{\mathrm{rec}}$) to lie below the 90 % CL of the nuclear recoil band ($Q < 0.5$). The threshold of the bolometers is set to $E_{\mathrm{heat}} = E_{\mathrm{ion}} = 1\,\mathrm{keV}$. The resolution of the bolometers is set according to Tab. 3.1. Through going muons deposit an energy of $E_{\mathrm{rec}} \approx 40\,\mathrm{MeV}$ in the germanium detector ($\rho_{\mathrm{Ge}} = 5.31\,\mathrm{g/cm^3}$ and $dE/dx \approx 2\,\mathrm{MeV}/(\mathrm{g\,cm^{-2}})$). At 511 keV, the annihilation line of electron-positron pairs is clearly visible. The peak at $E_{\mathrm{rec}} \approx 200\,\mathrm{keV}$ can be attributed to the Compton back scattering of the 511 keV annihilation photons. Before scattering back into the crystal, the 511 keV photons lose part (2/3) of their energy in Cu holders of bolometers via Compton scattering. Energy deposits above 100 keV are predominately caused by electronic recoils, energies below 50 keV by nuclear recoils.

The total multiplicity m_{tot} per event, i.e. the number of the 1254 bolometers which recorded a recoil energy with $E_{\mathrm{heat}} > 1\,\mathrm{keV}$ and $E_{\mathrm{ion}} > 1\,\mathrm{keV}$ as well as the multiplicity (m_{NR}) of bolometers where at least one bolometer recorded one nuclear recoil, i.e. $E_{\mathrm{rec}} \in [1, 250]\,\mathrm{keV} \wedge Q < 0.5$ is shown in Fig. 3.41. $E_{\mathrm{rec}} \in [1, 250]\,\mathrm{keV}$ is the favored region of interest (ROI) for a signature from WIMP-nucleon interactions in Ge. The average bolometer multiplicity is $\langle m_{\mathrm{tot}} \rangle = 16$. Due to the compact packing and the large amount of bolometers, the multiplicity is larger than in similar experiments with smaller detector numbers (e.g. EDELWEISS-II). The multiplicity of nuclear recoil events is shown in Fig. 3.41). The average bolometer multiplicity for events where at least one nuclear recoil is recorded is $\langle m_{\mathrm{NR}} \rangle = 106$. In total, 1285 events with at least one nuclear recoil in an energy region of $E_{\mathrm{rec}} \in [1, 250]\,\mathrm{keV}$ and 12.08 years of exposure time are recorded in the bolometers. Out of the 1285 nuclear recoil events, the bolometers recorded 15 events with single nuclear recoils in the region of interest and 12.08 years of exposure time. A single nuclear recoil requires the ratio of the recorded ionization energy and recoil energy ($Q = E_{\mathrm{ion}}/E_{\mathrm{rec}}$) to lie below the 90 % CL of the nuclear recoil band ($Q < 0.5$) and that

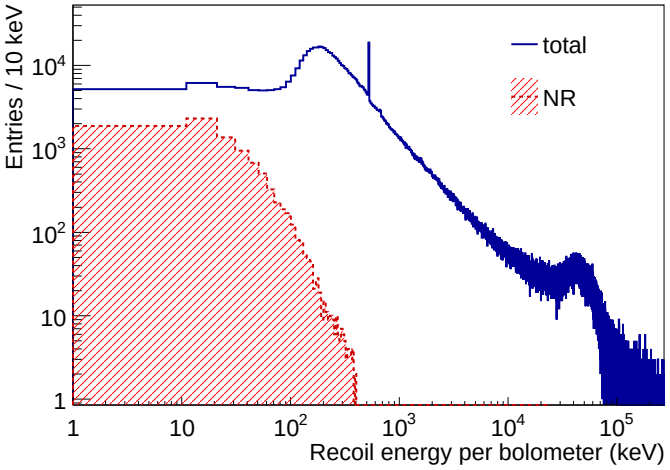

Figure 3.40.: Recoil energy distribution per detector. Blue spectrum: total selection. Red spectrum: events with $Q < 0.5$ (nuclear recoil events). See text for details.

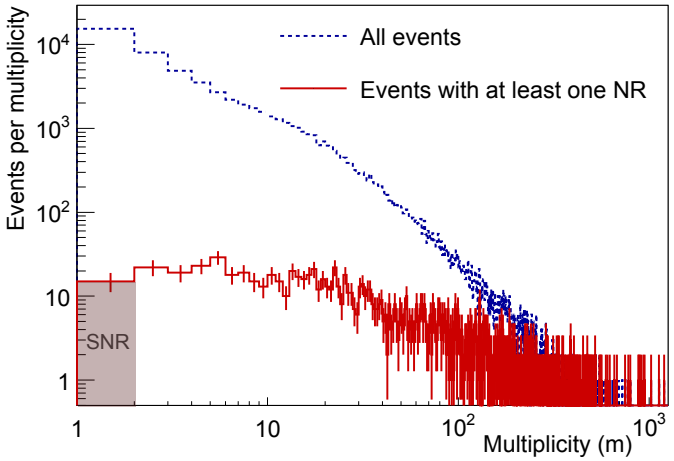

Figure 3.41.: Number of bolometers out of 1254 (1 tonne) in $t_{\mathrm{exp}} = 12.08$ years. Blue: All bolometers, red: bolometers with at least one recorded nuclear recoil ($Q < 0.5$). The entries in the first bin represent the number of recorded single nuclear recoils.

no other of the 1254 bolometers recorded an energy deposit with $E_{\mathrm{rec}} > 1\,\mathrm{keV}$. The single nuclear counts translate into a rate of:

$$\Gamma_{\mu\text{–n–bg}} = 1.24 \pm 0.32\,(\mathrm{stat})\,^{+0.41}_{-0.49}\,(\mathrm{syst})\,\mathrm{events/tonne/year}. \tag{3.18}$$

The systematic error derives from the error on the muon flux at LSM which is of the order of 20 % [80] and the error on the neutron production in GEANT4 which is stated as 16 % by [107] and 21 % by [142].

In a next step, coincidences between bolometer hits and the muon veto system are studied. For this purpose, coincidences between a tagged muon according to the afore developed muon trigger and a single nuclear recoil within a time window of 10 µs in the 12 years of exposure time are analysed. No single nuclear recoil in anti-coincidence with a tagged muon were found.

This sets an upper limit of 2.3 events at 90 % CL in $12.08\,^{+1.32}_{-2.42}$ years of exposure time and 1 tonne of Ge [5]:

$$\Gamma^{\text{veto}}_{\mu\text{–n–bg}} \leq 0.18\,^{+0.02}_{-0.03}\,\text{events/tonne/year at 90 \% CL.} \tag{3.19}$$

of untagged muon-induced neutron background for the WIMP search.

3.7.2. EURECA 40 kg

Currently, cryogenic solid sate dark matter experiments are focusing on the search for low mass dark matter particles. In contrast to current and future standard WIMP searches, low mass dark matter experiment require an excellent detector energy thresholds instead of large target masses (see Sec. 1.5.1). Considering the strategy changes , it is thus also interesting to study the muon-induced neutron rate in a reduced mass scenario of 43.2 kg of detector material instead of one tonne in cryogenic dark matter experiments. Due to a change in detector arrangement and target mass, one cannot expect to get the same multiplicity and ratio of single to multiple recoils compared to one tonne of detectors. To make sure that the afore developed muon veto and trigger requirements also suppress muon-induced background in a 43.2 kg dark matter experiment, $t_{\text{exp}} = 12.38^{+1.61}_{-2.48}$ years of exposure time is simulated in the reduced mass scenario. In order to get about 40 kg of detector mass, the detectors are arranged in three towers of six layers and three bolometers per layer (43.2 kg, see Fig. 3.38). The ionization threshold of the bolometers are set to $E_{\text{ion}} = 1\,\text{keV}$. No heat cut is applied.

Fig. 3.42 shows the event distribution of ionization yield against recoil energy in all 54 bolometers.

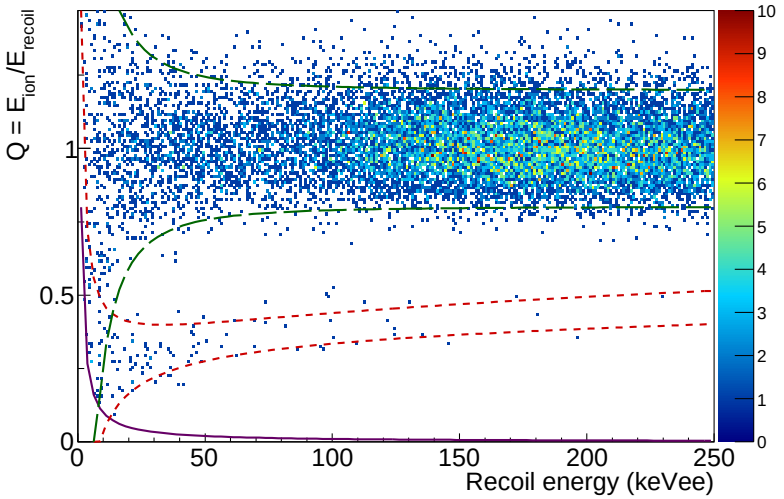

Figure 3.42.: Event distribution of ionization yield ($Q = E_{\text{ion}}/E_{\text{rec}}$) against recoil energy in electron equivalent in all 54 bolometers and in $t_{\text{exp}} \sim 12$ years of exposure time. Electronic recoils can be found in the 90 % CL electronic recoil band (dashed green) with $Q \sim 1$, nuclear recoils can be found in the 90 % CL nuclear recoil band (red) with $Q < 0.5$.

In 12.38 years, 84 events with at least one nuclear recoil in the region of interest $E_{\text{rec}} \in [1, 250]\,\text{keV} \wedge Q < 0.5$ are recorded. Out of these, 19 events are single nuclear recoil events. The multiplicity of bolometers which recorded a signal is shown in Fig. 3.43. The average multiplicity of bolometer hits if at least one bolometer was above threshold

is $\langle m_{\text{tot}} \rangle = 3.7$ bolometers. The average multiplicity for events where at leas one nuclear recoil is recorded is $\langle m_{\text{NR}} \rangle = 7$. The single nuclear recoil rate in 43.2 kg is higher than in 1 tonne of target material. This can be explained by the more compact packing of the 1256 bolometers in one tonne of Ge-crystal compared to 43.2 kg bolometer arrangement. The compact packing allows for an efficient event by event discrimination of single to multiple nuclear recoils with a resulting ratio of the multiplicity of single to multiple nuclear recoils of $m(\text{SNR})/m(\text{NR}) = 15\,/\,1270 = 0.01$. In contrast, the packing of 54 bolometers in 43.2 kg of detector mass results in a ratio of $m(\text{SNR})/m(\text{NR}) = 19\,/\,65 = 0.29$, a higher fraction of single nuclear recoils is to be expected. The single nuclear counts translate into a rate of:

$$\Gamma_{\mu\text{–n–bg}} = 0.035 \pm 0.008\,(\text{stat})\,^{+0.012}_{-0.014}\,(\text{syst})\,\text{events/kg/year}. \tag{3.20}$$

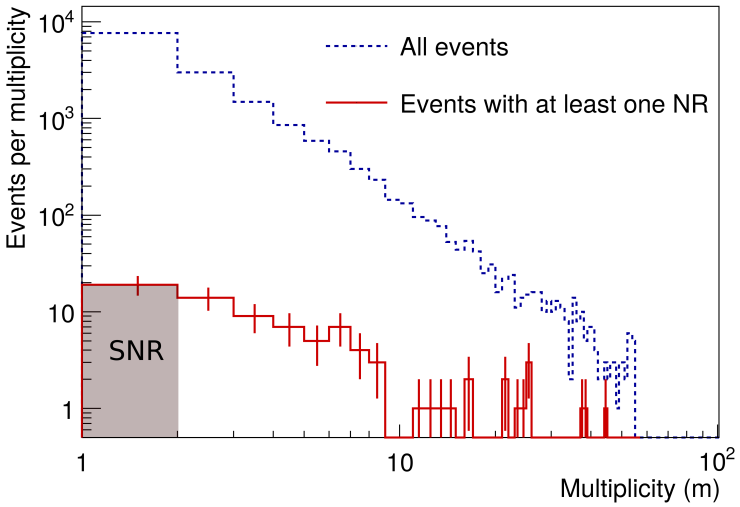

Figure 3.43.: Number of bolometers out of 54 (43.2 kg) which recorded a recoil energy with $E_{\text{heat}} > 1$ keV and $E_{\text{ion}} > 1$ keV in $t_{\text{exp}} = 12.38$ years. Blue: All bolometers, red: bolometers with at least one recorded nuclear recoil ($Q < 0.5$). The entries in the first bin of the red spectrum correspond to the number of recorded single nuclear recoils (SNR).

No single nuclear recoil in anti-coincidence with a tagged muon is found in the region of interest. This sets an upper limit of:

$$\Gamma^{\text{veto}}_{\mu\text{–n–bg}} \leq 4.33^{+0.46}_{-0.91} \cdot 10^{-3}\,\text{events/kg/year at 90 \% CL}. \tag{3.21}$$

To conclude: No muon-induced neutron signal in anti-coincidence with the water Cherenkov muon veto system at LSM is to be expected in 1 tonne or 43.2 kg of Ge-target material for a simulated muon flux corresponding to an exposure time of 12.38 years. This sets an upper limit of muon-induced neutron events of $\Gamma^{\text{veto}}_{\mu\text{–n–bg}} \leq 4.33 \cdot 10^{-3}$ events/kg/year in 43.2 kg and $\Gamma^{\text{veto}}_{\mu\text{–n–bg}} \leq 0.18\,^{+0.02}_{-0.03}$ events/tonne/year in 1 tonne of target mass. $\Gamma^{\text{veto}}_{\mu\text{–n–bg}}$ is limited by the MC-statistics of the simulated muon flux, which in turn are limited by the CPU time of optical simulations.

4. Design of a Combined Active Muon and Neutron Veto System for Future Dark Matter Experiments

The sensitivity of dark matter experiments is limited by radiogenic and cosmogenic backgrounds. As we need to increase sensitivities of future experiments, it becomes more and more challenging to ensure the corresponding reduction of backgrounds. The dominant background source in dark matter experiments are muon-induced and radiogenic neutrons as the elastic scattering of neutrons can mimic WIMP signals in the detector. Muon-induced background can be reduced by actively tagging events in coincidence with a dedicated muon veto. A commonly used technology is to tag muons events in water Cherenkov detectors as they exhibit high muon veto efficiencies and allow for a large geometrical coverage around the target (see Chap. 3). Radiogenic neutron background can be reduced by selecting radio-pure materials in the vicinity of the target material and by actively vetoing neutron events. At increasing sensitivities, material selection and screening campaigns alone will not provide the necessary background reduction, thus the vetoing of neutrons becomes more and more important. Most dark matter experiments therefore veto neutron events by an event by event discrimination of single and multiple recoils either by segmenting the target material (e.g. SuperCDMS, EDELWEISS) or via a 3D position reconstruction of the interaction (e.g. LUX, XENON). The WIMP-nucleon interaction are weak and WIMPs expected to interact only once with the target material (single nuclear recoil) while neutrons can interact more than once (multiple nuclear recoil). Single nuclear recoils from neutron interactions are then an irreducible background. Recently, Gd- or B-loaded scintillators surrounding the target material have been proposed to tag single scatter neutron events in dark matter detectors in coincidence with a signal in the scintillator [143] [99] [144].

A potentially cheap and efficient solution to reduce both ambient and cosmogenic neutrons in future dark matter experiments is a combined muon and neutron veto which is read out by the same optical system, namely the photo-detectors of the muon veto system. Keeping the optical system further away from the active neutron veto reduces radioactive contaminations and background rates of the veto due to ambient radiation in the vicinity of the neutron veto. The water shield of the water Cherenkov detector around the veto reduces the gamma-flux and corresponding ambient background count rate from the surrounding rock and concrete. As will be discussed later in this chapter, background count rate is one

of the limiting factors of the neutron veto efficiency.

This chapter demonstrates the basic layout of possible combined muon and neutron veto which is read out by the same optical system. It is realized in the context of a one tonne cryogenic solid state dark matter detector. In this chapter we will focus on the design of the neutron veto: including the PMT setup, neutron tagging efficiencies and trigger conditions as well as the veto dead time.

Complimentary, a neutron veto system with its own readout system as proposed by SuperCDMS [144] is presented in the second part of this chapter. In this context, the emphasis is put on the assessment of optical parameters of the veto readout system.

This chapter is organized as follows: Sec. 4.1 outlines the layout and mode of operation of a loaded scintillator as neutron veto. Sec. 4.2 illustrates the implementation of the Monte Carlo model of the neutron veto system. Sec. 4.3 concentrates on the optimization and veto efficiency of the PMT system of the neutron veto. Sec. 4.3.5 determines the optimal trigger condition of the neutron veto system and estimates the expected dead time of the system. Sec. 4.4 briefly outlines the layout of the B- or Gd-loaded organic scintillator as proposed by the SuperCMDS SNOLAB experiment. Sec. 4.5.1 focuses on the assessment of optical parameters of the optical Monte Carlo model of the SuperCDMS veto system with the help of prototype measurements and standalone GEANT4 simulations. Sec. 4.6 illustrates the implementation of the optical readout system of the full scale neutron veto in the SuperCDMS Monte Carlo model. Sec. 4.6.1 gives a first estimate of the SuperCDMS veto efficiency using the optical model of the full scale neutron veto.

4.1. Concept of a Combined Water Cherenkov and Doped Scintillating Active Veto

This section depicts the design of a combined active muon and neutron veto system. The muon veto system is realized based on to the EURECA active muon veto [76]. The baseline design of the EURECA muon veto is described in Sec. 3.1. It consists of a cylindrical steel tank of 8 m height and 8 m diameter, filled with ultra-pure water and lined with a highly reflective specular foil (DF-2000 by 3M). The system will be read out by 72 encapsulated 8" PMTs of the style R5912 by Hamamatsu. The detection principle of muons with a water Cherenkov detector can be found in Sec. 3.1.

The neutron veto is based on a liquid scintillator either doped with ^{157}Gd or ^{10}B. The layout of the neutron veto consists of a plastic tank of 4 m height and 4 m diameter filled with a mineral oil based Gd- or linear alkylbenzene (LAB) based B-doped liquid scintillator. The H:C ratio in the scintillator is 1.56 with a density of $\rho_{\text{scint}} = 0.88\,\text{g/cm}^3$. The detection principle of neutrons by means of doped scintillators is based on two principles: the capture of a neutron on a nucleus with a high neutron capture cross-section, the subsequent production of scintillation light and its detection with photo-detectors.

Neutron capture

Before the neutron gets captured on the nucleus, it is moderated through elastic scattering on H or C in the scintillator. The scintillator must be big enough to ensure the needed scatterings. The elastic scattering results in a prompt light signal $\mathcal{O}$(ns). After thermal equilibrium with the liquid scintillator has been achieved, the neutron gets captures after a diffusion time of $\mathcal{O}(\mu\text{s})$. The neutron is captured on a nucleus $^{\text{A}}X$ via an excited compound nucleus ($^{\text{A+1}}X^*$) or direct capture. In the case of B or Gd, the capture results in the

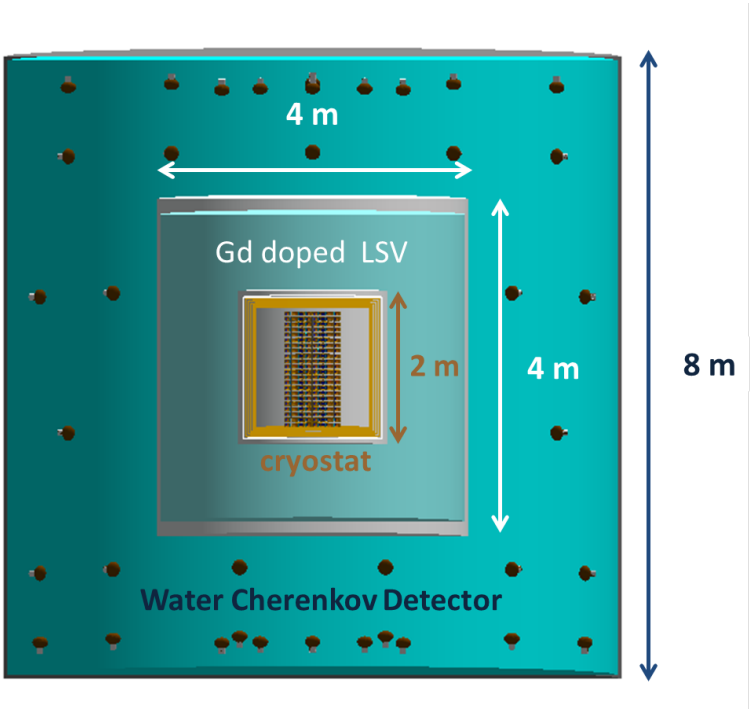

Figure 4.1.: Conceptual design of the combined future active muon and neutron veto system as implemented in GEANT4. The water Cherenkov detector consists of a stainless steel tank of 8 m diameter and 8 m height, it is equipped with 72 8" PMTs and filled with 400 m^3 of ultra-pure water. The tank is lined with the highly reflective specular foil DF200MA. The water Cherenkov detector is built around a cylindrical 2 m × 2 m Cu cryostat which contains 1254 800 g Ge-crystals. The cryostat is placed inside the neutron veto which consists of a plastic tank of 4 m height and 4 m diameter filled with a Gd- or B doped liquid scintillator (LSV). See text for details.

transmutation of the nucleus on the subsequent decay via the emission of a photon (Gd) and/or charged particles (B) [82]. 93.7 % of the captures on ^{10}B result in the emission of a high energy α-particle, high energy ^{7}Li ion and a gamma:

$$^{10}\mathrm{B} + \mathrm{n_{th}} \rightarrow {}^{11}\mathrm{B}^{*} \rightarrow \alpha\,(1.47\,\mathrm{MeV}) + {}^{7}\mathrm{Li}\,(0.84\,\mathrm{MeV}) + \gamma\,(0.48\,\mathrm{MeV})\ (\mathrm{BR}\ 93.7\,\%) \quad (4.1)$$

At a branching ratio of 6.3 %, the ^{11}B decays into the ground state of Li without emission of a high energy gamma:

$$^{10}\mathrm{B} + \mathrm{n_{th}} \rightarrow {}^{11}\mathrm{B}^{*} \rightarrow \alpha\,(1.78\,\mathrm{MeV}) + {}^{7}\mathrm{Li}\,(1.01\,\mathrm{MeV})\ (\mathrm{BR}\ 6.3\,\%) \quad (4.2)$$

The highest capture cross-section in naturally occurring nuclei can be found in ^{157}Gd:

$$^{157}\mathrm{Gd} + \mathrm{n_{th}} \rightarrow {}^{158}\mathrm{Gd}^{*} \rightarrow {}^{158}\mathrm{Gd} + \text{conversion electron} + \gamma\mathrm{s}\,(7.9\,\mathrm{MeV}) \quad (4.3)$$

Neutron capture on ^{157}Gd releases on average 3.2 photons with a mean energy of 2.3 MeV and 0.6 conversion electrons with 71 keV [145]. Neutron capture can be described as a neutron-nucleus resonance scattering and the cross-section can be obtained by the Breit-Wigner equation for reactions of slow neutrons[1]:

$$\sigma_{\mathrm{cap}} = \pi \lambda\!\!\!^{-}_{\mathrm{res}} \Gamma_{\mathrm{n}} \Gamma_{\mathrm{res}} \frac{\lambda\!\!\!^{-}}{(E - E_0 + 1/4\Gamma^2)} \quad (4.4)$$

[1] in the S-wave approximation

Table 4.1.: Neutron capture cross-section σ_{capture}, relative abundance and neutron binding energy S_n for the nuclei of the loaded liquid scintillator [146]

Isotope	σ_{capture} (barn)	abundance (%)	S_n
^{1}H	3.326×10^{-1}	99.9885	2224.576
^{2}H	4.92×10^{-4}	0.0115	6257.2482
^{12}C	3.89×10^{-3}	98.93	4946.311
^{13}C	1.22×10^{-3}	1.07	8176.61
^{152}Gd	3.7×10^{2}	0.20	6247.48
^{154}Gd	85	2.18	6435.29
^{155}Gd	5.17×10^{4}	14.80	8536.04
^{156}Gd	1.8	20.47	6360.05
^{157}Gd	2.10×10^{5}	15.65	7937.39
^{158}Gd	2.2	24.84	5943.29
^{160}Gd	1.4	21.86	5635.4
^{10}B	5×10^{-1}	19.9	11454.15
^{11}B	5×10^{-3}	80.1	3370.4
^{63}Cu	4.75	69.2	7915.96
^{65}Cu	2.13	30.8	7065.93

where λ corresponds to the de Broglie wavelength of the neutron and Γ is the partial decay width which is defined by the lifetime τ of the exited state of the nucleus:

$$\Gamma = \frac{\hbar}{\tau} \tag{4.5}$$

Neutron capture cross-sections and neutron binding energy for the nuclei of the loaded liquid scintillator are given in Tab. 4.1.

^{10}B-loaded scintillator allow for a comparably compact build of the neutron veto as light originates mainly from localized energy deposits. A ^{10}B-loaded neutron veto is currently employed by DarkSide dark matter experiment [59]. The advantage of Gd-loaded scintillator is its high neutron capture cross-section and less quenching compared to B. Furthermore, doping with Gd provides a better discrimination of the neutron capture signal from environmental gammas having an higher (8 MeV) energy spectrum than the most energetic gamma from the U/Th chain (^{208}Tl: 2.7 MeV). So far, Gd-loaded scintillators are used in neutrino experiments e.g.in DayaBay[147] [148] and Double CHOOZ [149].

Scintillation mechanism in organic scintillators

The detection principle of neutrons through the proposed neutron veto is based on a Gd- or B-loaded liquid scintillator. Liquid scintillators belong to the category of organic scintillators. Organic scintillators are made of hydrocarbon compounds with benzenic cycles (C_6H_6). Charged particles can excite the delocalized π-bound electrons in the benzenic cycle which after decaying to the lowest vibrational level are de-excited via the emission of photons (luminescence). The emitted light is Stokes shifted, i.e. the wavelength of the emitted light is longer than wavelength of the absorbed light. The de-excitation of the excited state can either be directly (fluorescence) or via forbidden energy states (phosphorescence). Fluorescence can be attributed to the de-excitation of singlet states (S1) and decay times are fast (prompt light signal $\mathcal{O}$(ns)), phosphorescence is attributed to the de-excitation of triplet states (T1) and decay times are slow compared to fluorescence (delayed light signal $\mathcal{O}$(µs)) [100].

The light signal of organic scintillator lies usually in the visible to near UV range. The response of the organic scintillator is not linear in ionization energy density, dE/dX, and therefore depends on the type of interacting particle. This phenomenon is known as ionization quenching. Highly ionizing particles damage the molecules and reduce the scintillation efficiency. This effect is more pronounced the greater the density of the excited molecules. The number of photons emitted per energy deposit

$$E_{\text{dep}} = \int_X \frac{dE}{dX} dX$$

can be parametrized semi-empirically according to J.B. Birks [150]:

$$N_{\text{ph}} = \frac{S}{1 + kB\frac{dE}{dX}} E_{\text{dep}} \tag{4.6}$$

where $1/(1 + kB\, dE/dX)$ is referred to as the quenching factor, S is the light yield and kB is the empirical Birks constant, which has to be determined by measurements. Scintillators are characterized by the scintillation efficiency and decay time of emitted scintillation photons: $I = I_0 \cdot \mathrm{e}^{-t/\tau}$, where I is the intensity of the scintillation and τ the decay time. The scintillation efficiency gives the amount of energy deposit that is converted into scintillation light. The base of organic scintillators emits light in the range of UV-light. It is not transparent to the luminescence and light is reabsorbed after several mm. Thus, most organic scintillators are doped with a second fluorphore which shifts the luminescence wavelength from UV light towards the visible spectrum. As the carbon to hydrogen ratio in organic scintillators is about 1, they are well suited for the absorption and detection of (fast) neutrons. Due to low the Z components, gamma detection is mainly possible via Compton scattering. Organic scintillators are commonly found in the form of plastic or liquid scintillators. Plastic scintillators are cheap and easy to fabricate. Liquid scintillators are mainly applied to large scale applications. The typical photon yield of organic scintillators is 1 photon/100 eV of energy deposit [100]. The light is detected by photo-sensors. Often, the light is guided to the photo-detectors via light guides or wavelength shifting fibers.

In contrast to other proposed active neutron vetos in the field of dark matter and rare event searches, the neutron veto of this chapter will be read out by the photo-detectors (PMTs) of the muon veto system (see Fig. 4.1).

4.2. Monte Carlo Model of a Doped Scintillating Active Neutron Veto

In Sec. 3.2.2, a GEANT4 (version Geant4.10.00.p02) based Monte Carlo (MC) simulation toolkit was developed and applied to model the response of future water Cherenkov systems for rare event searches. The toolkit is extended to include the response of doped liquid scintillator. The extended simulation toolkit allows to evaluate the performance of the afore described active neutron veto which is read out via the PMT system of the water Cherenkov detector of the muon veto system. This section will detail the implementation of the optical MC-model of the active neutron veto system. The implementation of the water Cherenkov detector MC-model is given in Section 3.2. The geometry of the neutron veto is based around a polyethylene tank of 2 m height, 2 m diameter filled with a loaded scintillator (see Sec. 4.1). It is placed centrally inside the water volume of the water Cherenkov detector. The scintillation mechanism of the liquid scintillator is implemented in GEANT4 using the `G4OpticalPhysics` physics list, which includes the production and tracking of scintillation light via `G4Scintillation` (see Sec. 3.2.2 for details on optical physics in GEANT4). In

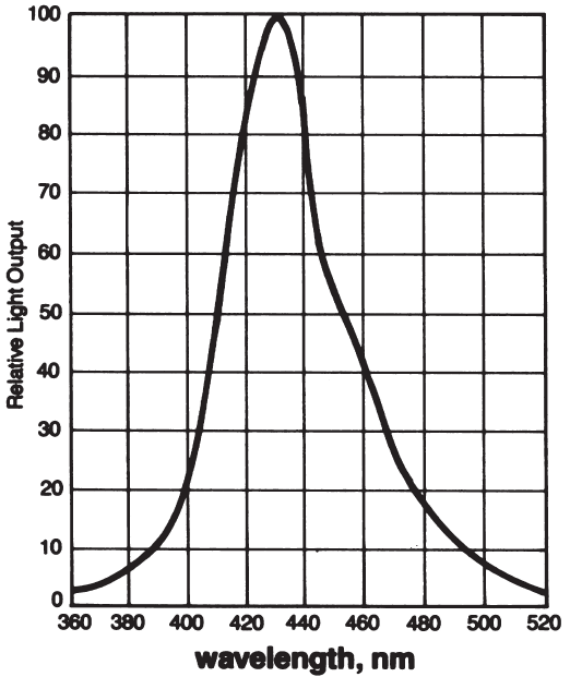

Figure 4.2.: Emission spectrum of the mineral oil based Gd-loaded liquid scintillator BC525 from St. Gobain [151]. The peak emission lies at $\lambda_{\text{peak}} = 425\,\text{nm}$.

GEANT4, a scintillator is characterized by its scintillation efficiency, its emission spectrum, its fast and slow exponential decay constants as well as its Birks constant. All scintillation properties have to be provided by the user either as constants or via wavelength depended property vectors. The scintillation efficiency (55 % of anthracene), the emission spectrum ($\lambda_{\text{peak}} = 425\,\text{nm}$ see Fig 4.2) and fast exponential decay constants (3.8 ns) were implemented according to the Gd-doped liquid scintillator BC525 from St.Gobain [151].

The non-linear response in ionization density of the scintillator is accounted for via the empirical Birks constant according to the ionization of the particle. For BC525, the Birks constant was found to be $kB_{\text{BC525}} = 0.14\,\text{mm/MeV}$ [107]. The Birks constant of the B-loaded LAB scintillator is set to $kB_{\text{LAB}} = 0.07\,\text{mm/MeV}$ [152]).

The optical parameters of the PMT readout and reflective foil of the system were validated with the help of prototype measurements in Sec. 3.3.7. The optical model of the Gd-loaded liquid scintillator was provided and assessed in [107].

The neutron veto is built around the EURECA cryostat which can hold up to one tonne of Ge- or $CaWO_4$ crystals. The arrangement of the crystals inside the cryostat as implemented in GEANT4.10 is shown in Fig. 3.38 of the previous chapter. The geometry and readout of the crystals is implemented based on the the nuclear and electronic recoil as described in Sec. 3.2.3.

4.2.1. Neutron Flux in Underground Laboratories

Ambient neutron background in underground laboratories predominately originates from material contamination of ^{235}U, ^{238}U and ^{232}Th in rock, the concrete wall and internal detector parts such as polyethylene and Cu (see Sec 2.1). The neutrons are produced via spontaneous fission and (α, n)-reactions. In (α, n)-reactions, α–particles from ^{235}U, ^{238}U and ^{232}Th decay initiate nuclear reactions in lighter elements with a subsequent emission of a neutron and possible gamma. Secular equilibrium has been assumed for U and Th

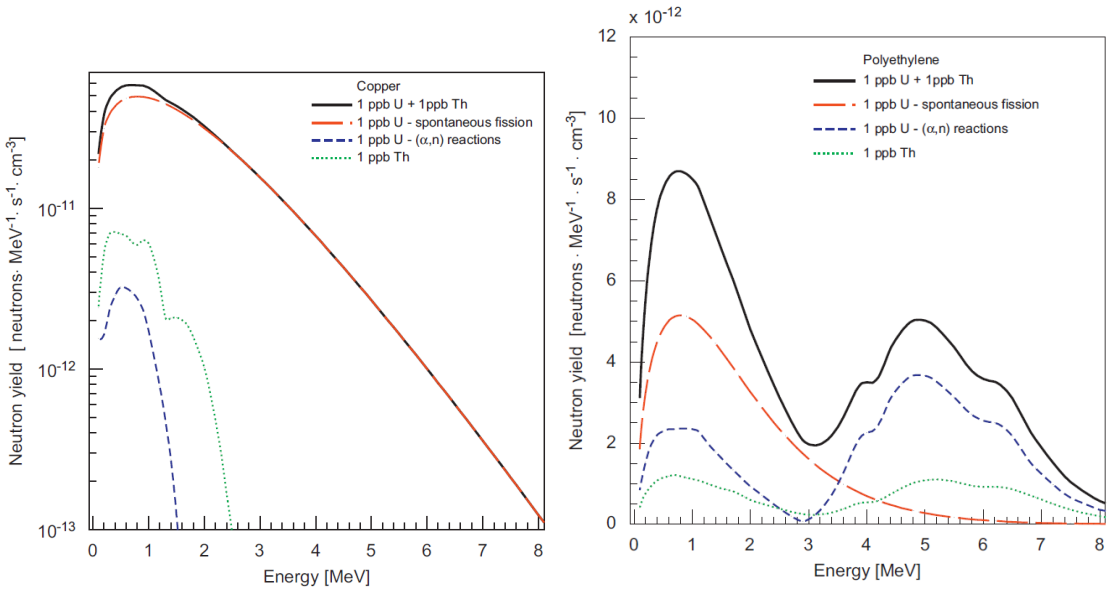

Figure 4.3.: Neutron yield in Cu (left) and polyethylene (right). The black solid line represents the total expected neutron yield from 1 ppb of U and 1 ppb of Th. Contributions to the spectrum are: spontaneous fission U (red dashed), (α,n) reactions from U (blue dashed) and (α,n) reactions from Th (green dotted) [81].

decay chains. The natural abundance considered is 99.28 % for ^{238}U, 0.72 % for ^{235}U and 100 % for ^{232}Th.

The knowledge of neutron yields, energies, material composition and contamination of each material is necessary for the prediction of single scatter nuclear background. Neutron spectra $E_n \in [0, 10]$ MeV from fission and (α n)-reactions depend on the material composition. The neutron yield and energy spectra from fission and (α,n)-reactions of Th and U in Cu, polyethylene (see Fig. 4.3) and rock were evaluated via the SOURCES4 code [153] and provided by [154]. Material contaminations of detector components can be found in Tab. 2.2 of Chap. 2. The subsequent interaction of neutrons with the surrounding rock and detector parts is handled by GEANT4 via the `Shielding Physics List 2.0` (see Sec 3.2.4 for details on the Shielding physics list). The cross-sections for neutron capture processes and interactions are given by evaluated nuclear data files (ENDF) of the national nuclear data center [155] which are included in the GEANT4 `Shielding physics list`.

4.3. Optimization of the Neutron Veto Setup

The purpose of an active neutron veto system in dark matter experiments is to tag single nuclear recoil events in the target material in coincidence with a neutron veto signal, since single nuclear recoil events from neutrons are indistinguishable from WIMP signals in dark matter experiments. The veto efficiency is one of the key parameters of an active neutron veto system, since the higher the veto efficiency, the better the background suppression of single nuclear recoil events. The better the background suppression, the better the sensitivity of the dark matter experiment.

This section is dedicated to the study and optimization of the neutron detection efficiency in coincidence with single nuclear scatters. The dedicated MC-model of a loaded scintillator and a water Cherenkov detector is applied in order to optimize the PMT configuration, scintillator doping and trigger conditions of future neutron veto designs; aiming at high neutron veto efficiencies. The optimization process is carried out for the neutron veto

setup as described in Sec. 4.1, where the neutron veto is placed inside the water Cherenkov detector around the cryostat of EURECA. EURECA planned to employ up to 1254 HpGe Ge-bolometer inside a Cu cryostat of 2 m height and 2 m diameter. Each of the crystals is placed inside a 0.5 cm thick Cu encasing. The cryostat consists of five thermal Cu shields, of 3 mm thickness each. An extra layer of 8 cm internal polyethylene acts as a passive shield against ambient neutrons from the cold front end electronics. Complimentary, the influence of the passive internal polyethylene and Cu shields on the light collection and neutron veto efficiency are studied. For this purpose, an alternative geometry of the cryostat and crystals is implemented. This allows to keep the veto design as universal as possible. The alternative geometry consists of one 3.25 mm thick single layer of Cu serves as the cold shield of the cryostat. Bare crystals are placed within the simplified cryostat. No internal passive shield of polyethylene is employed. In the following, we will refer to this configuration as the setup without internal polyethylene (poly) shield.

The following studies assume that the inside surface of the water tank is lined with the highly reflective specular film DF-2000, which shows good performance with respect to light collection (see Sec. 3.3.6). All studies are performed with the afore developed and verified GEANT4 framework. A description of the implementation of the neutron veto is given in Sec. 4.2. The response of the water Cherenkov detector and the dark matter detectors is detailed in Sec. 3.2. The nuclear recoil signal from ambient neutrons originates from material contaminations in the vicinity of the target material (see Tab. 2.2). Here, studies are limited to neutrons from the Cu 10 mK cold shield of the cryostat. The Cu cold shield is chosen as a benchmark simulation, as it is closest to the target material and U/Th contaminations contribute significantly to the single nuclear recoil background budget in EURECA [76]. Each simulation in the following optimization process is based on 2.5×10^6 primary neutrons which are distributed randomly within the Cu shield volume. The neutron flux and energy spectra from ^{232}Th and ^{238}U in Cu in 10 ppb (parts per billion) are provided according to SOURCES [81].

In the following, the neutron veto is optimized with respect to:

- number of PMTs
- arrangement of PMTs
- doping of liquid scintillator: Gd (0.2 %, 2 %) or B (3 %)
- presents of internal polyethylene and Cu shields

Starting point of the study is the PMT-configuration of the afore developed muon veto system (see Chap. 3) and the BC525 liquid scintillator for the neutron veto as active material, which is doped with 0.2 % of Gd by weight.

As a first reference, the water tank illumination from the scintillation light of neutron captures inside the scintillator is studied. Based on the outcome of this study three further PMT setups with different numbers of PMTs and arrangements are defined.

4.3.1. Water Tank Illumination by Scintillation Light

The knowledge of the inner tank surface illumination from scintillation light is a first measure to deduce sensible PMT arrangements. An efficient way to study the tank illumination as seen by a PMT is to cover the entire inner tank surface with a photocathode like foil and investigate the average number of photoelectrons per PMT-bin. The study focuses on the tank illumination from neutron interactions in the scintillator if a single nuclear recoil is

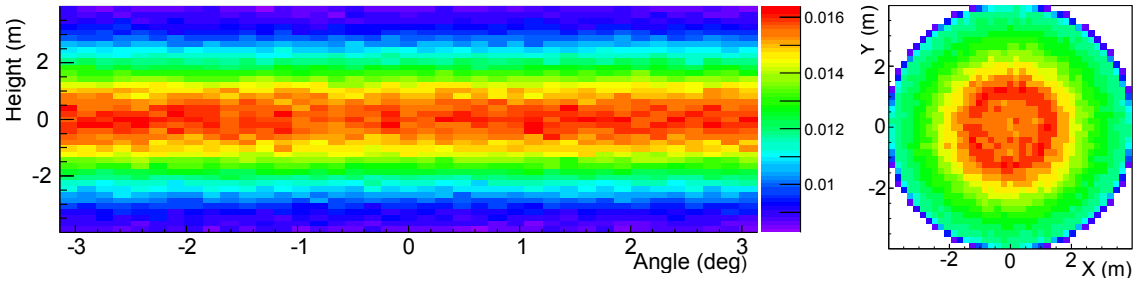

Figure 4.4.: Tank illumination from neutron interactions in the scintillator if a single nuclear recoil is recorded. The neutrons originat from Th-contaminations in the 10 mk Cu cold shield. Left: The illumination of the lateral surface. Most of the light is detected ±2 m around the centre of the tank which corresponds to the dimensions of the scintillator. Right: The illumination of the bottom surface of the tank.

recorded in one of the dark matter detectors. The illumination is shown in Fig. 4.4. Each bin corresponds to the size of an 8" PMT. In contrast to the homogeneous illumination by cosmic muons, most light would be detected by PMTs placed within ±2 m from the center of the tank for ambient neutron events. The illuminated area corresponds to the dimensions of the scintillator, both for the later surface as well the top and the floor of the tank surface. This suggests to add a centrally placed ring to the floor and top of the tank surface. The avarage number of photoelectrons per PMT bin is reduced by two to three orders of magnitude compared to muon events. At the center of the lateral tank surface, where the illumination of the tank is highest $\langle N_{\mathrm{PE}} \rangle$/bin $\approx$ 0.015PE. This suggests to increase the overall number of PMTs in order to increase light collection and thus increase the sensitivity to scintillation light.

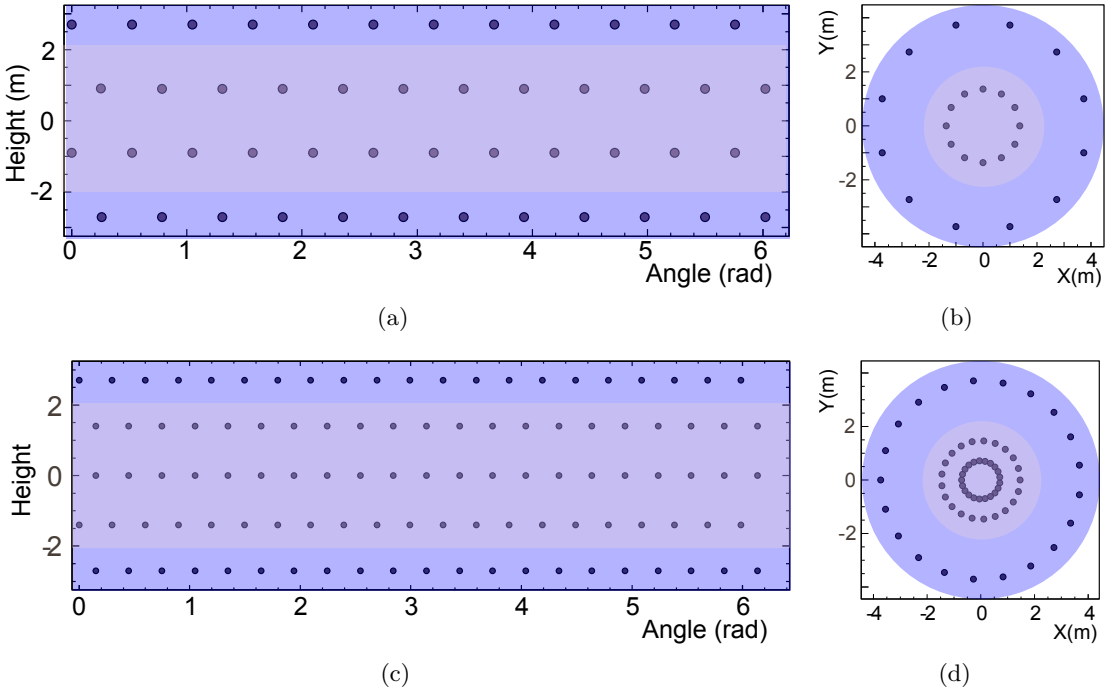

Figure 4.5.: Top: Setup 2 with 96 PMTs in total: 12 PMTs in 4 lateral rings (a), 12 PMTs in two lower and two upper rings each (b). Bottom: Setup 3 with 231 PMTs in total: 21 PMTs in 5 lateral rings (c), 21 PMTs in three lower and three upper rings each (d).

4.3.2. Neutron Veto Performance Studies

The performance of four different PMT setups with different number of PMTs and PMT arrangement will be studied in the following. The total number of PMTs per setup studied is: 72, 96, 120 and 231. The PMTs are arranged in alternating rings of 12, 15 or 21 PMTs in 6, 8 or 11 rings. Starting point is the PMT setup of the muon veto system from the previous chapter (see Sec. 3.4.3) which arranges 12 PMTs in each of the five lateral rings and 12 PMTs in one lower and one upper ring each. In the following, this setup is called setup 1-72. We resume the naming convention of the previous section, i.e. setup *K*-*L*, where $K = 1, 2, 3$ refers to the number of rings on the floor surface and $L = 72, 96, 102$ and 231 refers to the total number of PMTs. The results from the illumination study suggests to add centrally placed rings to the bottom and top and possibly to the lateral surface of the tank in order to increase light collection. Setup 2-96 realizes this by adding a complimentary ring of 12 PMTs to the bottom and top of the tank surface (setup 2-96 see Fig. 4.5 top). Setup 2-120 arranges 15 PMTs instead of 12 PMTs per ring in the style of setup 2-96. In setup 3-231, the number of rings as well as the number of PMTs is increased. The setup adds another ring to the bottom, top and lateral surface of the tank. It arranges 21 PMTs in five later and three rings at the top as well as at the bottom of the tank (setup 3-231 see Fig. 4.5 bottom).

For each PMT setup, 2.5×10^6 primary neutrons are shot randomly within the cold shield Cu volume according to the energy spectrum of neutrons in Cu as shown in Fig. 4.3. Amongst other variables, the GEANT4 framework records the number of detected photoelectrons, the total energy deposit in the scintillator, the nuclear and electronic recoil energies in the Ge-crystals as well as neutron track information such as capture volume and number of interactions.

To begin with, different doping options of the liquid scintillator are studied with respect to scintillation light production and energy deposit inside the scintillator. The study distinguishes between setups with and without internal polyethylene and Cu in the shielding scheme of the dark matter detector.

Gd-doping 0.2 % (2 %)

On average, a neutron event produces $\langle N_{\text{scinti}} \rangle = 2.79\,(2.9) \times 10^4$ scintillation photons, which is directly related to the mean energy deposit within the scintillator: $\langle E_{\text{dep}}^{\text{veto}} \rangle = 2.72\,\text{MeV}\,(2.8\,\text{MeV})$. Fig. 4.6 shows the energy deposit in the scintillator. Only 34 % (37 %) of the neutrons get captured inside the scintillator volume either on Gd, H or C and produce on average $\langle N_\gamma \rangle = 2.38$ (2.48) capture gammas. Of the remaining 66 %, 30 % of the neutrons get captured in the Cu components of the five cold shields and about 25 % on the internal poly-shield. The remaining neutrons get captured inside the crystals, screws or rods of the cryostat.

Gd-doping 0.2 % (2 %) without polyethylene

Without internal polyethylene, 90 % (96 %) of the neutrons get capture inside the Gd doped scintillator, producing $\langle E_{\text{dep}}^{\text{veto}} \rangle = 6.02\,(6.3)\,\text{MeV}$ and $N_{\text{scinti}} = 5.84\,(6.5) \times 10^4$ scintillation photons. From the remaining neutron, 5 % (2 %) get captured in the Cu shield of the cryostat. On average $\langle N_\gamma \rangle = 3.25\,(3.52)$ gammas are produced in capture process.

The doping of the liquid scintillator with 0.2 % Gd compared to no doping increases the number of neutron captures inside the scintillator. The increase is more significant for setups without internal shielding. In comparison, without any doping 27 % of the neutrons

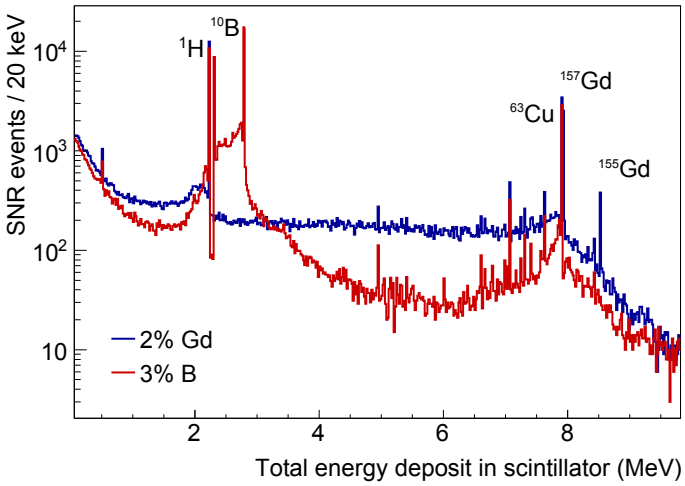

Figure 4.6.: Total energy deposit inside the scintillator for single nuclear recoil events. The blue solid spectrum shows the energy deposit inside a 2 % Gd-loaded scintillator. The gamma-lines from n-capture on ^{157}Gd and ^{155}Gd are visible at 7.9 MeV and 8.5 MeV. The red line shows the energy deposit in a 3 % B-loaded scintillator. Neutron capture on B produces an alpha and ^{7}Li that deposit in total 2.3 MeV in the scintillator, the gamma-peak lies at 0.48 MeV. The lines at 2.2 MeV, 4.9 MeV and 7.9 MeV correspond to the total energy deposit from gammas released in n-capture processes on ^{1}H, ^{12}C and ^{63}Cu respectively.

get captured inside the scintillator which is about 70 % less than in the 0.2 % Gd-option of the scintillator with no internal poly. Overall, one can observe that an increase in doping increases the amount of neutron capture processes, as is to be expected. Consequently, the number of capture gammas and thus the energy deposit inside the scintillator and the amount of scintillation light produced increases. In case of setups without internal shielding, the percentage of captured neutrons on Gd is very high for both 0.2 % of Gd and 2 % of Gd. An increase in doping from 0.2 % to 2 % does not increases the percentage of neutron captures significantly. Internal shielding reduces the fraction of neutron captures and scintillation light by 37 %, as neutrons are absorbed in the shielding components of the detector. As a consequence, the optimization of light collection becomes more important for setups with internal shielding compared to detector setups without internal polyethylene.

B-doping (3 %) with internal polyethylene

If the scintillator is doped with 3 % ^{10}B, 36 % of the neutrons get captured inside the scintillator volume. Again, 30 % of the neutrons get captured in the Cu components of the five cold shields and 25 % on the internal polyethylene. In the B-doped option of the scintillator, the average energy deposit per neutron event in the scintillator is $\langle E_{\mathrm{dep}}^{\mathrm{veto}} \rangle = 2.3\,\mathrm{MeV}$. This is a reduction of 20 % compared to the 2 % Gd-doped scintillator. This is expected since the average energy after the capture is smaller in case of ^{10}B (2.3 MeV for α and ^{7}Li, 0.48 MeV for gamma) compared to energies available after neutron capture on Gd (7.9 MeV for gammas see also Eqn.4.1, 4.1). In 3 % B doped scintillators, a neutron event produces on average $\langle N_{\mathrm{scinti}} \rangle = 1.5 \times 10^4$ scintillation photons. As a reference, the energy deposit (for single nuclear recoil events) in the scintillator for B and Gd-doping with internal polyethylene is shown in Fig. 4.7. This is 55 % less compared to setups with 0.2 % of Gd doping (and internal poly). This can be explained by the fact that for one, less energy is available to produce the scintillation light and, more importantly, that the scintillation

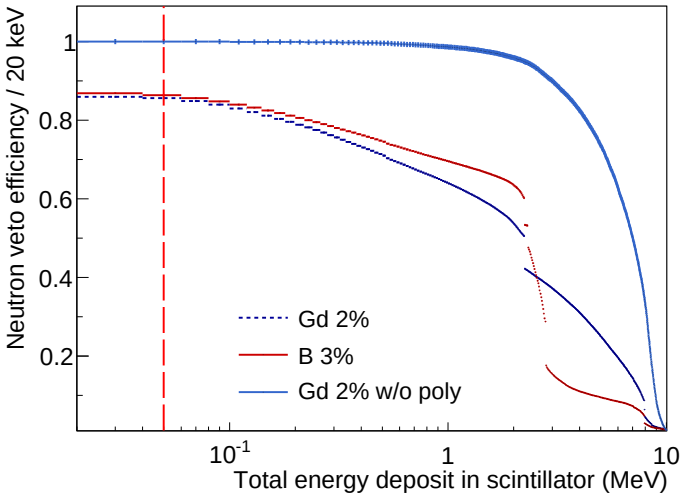

Figure 4.7.: Neutron veto efficiency ($\epsilon^{\text{veto}}_{\text{SNR}}$) as a function of the neutron veto energy threshold for single nuclear recoil events (SNR). Blue dashed spectrum: $\epsilon^{\text{veto}}_{\text{SNR}}$ of a 2 % Gd-loaded liquid scintillator. Red spectrum: $\epsilon^{\text{veto}}_{\text{SNR}}$ of a 3 % B-loaded liquid scintillator. Light blue spectrum: $\epsilon^{\text{veto}}_{\text{SNR}}$ of a 2 % Gd-loaded liquid scintillator for a detector setup without internal polyethylene and Cu-shielding. In order to tag SNR with an efficiency of 86 % (99 % w/o poly), a threshold $E^{\text{veto}}_{\text{thr}} = 50\,\text{keV}$ is required (red dashed line).

yield of the ^{7}Li and α-particles is quenched by a factor of about 10 in comparison to gammas [82].

Whether the light collection in the PMTs is sufficient to detect neutrons in the scintillator with high efficiency has to be evaluated in a separate study (see Sec. 4.3.5). From the stand-point of scintillation light production, both the 0.2 % and the 2 % of Gd-doped options outperform the 3 % B-doped option.

4.3.3. Veto Energy Threshold

As the purpose of an active neutron veto system in dark matter experiments is to tag single nuclear recoil (SNR) events, performance studies are focused in the following on neutron events which cause single nuclear recoils. A SNR event is tagged if the light signal in the PMTs comply with a given trigger condition. Out of the 2.5×10^6 primary neutrons, 6 % produced single nuclear recoils in one tonne of Ge-crystals. A nuclear recoils is defined according to the ionization yield of the Ge-crystal ($Q = E_{\text{ion}}/E_{\text{rec}} < 0.5$) see Sec. 3.2.3 for a detailed account on the response of Ge-bolometer). As a first reference, the total energy deposit in the scintillator normalized to SNR events is studied (see Fig. 4.7). This allows to estimate the maximal possible neutron veto efficiency as well as to determine a sensible energy threshold for the neutron veto (see also Fig. 4.6).

It clearly shows that setups without internal shielding achieve very high neutron veto efficiencies. Over 99 % of the neutrons which produce a SNR also deposit at least $E^{\text{veto}}_{\text{dep}} = 50\,\text{keV}$ of energy in the neutron veto. Consequently, a neutron veto threshold with respect to energy deposit in the scintillator of $E^{\text{veto}}_{\text{thr}} = 50\,\text{keV}$, allows to tag SNR with an efficiency of $\epsilon^{\text{veto}}_{\text{Edep}} > 99\,\%$. The threshold is of the same order as similar proposed neutron veto systems [143].

In case of dark matter detector setups with internal polyethylene shielding, not all of the neutrons which produce a SNR in the bolometer also deposit energy in the neutron veto,

as neutrons get absorbed in the shielding components of the detector setup. This limits the maximal possible neutron detection efficiency of the neutron veto to $\epsilon_{\mathrm{Edep}}^{\mathrm{veto}} < 86\,\%$ at a threshold of $E_{\mathrm{thr}}^{\mathrm{veto}} = 50\,\mathrm{keV}$. Furthermore, the reduced energy deposit in the scintillator due to the reduced number of neutron captures on Gd (or B) causes a stronger drop in efficiency with increasing energy threshold in comparison to setups without internal shielding. Below a threshold of 100 keV, the 3 % B and 2 % Gd doped scintillators are comparable in efficiency to detect neutrons. The efficiency of the 3 % B-loaded scintillator drops below the efficiency of the 2 % Gd-loaded scintillator above a veto threshold of 2 MeV as is to be expected due to the maximal possible energy available from n-capture processes on B (2.3 MeV) compared to Gd (8 MeV). The efficiencies have to be treated with caution though as the study does not take into account the quenching of α and Li from n-capture on B and the possibility of incomplete light detection in the PMTs. Consequently, a reduced efficiency is to be expected which will be more prominent for the 3 % B option of the scintillator.

The following studies investigate how a threshold of $E_{\mathrm{thr}}^{\mathrm{veto}} = 50\,\mathrm{keV}$ translates into light collection and tagging efficiencies.

4.3.4. Light Collection in the PMT System of the Muon Veto

The light collection of the neutron veto is defined as the number of detected photons per energy deposit in the scintillator $L = N_{\mathrm{PE}}/E_{\mathrm{dep}}^{\mathrm{veto}}$. Exemplary, the number of detected photons as a function of energy deposit in the scintillator for setup 2-96 doped with 2 % Gd or 3 % B is shown in Fig. 4.8 and Fig. 4.9 respectively. The light collection of the four previously defined PMT setups is studied. Exemplary, the detector geometry of setup 2-96 is used to study the influence different percentages (0.2 %, 2 %, 3 %) and types (Gd, B) of doping. The influence of the internal polyethylene shield on the light yield is studied using setup 3-120 (see Tab. 4.2).

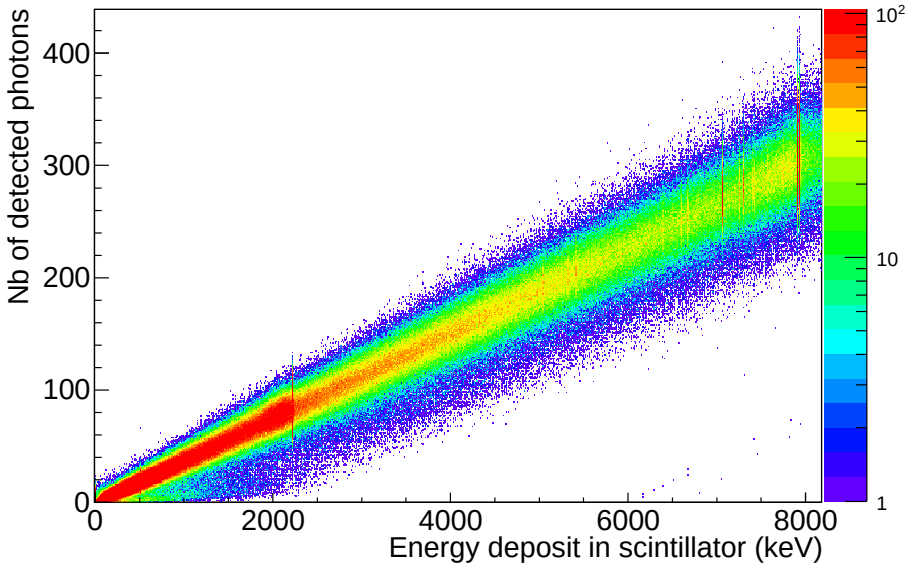

Figure 4.8.: Number of detected photons as a function of energy deposit in the scintillator for setup 2-96 doped with 2 % Gd. The 2 MeV, 5 MeV and 8 MeV gamma from n-capture on H, C, Cu and Gd are visible.

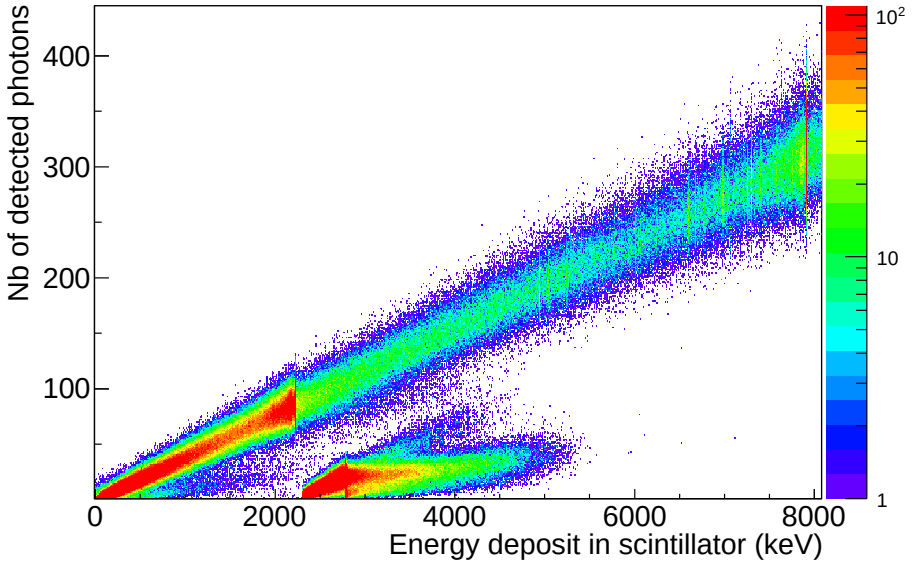

Figure 4.9.: Number of detected photons as a function of energy deposit in the scintillator for setup 2-96 doped with 3 % B. The spectrum shows the 0.48 MeV gamma as well as the quenched light emission from the 2.31 MeV α and ^{7}Li from n-capture on ^{10}B. The total energy deposit from the emitted gamma from n-capture on H, C and Cu are visible at 2 MeV, 5 MeV and 7.9 MeV respectively. The reduced light yield of the α-particle and Li is due to the non-linear quenching of highly ionizing particles.

In the following, the influence is discussed in the two extremes of small energy deposits, which is the energy range where an effective threshold applies ($E_{\text{dep}}^{\text{veto}} < 50\,\text{keV}$), as well as large energy deposits ($E_{\text{dep}}^{\text{veto}} < 10\,\text{MeV}$) in order to deduce the optimal setup with respect to light collection. Starting point of the study is setup 1-72 and a liquid scintillator doped with 0.2% of Gd. An increase in light collection can be observed when adding an extra ring of PMTs opposite of the scintillator (setup 2-96) to the top and floor surface of the tank as suggested by the tank illumination study is investigated. The increase is more prominent at high energy deposits. An increase in percentage of Gd-doping inside the scintillator from 0.2 % to 2 % in setup 2-96 increases the light collection, though the effect is not very strong as neutrons only get captured in about 30 % of the cases. The influence is stronger at small energy deposits. Using 3 % of B instead of 2 % of Gd does not change the light collection in setup 2-96 at small energy deposits. At high energy deposits though, a significant decrease of light collection can be observed as in B-doped scintillators overall less energy is deposited and light output is reduced further due to quenching. Increasing the number of PMTs opposite of the scintillator first by 20 %, than by 50 % increases the light collection. The increase in the is more pronounced for large energy deposits. Here, the increase of collected photoelectrons is of the same order as the increase in numbers of PMTs. The influence on the light collection of the internal polyethyleneand Cu shield for setup 2-120 is significant at low energy deposits. For the same arrangement and number of PMTs, setups without internal shields detect twice as much photoelectrons for small energy deposits. To conclude: In an energy range of $E_{\text{dep}}^{\text{veto}} < 50\,\text{keV}$, where an effective threshold of the veto applies, both, a higher doping as well as a larger number of PMTs help to lower the threshold of the neutron veto. At higher energy deposits ($E_{\text{dep}}^{\text{veto}} < 10\,\text{MeV}$), setups with larger numbers of PMTs and PMT rings placed opposite of the scintillator help increase the light collection significantly. Setups with 0.2 % or 2 % Gd-doped scintillators

Table 4.2.: Light collection of four different PMT setups and different percentages (0.2 %, 2 %, 3 %) and types (Gd, B) of doping of the liquid scintillator with and without internal polyethylene-shield in relation to energy deposit in the neutron veto. Energy ranges are given in keV. Statistical error < 0.5 %.

Setup	$E_{\mathrm{dep}}^{\mathrm{veto}} < 50\,\mathrm{keV}$ (PE/MeV)	[50-100] (PE/MeV)	[100-200] (PE/MeV)	[0-10000] (PE/MeV)
Setup 1-72 0.2 % Gd	89.8 ±0.4	194 ±1	334 ±1	6947 ±5
Setup 2-96 0.2 % Gd	109 ±1	282 ±1	513 ±2	11440 ±8
Setup 2-96 3% B	125 ±1	302 ±1	551 ±2	5765 ±4
Setup 2-96 2 % Gd	125 ±1	299 ±1	542 ±2	11880 ±8
Setup 2-120 2 % Gd	144 ±1	369 ±2	672±2	14950 ±10
Setup 2-120 2 % Gd w/o poly	306 ±17	306 ±17	350 ±10	16220 ±11
Setup 3-231 2 % Gd	229 ±4	678 ±7	1271 ±3	29150 ±21

outperform the B-doped scintillator option for the same number and arrangement of PMTs. The light collection is higher in setups without internal poly, as 96 % instead of 37 % of the neutrons get captured inside a 2 % Gd-doped scintillator, producing roughly twice as much scintillation photons. In the specific case of the EURECA geometry, which includes five cold shields for the cryostat and where each crystal in embedded inside a Cu encasing including diverse cables, 30 % of the neutrons get captured inside the cryostat, reducing the efficiency to tag them inside the neutron veto. A neutron veto is likely to act less efficiently for detector geometries with increased amounts of material in vicinity of the target material. With respect to light collection, setup 3-231 with a doping of 2 % of Gd is the best performing setup. An energy deposit of $E_{\mathrm{dep}}^{\mathrm{veto}} = E_{\mathrm{dep}}^{\mathrm{thr}} = 50\,\mathrm{keV}$ yields on average a total of $N_{\mathrm{PE}} = 25$.

4.3.5. Neutron Detection Efficiency and Trigger Conditions

The neutron detection efficiency determines the quality of a neutron veto system and gives a complimentary measure of the performance of the afore defined setups. This will help to deduce an optimal design of the neutron veto. Two veto efficiencies are defined in this context:
1. The percentage of tagged neutrons which caused a single nuclear recoil $N_{\mathrm{tagged}}(\mathrm{SNR})$ in a dark matter detector over all events with a single nuclear recoil ($N(\mathrm{SNR})$)

$$\epsilon_{\mathrm{SNR}}^{\mathrm{veto}} = \frac{N_{\mathrm{tagged}}(\mathrm{SNR})}{N(\mathrm{SNR})} \tag{4.7}$$

Again, we call a SNR event tagged if the event complies with a given PMT trigger condition. Within the optimization process the trigger condition is defined as a coincident number of PMTs above a given threshold of photoelectrons ($N(\mathrm{PMT}_{\mathrm{PE>thr}})$) in a given coincidence interval.

2. The percentage of tagged neutron events which produce an energy deposit $E_{\mathrm{dep}}^{\mathrm{veto}} > 50\,\mathrm{keV}$ over all events with $E_{\mathrm{dep}}^{\mathrm{veto}} > 50\,\mathrm{keV}$

$$\epsilon_{\mathrm{thr}}^{\mathrm{veto}} = \frac{N_{\mathrm{tagged}}(E_{\mathrm{dep}} > 50\mathrm{keV})}{N(E_{dep} > 50\mathrm{keV})}. \tag{4.8}$$

The latter efficiency is defined as a more general alternative to the detection of single nuclear recoils in the EURECA specific geometry and relies on the afore derived 50 keV threshold of the neutron veto and is also proposed in other dark matter neutron vetos.

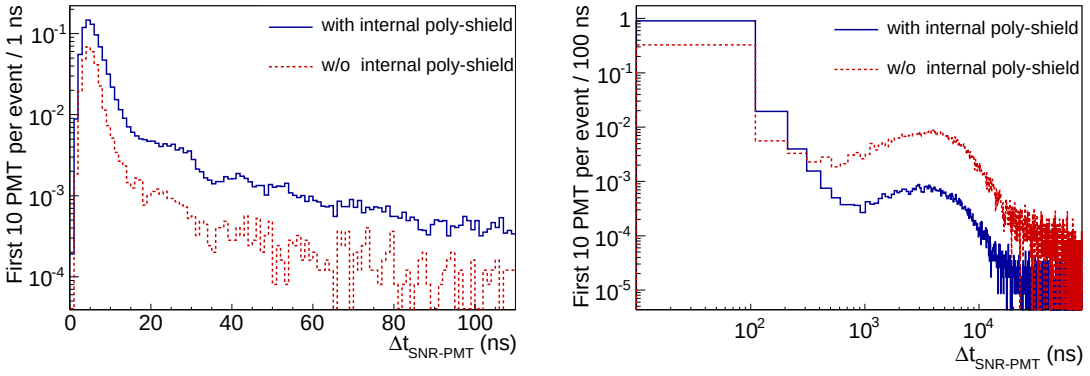

Figure 4.10.: Time difference ($\Delta t_{\mathrm{SNR-PMT}}$) between a recorded single nuclear recoil in a bolometer and the arrival time of the first photoelectron on the photo-cathode of the first 10 PMTs of the system. The prompt scintillation signal is at $\mathcal{O}$(ns) (see left plot) and delayed neutron capture signal on Gd at $\mathcal{O}$(µs) (see right plot). The blue line shows the normalized spectrum of Δt for a geometry with internal polyethylene shield. The average time difference is $\langle \Delta t \rangle = 700\,\mathrm{ns}$. The red dashed line shows the normalized spectrum of Δt for a setup without internal polyethylene shield, here the average time difference is $\langle \Delta t \rangle = 6\,\mu\mathrm{s}$.

The neutron detection efficiency depends on the chosen trigger of the system. The trigger of the neutron veto system and the trigger time window is a key element for the entire setup. In this context, the timing of coincident PMTs is of great importance. The capture time of neutrons in the liquid scintillator doped with 2 % of Gd is of the order of 3 µs, which, depending on the chosen trigger requirements, can result in large dead times of the system. Fig. 4.10 shows the time difference ($\Delta t_{\mathrm{SNR-PMT}}$) between a recorded single nuclear recoil in one tonne of Ge and the arrival time of the first photoelectrons in the first 10 PMTs of the system. $\Delta t_{\mathrm{SNR-PMT}}$ is characterized by a prompt light signal ($\mathcal{O}$(ns)) from neutron proton scattering inside the scintillator and a delayed light signal from neutron captures on Gd ($\mathcal{O}(3\,\mu\mathrm{s})$). The average time difference between a recorded single nuclear recoil and a PMT signal is roughly one order of magnitude larger for detector setups without internal polyethylene $\langle \Delta\, t^{\mathrm{w/o-poly}}_{\mathrm{SNR-PMT}} \rangle = 6\,\mu\mathrm{s}$ compared to setups with internal shield $\langle \Delta\, t^{\mathrm{w-poly}}_{\mathrm{SNR-PMT}} \rangle = 700\,\mathrm{ns}$. This can be explained by the fact, that more neutrons get captured on Gd without internal shielding which increases but delays the light signal in the PMTs. The background count rate of the PMTs as well as the trigger time window determine the rate of accidental triggers which in turn defines the dead time (see Eqn. 3.17). A sensible accidental rate of the trigger is set by the expected rate of veto signals. The expected rate of signals from n-capture in the veto is of the order of mHz or less[2]. Signals from gamma- and β-radiation on the other hand is of the order of 100 Hz.[3] The dominant source of background counts in the PMTs from signals in the neutron veto originates from ^{40}K-decays in the plastic of the neutron veto with its 1.46 MeV gamm-line and a β-spectrum with 1.33 MeV endpoint energy. The expected number of photoelectrons per PMT from ^{40}K-decays is shown in Fig. 4.11. Single photoelectron signals are expected at a rate of $\mathcal{O}$(20 Hz). In order to keep the dead time of the neutron veto at its possible

[2] Neutron rate from the plastic of the scintillator tank: $N\,(\mathrm{n/s})$ = contamination (Bq/kg) × conversion factor ppb/Bq/kg × neutron flux n/s/cm^3 × volume (cm^3) = 3 mHz with contamination 208 mBq/kg of U in plastic [156], neutron flux (SOURCES): 2.69×10^{-10} n/s/cm^3 in 10 ppb, volume plastic tank: 8×10^6 cm^3

[3] ^{40}K-decay rate in the plastic tank of the scintillator: contamination (Bq/kg) × component mass (kq) = 100 Hz with contamination 10 mBq/kg [156] of ^{40}K in plastic and mass of tank: 10×10^3 kg

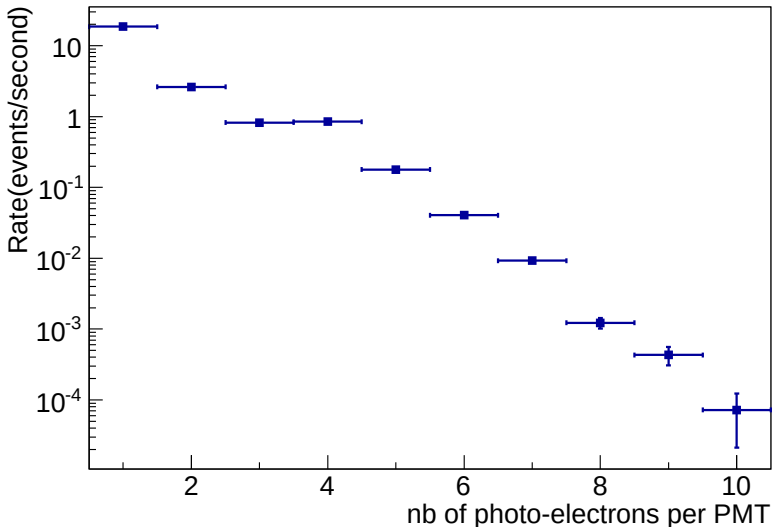

Figure 4.11.: The expected number of photoelectrons per PMT from ^{40}K-decays in the plastic tank of the scintillator, assuming a contamination 10 mBq/kg [156]. The expected rate of SPE is of the order of $R_{\mathrm{D}} = 20$ Hz from ^{40}K-decays.

Table 4.3.: Number of needed coincident PMTs with varying $\mathrm{PE}_{\mathrm{thr}}$ and varying trigger time windows t_{trig} to keep the accidental rate of of the neutron veto at or below 100 Hz. The dark count rates per PMT are 6.6 kHz for SPE signals. The rate per PMT drops to 100 Hz for 2 PE signals and to 1 Hz for 3 PE signals.

Trigger	$N(\mathrm{PMT}_{\mathrm{PE}\geq\mathrm{thr}})$	thr	R_{D} per PMT (Hz)	t_{trig}(µs)
a	5-6	1	6600	1
b	> 15	1	6600	10
c	3	2	100	1
d	3-4	2	100	10
e	6-7	2	100	100
f	2	3	1	1
g	2	3	1	10
h	2	3	1	100

minimum, it would be desirable to keep accidental rates at the same order as the expected background count from signals from ^{40}K-decays in the neutron veto, i.e. of 100 Hz or less. The background count rate in the PMTs is determined by its dark count (3.3 kHz for PMT R5912) and in the context of a water Cherenkov detector by ambient decays in the vicinity of the PMT within the water tank. The background rate depends on the photoelectron threshold and was estimated in Sec. 3.6. The rate per PMT drops to 100 Hz for 2 PE signals and to Hz for 3 photoelectron signals.

Trigger conditions for an accidental rate of 10 – 100 Hz are shown in Tab. 4.3. This sets the trigger according to Tab. 4.3. SPE triggers are only advisable for trigger time windows $t_{\mathrm{trig}} < 10$ µs. On the other hand, highest possible veto efficiencies are favorable in order to veto neutron background efficiently. To determine the best suited trigger condition with respect to accidental rate and high neutron veto efficiency, the two afore defined veto efficiencies (see Eqn. 4.7 and Eqn. 4.8) are studied for different trigger time windows t_{trig}as a function of $\mathrm{PMT}_{\mathrm{PE}\geq\mathrm{thr}}$. Three trigger time windows in the defined triggers are

Table 4.4.: Neutron veto efficiency to tag single nuclear recoils $\epsilon_{\mathrm{SNR}}^{\mathrm{veto}}$ for three different trigger conditions and for afore defined setups. The statistical error in this table is $< 1\,\%$.

Setup	$\epsilon_{\mathrm{SNR}}^{\mathrm{veto}}$(trigger 1) (%)	$\epsilon_{\mathrm{SNR}}^{\mathrm{veto}}$(trigger 2) (%)	$\epsilon_{\mathrm{SNR}}^{\mathrm{veto}}$(trigger 3) (%)
Setup3-231 2 %Gd	81	71	66
Setup2-120 2 %Gd	78	67	63
Setup2-96 2 %Gd	75	65	61
Setup2-96 0.2 %Gd	74	63	60
Setup2-96 3 % B	69	36	30
Setup2-120 w/o poly 2 % Gd	40	83	91

Table 4.5.: Neutron veto efficiency above a threshold of $E_{\mathrm{thr}} = 50\,\mathrm{keV}$ of energy deposit $\epsilon_{\mathrm{thr}}^{\mathrm{veto}}$ for three benchmark trigger conditions for the two best (setup 3-231 and setup 2-120 with 2 %Gd) and the worst performing setup (setup 2-96 with 3 % B) as well as the setup without internal polyethylene shield (setup2-120 w/o poly with 2 % Gd). The statistical error in this table is $< 1\,\%$.

Setup	$\epsilon_{\mathrm{thr}}^{\mathrm{veto}}$(trigger 1) (%)	$\epsilon_{\mathrm{thr}}^{\mathrm{veto}}$(trigger 2) (%)	$\epsilon_{\mathrm{thr}}^{\mathrm{veto}}$(trigger 3) (%)
Setup 3-231 2 % Gd	92	82	76
Setup 2-120 2 % Gd	88	77	72
Setup 2-96 3 % B	80	43	34
Setup 2-120 2 % Gd w/o poly	37	82	89

based on the timing study of $\Delta\, t_{\mathrm{SNR-PMT}}$ (see Fig. 4.10): $t_{\mathrm{trig1}} = 1\,\mu\mathrm{s}$, $t_{\mathrm{trig2}} = 10\,\mu\mathrm{s}$ and $t_{\mathrm{trig3}} = 1\mu\mathrm{s}$. They cut before, around and after n-capture times on Gd and allow hereby to study the influence of n-capture processes on Gd on the veto efficiency. As increasing the trigger time window also increases the accidental rate, three benchmark triggers are defined which all allow to keep the accidental rate of the neutron veto of the order of $R_{\mathrm{acc}} < 100\,\mathrm{Hz}$:

- Trigger 1: $6\,\mathrm{PMT}_{\mathrm{PE>0}}$ and $t_{\mathrm{trig}} = 1\,\mu\mathrm{s}$
- Trigger 2: $4\,\mathrm{PMT}_{\mathrm{PE>1}}$ and $t_{\mathrm{trig}} = 10\,\mu\mathrm{s}$
- Trigger 3: $2\,\mathrm{PMT}_{\mathrm{PE>2}}$ and $t_{\mathrm{trig}} = 100\,\mu\mathrm{s}$

Overall, the EURECA neutron veto efficiency $\epsilon_{\mathrm{SNR}}^{\mathrm{veto}}$ is limited by the fact that not all events with a single nuclear recoil register an energy deposit in the neutron veto. Thus, the maximum possible detection efficiency is 86 % for Gd- and 87 % for B-loaded scintillators (see Fig. 4.7). Fig. 4.13 shows $\epsilon_{\mathrm{SNR}}^{\mathrm{veto}}$ with $\mathrm{PMT}_{\mathrm{PE}\geq 1}$ and $t_{\mathrm{trig}} < 1\,\mu\mathrm{s}$, $\epsilon_{\mathrm{SNR}}^{\mathrm{veto}}$ with $\mathrm{PMT}_{\mathrm{PE}\geq 2}$ and $t_{\mathrm{trig}} < 10\,\mu\mathrm{s}$ and $\epsilon_{\mathrm{SNR}}^{\mathrm{veto}}$ for $\mathrm{PMT}_{\mathrm{PE}\geq 3}$ and $t_{\mathrm{trig}} < 100\,\mu\mathrm{s}$ for the afore defined setups. The benchmark triggers are indicated.

The efficiency to tag single nuclear recoils for trigger 1, 2, and 3 is summarized in Tab. 4.4. The complimentary neutron veto efficiency to tag events above a veto threshold of $E_{\mathrm{dep}}^{\mathrm{veto}} = 50\mathrm{keV}$ $\epsilon_{\mathrm{thr}}^{\mathrm{veto}}$ is given in Tab. 4.5.

The following trends can be observed:

Trigger 1

The best performing setup together for trigger 1 is setup 2-231, though only 4 % of efficiency is lost, if the number of PMTs is halved. A higher percentage of doping results in a higher detection efficiency for the same PMT setup, but the influence is weak. This is to be expected as the short trigger time window does not allow to detect all of the scintillation light from neutron captures on Gd. Mostly light from prompt scintillation light is seen. When removing the internal shielding of polyethylene and Cu from the detector setup, nearly half of the veto efficiency is lost compared to the same PMT setup with internal shield. The efficiency loss can be attributed to the short trigger time window.

Trigger 2

In contrast to trigger 1, Setup 3-120 without internal shield shows the highest veto efficiency. More light is collected, as the larger time window allows to detect light from Gd-capture processes. The maximal possible efficiency achieved for detector setups with internal polyethylene drops slightly compared to trigger 1. Both, 0.2 % Gd as well 2 % Gd-doped scintillators allow for higher veto efficiencies compared to B-loaded scintillators when studying the same PMT setup. The difference is stronger at higher numbers of coincident PMTs as B-doped scintillators produce less scintillation light. The difference between 0.2 % and 2 % Gd doping is more pronounced compared to trigger 1, as more light from Gd-capture processes is collected. The efficiency loss due to a reduced doping of 0.2 % Gd instead of 2 % can be compensated by increasing the number of PMTs in the setup e.g. from 96 PMTs to 120 PMTs.

Trigger 3

In comparison to trigger 2, the neutron veto efficiency to tag SNR events in setups without internal shielding increases by 10 %. The maximum possible efficiency for setups with internal shielding is reduced significantly. Due to a lower number of neutron captures on Gd, less light is produced in comparison to setups without internal polyethylene. This results in a weaker light signal. A high photoelectron threshold thus reduces the performance. The worst performance can be observed for the B-doped scintillator setups which is the setup with the lowest scintillation light production. The different trigger performances for setups with and without polyethylene shield can be explained as follows. In case of a setup without internal polyethylene, 96 % of the neutrons get captured inside the scintillator which results in a strong but delayed signal ($t_{\mathrm{cap}} = 3\,\mu\mathrm{s}$) of in the PMTs. As expected from the timing study of $\Delta\, t_{\mathrm{SNR–PMT}}$, a time cut $< 3\mu$s significantly reduces the veto efficiency, while a higher photoelectron threshold has no strong influence due to the strong light signal. In case of the EURECA cryostat, only 37 % of the neutrons get captured inside the scintillator. Here, 60 % of the neutrons get captured in the Cu and the polyethylene inside the cryostat which results in a more prompt but weaker light signal. Consequently, the influence of the trigger window is not as strong. The requirement of a higher photoelectron threshold on the other hand reduces the efficiency more strongly, as less scintillation light is produced compared to the setup without internal shield. The influence on the veto efficiency is separately shown for a setup with and without internal shield in Fig. 4.12 using setup 2-120 (2 % Gd) as an example.

The same trends as have been discussed for $\epsilon_{\mathrm{SNR}}^{\mathrm{veto}}$ can be observed with respect to doping, PMT number and arrangement for $\epsilon_{\mathrm{thr}}^{\mathrm{veto}}$. Setups without internal shielding show the same performance for tagging SNR events and for tagging events above a veto threshold of

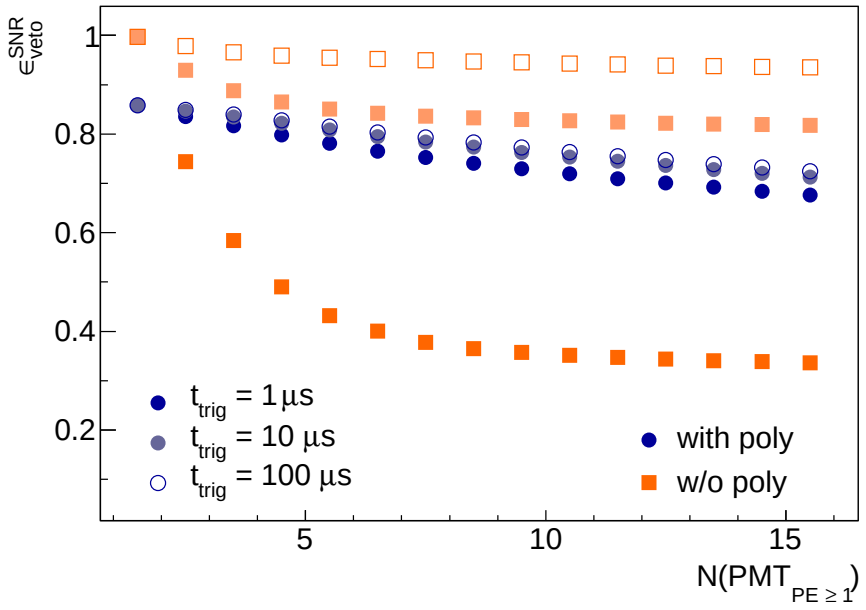

Figure 4.12.: Integral neutron veto efficiency $\epsilon^{\text{veto}}_{\text{SNR}}$ as a function of N($\text{PMT}_{\text{PE}\geq 1}$) for setup2-120 (2 % Gd) which is represented by round markers and setup2-120 w/o poly (2 % Gd) which is represented by square markers. A time cut of $t_{\text{trig}} = 1\,\mu\text{s}$ is given by dark colored markers, $t_{\text{trig}} = 10\,\mu\text{s}$ corresponds to light colored markers and $t_{\text{trig}} = 100\,\mu\text{s}$ is shown by empty markers.

$E^{\text{veto}}_{\text{dep}} = 50\,\text{keV}$. About 10 % higher veto efficiencies are achieved for setups with internal shielding compared to $\epsilon^{\text{veto}}_{\text{SNR}}$ which is limited by the fact that not all events with a single nuclear recoil register an energy deposit in the neutron veto. With a setup of 120 PMTs (2 % Gd) and the respective optimized trigger condition, setups with and without poly can achieve the same veto efficiency of $\epsilon^{\text{veto}}_{\text{thr}} = 89\,\%$.

The trigger condition strongly depends on the internal geometry of the cryostat and detectors and the required dead time of the system. The neutron veto of EURECA with one tonne of Ge performs best for a trigger condition with low PMT thresholds ($\text{PMT}_{\text{PE}\geq 1}$) and small trigger time windows ($t_{\text{trig}} = 1\,\mu\text{s}$). Out of the 5 studied setups, setup 3-231 shows the best performance. With a trigger of N($\text{PMT}_{\text{PE}\geq 1}$) and $t_{\text{trig}} = 1\,\mu\text{s}$, a neutron veto efficiency to tag SNR events of $\epsilon^{\text{veto}}_{\text{SNR}} = 81\,\%$ and an efficiency of $\epsilon^{\text{veto}}_{\text{thr}} = 92\,\%$ to tag events above a veto threshold of $E^{\text{dep}}_{\text{veto}} = 50\,\text{keV}$ can be achieved while keeping the accidental rate of the veto at $R_{\text{acc}} = 20\,\text{Hz}$. Experiments with no internal polyethylene shield and reduced detector material in the vicinity of the target can achieve veto efficiencies of $\epsilon^{\text{veto}}_{\text{SNR}} = 91\,\%$ and $\epsilon^{\text{veto}}_{\text{thr}} = 89\,\%$ at an accidental rate of 20 Hz. Here, trigger conditions with larger trigger time windows $t_{\text{trig}} = 100\,\mu\text{s}$ are favored which sets the trigger to $N(\text{PMT}_{\text{PE}\geq 3}) = 2$ if an accidental time of 20 Hz. Using setups with 120 PMTs instead of 231 would degrade the neutron veto efficiency by 4 % but simplify the setup and reduce the amount of readout channels, workload and cost. About 2 % of veto efficiency is lost if the percentage of doping is reduced from 2 % of Gd to 0.2 % of Gd in the scintillator. The feasibility of 2 % of Gd-doping in liquid scintillators with respect to stability in operation and radio-purity should be investigated further. If in doubt, an increase in PMTs could compensate for the loss in performance. In the case of a combined muon and neutron veto system of EURECA, the same readout and trigger system as the muon veto could be used as trigger conditions for muons and neutrons are the same apart from the trigger time window. In order to tag

neutrons efficiently, the trigger time window should be set to $t_{\mathrm{trig}} = 1\,\mu\mathrm{s}$. A time window of $t_{\mathrm{trig}} = 1\,\mu\mathrm{s}$ should be feasible for the front-end electronics of the muon veto trigger system as described in the previous chapter.

To conclude: Single nuclear recoils can be tagged with an efficiency of $\epsilon_{\mathrm{SNR}}^{\mathrm{veto}} = 78\,\%$ in the EURECA experiment with a combined muon and neutron veto system which is read out by 120 PMTs and uses with a trigger of $\mathrm{N}(\mathrm{PMTs}_{\mathrm{PE}\geq 1}) = 6$ in a time window of $1\,\mu\mathrm{s}$. With the same trigger, muons can be tagged with an efficiency of $\epsilon_{\mu}^{\mathrm{veto}} > 99\,\%$. The dead time of the system is dominated by the trigger time window of the neutron veto. Accidental rates are of the same order as expected background signals ($\mathcal{O}(20\,\mathrm{Hz})$) in the PMTs from $^{40}\mathrm{K}$ in the neutron veto.

The neutron veto efficiency is comparable to veto efficiencies of similar proposed concepts of neutron veto systems for dark matter experiments. As will be detailed in Sec. 4.4, the cryogenic dark matter experiment SuperCDMS proposes to employ a B- or Gd-loaded scintillator which is read out by multi pixel photodetectors and a system of wavelength shifting fibers. SuperCDMS estimates a $\epsilon_{\mathrm{SNR}}^{\mathrm{veto}} = 91\,\%$ neutron veto efficiency to tag single nuclear recoils above a veto threshold of $E_{\mathrm{thr}}^{\mathrm{veto}} = 50\,\mathrm{keV}$ [157]. In contrast to our setup, the SuperCDMS experiment does not foresee any internal polyethylene to shield against cold electronics which helps to achieve higher veto efficiencies, as we saw above. The dark matter experiment DarkSide currently installed a 30 tonne B-loaded liquid scintillator as active neutron veto around their 50 kg of liquid Argon target mass at Gran Sasso[158]. The neutron veto is read out by 110 8" PMTs. A 1000 tonne water Cherenkov muon veto read out by 80 8" PMTs tags muons with $\epsilon_{\mu}^{\mathrm{veto}} \sim 99\,\%$ efficiency. Again, no internal shield reduces the efficiency of the neutron veto. DarkSide estimates a $\epsilon_{\mathrm{n}}^{\mathrm{veto}} \approx 99.2\,\%$ veto efficiency to detect neutrons. This number is, however, not directly comparable to our efficiency, as we study the efficiency to tag neutrons in coincidence with single nuclear recoils, while the DarkSide neutron veto efficiency was estimated through AmBe data an simulations. In order to be able to directly compare the efficiencies, it would thus be necessary to simulate the response of the neutron veto to neutrons from AmBe.

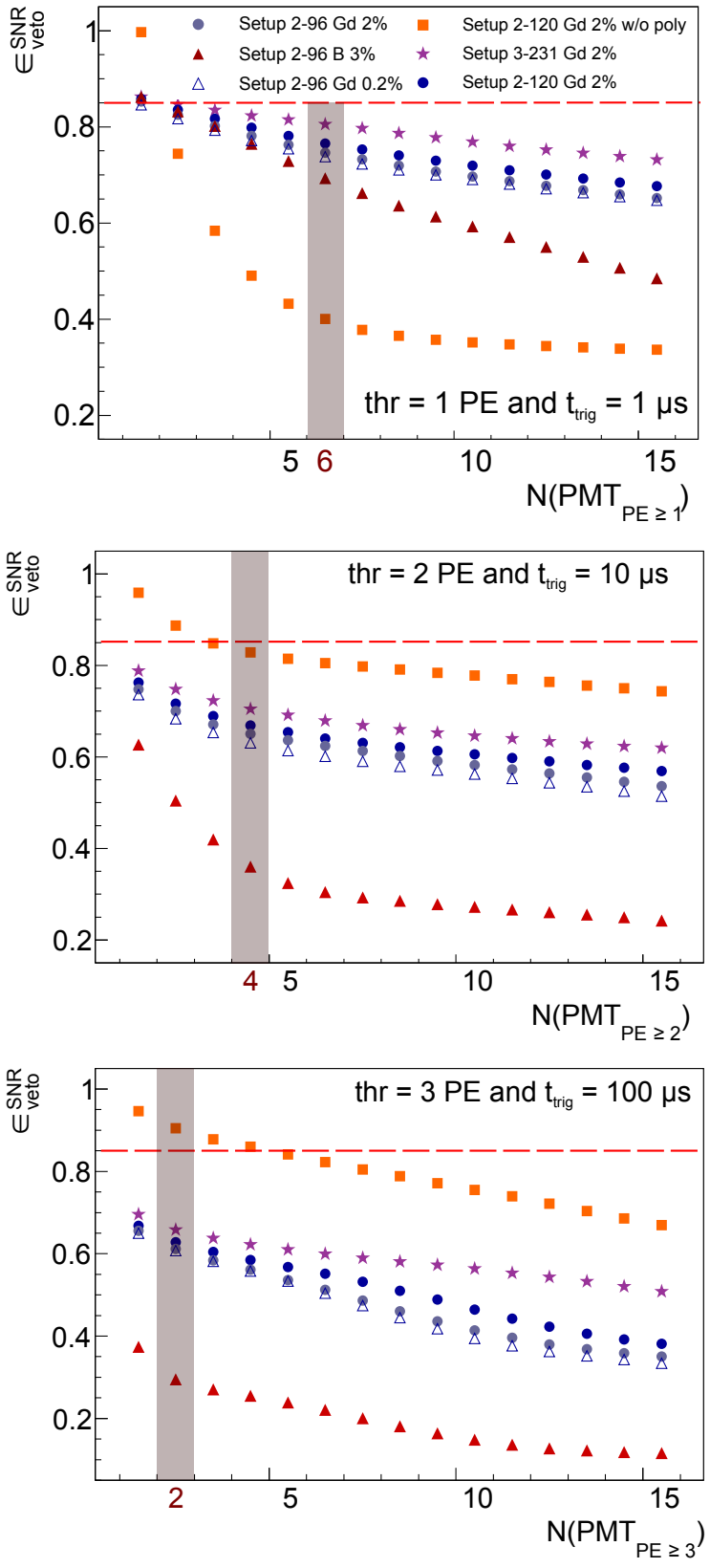

Figure 4.13.: Integral neutron veto efficiency $\epsilon_{\mathrm{SNR}}^{\mathrm{veto}}$ as a function of $\mathrm{PMT}_{\mathrm{PE}\geq\mathrm{thr}}$ with $t_{\mathrm{trig}} = 1\,\mu\mathrm{s}$ (top) or $t_{\mathrm{trig}} = 10\,\mu\mathrm{s}$ (middle) or $t_{\mathrm{trig}} = 100\mu\mathrm{s}$ (bottom) for setup 2-120 with 2 % Gd w/o poly (orange squares), setup 2-231 with 2 % Gd (purple stars), setup 2-120 with 2 % Gd (dark blue circles), setup 2-96 with 2 % Gd (purple circles), setup 2-96 with 0.2 % Gd (empty triangles) and setup 2-96 with 3 % B (red triangles). Statistical uncertainties are determined via Clopper-Pearson and are for most points smaller than the marker.

Source	Material	Mass kg	Contaminations U/ Th, ppb	Neutrons events/ tonne/ year
Screens, Cu parts	Cu	3000	< 0.002	< 0.2
Support rods	Cu-Ni alloy	200	0.01	0.05
Cables, 10 mK	Cu, Kapton	6	0.5	0.08
Holders	Kapton	0.4	1	0.02
Holders	Acrylic	1	0.01	0.002
Screws	Cu, Zn	6	0.4	0.14
Electrodes	Al	0.0002	200	0.02
Connectors	Cu, Delrin	2	1	0.02
Cables	Cu, Kapton	4	0.5	0.02
Neutron shielding	Acrylic	200	0.01	0.004
Neutron shielding	CH_2	150	0.1	0.007
Electronics	FR4	2	200	0.11
Water shielding	Water	0.4 kt	0.001	< 0.001
Total				< 1.0

Figure 4.14.: Expected background event rates due to neutrons in one tonne of Ge. The rates are given in an energy range of 20-200 keV. Only single hits were counted. The first seven rows show the contribution to the background event rate from materials close to the detectors (inside the inner shielding) [76].

4.3.6. EURECA 1 Tonne

The passive shielding concept and the material selection of detector components of the EURECA 1 tonne experiment was optimized to provide a low background environment in the region of interest (ROI) $E_{\mathrm{rec}} \in [10, 50]$ keV for WIMP-nucleon interactions. The passive shielding scheme consists of 3 m of water against gamma and neutron radiation from the surrounding rock and concrete as well as 15 cm of Cu and 20 cm acrylic as internal shieldings. If a radio-purity of $\leq$ 0.02 mBq/kg (U/Th) in the Cu cryostat, and $\leq$ 10 mBq (U/Th) for materials of the inner shielding can be ensured, most notably in the vicinity of the Ge-target, EURECA expects a gamma background rate of $< 6.1 \times 10^5$ events/tonne/year in an energy region of $E_{\mathrm{rec}} \in [20, 200]$ keV and a neutron background rate of < 1 event/tonne/year in an energy region of $E_{\mathrm{rec}} \in [10, 50]$ keV [76]. The gamma background is expected to be significantly reduced due to the high discrimination power of the Ge-bolometers between nuclear and electronic recoils (discrimination of 10^5 or better in the ROI).

In this context, EURECA determined the background budget from intrinsic material contaminations for various detector components [76]. The background rate from the most massive components was estimated through detailed GEANT4 simulations of the EURECA baseline design. The result is shown in Fig. 4.14 and Fig. 4.15 [76]. A large contribution of the irreducible single nuclear recoil rate originates from Th and U contaminations in the Cu detector components, and depends strongly on the radio-purity of Cu.

The most radio-pure Cu is currently provided by NOSV (Norddeutsche Affinerie) with < 1.6 ppt (parts per trillion) for U and < 5.6 ppt for Th. If NOSV Cu is installed in the vicinity of the target crystals, the irreducible single nuclear recoil rate is estimated to lie below 1 event/tonne/year with $\Gamma_{\mathrm{SNR}}^{\mathrm{nosv}} < 0.2$ events/tonne/year. If instead a contamination of 0.01 ppb in U/Th is assumed in the Cu components of the cryostat, vessel and plates, the irreducible single nuclear recoil rate can be as high as $\Gamma_{\mathrm{SNR}}^{\mathrm{Cu}} = 1.6$ events/tonne/year (see Fig. 4.15). With a dedicated active neutron veto, which was optimized for the EURECA geometry including the internal shield of Cu and polyethylene, the ambient neutron background rate can be reduced below $\Gamma_{\mathrm{SNR}}^{\mathrm{Cu}} = 0.34$ events/tonne/year for the Cu components

Source	δ [cm]	Mass [tonne]	Shielding	Contamination level	n-Recoils, events/ tonne/ year
Concrete	30	1291	3 m H_2O, Cu§	Tot	
				U 1.9 ppm	-
				Th 1.4 ppm	-
				K 2480 ppm	-
Copper§	Seetext	2.86	–	Tot (U,Th,K)	1.44/ 1.60 †
				U 0.01 ppb	1.33/ 1.48 †
				Th 0.01 ppb	0.105/ 0.118 †
				K 10 ppb	-
				^{60}Co 10 μBq/ kg	-
Copper(vessels)	Seetext	2.17	plates, holders	Tot	0.789 †
				U 0.01 ppb	0.731 †
				Th 0.01 ppb	0.058 †
				K 10 ppb	

δ - thickness.
† 506 kg of Ge.
§ Cryostat vessels, plates and holders.

Figure 4.15.: Background event rates per year at 10-50 keV due to single nuclear from neutrons in 253 kg of Ge or 506 kg of Ge (marked as blue cross). Rates have been re-scaled to 1 tonne of target material. The first three columns specify the source of background radiation, its thickness and mass used in simulations. The composition and thickness of the shielding between the source of background radiation and the detectors are shown in the fourth column. Individual contaminations for each radioactive isotope considered are given in the fifth column. The last column shows the expected rate for nuclear recoils [76].

of EURECA or below $\Gamma_{\mathrm{SNR}}^{\mathrm{NOSV}} < 0.04$ events/tonne/year for NOSV Cu components.

MC-studies of different realizations of the passive shielding scheme showed that an inner passive shield of Cu and polyethylene/acrylic against the ambient radiation from cold electronics is necessary to reduce the total neutron background rates below 1/tonne/year. From the stand point of an active neutron veto, detector setups without internal polyethylene shield allow for higher neutron veto efficiencies. It would thus be of interest to estimate the background budget from intrinsic material contaminations with and without internal shield as well as with and without active neutron veto. In this context, the single nuclear background budget from detector components of the neutron veto itself should be investigated and the trade off between the background reduction and the background increase caused by the neutron veto should be evaluated.

To conclude: The background budget of EURECA, or any dark matter experiment, relies on the selection of ultra radio-pure materials. The selection of materials is based on the screening of material samples of the detector components as it is impossible to screen every component of the experimental setup. At proposed radio-purities, the variation in radio-purity from sample to sample may be large. A dedicated neutron veto would not only allow to tag ambient neutron-induced background but also measure neutron rates *in situ* and thus help to reliably identify a dark matter signal.

4.3.7. EURECA 40 kg

Seeing the strategy change in cryogenic solid state dark matter experiments, the collaborations of SuperCDMS and EURECA are investigating the possibility of a joined next phase cryogenic dark matter experiment with a total payload of about 100 kg of target mass. In this scenario, it is currently foreseen that EURECA contributes about 30 kg of Ge target [159]. The dark matter detectors would be operated inside the cryostat of the SuperCDMS experiment at SNOlab. In consequence, it is also interesting to study the neutron veto efficiency for tagging single nuclear recoils for a payload of roughly 40 kg target mass instead of one tonne. The detectors are arranged in three towers of six layers and three bolometers per layer which gives 43.2 kg of target mass (see Fig. 3.38). Due to the less compact packing of the detectors compared to the 1 tonne packing in EURECA, a higher ratio of single to multiple recoils is expected (see Sec. 3.7.2) and thus a higher rate of single nuclear recoils. To make sure that the afore developed neutron veto and trigger requirements also suppress ambient background in a about 43.2 kg dark matter experiment, we estimated the veto efficiency to tag single nuclear recoils in the reduced mass setup. The detectors are placed inside the EURECA cryostat which consists of 5 Cu cold shields and one polyethylene shield. 2.5×10^6 ambient neutron are started randomly from the inner most Cu shield volume. The neutron veto shows the same performance in 43.2 kg of target mass and in one tonne of target mass at an increased ratio of single to multiple nuclear recoils. Single nuclear recoils can be tagged with an efficiency of 81 % (78 %) in the EURECA experiment with a combined muon and neutron veto system which is read out by 231 (120) PMTs and uses a trigger of $N(\mathrm{PMTs}_{\mathrm{PE}\geq 1}) = 6$ in a time window of 1 µs. It has been seen in the 4.3.5, that the internal geometry of the cryostat has a great influence on trigger conditions and veto efficiencies. Seeing that a likely location of the SuperCDMS-EURECA tower is the SuperCMDS at SNOlab cryostat, it would also be interesting for future investigations to study the influence of the SuperCDMS cryostat.

Fig. 4.16 shows the neutron veto efficiency to tag single nuclear recoils for trigger 1, trigger 2 and trigger 3 as defined in section 4.3.5. By applying the same final trigger condition as in the previous section, i.e. $N(\mathrm{PMTs}_{\mathrm{PE}>0}) = 6$ inside a trigger time window of 1 µs, a veto efficiency $\epsilon^{\mathrm{veto}}_{\mathrm{SNR}}$ of 81 % is achieved. This is the same efficiency as in the case of one tonne of detector mass.

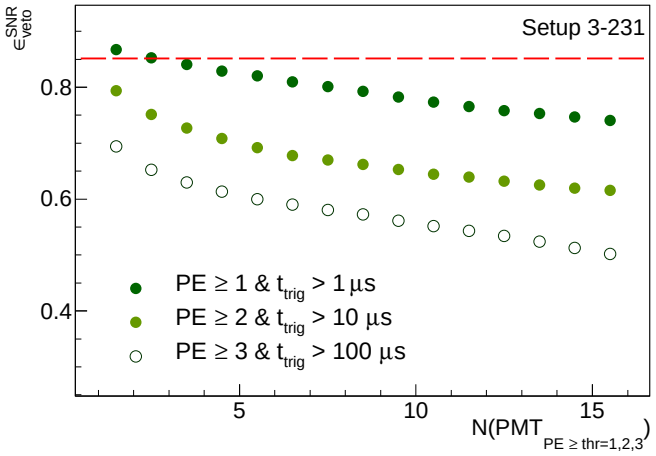

Figure 4.16.: Integral neutron veto efficiency $\epsilon^{\mathrm{veto}}_{\mathrm{SNR}}$ as a function of $\mathrm{PMT}_{\mathrm{PE}\geq\mathrm{thr}=1,2,3}$ with $t_{\mathrm{trig}} = 1$ µs (dark green marker) or $t_{\mathrm{trig}} = 10$ µs (light greed marker) or $t_{\mathrm{trig}} = 100$ µs (empty green marker) for setup3-231 with 2 % Gd in 43.2 kg of target material.

4.4. The SuperCDMS Neutron Veto

This section details an alternative design of a dark matter neutron veto. The veto was proposed by the SuperCDMS collaboration for the SuperCDMS upgrade at the underground laboratory SNOLAB [144]. In the framework of a closer collaboration between SuperCDMS and EURECA, optical simulations of the SuperCDMS neutron veto are conducted as part of this thesis. The results of the work are described here.

SuperCDMS is a calorimetric solid state experiments which employs Ge- and Si-crystals to search for the elastic scattering of dark matter particles. Currently, about 45 kg of target mass is foreseen to search for low and standard mass dark matter particles (four towers of high purity Ge-, one tower of Si- and one tower of Neganov-Luke amplified Ge-detectors). The passive shielding scheme of SuperCDMS consists of Pb, polyethylene and possibly water, which are placed outside of the cryostat. In contrast to the conceptual design of the previously discussed cryogenic dark matter experiment EURECA, no internal polyethylene against cold electronics inside the cryostat is foreseen. The setup of SuperCDMS at SNOLAB is shown in Fig. 4.17. The baseline design of the SuperCDMS neutron veto is proposed as a modular setup of 6 scintillator wedges of 2 m height filled with doped liquid scintillator. The layout of the neutron veto is shown in Fig. 4.18.

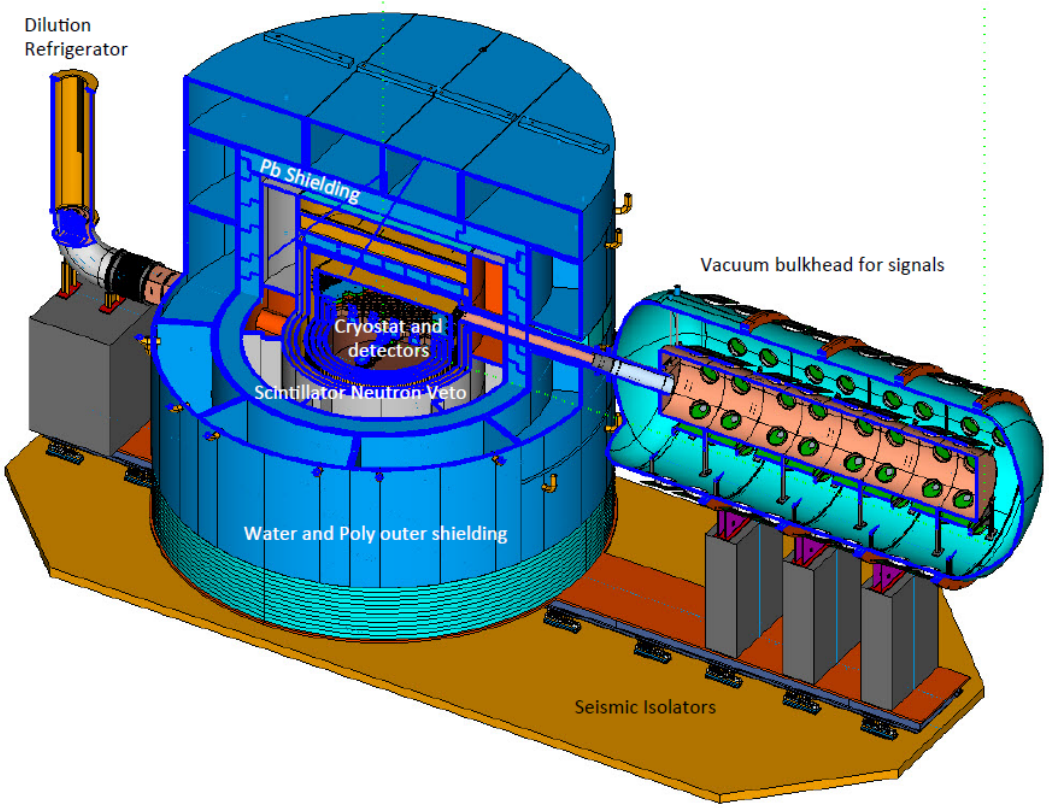

Figure 4.17.: Basic layout of the SuperCDMS SNOLAB experiment. The Ge- and Si-detectors (centre) are cooled by a dilution fridge (left) and sourrunded by the thermal cans. Layers of lead, polyethylene and water shield the detector against ambient gamma and neutron radiation. The active neutron veto is placed outside of the thermal cans and inside the lead shield. The cold box is designed to hold up to 400 kg of target mass [77]. Fig. from `https://www.slac.stanford.edu/exp/cdms/`

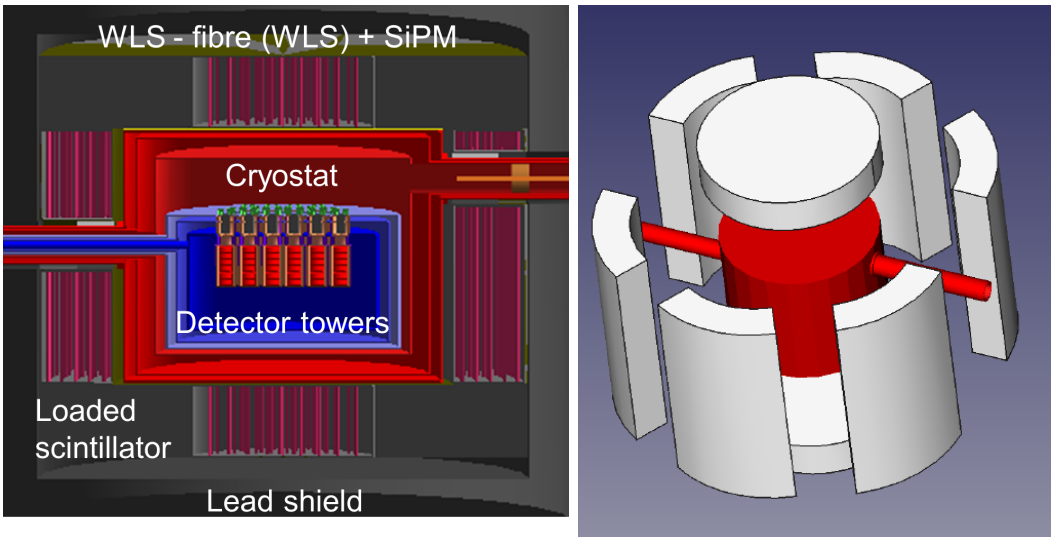

Figure 4.18.: The SuperCDMS active neutron veto as implemented in GEANT4 using SuperSim. The neutron veto consists of 6 modular wedges of 2 m height and diameter made of ^{10}B-loaded liquid or Gd-loaded plastic scintillator. The wedges are internally furnished with WLS-fibers which are read out by MPPCs. The number and spacing of the MPPCs, the diameter of the WLS-fibers as well as the reflectivity of the tank lining are free parameters within the simulation framework.

The neutron veto scintillator will be doped with 3 % per weight of ^{10}B. A likely choice for the liquid scintillator is linear alkylbenzene (LAB) loaded with primary and secondary fluors (PPO ($C_{15}H_{11}NO$)). Doped plastic scintillator wedges made of polymerized polystyrene (PS) or polyvinyltoluene (PVT) are a possible alternative. An alternative doping is Gd. The scintillator will be read out by $\sim$ 100 silicon multi pixel photon counters (MPPC) per module, which are known to be highly radio-pure. Wavelength shifting fibers (WLS) will collect and guide the light to the photo-detectors. Silicon multi pixel photon counters are sequentially connected silicon avalanche photo diodes (APDs) operated in Geiger mode [160], i.e. in reverse bias above breakdown voltage. A sufficiently high reverse bias allows for in-built signal amplification based on the avalanche breakdown. After breakdown, the voltage will be quenched below breakdown voltage. The advantages of MPPCs compared to standard photo-detector such as PMTs (see Sec. 3.1) are high gains (10^6) at low operating voltages ($V_{\mathrm{op}} < 100\,\mathrm{V}$) , high photon detection efficiency (up to 50 %) and wide spectral response. Downsides are the large dark count rates at room temperature (10^6 Hz) and the high sensitivity to temperature changes [160]. Wavelength shifting fibers trap, guide and shift the light from scintillator to increase light detection. WLS fibers consist of a (scintillating) core of refractive index n_{core} and one or two claddings of lower refractive index. Light is trapped by total internal reflection according to Snell's law with an efficiency of 3 - 8 % (see Fig. 4.20). The inner surface of wedges will be lined with a highly reflective foil.

For the SuperCDMS SNOLAB neutron veto, MPPCs are supplied by Hamamatsu Photonics [161], type S12572-100 (see Fig. 4.19(a)).The MPPCs have an effective photosensitive area of 3 $\times$ 3 mm, with 900 pixels each and an epoxy resin window. The peak photo-detection efficiency of the MPPC-S12572-100 is 35 % for a wavelength of 450 nm and it covers a spectral range of 320 nm – 900 nm (see Fig. 4.19(a) right). The gain of the MPPC lies around $G = 10^5 - 10^6$. The recommended voltage of operation is $V_{\mathrm{op}} = 1.4\,\mathrm{V}$ above breakdown voltage $V_{\mathrm{BR}} = 65\,\mathrm{V}$ [161]. The response of the MPPCs will be calibrated and monitored

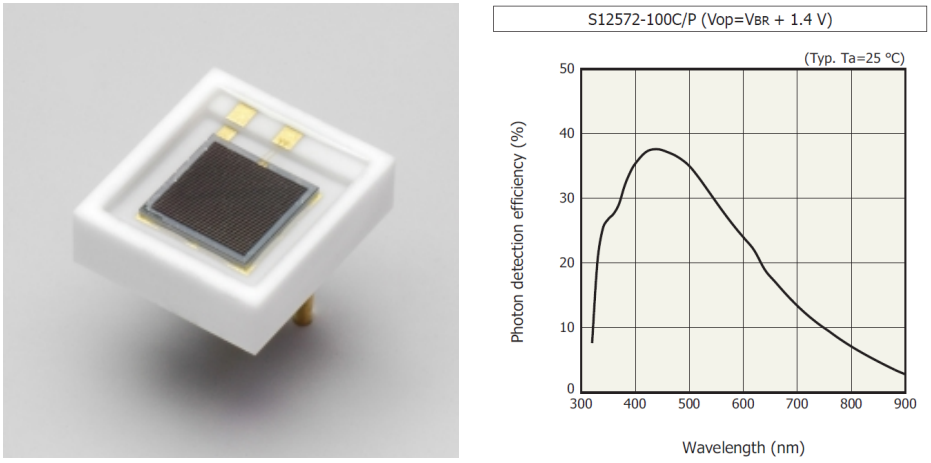

(a) (b)

Figure 4.19.: (a) MPPC S12572 and (b) photo-detection efficiency of the MPPC S12572 as a function of wavelength [161].

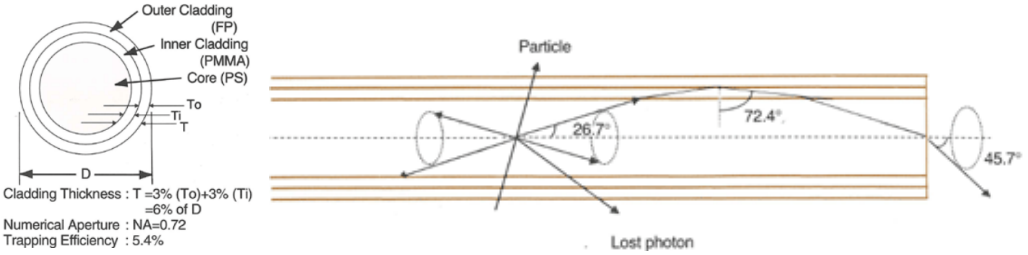

Figure 4.20.: Schematic of a double clad WLS-fiber [162]. Light is trapped by total internal reflection according to Snell's law. The angle of total reflection between core and clad is 26.7°. Typical core materials are polystyrene or glass (n = 1.59). Typical cladding material is acrylic (n =1.49) and fluorinated polymer (n = 1.42).

with pulsed LEDs. Typical dark count rates at room temperature are at the order of 10 MHz. The MPPCs will be cooled to -20 C° to reduce dark count and thus keep dead time as low as possible. The biasing, LED pulser calibration, temperature sensing, amplification and waveform digitization will be driven via an in-house build custom board developed by the collaboration of the Mu2e experiment at Fermi National Laboratory (Fermilab). The WLS-fiber will be supplied by Kuraray, type Y-11(200) [162]. The diameter of the fiber is 2 mm. Y-11 shifts blue to green light, exhibits long attenuation and high light yield. The peak absorption wavelength is 430 nm, the peak emission wavelength is 476 nm, which matches well the efficiency spectrum of MPPC-S12572. A likely choice of reflective film is Tyvek by DuPont. Tyvek consists of pressed polyethylene terephthalate (PET) fibers, non-corroding, non-conducting and provides a reflectivity of $R_f \sim 99\,\%$ in the visible spectral range (400 nm – 775 nm). The reflection is purely diffuse.

4.5. Scintillator Prototype Measurements and Simulations

A reliable optical model of the neutron veto is essential in order to predict the response and devise an efficient trigger for single nuclear recoil events. For this purpose, an end-to-end model of SuperCDMS and its scintillator system is required. The end-to-end SuperCDMS model should include an optical MC-model of both scintillator and loading options as well as its its readout. Here, we will concentrate on the optical implementation of the Gd-loaded

plastic scintillator option of the neutron veto within SuperSim, the GEANT4 based MC framework of SuperCDMS (see Sec. 4.6). Standalone simulations, which are developed in the context of this thesis, together with prototype measurements at the University of Minnesota allow to asses the optical parameters of the Gd-doped plastic scintillator option. Furthermore, the influence of optical parameters such as the reflectivity of the foil on the light output of the scintillator is studied with simulations.

In GEANT4, the modeling of optical physics strongly relies on the provision of user defined optical material property tables. For industrial components, the optical properties are usually provided by the manufacturer though they might not be provided in the required detail. For in-house built components, the spectra have to be measured. In both cases, the optical model has to be tested for its accuracy preferably with prototype measurements. For both, the liquid and the plastic option of the neutron veto, quarter-scale prototypes are in the process of being built at Fermilab and the University of Minnesota respectively. The quarter scale of the plastic option of the neutron veto system is shown in Fig. 4.23.

This following work focuses on the modeling of the plastic scintillator option loaded with Gd. The plastic option of the quarter scale is still under construction and measurements of the scintillator response is not yet available. Next to the quarter scale prototype, small plastic scintillator samples with and without Gd-doping are fabricated and tested at the University of Minnesota. The samples allow to determine the emission spectrum of the scintillator as well as the light trapping efficiency of the WLS-fiber. If the MC-model describes the scintillator measurements adequately, it can be added to SuperSim, to design and optimize the full-size neutron veto.

4.5.1. Prototype Setup and Measurements

The experimental prototype is based around a plastic scintillator sample of 19.3 mm diameter × 21.14 mm length. The scintillator is wrapped with a highly reflective and diffuse Teflon foil. The scintillator is in-house build by the chemistry department of the university of Minnesota. The polystyrene based plastic scintillator is doped with 0.1 wt% PPO and 0.01 wt% POPOP[4]. A 1 mm WLS-fiber (type Y11 from Kuraray [162]) is embedded at the center of the scintillator sample (see Fig. 4.21). All measurements were conducted at the University of Minnesota [163].

The spectral response of the scintillator and the WLS-fiber is measured using a monochromator (Oriel 74000). The monochromator is calibrated beforehand via five LEDs of differing wavelength (377 nm, 468 nm, 565 nm, 590 nm and 660 nm). A UV LED (377 nm) is embedded within the scintillator in order to illuminate the sample. The light emission of the full scintillator sample as well as the emission of the WLS-fiber alone is then measured with the help of the calibrated monochromator. A mask is placed on top of the scintillator in order to measure the light output of the WLS-fiber. Measurements are taken in 2 nm steps from 200 nm to 800 nm. Fig. 4.22 (top) shows the measured emission spectra. The light loss of the WLS-fiber is estimated by the ratio of integral area of the masked ($\int_\lambda \mathrm{I}_{\mathrm{masked}}(\lambda)\mathrm{d}\lambda$) and unmasked spectrum via:

$$\eta_{\mathrm{loss}} = 1 - \frac{\int_\lambda I_{\mathrm{masked}}(\lambda)\, d\lambda}{\int_\lambda I_{\mathrm{unmasked}}(\lambda)\, d\lambda - \int_\lambda I_{\mathrm{masked}}(\lambda)\, d\lambda} \tag{4.9}$$

It is found to be $\eta_{\mathrm{loss}} = 6.67\,\%$. The trapping efficiency of light within an isolated double clad WLS-fiber is stated as 5.4 % by Kuraray.

[4]The sample in question is not doped with Gd

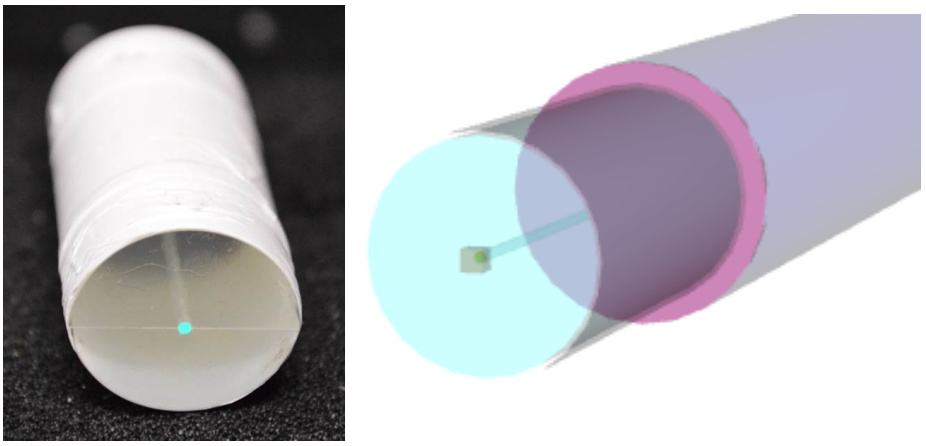

Figure 4.21.: Left: In-house build polystyrene scintillator sample with embedded WLS-fiber. The sample scintillator (19.3 mm diameter × 21.14 mm length) is wrapped with a highly reflective and diffuse Teflon tape. A 1 mm WLS-fiber is embedded at the center of the scintillator sample. Right: Scintillator sample as implemented in GEANT4.

4.5.2. Prototype Simulations

Goal of the prototype simulation is the assessment and adjustment of optical parameters which describe the optical response of the plastic scintillator sample, the reflective foil and the response of the WLS-fiber. If the optical parameters describe the scintillator setup adequately, they will be included in in the SuperSim framework. For this purpose, the prototype geometry is implemented in a standalone GEANT4 simulation as realistically as possible and the outcome of the simulation is compared to the measurements above. Key elements to the prototype simulation are the production and tracking of scintillation light as well as the trapping, absorption and re-emission of light in the WLS-fiber. The prototype geometry is implemented in GEANT4 according to the prototype setup in Sec. 4.5.1 and is shown in Fig. 4.21 (right).

The scintillator is modeled by `G4Scintillation`. A scintillator is defined by its light yield, its emission spectrum, decay time and Birks constant (see Sec. 4.1) [112]. The emission spectrum of the in-house built Gd-doped plastic scintillator is provided by the monochromator measurements of the previous section (see Sec. 4.5.1) and implemented accordingly. The light yield of the Gd-loaded plastic scintillator has not been measured yet. Instead, a typical light yield for plastic scintillators of 10 000 photons/MeV energy loss is assumed. The Birks constant of the plastic scintillator is set to $kB = 149\,\mu\text{m/MeV}$ [164]. The decay time is set to $\tau_{\text{LAB}} = 2.4\,\text{ns}$. The wavelength shifting fiber (Y11 from Kurary) is modeled with the help of `G4OpPWLS` which is included in the `G4OpticalPhysics` module. WLS-fibers are characterized by three properties in GEANT4 which have to be provided by the user: the refractive indices of the core and the cladding(s) of the fiber, the wavelength depended absorption length of the core and the wavelength depended emission spectrum. All optical property vectors were implemented based on Benton Pahlka's Geant4-based software model for NEMO-3 [165]. The reflectivity of the Teflon tape is set to 99 % and is purely diffuse [166]. Fig. 4.22 (bottom) shows the resulting simulated emission spectrum of the scintillator and WLS-fiber.

Following the approach of the previous section, the ratio of the area under each spectrum is determined: $\eta_{\text{loss}} = 6.1\,\%\,(\pm 0.1\,\%)$. The ratio deviates by 10 % from the measured value.

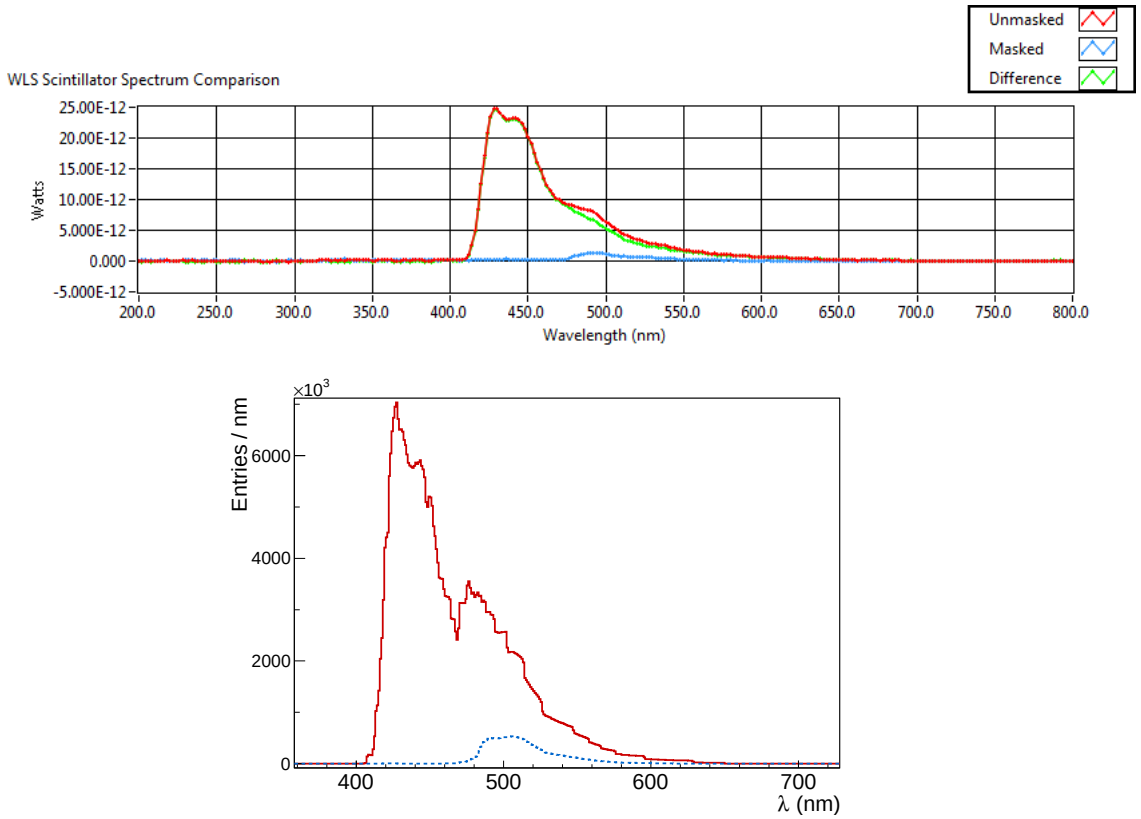

Figure 4.22.: Top: Emission spectrum of the unmasked and masked polystyrene scintillator sample. The masked emission spectrum corresponds to the response of the WLS-fiber. The difference of masked and unmasked spectrum yields the pure emission spectrum of the plastic scintillator. The WLS-fiber peaks around 494 nm as stated by the fabricator. The peak emission of POPOP can be seen between 400 nm and 450 nm. Bottom: Simulated spectrum of the scintillator sample and the WLS-response. The solid red line represents the emission spectrum of the scintillator sample, the blue dashed line shows the wavelength spectrum of the WLS fiber output.

To conclude: Within 10 %, the ratio of the measured light output of the scintillator and light output of the WLS fiber can be reproduced. For further assessment of the optical model of the scintillator and WLS-fiber, the measurement of absolute number of the respective light output would be of interest, e.g. via dedicated measurement of the scintillator and WLS-fiber response to atmospheric muons using a muon telescope.

Muon telescope simulations

The influence of different optical parameters on the light yield of the scintillator sample with and without fiber readout is studied via simulations with the help of through going muons (muon telescope). For this purpose, 10 000 zenith muons with an energy of $E_\mu = 4\,\mathrm{GeV}$ are started centrally above a plastic scintillator sample of size 20.95 mm short axis and 44.45 mm long axis. At the center of the scintillator, a 1 mm WLS-fiber (Y-11) is embedded. The sample is wrapped with a highly reflective foil. The optical parameters studied are:

- Foil surface polish: specular or diffuse
- Foil reflectivity: $R_\mathrm{f} = 0.9, 0.95, 0.99, 1.0$
- Refractive index of: WLS-clad (n_cl), WLS-core (n_core)

Both, the surface polish as well as the reflectivity of the foil influence the number of photons detected. The influence of reflectivity and polish is studied for the light output of the full scintillator and the light output of the WLS-fiber respectively.

Influence on light output of WLS-fiber:
A change from a specular to a purely diffuse surface polish of the foil increases the light output of the fiber by 484 %. The diffuse reflection randomizes the direction of the photons within the scintillator and by this increases the probability to hit the fiber. An increase of reflectivity from $R_\mathrm{f} = 90\,\%$ to 95 % or 100 % increases the light output of the fiber by 168 % and 610 % respectively. A change in refractive index by $\Delta n_\mathrm{core} = 0.03$ of the WLS-core ($n_\mathrm{core} = 1.42 \rightarrow n_\mathrm{core} = 1.39$) or clad ($\Delta n_\mathrm{cl} = 0.03$) both influences the light output by 15 %. The light output increases with increasing difference between core and clad refractive index as this increases the probability of total reflection inside the fiber.

Influence on light output of the full scintillator:
The change of surface polish has a smaller and opposite effect on the light output of the full scintillator. At a reflectivity of $R_\mathrm{f} = 95\,\%$, the light output decreases by 15 % when changing from a specular to a diffuse reflector. Here, the randomization of the photon direction decreases the chance to reach the PMT as the light is reflected more often. With each reflection, there is a 5 % probability of absorption.

To conclude: The type and strength of reflectivity of the reflective foil in the scintillator setup influences the light output significantly if the scintillator is read out by WLS-fibers. The small scale prototype simulations suggest to use reflective foils with the highest reflectivity possible and a diffuse surface (e.g. foils made of PTFE such as Teflon). Furthermore, precise knowledge of the optical parameters of the foil are important in order to adequately model the response of the scintillator setup. Quarter scale prototype measurements and simulations are advisable to check if this is only an effect for small sample sizes or also important for large scale scintillator setups. Also, at large scales, optical parameters such as the absorption length and light transmittance become more dominant. Thus, the influence on the light output should be studied. Though the optical model describes the light output of the scintillator sample and light trapping of the fiber within an accuracy of 10 %, quaterscale measurements and simulations are advisable before adding the optical model to SuperSim in order to design and optimize the full scale SuperCDMS neutron veto system.

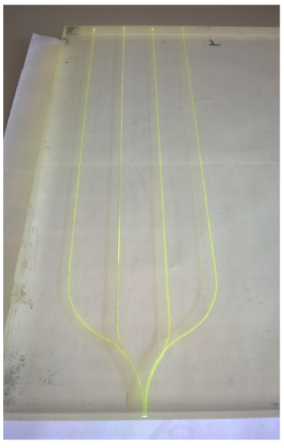

Figure 4.23.: Prototype of the plastic scintillator option of the SuperCDMS neutron veto. WLS-fibers are embedded between two plastic scintillator panels and guide the light to the MPPCs [144].

4.6. Modeling of the SuperCDMS Active Neutron Veto

The response of the SuperCDMS neutron veto and the dark matter detectors to background sources can be modeled with the help of SuperSim, a GEANT4 based modular simulation toolkit developed and maintained at SLAC for the SuperCDMS collaboration [167]. The toolkit includes a detailed model of the detector geometry, material composition, passive and active shielding as well as multiple background sources. The installation of the SuperCDMS detector can be realized at SNOLAB as well as the Soudan underground laboratory with according rock composition and laboratory dimensions. Physics processes are provided by GEANT4 via the `shielding physics list` (see Sec. 3.2.4). Dark matter detector and neutron veto readout as well as the particle flux and energy deposit in passive components can be stored in ROOT files. The different options of the SuperCDMS neutron veto, consisting of a modular setup of B- or Gd-doped plastic or liquid scintillator wedges of 2 m height, are implemented according to the conceptual design as described in Sec. 4.4 (see Fig. 4.18). The number of scintillator wedges can be changed within the code.

The inclusion of optical physics into the SuperSim framework in currently in process in order to predict to the SuperSim framework with the intention to predict light collection in the MPPCs and in order to design and optimize the response of the active neutron veto as accurately as possible. For this purpose, the geometry of the MPPCs which are connected to their corresponding WLS-fibers were added to the implementation of the scintillator modules [167]. The optical responses of the scintillator, WLS-fibers and MPPCs is included via `G4OpticalPhysics` and user defined optical material property tables. An account on optical modeling of light reflection, refraction and absorption in GEANT4 is given in Sec. 3.2.2.

4.6.1. SuperCDMS Neutron Veto Efficiency

Non-optical simulations by the SuperCDMS collaboration of the B and Gd-loaded liquid scintillator option showed that with a veto threshold of $E_{\mathrm{thr}}^{\mathrm{veto}} > 50\,\mathrm{keV}$ together with a trigger time window of 100µs a veto efficiency of $\epsilon_{\mathrm{SNR}}^{\mathrm{veto}} > 90\,\%$ can be met [157] (see Fig. 4.24). The afore developed optical models of the loaded scintillator, WLS and MPPC were added to SuperSim in order to study the influence of the light collection on the neutron veto efficiency to tag single nuclear recoil events. The interieur of the tank is furnished with MPPCs which are connected to their corresponding WLS-fibers. The number and spacing of the MPPCs, the diameter of the WLS-fibers as well as the reflectivity of the tank lining are free parameters within the simulation framework. Simulations are conducted to obtain a first estimate of the veto efficiency if the optical model is included in the MC-model of the neutron veto. Furthermore, the influence of WLS-spacing and doping on the veto efficiency is studied for:

- Doping: 0.12 % Gd, 1.2 % Gd, 3 % B
- Fiber spacing: 5 cm, 10 cm.

For this purpose, the SuperCDMS Cu cold pot is contaminated with 10^6 neutrons from Th (α, n)-reactions. Nuclear recoils are recorded by a total of 150 Ge-detectors which are arranged in 25 towers which each contain 6 detectors. The neutron veto efficiency to tag single nuclear recoil events as a function of detected photons for different realizations of the plastic scintillator are shown in Fig. reffig:opticsEff. The following trends can be observed:

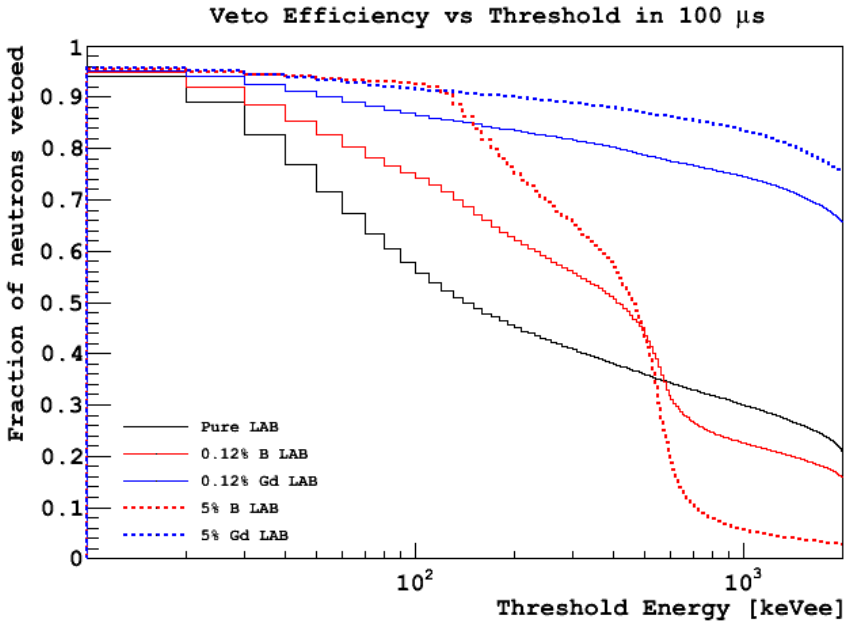

Figure 4.24.: Neutron veto efficiency as a function of the energy threshold of the B- and Gd-loaded liquid scintillator options [157]. Different doping levels are studied. The energy deposit is corrected for Birk's quenching (kb = 79 µm/MeV) which causes a drop in efficiency for the B-doped option above 100 keV.

- Doping: Both, the 0.12 % Gd as well as the 1.2 % Gd-doped scintillator option allow for higher veto efficiencies compared to the 3 % B-loaded option when studying the same WLS-spacing. Since the B-doped scintillators produce less scintillation light, this effect es more evident the more MPPCs are coincident. A higher percentage of Gd-doping results in higher veto efficiencies. This are the same trends as already observed in Sec. 4.3.5.
- Fiber spacing: A smaller spacing of the WLS-fibers, i.e. higher number of fibers and MPPC increases the veto efficiency. Doubling the number of fibers increases the veto efficiency by about 10 %.

The maximum veto efficiency to tag single nuclear recoil events of $\epsilon_{\mathrm{SNR}}^{\mathrm{veto}} = 76\,\%$ can be achieved using a one photoelectron trigger condition ($N_{\mathrm{PE}} = 1$) on a 1.2 % Gd-doped plastic scintillator setup, consisting of six plastic scintillator modules. The modules are read out via WLS-fibers with an equidistant spacing of 5 cm which are individually connected to MPPC. The reflectivity of the foil is set to $R_{\mathrm{f}} = 1.0$. The efficiency of the veto decreases rapidly and lies below $\epsilon_{\mathrm{SNR}}^{\mathrm{veto}} < 60\,\%$ for $N_{\mathrm{PE}} > 3$. As has been seen in Sec. 4.3.5 the ultimate trigger condition will be a trade-off between highest possible detection efficiency and lowest possible accidental rate. As dark count rate of the MPPCs are known to be high, the optimization of the trigger might turn out as a challenging task.

The absolute veto efficiencies have to be treated with caution though. Most importantly, the optical model of the scintillator, the WLS-fiber, the reflective foil and the MPPCs need to be assessed with reliable quarter scale prototype measurements in order to trust the outcome of the full scale neutron veto simulations. Further more, a known bug in the optical module of the GEANT4 code, which appears in every other simulated event[5], might affect the surface normal of the optical photons in cylindrical volumes (`G4Tubs`).

[5]The bug did not appear in the standalone MC-model of the scintillator nor in the simulations of Sec. 4.3.

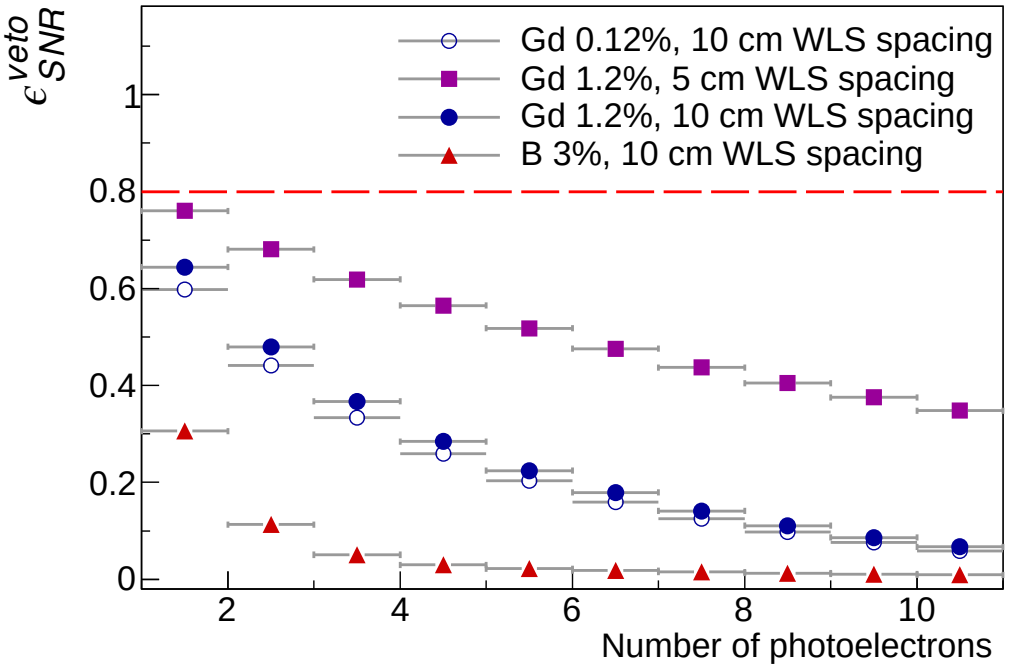

Figure 4.25.: SCDMS Neutron veto efficiency to tag single nuclear recoil events as a function of detected photons for different realizations of the plastic scintillator. Square: 1.2 % Gd and a fiber spacing of 5 cm, solid circle: 1.2 % Gd and a fiber spacing of 10 cm, empty circle: 0.12 % Gd and a fiber spacing of 10 cm, red triangle: 3 % B and a fiber spacing of 10 cm.

To conclude: Overall, Gd-loaded scintillators are a promising technology to reduce ambient neutron backgrounds in cryogenic dark matter experiments. Two Gd-loaded scintillator options were studied in this chapter: a 2 % by weight Gd-loaded cylindrical liquid scintillator (4 m × 4 m), which is read out by the 120 PMTs of the surrounding water Cherenkov detector muon veto system and a Gd-loaded scintillator consisting of 6 plastic scintillator modules of 2 m height which are read out by MMPCs and WLS fibers of 5 cm spacing. From the current state of investigation of these two options, the combined neutron and muon veto system designed in Sec. 4.3 achieves higher veto efficiencies (at a sensible dead time of the system) to tag single nuclear recoil events compared to the modular option read out by WLS-fibers and MPPCs.

5. Conclusion

One of the greatest puzzles in physics is the composition of our Universe. The fundamental forces and particles of our Universe, as physicists understand it today, can be described with high accuracy by the Standard Model of particle physics. Since its postulation, the Standard Model of particle physics has been tested and confirmed in numerous experiments. A recent milestone is the discovery of the Higgs boson by the ATLAS and CMS experiments. Despite the success of the Standard Model, there is clear evidence from neutrino physics and cosmology that the theory is incomplete and outstanding questions remain that can only be answered with theories beyond the Standard Model. One of the long-standing questions is the existence and the nature of dark matter. Anomalies at all scales of astrophysical systems point towards the existence of non-luminous (dark) matter. For now, it is commonly assumed that dark matter is a weakly interacting massive particle (WIMP) as proposed in diverse models beyond the Standard Model. One experimental way to shine light on the nature of dark matter is its direct detection with the help of highly sensitive, ultra clean and radio-pure experiments. As the scattering cross section of dark matter is very small, it is of utmost importance to understand and suppress background sources in and around the experimental setup. Though tremendous efforts and improvements have been made by means of detector development as well as low background techniques, no convincing dark matter signal has been detected so far. As of today, dark matter experiments are exploring the parameter space of 10 – 100 GeV WIMPs with spin-independent scattering cross sections at the order of down to $\sigma_{\mathrm{SI}} \sim 10^{-45}\,\mathrm{cm}^2$. Experiments are limited by their detector mass, detector threshold as well as their background levels. To improve the sensitivity of future dark matter detectors, one has to increase the mass and the exposure time of the experiment or lower the detector threshold while at the same time drastically reducing background levels. Future dark matter experiments are being planned to explore the parameter space of spin-independent WIMP-nucleon cross-sections for standard WIMP masses of 10 – 1000 GeV down to $\mathcal{O}(10^{-48}\,\mathrm{cm}^2)$. Cryogenic solid sate dark matter experiments will at the same time push the limits towards low WIMP masses $< 1\,\mathrm{GeV}$ at cross-sections of $\mathcal{O}(10^{-43}\,\mathrm{cm}^2)$. The reduction of background levels by one to three orders of magnitude in future rare event searches is crucial to achieve the proposed sensitivities. Sensitivities of $\sigma \sim 10^{-48}\,\mathrm{cm}^{-2}$ require a background reduction below 1 event/tonne/year to stay background free. Limiting background sources at these sensitivities are neutrons from radio-impurities in the detector and shielding components and muon-induced spallation in the surrounding materials and ultimately the “neutrino floor”.

This work presents two active shielding concepts to reduce both *muon-induced and ambient background sources* in future large scale dark matter experiments below 1 event/tonne/year. In this context, we focused on the conceptual design of active shields for large scale cryogenic dark matter experiments. The predominant *irreducible* background source from cosmic ray muons and radio-impurities in the search for dark matter are *neutrons* from natural fission, (α, n)-reactions and muon-induced spallation in the surrounding materials, as the *single* elastic scattering of a neutron $E_{\mathrm{n}} = \mathcal{O}(\mathrm{MeV})$ off the target can mimic a WIMP-nuclear elastic scatter. Ambient neutrons from external radioactivity of the surrounding rock and laboratory can be minimized via a suitable shielding setup. Radioactivity within the experimental setup (shielding and target) can be reduced by the selection and subsequent screening of radio-pure materials. At increasing sensitivities, the active vetoing of residual neutrons becomes more and more important. To reduce the atmospheric muon flux and muon-induced background sources, most dark matter experiments are operated in deep underground laboratories such as the Modane Underground Laboratory (LSM), Gran Sasso or Soudan. Signals from residual high-energy neutrons from deep-inelastic muon-nucleus scattering in the surrounding rock and detector materials are vetoed by actively tagging the associated muons with dedicated muon vetos.

The first part of this work focused on the design of a high-performance water Cherenkov detector as an active muon shield for large scale cryogenic dark matter experiments. In the last couple of years, water Cherenkov detectors have found an application as active muon vetos in various dark matter and rare event searches such as DarkSide, Xenon1T and GERDA. The typical 400 tonnes of water are a clean and low Z alternative to classic passive Pb-shields in rare events searches and an efficient shield against ambient neutrons. When equipped with photomultiplier tubes (PMTs), the water shield acts as a water Cherenkov detector and allows to tag muons actively via the muon-induced production of Cherenkov radiation in water ($n_{\mathrm{w}} = 1.33$). Our conceptual design of the muon veto water Cherenkov detector is based around a cylindrical $8\,\mathrm{m}\times 8\,\mathrm{m}$ stainless steel tank which is filled with $400\,\mathrm{m}^3$ of ultra-pure water and equipped with encapsulated PMTs of type R5912. The inner surface of the tank is lined with the highly reflective specular foil DF2000MA by 3M. The design derives from the muon veto design of the proposed future cryogenic one tonne dark matter experiment EURECA (European Underground Rare Event Calorimeter Array) originally planned at LSM.

In order to be able to reduce muon-induced neutron events to rates < 1 event/tonne/year for future experiments, highest possible muon tagging efficiencies are required. At the same time, the dead time of the system should be kept at a minimum to ensure longest possible exposure times for the dark matter search. Since absolute muon rates are low, detailed modeling is necessary to predict rates and muon efficiencies in future experiments. To predict muon tagging efficiencies in a water Cherenkov detector, an accurate model of the light production, tracking and collection is needed.

Light collection in Cherenkov detectors can be predicted most accurately in MC models if the production and tracking of optical photons is considered in the MC model. The modeling of optical physics in GEANT4 strongly relies on the provision of user defined optical material property tables. Consequently, the MC model takes all specific optical parameters of the water Cherenkov detector components into account, including the wavelength dependent reflectivity of the specular foil DF2000MA, the photon detection on each of the PMTs according to the quantum efficiency of PMT type R5912 and the refractive indices of all detector materials, most notably water. We evaluated the accuracy

of the GEANT4 model with dedicated prototype measurements at KIT. For this purpose, we measured the light collection of two PMTs of type R5912 for throughgoing muons within a prototype water Cherenkov detector. The prototype has a length of 1 m and a diameter of 0.3 m, is filled with pure water and lined with DF2000MA-foil. Our optical model of the water Cherenkov detector prototype reproduces the measured photoelectron spectrum adequately. Around the photoelectron peak, the measured and simulated data follow the same distribution with a χ^2/n.d.f ≈ 1.06. The prototype detector components, including the 8" PMTs and the specular reflective lining, are commonly used in rare event searches. Consequently, the model of the water Cherenkov detector (PMT, foil, tank) can be broadly applied.

The adequate optical model of the detector components allows to reliably design and optimize a full scale water Cherenkov muon veto system. We conducted the design of the full scale muon veto system as follows: in a first step, the total number and arrangement of PMTs of the muon veto system was optimized based on the overall light collection, muon detection efficiency and cost. Second, the optimal trigger condition of the setup was determined as a compromise between veto efficiency and accidental rates of the system. Finally, the expected muon-induced neutron rate in anti-coincidence with the muon veto system was estimated for standard WIMP searches (1 tonne) as well as low mass dark matter searches (43.2 kg) in cryogenic dark matter experiments.

The specific requirements of the muon veto performance are dictated by muon events in coincidence with nuclear recoils as *single* nuclear recoils (SNR) constitute the *irreducible* background source of dark matter experiments. In order to save CPU time, we derived a muon veto threshold based on the muon track length in the veto $l_{\mu}^{\text{veto}} > 1\,\text{m}$ which allows to tag muon-induced nuclear recoil events with an efficiency of $> 99\,\%$ via the non-optical simulation of 2×10^7 primary muons which corresponds to more than 20 years of simulated data taking. We then included the production, tracking and detection of Cherenkov photons in our model and tested the performance of five PMT setups with differing PMT arrangements and numbers of PMTs based on their performance in respect to light collection and the muon detection above and close to the threshold. Furthermore, we tested the veto performance in the limit of low light production by studying muon events with short muon track length $l_{\mu}^{\text{veto}} < 1\,\text{m}$. We chose a setup with a total of 72 PMTs as the optimal setup in relation to muon detection efficiency and cost. Though an increase in the number of PMTs increases the light collection and detection efficiency of the veto, setups with 72 PMTs allow for sufficient veto efficiencies of 99 % or better at sensible trigger conditions and an average light collection of $N_{\text{PE}} = 25$ at veto threshold. The 72 PMTs are arranged in six alternating rings of 12 PMTs. Four rings of PMTs are fixed to the lateral surface of the tank. One ring is fixed to the outer rim of floor surface (facing upwards) and one to the outer rim of the top surface (facing downwards). The PMTs at the top and floor surface of the tank were added to allow for an efficient detection of muons with short track length.

Next, a major effort was made in order to optimize the trigger of the optimal PMT setup of the water Cherenkov detector via extensive and CPU intensive optical simulations. The final trigger setting is a compromise between high muon detection efficiencies and the accidental rate of the muon veto system. Veto efficiencies studies showed that the highest veto efficiencies are achieved for triggers with single photoelectron (SPE) thresholds, the lowest possible number of coincident PMTs and a trigger time window above 200 ns. At the same time, low accidental rates are required to keep the dead time of the muon veto at a minimum which requires a large number of coincident PMTs, a high photoelectron

threshold of the individual PMT and a small trigger time window. In order to determine the accidental rate of the muon veto system, we determined the background count rate in PMTs from ambient decays in the vicinity of the tank for different photoelectron thresholds of the PMT. Simulations showed that at SPE level the background count rate in the PMT is dominated by ^{208}Tl-decays in the surrounding rock and concrete and is of the order of $R_{\mathrm{D}} = 6.5\,\mathrm{kHz}$. To keep the accidental rate of the veto at the same level as expected muon trigger rates $\mathcal{O}(10^{-3}\,\mathrm{Hz})$, the SPE trigger condition together with a trigger time window of 200 ns requires at least six coincident PMTs at SPE threshold: $N(\mathrm{PMT}_{\mathrm{PE}\geq 1}) \geq 6$. The deduced trigger allows for high veto efficiency to tag muons inside the veto as well as muons with short track length:

$$\epsilon_{\mu}^{\mathrm{veto}} = \frac{N_{\mathrm{tagged}}(l_{\mu}^{\mathrm{veto}} > 0\,\mathrm{m})}{N(l_{\mu}^{\mathrm{veto}} > 0\,\mathrm{m})} > 99.9\,\%, \tag{5.1a}$$

$$\epsilon_{\mu}^{\mathrm{short}} = \frac{N_{\mathrm{tagged}}(l_{\mu}^{\mathrm{veto}} < 1\,\mathrm{m})}{N(l_{\mu}^{\mathrm{veto}} < 1\,\mathrm{m})} > 99\,\%. \tag{5.1b}$$

The muon tagging efficiencies are competitive with other current and future rare event searches which employ a water Cherenkov detector as muon veto system.

Finally, we estimated the expected muon-induced background rate for future cryogenic dark matter experiment for a typical detector target mass of standard WIMP searches (1 tonne) and low mass dark matter searches (43.2 kg) at LSM. The dark matter target was implemented based to the response of cryogenic high purity Ge-bolometers as used in EDELWEISS-III. The Ge-bolometer recorded heat and ionization simultaneously as the ratio $Q = \mathrm{ionization/recoilenergy}$ allows to discriminate between nuclear and electrons recoils. We searched for single nuclear recoil events in an energy window of $E_{\mathrm{rec}} \in [1, 250]\,\mathrm{keV}$ and $Q < 0.5$, which is the favored region of interest (ROI) for a signature from dark matter-nucleon interactions in Ge. In order to be sensitive to low mass WIMP searches, we adopted a low threshold ($E_{\mathrm{thr}}^{\mathrm{bolo}} = 1\,\mathrm{keV}$) of the cryogenic Ge dark matter detectors to measure recoil energies. From our simulations, the expected single nuclear recoil rate in one tonne of target, i.e. 1256 Ge-bolometers, is low due to the compact packing of the bolometer:

$$\Gamma_{\mu\text{–n–bg}} = 1.24 \pm 0.32\,(\mathrm{stat})\,^{+0.41}_{-0.49}\,(\mathrm{syst})\,\mathrm{events/tonne/year}. \tag{5.2}$$

No muon-induced neutron signal was recorded in more than 12 years of simulated data taking, setting an upper limit for the neutron background rate in one tonne and 43.2 kg of target material, respectively, of:

$$\Gamma_{\mu\text{–n–bg}}^{\mathrm{veto}} \leq 0.18\,^{+0.02}_{-0.03}\,\mathrm{events/tonne/year\ at\ 90\,\%\,CL\ (1\,tonne)}, \tag{5.3a}$$

$$\Gamma_{\mu\text{–n–bg}}^{\mathrm{veto}} \leq 4.33\,^{+0.46}_{-0.91} \times 10^{-3}\,\mathrm{events/kg/year\ at\ 90\,\%\,CL\ (43.2\,kg)}. \tag{5.3b}$$

$\Gamma_{\mu\text{–n–bg}}^{\mathrm{veto}}$ is purely limited by the MC-statistics of the simulated muon flux, which in turn are limited by the CPU time of optical simulations. The study showed that the sensitivities of future large scale cryogenic dark matter experiments are not limited by muon-induced backgrounds if the devised water Cherenkov muon veto is employed. Our water Cherenkov detector thus fulfills all requirements for (future) active muon veto systems.

In the second part of this work, we designed an active neutron veto which allowed us to efficiently veto ambient neutrons from detector component contaminations in the vicinity of the target material. The conceptual design of the neutron veto is based around a cylindrical

$4\,\mathrm{m} \times 4\,\mathrm{m}$ plastic tank filled with liquid scintillator. Gd- and B-doping options were studied for the liquid scintillator. The neutrons were detected via the production of scintillation light from prompt proton-neutron scattering or via delayed neutron capture processes on Gd or B, H and C in the scintillator. The scintillation light of the neutron veto was read out by the PMT system of the muon veto.

We optimized the optical setup up of the PMT system with extensive simulations for a cryogenic tonne scale dark matter experiment. We studied the influence of an internal 8 cm polyethylene and several Cu-shields in the passive shielding scheme of the dark matter experiment on the light yield and efficiency of the neutron veto.

For the five different setups and the three different dopings studied, a good performance with respect to light collection could be achieved for a setup with 120 PMTs and a doping of 2 % of Gd by weight. Though setups with higher number of PMTs were studied (up tp 231 PMTs), the increase in performance ($< 4\,\%$) would not justify the increase in cost and work load. We derived a threshold for the neutron veto system to efficiently tag *single* nuclear recoil events based on the total energy deposit inside the neutron veto, $E_{\mathrm{dep}}^{\mathrm{veto}} = 50\,\mathrm{keV}$. At threshold, we expect to detect on average $N_{\mathrm{PE}} = 25$ photoelectrons.

Finally, we designed the optimal trigger for the neutron veto system. The trigger was optimized for tonne scale dark matter experiments with and without internal polyethylene in the passive shielding scheme, respectively. The optimal trigger of the neutron veto system is a compromise between the accidental rate and the neutron veto efficiency. The dead time of the neutron veto is determined by $^{40}\mathrm{K}$ decays in the scintillator and is estimated via simulations to be $\mathcal{O}(20\,\mathrm{Hz})$. The trigger condition strongly depends on the internal passive shielding scheme and the dead time of the system. Dark matter experiments without internal polyethylene favor large trigger time windows $\mathcal{O}(100\,\mu\mathrm{s})$ in order to be sensitive to the delayed capture processes in the veto. To keep accidental rates at the level of 20 Hz, the optimal trigger requires a higher photoelectron threshold: $N(\mathrm{PMT}_{\mathrm{PE}\geq 3}) \geq 2$ in a trigger time window of $t_{\mathrm{trig}} = 100\,\mu\mathrm{s}$. With internal polyethylene shielding, the veto is mostly sensitive to prompt scintillation light and the best performance is achieved for trigger conditions with SPE thresholds and a trigger time window of $t_{\mathrm{trig}} = 1\,\mu\mathrm{s}$. The corresponding trigger at an accidental rate of 20 Hz was $N(\mathrm{PMT}_{\mathrm{PE}\geq 1}) \geq 6$ and $t_{\mathrm{trig}} = 1\,\mu\mathrm{s}$. We found that about 10 % of efficiency to tag single nuclear recoils is lost when internal polyethylene and Cu-shields are installed as neutrons get absorbed in the internal shield without producing any visible signal in the neutron veto. Overall, neutron veto efficiencies to tag neutrons in coincidence with single nuclear recoils in the dark matter detectors or to tag events above veto threshold with (without) internal poly-shield are high at justifiable accidental rates, with room for improvement:

$$\epsilon_{\mathrm{n}}(\mathrm{SNR}) > 78\,\%\ (91\,\%) \tag{5.4a}$$

$$\epsilon_{\mathrm{n}}(E_{\mathrm{dep}}^{\mathrm{veto}} > 50\,\mathrm{keV}) > 89\,\%\ (89\,\%) \tag{5.4b}$$

The study showed that the PMT system of the water Cherenkov detector is apt to efficiently detect light of the scintillator. This enables a cost and work load efficient realization of the neutron veto. The performance of our neutron veto is comparable to similar proposed neutron veto systems, even though we do not employ a dedicated optical read out system as is generally realized in other layouts of neutron veto systems.

We designed two high-performance active shields against ambient and cosmogenic neutron

backgrounds in large scale cryogenic dark matter experiments through elaborate GEANT4 optical simulations: a water Cherenkov detector as muon veto and a Gd-loaded liquid scintillator as neutron veto. For the first time, the performance of a neutron veto which shares the optical system of a water Cherenkov detector muon veto system was evaluated. The dead time of the combined system is defined by the accidental rates of the neutron veto, and of the order of per mill. By implementing our active shielding techniques, future large scale dark matter experiments will be able to reduce background rates from muon-induced neutrons and radio-impurities to the order of 1 event/tonne/year and less – making way for new physics.

Bibliography

[1] C. Grupen, "Astroparticle physics," *Heidelberg: Springer*, 2005.

[2] United Academics, 2015. http://www.united-academics.org/magazine/space-physics/latest-theory-of-everything-to-hit-the-physics-shelves/.

[3] B. Povh *et al.*, *Teilchen und Kerne*. Springer-Verlag Berlin Heidelberg, 6 ed., 2006.

[4] G. Bertone, D. Hooper, and J. Silk, "Particle dark matter: Evidence, candidates and constraints," *Phys. Rept.*, vol. 405, pp. 279–390, 2005.

[5] K. A. Olive *et al.*, "Review of Particle Physics," *Chin. Phys.*, vol. C38, p. 090001, 2014.

[6] Yinweichen, "History of the Universe," 2015. Licensed under CC BY-SA 3.0 via Wikimedia Commons.

[7] L. Bergstrom and A. Goobar, "Cosmology and particle astrophysics," *Berlin, Germany: Springer (2004) 364 p*, 1999.

[8] P. Ade *et al.*, "Planck 2015 results. XIII. Cosmological parameters," `arXiv:astro-ph/1502.01589`, 2015.

[9] G. Aad *et al.*, "Observation of a new particle in the search for the Standard Model Higgs boson with the ATLAS detector at the LHC," *Phys. Lett.*, vol. B716, pp. 1–29, 2012.

[10] S. Chatrchyan *et al.*, "Observation of a new boson at a mass of 125 GeV with the CMS experiment at the LHC," *Phys. Lett.*, vol. B716, pp. 30–61, 2012.

[11] M. Milgrom, "A modification of the Newtonian dynamics as a possible alternative to the hidden mass hypothesis," *Astrophysical Journal*, vol. 270, pp. 365–370, July 1983.

[12] J. D. Bekenstein, "Relativistic gravitation theory for the MOND paradigm," *Phys. Rev.*, vol. D70, p. 083509, 2004. [Erratum: Phys. Rev.D71,069901(2005)].

[13] F. Zwicky, "Die Rotverschiebung von extragalaktischen Nebeln," *Helvetica Physica Acta*, vol. 6, pp. 110–127, 1933.

[14] P. Ade *et al.*, "Planck 2013 results. I. Overview of products and scientific results," *Astron. Astrophys.*, vol. 571, p. A1, 2014.

[15] A. V. Kravtsov, "Dark matter substructure and dwarf galactic satellites," *Adv. Astron.*, vol. 2010, p. 281913, 2010.

[16] Harvard-Smithsonian Center for Astrophysics, "1e 0657-56:NASA finds direct proof of dark matter," 2006. `http://chandra.harvard.edu/photo/2006/1e0657/index.html`.

[17] M. Bartelmann and P. Schneider, "Weak gravitational lensing," *Physics Reports*, vol. 340, no. 4-5, pp. 291–472, 2001.

[18] D. Harvey, R. Massey, T. Kitching, A. Taylor, and E. Tittley, "The non-gravitational interactions of dark matter in colliding galaxy clusters," *Science*, vol. 347, pp. 1462–1465, 2015.

[19] V. C. Rubin, N. Thonnard, and W. K. Ford, Jr., "Extended rotation curves of high-luminosity spiral galaxies. IV - Systematic dynamical properties, SA through SC," *Astrophysical Journal*, vol. 225, pp. L107–L111, Nov. 1978.

[20] K. G. Begeman, A. H. Broeils, and R. H. Sanders, "Extended rotation curves of spiral galaxies - Dark haloes and modified dynamics," *Monthly Notices of the Royal Astronomical Society*, vol. 249, pp. 523–537, Apr. 1991.

[21] C. Alcock *et al.*, "The MACHO project: Microlensing results from 5.7 years of LMC observations," *Astrophys. J.*, vol. 542, pp. 281–307, 2000.

[22] A. Boyarsky, J. Lesgourgues, O. Ruchayskiy, and M. Viel, "Lyman-alpha constraints on warm and on warm-plus-cold dark matter models," *JCAP*, vol. 0905, p. 012, 2009.

[23] D. Hooper, "Particle Dark Matter," in *Proceedings of Theoretical Advanced Study Institute in Elementary Particle Physics on The dawn of the LHC era (TASI 2008)*, pp. 709–764, 2010.

[24] G. Jungman, M. Kamionkowski, and K. Griest, "Supersymmetric dark matter," *Phys. Rept.*, vol. 267, pp. 195–373, 1996.

[25] T. M. Undagoitia and L. Rauch, "Dark matter direct-detection experiments," `arXiv:physics.ins-de/1509.08767`, 2015.

[26] The ATLAS Collaboration *et al.*, "The ATLAS Experiment at the CERN Large Hadron Collider," *Journal of Instrumentation*, vol. 3, no. 08, p. S08003, 2008.

[27] The CMS Collaboration *et al.*, "The CMS experiment at the CERN LHC," *Journal of Instrumentation*, vol. 3, no. 08, p. S08004, 2008.

[28] V. Khachatryan *et al.*, "Search for dark matter, extra dimensions, and unparticles in monojet events in proton-proton collisions at $\sqrt{s} = 8$ TeV," *Eur. Phys. J.*, vol. C75, no. 5, p. 235, 2015.

[29] L. E. Strigari, "Galactic searches for dark matter," *Physics Reports*, vol. 531, no. 1, pp. 1 – 88, 2013. Galactic searches for dark matter.

[30] M. G. Aartsen *et al.*, "Search for dark matter annihilations in the Sun with the 79-string IceCube detector," *Phys. Rev. Lett.*, vol. 110, no. 13, p. 131302, 2013.

[31] K. Choi *et al.*, "Search for neutrinos from annihilation of captured low-mass dark matter particles in the Sun by Super-Kamiokande," *Phys. Rev. Lett.*, vol. 114, no. 14, p. 141301, 2015.

[32] J. Aleksic *et al.*, "Searches for Dark Matter annihilation signatures in the Segue 1 satellite galaxy with the MAGIC-I telescope," *JCAP*, vol. 1106, p. 035, 2011.

[33] A. Abramowski *et al.*, "Search for Photon-Linelike Signatures from Dark Matter Annihilations with H.E.S.S.," *Phys. Rev. Lett.*, vol. 110, p. 041301, 2013.

[34] A. Abramowski *et al.*, "Constraints on an Annihilation Signal from a Core of Constant Dark Matter Density around the Milky Way Center with H.E.S.S.," *Phys. Rev. Lett.*, vol. 114, no. 8, p. 081301, 2015.

[35] T. Arlen *et al.*, "Constraints on Cosmic Rays, Magnetic Fields, and Dark Matter from Gamma-Ray Observations of the Coma Cluster of Galaxies with VERITAS and Fermi," *Astrophys. J.*, vol. 757, p. 123, 2012.

[36] E. Bulbul, M. Markevitch, A. Foster, R. K. Smith, M. Loewenstein, and S. W. Randall, "Detection of An Unidentified Emission Line in the Stacked X-ray spectrum of Galaxy Clusters," *Astrophys. J.*, vol. 789, p. 13, 2014.

[37] A. Boyarsky, O. Ruchayskiy, D. Iakubovskyi, and J. Franse, "Unidentified Line in X-Ray Spectra of the Andromeda Galaxy and Perseus Galaxy Cluster," *Phys. Rev. Lett.*, vol. 113, p. 251301, 2014.

[38] T. Higaki, K. S. Jeong, and F. Takahashi, "The 7 keV axion dark matter and the X-ray line signal," *Phys. Lett.*, vol. B733, pp. 25–31, 2014.

[39] M. Aguilar *et al.*, "First Result from the Alpha Magnetic Spectrometer on the International Space Station: Precision Measurement of the Positron Fraction in Primary Cosmic Rays of 0.5-350 GeV," *Phys. Rev. Lett.*, vol. 110, p. 141102, 2013.

[40] O. Adriani *et al.*, "An anomalous positron abundance in cosmic rays with energies 1.5-100 GeV," *Nature*, vol. 458, pp. 607–609, 2009.

[41] L. E. Strigari, "Galactic Searches for Dark Matter," *Phys. Rept.*, vol. 531, pp. 1–88, 2013.

[42] M. Klasen, M. Pohl, and G. Sigl, "Indirect and direct search for dark matter," *Prog. Part. Nucl. Phys.*, vol. 85, pp. 1–32, 2015.

[43] J. Lewin and P. Smith, "Review of mathematics, numerical factors, and corrections for dark matter experiments based on elastic nuclear recoil," *Astroparticle Physics*, vol. 6, no. 1, pp. 87 – 112, 1996.

[44] J. F. Navarro, C. S. Frenk, and S. D. M. White, "The Structure of Cold Dark Matter Halos," *ApJ*, vol. 462, p. 563, May 1996.

[45] M. Vogelsberger *et al.*, "Phase-space structure in the local dark matter distribution and its signature in direct detection experiments," *Mon. Not. Roy. Astron. Soc.*, vol. 395, pp. 797–811, 2009.

[46] A. M. Green, "Astrophysical uncertainties on direct detection experiments," *Mod. Phys. Lett.*, vol. A27, p. 1230004, 2012.

[47] L. Baudis, "A review of direct WIMP search experiments," *Nuclear Physics B - Proceedings Supplements*, vol. 235-236, pp. 405–412, 2013.

[48] Z. Ahmed *et al.*, "Dark Matter Search Results from the CDMS II Experiment," *Science*, vol. 327, pp. 1619–1621, 2010.

[49] E. Armengaud *et al.*, "Final results of the EDELWEISS-II WIMP search using a 4-kg array of cryogenic germanium detectors with interleaved electrodes," *Phys. Lett.*, vol. B702, pp. 329–335, 2011.

[50] E. Armengaud *et al.*, "A search for low-mass WIMPs with EDELWEISS-II heat-and-ionization detectors," *Phys. Rev.*, vol. D86, p. 051701, 2012.

[51] F. Scholze, H. Rabus, and G. Ulm, "Mean energy required to produce an electron-hole pair in silicon for photons of energies between 50 and 1500 ev," *Journal of Applied Physics*, vol. 84, no. 5, pp. 2926–2939, 1998.

[52] G. Angloher *et al.*, "Limits on WIMP dark matter using scintillating $CaWO_4$ cryogenic detectors with active background suppression," *Astropart. Phys.*, vol. 23, pp. 325–339, 2005.

[53] EDELWEISS, "FID full InterDigit germanium bolometer," 2015-09-30. `http://edelweiss.in2p3.fr/`.

[54] SuperCDMS, "SuperCDMS-Soudan iZip," 2015-09-30. `http://cdms.berkeley.edu/gallery.html`.

[55] CRESST, "One of the CRESST detector modules," 2015-09-30. `http://www.cresst.de/cresst.php`.

[56] E. Aprile *et al.*, "Dark Matter Results from 225 Live Days of XENON100 Data," *Phys. Rev. Lett.*, vol. 109, p. 181301, 2012.

[57] D. S. Akerib *et al.*, "The Large Underground Xenon (LUX) Experiment," *Nucl. Instrum. Meth.*, vol. A704, pp. 111–126, 2013.

[58] X. Cao *et al.*, "PandaX: A Liquid Xenon Dark Matter Experiment at CJPL," *Sci. China Phys. Mech. Astron.*, vol. 57, pp. 1476–1494, 2014.

[59] P. Agnes *et al.*, "First results from the darkside-50 dark matter experiment at laboratori nazionali del gran sasso," *Physics Letters B*, vol. 743, pp. 456 – 466, 2015.

[60] R. Bernabei *et al.*, "Final model independent result of DAMA/LIBRA-phase1," *Eur. Phys. J.*, vol. C73, p. 2648, 2013.

[61] S. C. Kim *et al.*, "New limits on interactions between weakly interacting massive particles and nucleons obtained with csi(tl) crystal detectors," *Phys. Rev. Lett.*, vol. 108, p. 181301, Apr 2012.

[62] E. Behnke *et al.*, "First Dark Matter Search Results from a 4-kg CF_3I Bubble Chamber Operated in a Deep Underground Site," *Phys. Rev.*, vol. D86, no. 5, p. 052001, 2012. [Erratum: Phys. Rev.D90,no.7,079902(2014)].

[63] S. Archambault *et al.*, "Constraints on Low-Mass WIMP Interactions on ^{19}F from PICASSO," *Phys. Lett.*, vol. B711, pp. 153–161, 2012.

[64] C. Amole *et al.*, "Dark Matter Search Results from the PICO-2L C_3F_8 Bubble Chamber," *Phys. Rev. Lett.*, vol. 114, no. 23, p. 231302, 2015.

[65] J. Billard *et al.*, "In situ measurement of the electron drift velocity for upcoming directional Dark Matter detectors," *JINST*, vol. 9, no. 01, p. P01013, 2014.

[66] C. E. Aalseth *et al.*, "CoGeNT: A Search for Low-Mass Dark Matter using p-type Point Contact Germanium Detectors," *Phys. Rev.*, vol. D88, p. 012002, 2013.

[67] R. Agnese *et al.*, "Silicon Detector Dark Matter Results from the Final Exposure of CDMS II," *Phys. Rev. Lett.*, vol. 111, no. 25, p. 251301, 2013.

[68] D. S. Akerib *et al.*, "First results from the LUX dark matter experiment at the Sanford Underground Research Facility," *Phys. Rev. Lett.*, vol. 112, p. 091303, 2014.

[69] G. Angloher *et al.*, "Results on low mass WIMPs using an upgraded CRESST-II detector," *Eur. Phys. J.*, vol. C74, no. 12, p. 3184, 2014.

[70] E. Aprile, "The XENON1T Dark Matter Search Experiment," *Springer Proc. Phys.*, vol. 148, pp. 93–96, 2013.

[71] D. C. Malling *et al.*, "After LUX: The LZ Program," `arXiv:1110.0103`, 2011.

[72] C. Weinheimer, "Direct Dark Matter Search with XENON100 and XENON1T," 2015. 25th International Workshop on Weak Interactions and Neutrinos (WIN2015).

[73] A. Dobi, "The LZ experiment," 2015. 25th International Workshop on Weak Interactions and Neutrinos (WIN2015).

[74] D. G. Cerdeno, J.-H. Huh, M. Peiro, and O. Seto, "Very light right-handed sneutrino dark matter in the NMSSM," *JCAP*, vol. 1111, p. 027, 2011.

[75] K. M. Zurek, "Asymmetric Dark Matter: Theories, Signatures, and Constraints," *Phys. Rept.*, vol. 537, pp. 91–121, 2014.

[76] G. Angloher *et al.*, "EURECA Conceptual Design Report," *Phys. Dark Univ.*, vol. 3, pp. 41–74, 2014.

[77] P. Cushman *et al.*, "Working Group Report: WIMP Dark Matter Direct Detection," in *Community Summer Study 2013: Snowmass on the Mississippi (CSS2013) Minneapolis, MN, USA, July 29-August 6, 2013*, 2013.

[78] G. Angloher *et al.*, "Results on light dark matter particles with a low-threshold CRESST-II detector," `arXiv:astro-ph/1509.01515`, 2015.

[79] R. Agnese *et al.*, "WIMP-Search Results from the Second CDMSlite Run," *Submitted to: Phys. Rev. Lett.*, 2015.

[80] B. Schmidt *et al.*, "Muon-induced background in the EDELWEISS dark matter search," *Astropart. Phys.*, vol. 44, pp. 28–39, 2013.

[81] V. Tomasello, M. Robinson, and V. Kudryavtsev, "Radioactive background in a cryogenic dark matter experiment," *Astroparticle Physics*, vol. 34, no. 2, pp. 70 – 79, 2010.

[82] G. F. Knoll, *Radiation detection and measurement; 4th ed.* New York, NY: Wiley, 2010.

[83] H. Ohsumi *et al.*, "Gamma-ray flux in the fréjus underground laboratory measured with nai detector," *Nuclear Instruments and Methods in Physics Research Section A: Accelerators, Spectrometers, Detectors and Associated Equipment*, vol. 482, no. 3, pp. 832 – 839, 2002.

[84] S. Rozov *et al.*, "Monitoring of the thermal neutron flux in the LSM underground laboratory," *arXiv:astro-ph/1001.4383*, 2010.

[85] W. Maneschg, M. Laubenstein, D. Budjas, W. Hampel, G. Heusser, K. T. Knopfle, B. Schwingenheuer, and H. Simgen, "Measurements of extremely low radioactivity levels in stainless steel for GERDA," *Nucl. Instrum. Meth.*, vol. A593, pp. 448–453, 2008.

[86] E. Hoppe, C. Aalseth, O. Farmer, T. Hossbach, M. Liezers, H. Miley, N. Overman, and J. Reeves, "Reduction of radioactive backgrounds in electroformed copper for

ultra-sensitive radiation detectors," *Nuclear Instruments and Methods in Physics Research Section A: Accelerators, Spectrometers, Detectors and Associated Equipment*, vol. 764, pp. 116 – 121, 2014.

[87] S. Scorza and for the EDELWEISS Collaboration, "Background investigation in edelweiss-iii," *AIP Conference Proceedings*, vol. 1672, 2015.

[88] C. Kéfélian, "Search for dark matter with EDELWEISS-III excluding background from muon-induced neutrons," 2015. PhD Thesis.

[89] I. Guinn *et al.*, "Low background signal readout electronics for the MAJORANA DEMONSTRATOR," *AIP Conference Proceedings*, vol. 1672, 2015.

[90] F. Alessandria *et al.*, "Validation of techniques to mitigate copper surface contamination in CUORE," *Astropart. Phys.*, vol. 45, pp. 13–22, 2013.

[91] L. Baudis, "Direct dark matter detection: The next decade," *Phys. Dark Universe*, vol. 1, no. 1-2, pp. 94–108, 2012.

[92] E. Aprile, T. Yoon, A. Loose, L. W. Goetzke, and T. Zelevinsky, "An atom trap trace analysis system for measuring krypton contamination in xenon dark matter detectors," *Review of Scientific Instruments*, vol. 84, no. 9, 2013.

[93] E. Aprile *et al.*, "Conceptual design and simulation of a water Cherenkov muon veto for the XENON1T experiment," *JINST*, vol. 9, p. 11006, 2014.

[94] H. Araújo, V. Kudryavtsev, N. Spooner, and T. Sumner, "Muon-induced neutron production and detection with GEANT4 and FLUKA," *Nuclear Instruments and Methods in Physics Research Section A: Accelerators, Spectrometers, Detectors and Associated Equipment*, vol. 545, no. 1-2, pp. 398 –411, 2005.

[95] A. Lindote, H. Araújo, V. Kudryavtsev, and M. Robinson, "Simulation of neutrons produced by high-energy muons underground," *Astroparticle Physics*, vol. 31, no. 5, pp. 366 – 375, 2009.

[96] A. Gütlein *et al.*, "Solar and atmospheric neutrinos: Background sources for the direct dark matter searches," *Astroparticle Physics*, vol. 34, no. 2, pp. 90 – 96, 2010.

[97] J. Billard, L. Strigari, and E. Figueroa-Feliciano, "Implication of neutrino backgrounds on the reach of next generation dark matter direct detection experiments," *Phys. Rev.*, vol. D89, no. 2, p. 023524, 2014.

[98] D. S. Akerib *et al.*, "Radiogenic and Muon-Induced Backgrounds in the LUX Dark Matter Detector," *Astropart. Phys.*, vol. 62, pp. 33–46, 2015.

[99] L. Pagani, "The DarkSide veto: muon and neutron detectors," *Nuovo Cim.*, vol. C038, no. 01, p. 35, 2015.

[100] C. Leroy and P. G. Rancoita, "Principles of radiation interaction in matter and detection," *World Scientific*, 2004.

[101] K. Nakamura and P. D. Group, "Review of particle physics," *Journal of Physics G: Nuclear and Particle Physics*, vol. 37, no. 7A, p. 075021, 2010.

[102] R. M. Pope and E. S. Fry, "Absorption spectrum (380–700 nm) of pure water. ii. integrating cavity measurements," *Appl. Opt.*, vol. 36, pp. 8710–8723, Nov 1997.

[103] T. Hakamata, H. Kume, K. Tomiyama, and A. Kamiya, *Photomultiplier Tubes*. Hamamatsu Photonics K.K. Electron Tube Division, 3 ed., 2006.

[104] Hamamatsu Photonics, "Large Photocathode Photomultiplier Tubes," 1998. `http://www.hamamatsu.com`.

[105] M. C. Solutions, "3M Specular Film DF2000MA," *Technical Data Sheet: DF2000MA*, 2015.

[106] S. Agostinelli *et al.*, "GEANT4 - A simulation toolkit," *Nucl. Instruments Methods Phys. Res. Sect. A Accel. Spectrometers, Detect. Assoc. Equip.*, vol. 506, pp. 250–303, 2003.

[107] H. Kluck, "Measurement of the Cosmic-Induced Neutron Yield at the Modane Underground Laboratory," *KIT, Karlsruhe*, 2013. PhD thesis.

[108] T. K. Gaisser, "Cosmic rays and particle physics," *Cambridge, UK: Univ. Pr. (1990) 279 p*, 1990.

[109] W. Rhode, "Study of Ultra High Energy Muons with the Fréjus Detector," *Bergische Universität Gesamthochschule Wuppertal*, 1993. PhD thesis.

[110] A. Heikkinen, N. Stepanov, and J. P. Wellisch, "Bertini intranuclear cascade implementation in GEANT4," *eConf*, vol. C0303241, p. MOMT008, 2003.

[111] M. Asai, A. Dotti, M. Verderi, and D. H. Wright, "Recent developments in geant4," *Annals of Nuclear Energy*, vol. 82, pp. 19 – 28, 2015. Joint International Conference on Supercomputing in Nuclear Applications and Monte Carlo 2013, SNA + MC 2013. Pluri- and Trans-disciplinarity, Towards New Modeling and Numerical Simulation Paradigms.

[112] CERN, "Physics reference manual - geant4," 2015.

[113] A. Levin and C. Moisan, "A more physical approach to model the surface treatment of scintillation counters and its implementation into detect," *Nuclear Science Symposium, 1996. Conference Record., 1996 IEEE*, vol. 2, pp. 702–706 vol.2, Nov 1996.

[114] S. Nayar, K. Ikeuchi, and T. Kanade, "Surface reflection: physical and geometrical perspectives," *Pattern Analysis and Machine Intelligence, IEEE Transactions on*, vol. 13, pp. 611–634, Jul 1991.

[115] `http://wiki.opengatecollaboration.org`.

[116] S. Scorza, "EDELWEISS-III Experiment: Status and First Low WIMP Mass Results," *Journal of Physics: Conference Series*, 2015. XIV International Conference on Topics in Astroparticle and Underground Physics Proceedings.

[117] A. Benoit *et al.*, "Measurement of the response of heat-and-ionization germanium detectors to nuclear recoils," *Nucl. Instrum. Meth.*, vol. A577, pp. 558–568, 2007.

[118] J. Lindhard, "Approximation method in classical scattering by screened Coulomb fields," *Mat. Fys. Medd. Dan. Vid. Selsk*, 1968.

[119] M. Chadwick *et al.*, "Endf/b-vii.1 nuclear data for science and technology: Cross sections, covariances, fission product yields and decay data," *Nuclear Data Sheets*, vol. 112, no. 12, pp. 2887 – 2996, 2011. Special Issue on ENDF/B-VII.1 Library.

[120] D. Cullen *et al.*, "EPDL97: the Evaluated Photon DataLibrary," *UCRL-50400*, vol. 6, 1997.

[121] S. Perkins *et al.*, "Tables and Graphs of Electron-Interaction Cross Sections from 10 eV to 100 GeV Derived from the LLNL Evaluated Electron Data Library (EEDL)," *UCRL-50400*, vol. 31, 1997.

[122] S. Perkins *et al.*, "Tables and Graphs of Atomic Subshell and Relaxation Data Derived from the LLNL Evaluated Atomic Data Library (EADL), Z = 1 - 100," *UCRL-50400*, vol. 3o, 1997.

[123] R. Brun and F. Rademakers, "ROOT - an object oriented data analysis framework," *Nuclear Instruments and Methods in Physics Research Section A: Accelerators, Spectrometers, Detectors and Associated Equipment*, vol. 389, no. 1-2, pp. 81 – 86, 1997. New Computing Techniques in Physics Research V.

[124] R. Walker, G. Heuermann `et al`, "Prototype Measurements and Simulations of a Cherenkov Water Detector for Operation as an Active Muon Veto for Low Background Experiments," 2015. Article in preparation.

[125] S. Jokisch, "VME-LED-Module 1.0," *Karlsruhe Institute for Technology*, 2013.

[126] S. Jokisch, "Dokumentation uber den Diffusor," *Karlsruhe Institute for Technology*, 2013.

[127] BlueTec, "R.Plus Al," *R.Plus giving light a new direction*, 2012.

[128] Paul Scherrer Institut, "9 Channel, 5 GSPS," *Switched Capacitor Array*, 2013. `http://drs.web.psi.ch/datasheets`.

[129] W. Jiang and Z. Wang, "Study on pmt ringing signals of the daya bay neutrino experimet," Oct 2010. Nuclear Science Symposium Conference Record (NSS/MIC), 2010 IEEE.

[130] Johann Rauser, "Analyse μ-induzierter Signale in einem Prototyp-Wassertank für EURECA," *Karlsruhe Institute for Technology*, 2013. Bachelorthesis.

[131] O. Wack, "Charakterisierung von gekapselten Photomultipliern für das EURECA Vetosystem," *Karlsruhe Institute for Technology*, 2013. Bachelorthesis.

[132] A.-S. Frick, "Personal Communication," 2015.

[133] P. E. Ciddor, "Refractive index of air: new equations for the visible and near infrared," *Appl. Opt.*, vol. 35, pp. 1566–1573, Mar 1996.

[134] ISPOptics, "ISP optics infrared catalog," *ISP Optics, NY: ISP Optics*, 2010. `http://www.ispoptics.com/CatalogDownload.htm`.

[135] R. M. Pope and E. S. Fry, "Absorption spectrum of pure water. Integrating cavity measurements," *Appl. Opt.*, vol. 36, pp. 8710–8723, 1997.

[136] D. Chirkin, "Fluxes of Atmospheric Leptons at 600 GeV - 60 TeV," `arXiv:hep-ph/0407078`, 2004.

[137] N. D. Gagunashvili, "Comparison of weighted and unweighted histograms," `ArXiv:physics/0605123`, May 2006.

[138] O. M. Horn, "Simulations of the muon-induced neutron background of the EDELWEISS-II experiment for Dark Matter search.," *Forschungszentrum, Karlsruhe*, no. FZKA 7391, 2008.

[139] M. Knapp, P. Grabmayr, J. Jochum, B. Lubsandorzhiev, G. Meierhofer, F. Ritter, and B. Shaibonov, "The GERDA muon veto Cherenkov detector," *Nuclear Instruments and Methods in Physics Research Section A: Accelerators, Spectrometers, Detectors and Associated Equipment*, vol. 610, no. 1, pp. 280 – 282, 2009. New Developments In Photodetection NDIP08Proceedings of the Fifth International Conference on New Developments in Photodetection.

[140] L. Pandola *et al.*, "Monte Carlo evaluation of the muon-induced background in the GERDA double beta decay experiment," *Nuclear Instruments and Methods in Physics Research, Section A: Accelerators, Spectrometers, Detectors and Associated Equipment*, vol. 570, pp. 149–158, 2007.

[141] D. Akerib *et al.*, "The large underground xenon (lux) experiment," *Nuclear Instruments and Methods in Physics Research Section A: Accelerators, Spectrometers, Detectors and Associated Equipment*, vol. 704, pp. 111 – 126, 2013.

[142] L. Reichhart *et al.*, "Measurement and simulation of the muon-induced neutron yield in lead," *Astropart. Phys.*, vol. 47, pp. 67–76, 2013.

[143] A. Wright, P. Mosteiro, B. Loer, and F. Calaprice, "A highly efficient neutron veto for dark matter experiments," *Nucl. Instruments Methods Phys. Res. Sect. A Accel. Spectrometers, Detect. Assoc. Equip.*, vol. 644, no. 1, pp. 18–26, 2011.

[144] R. Calkins and B. Loer, "Prototyping an Active Neutron Veto for SuperCDMS," *AIP Conf. Proc.*, vol. 1672, p. 140002, 2015.

[145] P. Kandlakunta, L. Cao, and P. Mulligan, "Measurement of internal conversion electrons from gd neutron capture," *Nuclear Instruments and Methods in Physics Research Section A: Accelerators, Spectrometers, Detectors and Associated Equipment*, vol. 705, pp. 36 – 41, 2013.

[146] I. A. E. Agency, "Database of prompt gamma rays from slow neutron capture for elemental analysis," *Vienna: International Atomic Energy Agency*, 2007.

[147] X. Guo *et al.*, "A Precision measurement of the neutrino mixing angle θ_{13} using reactor antineutrinos at Daya-Bay," `arXiv:hep-ex/0701029`, 2007.

[148] W. Beriguete *et al.*, "Production of a gadolinium-loaded liquid scintillator for the daya bay reactor neutrino experiment," *Nuclear Instruments and Methods in Physics Research Section A: Accelerators, Spectrometers, Detectors and Associated Equipment*, vol. 763, pp. 82 – 88, 2014.

[149] A. Cabrera, "The double chooz experiment," *Nuclear Physics B - Proceedings Supplements*, vol. 229-232, pp. 87 – 91, 2012. Neutrino 2010.

[150] J. Birks, "The Theory and Practice of Scintillation Counting," *International Series of Monographs in Electronics and Instrumentation*, 1964.

[151] Saint-Gobain, "Gd Loaded Mineral Oil Based Liquid Scintillators," *BC525*, 2005.

[152] B. von Krosigk *et al.*, "Measurement of α-particle quenching in LAB based scintillator in independent small-scale experiments," `arXiv:physics.ins-det/1510.00458`, 2015.

[153] W. Wilson, R. Perry, W. Charlton, and T. Parish, "Sources: A code for calculating (alpha, n), spontaneous fission, and delayed neutron sources and spectra," *Progress in Nuclear Energy*, vol. 51, no. 4-5, pp. 608 – 613, 2009.

[154] V. Kudryavtsev, "Personal Communication," *Sheffield University*, 2013.

[155] I. A. E. Agency., "Nuclear data services: Evaluated nuclear data files," 2012.

[156] S. Cebrián *et al.*, "Radon and material radiopurity assessment for the NEXT double beta decay experiment," *AIP Conf. Proc.*, vol. 1672, p. 060002, 2015.

[157] B. Loer, "Personal Communication," 2014.

[158] P. Agnes *et al.*, "Low Radioactivity Argon Dark Matter Search Results from the DarkSide-50 Experiment," `arXiv:astro-ph.CO/1510.00702`, 2015.

[159] V. Kozlov, "Personal Communication," 2015.

[160] Hamamatsu Photonics, "MPPC and MPPC module for precision measurement," 2015. `https://www.hamamatsu.com/resources/pdf/ssd/mppc_kapd0002e.pdf`.

[161] S. S. D. Hamamatsu Photonics K.K., "MPPC (multi-pixel photon counter)," 2013. S12572-025,-050,-100C/P.

[162] L. Kuraray Co., "MPPC (multi-pixel photon counter)." `http://kuraraypsf.jp/psf/ws.html`.

[163] A. Medved and H. Rogers and P. Cushman, "Personal Communication," 2014.

[164] L. Reichhart *et al.*, "Quenching Factor for Low Energy Nuclear Recoils in a Plastic Scintillator," *Phys. Rev.*, vol. C85, p. 065801, 2012.

[165] J. Argyriades *et al.*, "Spectral modeling of scintillator for the NEMO-3 and SuperNEMO detectors," *Nucl. Instrum. Meth.*, vol. A625, pp. 20–28, 2011.

[166] M. Janecek, "Reflectivity spectra for commonly used reflectors," *Nuclear Science, IEEE Transactions on*, vol. 59, pp. 490–497, June 2012.

[167] M. Kelsey, "Personal communication," *SLAC-Stanford University*, 2015.

[168] Tosaka, "Decay chain 4n, Thorium series," 2015. Licensed under CC BY-SA 3.0 via Wikimedia Commons.

[169] Tosaka, "Uranium-238 decay chain diagram," 2015. Licensed under CC BY-SA 3.0 via Wikimedia Commons.

Appendix

A. Arrangement of PMTs

PMT setups with differing PMT arrangement and different numbers of PMTs used in Chap. 3 for the optimization process of the muon veto water Cherenkov detector. The PMTs are arranged in alternating rings of 8, 12 or 15 PMTs in 5, 6 or 7 rings. The naming of the setup is defined as follows: setup *K*-*L*, where K = 0, 1 refers to the number of rings on the floor surface and L = 40, 72, 105 refers to the total number of PMTs.

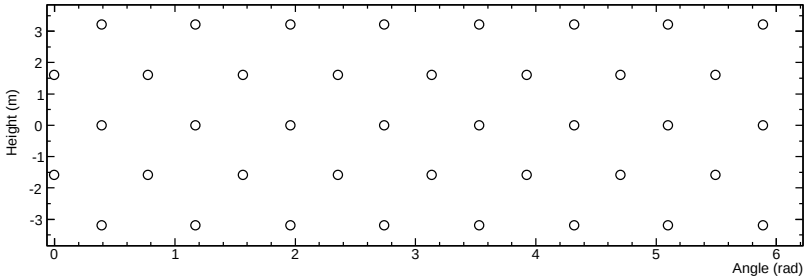

Figure A.1.: Setup0 with 40 PMTs in total: 8 PMTs in 5 lateral rings.

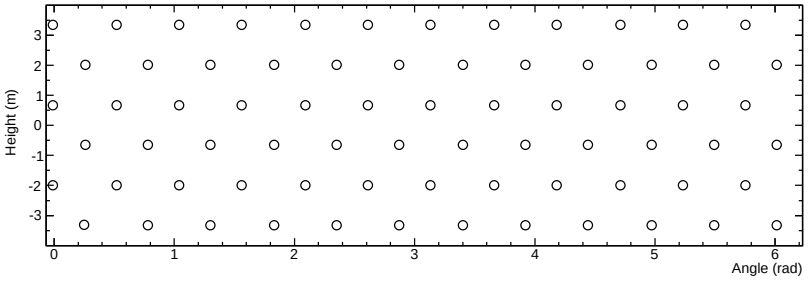

Figure A.2.: Setup0 with 72 PMTs in total: 12 PMTs in 6 lateral rings.

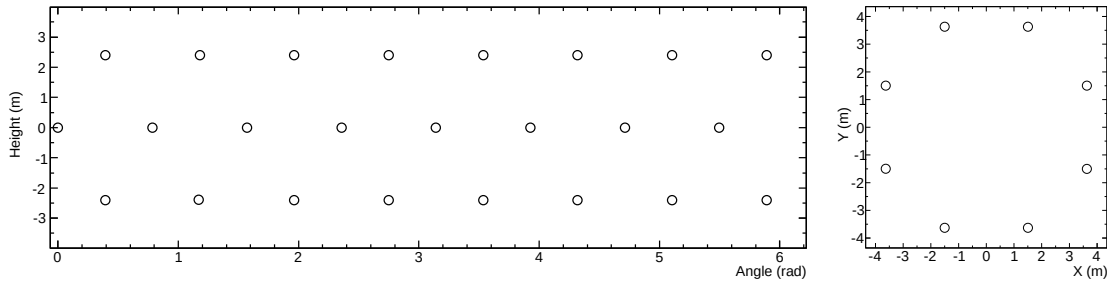

(a) (b)

Figure A.3.: Setup1 with 40 PMTs in total: 8 PMTs in 3 lateral rings (a), 8 PMTs in one lower and one upper ring (b).

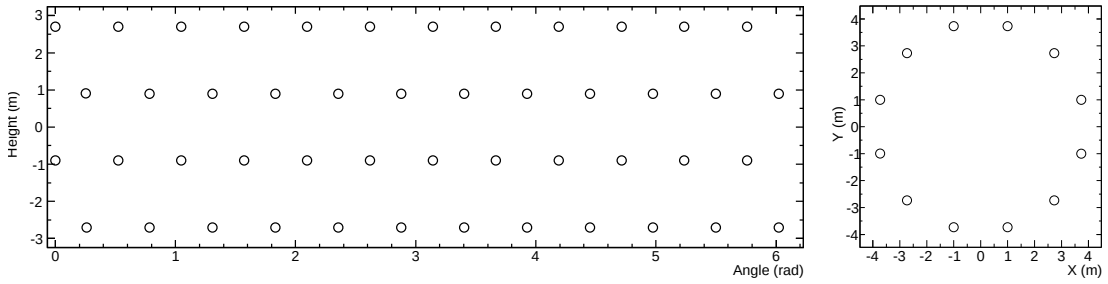

(a) (b)

Figure A.4.: Setup1 with 72 PMTs in total: 12 PMTs in 5 lateral rings (a), 12 PMTs in one lower and one upper ring each (b).

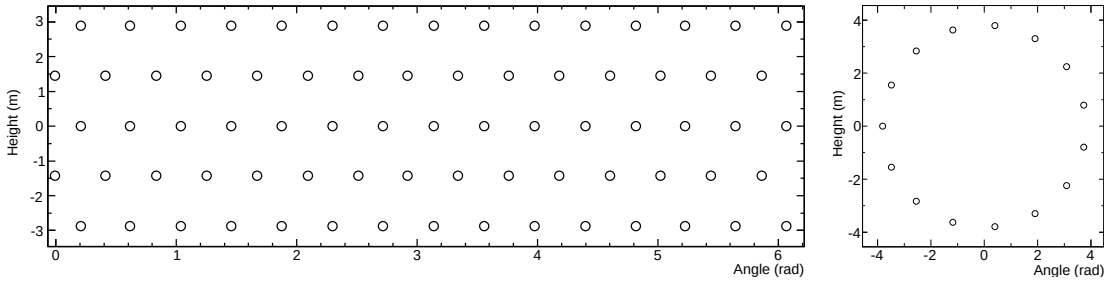

(a) (b)

Figure A.5.: Setup 1 with 105 PMTs in total: 15 PMTs in 5 lateral rings (a), 15 PMTs in one lower and one upper ring each (b).

B. Optical Properties

```
//------------------------------------------------------------------------
// Optical properties of DF2000
//------------------------------------------------------------------------
const G4int nEntriesDF2000Foil = 16;
G4double photonEnergy_DF2000Foil[nEntriesDF2000Foil] = { // optical photon energies
        4.57        * eV, 4.069576633 * eV, 3.543869677 * eV, 3.348636241 * eV,
        3.324396783 * eV, 3.299627461 * eV, 3.291744093 * eV, 3.275224511 * eV,
        3.259726604 * eV, 3.229166667 * eV, 3.134479272 * eV, 2.501008471 * eV,
        2.02020202  * eV, 1.868877167 * eV, 1.803898749 * eV, 1.6         * eV
};

G4double DF2000Foil_REFL[nEntriesDF2000Foil] = { // sheet info from 3M
        0.5117, 0.3342, 0.2665, 0.3014,
        0.4038, 0.5035, 0.6033, 0.7030,
        0.8027, 0.9024, 0.9886, 0.9933,
        0.9979, 0.9895, 0.9839, 0.99
};

G4MaterialPropertiesTable* mptDF2000Foil = new G4MaterialPropertiesTable();
mptDF2000Foil->AddProperty("REFLECTIVITY",photonEnergy_DF2000Foil,
        DF2000Foil_REFL, nEntriesDF2000Foil)->SetSpline(true);


//------------------------------------------------------------------------
// Optical properties of photocathode (PMT R5912)
//------------------------------------------------------------------------
const G4int nEntriesPMT = 51;
G4double photocath_EFF[nEntriesPMT] = { //Enables 'detection' of photons
        0.0,    0.0010, 0.0013, 0.0018, 0.0025, 0.0033, 0.0045, 0.0064, 0.0088, 0.0119,
        0.0167, 0.0284, 0.0420, 0.0530, 0.0715, 0.0989, 0.1438, 0.1740, 0.2233, 0.2446,
        0.2508, 0.2487, 0.2386, 0.2251, 0.2124, 0.1907, 0.1602, 0.1402, 0.1075, 0.0903,
        0.0704, 0.0553, 0.0403, 0.0306, 0.0233, 0.0173, 0.0129, 0.0105, 0.0072, 0.0054,
        0.0040, 0.0032, 0.0021, 0.0016, 0.0001, 0.0008, 0.0007, 0.0003, 0.0002, 0.0002,
        0.0
};

G4double photonEnergyPMT[nEntriesPMT] = {// optical photon energies
        4.57        * eV, 4.505813953 * eV, 4.491126403 * eV, 4.474918802 * eV, 4.446038006 * eV,
        4.431736955 * eV, 4.408105226 * eV, 4.381625442 * eV, 4.364660331 * eV, 4.346302138 * eV,
        4.250942749 * eV, 4.147157191 * eV, 4.092409241 * eV, 4.069576633 * eV, 4.04040404  * eV,
        3.996132775 * eV, 3.896920176 * eV, 3.80952381  * eV, 3.579676674 * eV, 3.381510772 * eV,
        3.2         * eV, 3.079215297 * eV, 2.88506282  * eV, 2.751886374 * eV, 2.664947346 * eV,
        2.55354201  * eV, 2.435192459 * eV, 2.374569131 * eV, 2.288245064 * eV, 2.248413418 * eV,
        2.194690265 * eV, 2.14532872  * eV, 2.0882452   * eV, 2.049586777 * eV, 2.019543974 * eV,
        1.993889693 * eV, 1.97044335  * eV, 1.953063475 * eV, 1.923972071 * eV, 1.902424056 * eV,
        1.882781658 * eV, 1.871698113 * eV, 1.85434425  * eV, 1.840308697 * eV, 1.831069108 * eV,
        1.814722669 * eV, 1.804161211 * eV, 1.777777778 * eV, 1.765375854 * eV, 1.751907318 * eV,
        1.6 * eV
};

G4MaterialPropertiesTable* mtphcath = new G4MaterialPropertiesTable();
mtphcath->AddProperty("EFFICIENCY",photonEnergyPMT,photocath_EFF,nEntriesPMT)->SetSpline(true);

//------------------------------------------------------------------------
// Optical properties of water
// Refractive Index of water at 25 C
//------------------------------------------------------------------------
const G4int nEntriesWa = 63;
G4double photonEnergyWa[nEntriesWa] = { // optical photon energies from Cherenkov light
        1.6  * eV, 2.07 * eV, 2.08 * eV, 2.1  * eV, 2.12 * eV, 2.14 * eV, 2.16 * eV, 2.18 * eV,
        2.19 * eV, 2.21 * eV, 2.23 * eV, 2.25 * eV, 2.27 * eV, 2.3  * eV, 2.32 * eV, 2.34 * eV,
        2.36 * eV, 2.38 * eV, 2.41 * eV, 2.43 * eV, 2.46 * eV, 2.48 * eV, 2.5  * eV, 2.53 * eV,
        2.56 * eV, 2.58 * eV, 2.61 * eV, 2.64 * eV, 2.67 * eV, 2.7  * eV, 2.72 * eV, 2.76 * eV,
        2.79 * eV, 2.82 * eV, 2.85 * eV, 2.88 * eV, 2.92 * eV, 2.95 * eV, 2.99 * eV, 3.02 * eV,
        3.06 * eV, 3.1  * eV, 3.14 * eV, 3.18 * eV, 3.22 * eV, 3.26 * eV, 3.31 * eV, 3.35 * eV,
        3.4  * eV, 3.44 * eV, 3.49 * eV, 3.54 * eV, 3.59 * eV, 3.65 * eV, 3.7  * eV, 3.76 * eV,
        3.81 * eV, 3.87 * eV, 3.94 * eV, 4.   * eV, 4.07 * eV, 4.13 * eV, 4.5  * eV
};

G4double RefractiveIndexWater[nEntriesWa] = {
        1.332,   1.332,   1.33218, 1.33239, 1.33261, 1.33282, 1.333,   1.33302, 1.33301,
        1.33299, 1.33298, 1.333,   1.33315, 1.33334, 1.33354, 1.33377, 1.334,   1.3342 ,
        1.3344,  1.3346,  1.3348,  1.335,   1.3352,  1.3354,  1.3356,  1.3358,  1.336,
        1.3362,  1.3364,  1.3366,  1.3368,  1.337,   1.3372,  1.3374,  1.3376,  1.3378,
        1.338,   1.33817, 1.33834, 1.33854, 1.33875, 1.339,   1.33935, 1.33974, 1.34014,
        1.34057, 1.341,   1.34137, 1.34174, 1.34214, 1.34255, 1.343,   1.34355, 1.34414,
        1.34474, 1.34537, 1.346,   1.34654, 1.34709, 1.34767, 1.3483,  1.349,   1.349
};

G4double AbsorptionWater[nEntriesWa] = {
        4.49  * m, 5.98  * m, 7.40  * m, 9.09  * m, 11.16 * m, 12.95 * m, 14.38 * m, 15.57 * m, 16.15 * m,
        16.77 * m, 17.69 * m, 19.56 * m, 21.09 * m, 22.12 * m, 23.04 * m, 23.98 * m, 24.44 * m, 25.25 * m,
        30.76 * m, 39.06 * m, 49.01 * m, 57.80 * m, 66.66 * m, 73.52 * m, 78.74 * m, 87.71 * m, 94.33 * m,
        98.91 * m, 102.14* m, 103.95* m, 108.45* m, 133.15* m, 157.48* m, 188.67* m, 202.02* m, 209.20* m,
        220.26* m, 225.22* m, 211.41* m, 188.67* m, 150.82* m, 123.00* m, 117.50* m, 106.26* m, 87.95 * m,
        87.95 * m, 87.95 * m, 87.95 * m, 87.95 * m, 87.95 * m, 87.95 * m, 87.95 * m, 87.95 * m, 87.95 * m,
        87.95 * m, 87.95 * m, 87.95 * m, 87.95 * m, 87.95 * m, 87.95 * m,  // approximation as unknown
        87.95 * m, 87.95 * m
};
G4MaterialPropertiesTable* mptWater = new G4MaterialPropertiesTable();
mptWater->AddProperty("RINDEX", photonEnergyWa, RefractiveIndexWater, nEntriesWa)->SetSpline(true);
mptWater->AddProperty("ABSLENGTH", photonEnergyWa, AbsorptionWater, nEntriesWa)->SetSpline(true);
G4Material::GetMaterial("Water")->SetMaterialPropertiesTable(mptWater);
```

```
//--------------------------------------------------------------------------
// Optical properties of air
//--------------------------------------------------------------------------
G4double Air_RIND[nEntriesWa] = {
        1.000277, 1.000277, 1.000277, 1.000277, 1.000277, 1.000277, 1.000278,
        1.000278, 1.000278, 1.000278, 1.000278, 1.000278, 1.000278, 1.000278,
        1.000278, 1.000279, 1.000279, 1.000279, 1.000279, 1.000279, 1.000279,
        1.00028 , 1.00028 , 1.00028 , 1.00028 , 1.00028 , 1.00028 , 1.000281, 1.000281,
        1.000281, 1.000281, 1.000281, 1.000282, 1.000282, 1.000282, 1.000282, 1.000282,
        1.000283, 1.000283, 1.000283, 1.000284, 1.000284, 1.000284, 1.000285, 1.000285,
        1.000285, 1.000286, 1.000286, 1.000287, 1.000287, 1.000287, 1.000288, 1.000288,
        1.000289, 1.00029 , 1.00029 , 1.000291, 1.000292, 1.00,     1.00
};

G4MaterialPropertiesTable* mptAir = new G4MaterialPropertiesTable();
mptAir->AddProperty("RINDEX", photonEnergyWa, Air_RIND, nEntriesWa)->SetSpline(true);
G4Material::GetMaterial("Air")->SetMaterialPropertiesTable(mptAir);
G4Material::GetMaterial("Vacuum")->SetMaterialPropertiesTable(mptAir);


//--------------------------------------------------------------------------
// Optical properties of borosilicate glass
//--------------------------------------------------------------------------
G4double BorGlass_RIND[nEntriesWa] = {
        1.5163 , 1.5163 , 1.5165 , 1.5167 , 1.51691, 1.51712, 1.51734, 1.51756, 1.51779,
        1.51803, 1.51827, 1.51852, 1.51878, 1.51904, 1.51931, 1.51958, 1.51987, 1.52016,
        1.52046, 1.52077, 1.52109, 1.52141, 1.52175, 1.5221 , 1.52246, 1.52283, 1.52321,
        1.52361, 1.52401, 1.52443, 1.52487, 1.52532, 1.52579, 1.52627, 1.52677, 1.52729,
        1.52783, 1.52839, 1.52897, 1.52957, 1.5302 , 1.53086, 1.53154, 1.53225, 1.53299,
        1.53376, 1.53456, 1.53539, 1.53626, 1.53716, 1.5381 , 1.53908, 1.54009, 1.54114,
        1.54223, 1.54337, 1.54455, 1.54577, 1.54703, 1.54835, 1.54971, 1.55111, 1.55111
};


G4double BorGlass_ABSL[nEntriesWa] = {
          43.8  * m,   43.8  * m,   38.2  * m,   33.4  * m,   29.3  * m,   25.9  * m,   23.   * m,   20.6  * m,
          18.5  * m,   16.8  * m,   15.3  * m,   14.1  * m,   13.   * m,   12.   * m,   11.2  * m,   10.5  * m,
           9.94 * m,    9.42 * m,    8.96 * m,    8.58 * m,    8.24 * m,    7.96 * m,    7.33 * m,    6.94 * m,
           6.73 * m,    6.65 * m,    6.67 * m,    6.79 * m,    7.01 * m,    7.32 * m,    8.34 * m,    9.4  * m,
          10.5  * m,   11.4  * m,   12.3  * m,   12.9  * m,   13.2  * m,   13.4  * m,   13.8  * m,   13.6  * m,
          13.1  * m,   12.7  * m,   13.1  * m,   14.9  * m,   18.5  * m,   24.2  * m,   26.6  * m,   29.5  * m,
          35.   * m,   43.6  * m,   57.2  * m,   78.5  * m,  109.   * m,  157.  * m,  237.   * m,  375.   * m,
         625.   * m, 1070.   * m, 1780.   * m, 2600.   * m, 3550.   * m, 7440.   * m, 7440.   * m
};

G4MaterialPropertiesTable* mptBorGlass = new G4MaterialPropertiesTable();
mptBorGlass->AddProperty("RINDEX", photonEnergyWa, BorGlass_RIND, nEntriesWa)->SetSpline(true);

//mptBorGlass->AddProperty("ABSLENGTH", photonEnergyWa, BorGlass_ABSL, nEntriesWa)->SetSpline(true);
//according to http://hypernews.slac.stanford.edu/HyperNews/geant4/get/opticalphotons.html?inline=-1
// only need to account for reflectivity as transmission is already included in the QE of the photocathode
G4Material::GetMaterial("BorGlass")->SetMaterialPropertiesTable(mptBorGlass);


//--------------------------------------------------------------------------
// Optical properties of plexiglass
//--------------------------------------------------------------------------
const G4int nEntries = 35;
G4double photonEnergyPMMA[nEntries] = { // optical photon energies for PMMA
        3.49 * eV, 3.44 * eV, 3.4  * eV, 3.35 * eV, 3.31 * eV, 3.26 * eV, 3.22 * eV,
        3.18 * eV, 3.14 * eV, 3.1  * eV, 3.06 * eV, 3.02 * eV, 2.99 * eV, 2.95 * eV,
        2.92 * eV, 2.88 * eV, 2.85 * eV, 2.82 * eV, 2.79 * eV, 2.76 * eV, 2.72 * eV,
        2.7  * eV, 2.67 * eV, 2.64 * eV, 2.61 * eV, 2.58 * eV, 2.56 * eV, 2.53 * eV,
        2.5  * eV, 2.48 * eV, 2.46 * eV, 2.43 * eV, 2.41 * eV, 2.38 * eV, 2.36 * eV
};

G4double Plexi_RIND[nEntries] = {
        1.517026, 1.51577,  1.514575, 1.513436, 1.512351, 1.511315, 1.510326, 1.509382,
        1.508479, 1.507616, 1.50679,  1.505999, 1.505241, 1.504515, 1.503819, 1.503151,
        1.50251,  1.501894, 1.501302, 1.500734, 1.500187, 1.499661, 1.499155, 1.498667,
        1.498198, 1.497746, 1.49731,  1.496889, 1.496483, 1.496092, 1.495714, 1.495349,
        1.494997, 1.494656, 1.494327
};


G4double PlexiG_ABSL[nEntries] = {
        0.00141116 * m, 0.00145027 * m, 0.0015777 * m, 0.00193495 * m, 0.00283463 * m, 0.00524941 * m,
        0.0128849  * m, 0.0396082  * m, 0.132349  * m, 0.414408   * m, 1.00799    * m, 1.65248    * m,
        1.99909    * m, 2.11951    * m, 2.15466   * m, 2.16438    * m, 2.16703    * m, 2.16775    * m,
        2.16794    * m, 2.16799    * m, 2.16801   * m, 2.16801    * m, 2.16801    * m, 2.16801    * m,
        2.16801    * m, 2.16801    * m, 2.16801   * m, 2.16801    * m, 2.16801    * m, 2.16801    * m,
        2.16801    * m, 2.16801    * m, 2.16801   * m, 2.16801    * m, 2.16801    * m
};


G4MaterialPropertiesTable* mptPlexiglass = new G4MaterialPropertiesTable();
mptPlexiglass->AddProperty("RINDEX", photonEnergyPMMA, Plexi_RIND, nEntries);
mptPlexiglass->AddProperty("ABSLENGTH", photonEnergyPMMA, PlexiG_ABSL, nEntries);
G4Material::GetMaterial("Plexiglass")->SetMaterialPropertiesTable(mptPlexiglass);
```

C. Material Composition and Properties

```
// --------------------------------------------------------------------
// GEANT 4 EDWIII Detector Material definitions file
//
// DetectorMaterial.icc
//
// Implementation of materials used in EDWIII
// --------------------------------------------------------------------
#include "G4NistManager.hh"
// Includes Physical Constants and System of Units
#include "G4PhysicalConstants.hh"
#include "G4SystemOfUnits.hh"
void eurDetectorConstruction::DefineMaterials()
{

// --------------------------------------------------------------------
// GEANT 4 EDWIII Detector Material definitions file
//
// DetectorMaterial.icc
//
// Implementation of materials used in EDWIII and EURECA
// --------------------------------------------------------------------

  //--------------------------------------------------------------------------
  // Elements
  //--------------------------------------------------------------------------
  G4double z,a;
  G4int iz, n;                //iz=number of protons  in an isotope;
                              // n=number of nucleons in an isotope;
  G4double abundance;
  G4double density;
  G4int ncomponents, natoms;
  G4double fractionmass;

  G4NistManager* nistMan = G4NistManager::Instance();

  G4Element* elementH = new G4Element( "Hydrogen", "H" ,  1. ,  1.00794 *g/mole);
  G4Element* elementHe= new G4Element( "Helium",   "He",  2. ,  4.0026  *g/mole);
  G4Element* elementLi= new G4Element(  "Lithium", "Li",  3. ,  6.94    *g/mole);
  G4Element* elementC = new G4Element( "Carbon",   "C" ,  6. , 12.011   *g/mole);
  G4Element* elementN = new G4Element( "Nitrogen", "N" ,  7. , 14.00674 *g/mole);
  G4Element* elementO = new G4Element( "Oxygen",   "O" ,  8. , 15.9994  *g/mole);
  G4Element* elementF = new G4Element(  "Fluor",   "F" ,  9. , 19.      *g/mole);
  G4Element* elementNa= new G4Element( "Natrium",  "Na", 11. , 22.98977 *g/mole);
  G4Element* elementMg= new G4Element( "Magnesium","Mg", 12. , 24.305   *g/mole);
  G4Element* elementAl= new G4Element( "Aluminium","Al", 13. , 26.981539*g/mole);
  G4Element* elementSi= new G4Element( "Silicon",  "Si", 14. , 28.0855  *g/mole);
  G4Element* elementP = new G4Element( "Phosphor", "P",  15. , 30.973761*g/mole);
  G4Element* elementS = new G4Element( "Sulfur",   "S",  16. , 32.066   *g/mole);
  G4Element* elementCl= new G4Element( "Chlorine", "Cl", 17. , 35.453   *g/mole);
  G4Element* elementK = new G4Element( "Potassium","K",  19. , 39.0983  *g/mole);
  G4Element* elementCa= new G4Element( "Calcium",  "Ca", 20. , 40.078   *g/mole);
  G4Element* elementTi= new G4Element( "Titanium", "Ti", 22. , 47.867   *g/mole);
  G4Element* elementMn= new G4Element( "Manganese","Mn", 25. , 54.93805 *g/mole);
  G4Element* elementFe= new G4Element( "Iron"  ,   "Fe", 26. , 55.854   *g/mole);
  G4Element* elementCo= new G4Element( "Cobalt",   "Co", 27. , 58.9332  *g/mole);
  G4Element* elementNi= new G4Element( "Nickel",   "Ni", 28. , 58.6934  *g/mole);
  G4Element* elementCr= new G4Element( "Cromium",  "Cr", 24.,  51.9961  *g/mole);
  G4Element* elementBi= new G4Element( "Bismuth",  "Bi", 83. , 209.0    *g/mole);
  G4Element* elementCu= new G4Element( "Copper",   "Cu", 29.,  63.55    *g/mole);
  G4Element* elementZn= new G4Element( "Zinc",     "Zn", 30.,  65.38    *g/mole);
  G4Element* elementCs = nistMan->FindOrBuildElement("Cs"); // Cesium;
  G4Element* elementSb = nistMan->FindOrBuildElement("Sb"); // Antimony;
  G4Element* elementB = nistMan->FindOrBuildElement("B"); // Boron;
  //-------------------------------------------------------
  // define an Element from isotopes, by relative abundance
  //-------------------------------------------------------
  G4Isotope* Ge70 = new G4Isotope("Ge70", iz=32, n=70, a=69.9240*g/mole);
  G4Isotope* Ge72 = new G4Isotope("Ge72", iz=32, n=72, a=71.9216*g/mole);
  G4Isotope* Ge73 = new G4Isotope("Ge73", iz=32, n=73, a=72.9233*g/mole);
  G4Isotope* Ge74 = new G4Isotope("Ge74", iz=32, n=74, a=73.9210*g/mole);
  G4Isotope* Ge76 = new G4Isotope("Ge76", iz=32, n=76, a=75.9213*g/mole);

  G4Element* Genat = new G4Element("naturalGermanium", "Ge",ncomponents=5);
  Genat->AddIsotope(Ge70,abundance=20.52*perCent);
  Genat->AddIsotope(Ge72,abundance=27.43*perCent);
  Genat->AddIsotope(Ge73,abundance=7.76*perCent);
  Genat->AddIsotope(Ge74,abundance=36.54*perCent);
  Genat->AddIsotope(Ge76,abundance=7.76*perCent);

  G4Material* Ge =
    new G4Material("Germanium", density = 5.310*g/cm3, ncomponents=1);
  Ge->AddElement(Genat, natoms=1);

  //--------------------------------------------------------------------------
  // Materials from Combination
  //--------------------------------------------------------------------------

  new G4Material("Galactic", z=1., a= 1.01*g/mole, universe_mean_density,
                 kStateGas, 2.73*kelvin, 3.e-18*pascal);

  G4Material* Air =
        new G4Material("Air", density= 1.290*mg/cm3, ncomponents=2,
                       kStateGas, 300.0*kelvin, 1.0*atmosphere);
  Air->AddElement(elementN, fractionmass=70.*perCent);
```

```
95  Air->AddElement(elementO, fractionmass=30.*perCent);
96
97  G4Material* Vacuum =
98  new G4Material("Vacuum", 1.29e-12 * g / cm3, 1, kStateGas,
99                       293. * kelvin, 1.e-9 * bar);
100 Vacuum->AddMaterial(Air, 1.);
101
102
103 G4Material* CaCO3 =
104   new G4Material("CaCO3", density= 2.80*g/cm3, ncomponents=3);
105 CaCO3->AddElement(elementCa, natoms= 1);
106 CaCO3->AddElement(elementC , natoms= 1);
107 CaCO3->AddElement(elementO , natoms= 3);
108
109 G4Material* Al2O3 =
110   new G4Material("Al2O3", density= 4.022*g/cm3, ncomponents=2);
111 Al2O3->AddElement(elementAl, natoms= 2);
112 Al2O3->AddElement(elementO , natoms= 3);
113
114 G4Material* LiF =
115   new G4Material("LiF", density= 2.35*g/cm3, ncomponents=2);
116 LiF->AddElement(elementLi, natoms= 1);
117 LiF->AddElement(elementF , natoms= 1);
118
119 G4Material* BGO =
120   new G4Material("BGO", density= 7.13*g/cm3, ncomponents=3);
121 BGO->AddElement(elementBi, natoms= 4);
122 BGO->AddElement(Genat , natoms= 3);
123 BGO->AddElement(elementO , natoms= 12);
124
125 G4Material* ZnMo =
126   new G4Material("ZnMo", density= 7.13*g/cm3, ncomponents=3);
127 ZnMo->AddElement(elementZn, natoms= 1);
128 ZnMo->AddElement(elementMn , natoms= 1);
129 ZnMo->AddElement(elementO , natoms= 4);
130
131 G4Material* Al =
132 new G4Material("Aluminium", z= 13., a= 26.981539*g/mole, density= 2.7*g/cm3);
133
134 G4Material* AlPMT =
135 new G4Material("AluminiumPMT", z= 13., a= 26.981539*g/mole, density= 2.7*g/cm3);
136
137 G4Material* C =
138 new G4Material("Carbon", z= 6., a= 12.01*g/mole, density= 2.265*g/cm3);
139
140 G4Material* metalFe =
141 new G4Material("Iron"  , z=26., a= 55.85*g/mole, density= 7.870*g/cm3);
142
143 G4Material* metalCu =
144 new G4Material("Copper", z=29., a= 63.55*g/mole, density= 8.96 *g/cm3);
145
146 G4Material* ldCopper =
147 new G4Material("LD_Copper",z=29, a=63.55*g/mole, density= 3.00*g/cm3);//LD copper to approximate E_box
148
149 G4Material* metalZn =
150 new G4Material("Tin"   , z=50., a= 118.7*g/mole, density= 7.310*g/cm3);
151
152 G4Material* metalPb =
153 new G4Material("Lead"  , z=82., a=207.19*g/mole, density= 11.36*g/cm3);
154
155 G4Material* silicium =
156 new G4Material("Silicium"  , z=14., a=28.0855*g/mole, density= 2.329*g/cm3);
157 //--------------------------------------------------
158 //salt
159 //--------------------------------------------------
160 G4Material* salt = new G4Material("NaCl", 2.2*g/cm3, 2);
161 salt->AddElement(elementNa, 1);
162 salt->AddElement(elementCl, 1);
163
164 //--------------------------------------------------
165 //polyethylen
166 //--------------------------------------------------
167 G4Material* PolyEthylen =
168   new G4Material("PolyEthylen", density= 0.94*g/cm3, ncomponents=2,
169                  kStateSolid, 300.0*kelvin, 1.0*atmosphere);
170 PolyEthylen->AddElement(elementH, 0.14);
171 PolyEthylen->AddElement(elementC, 0.86);
172
173 G4Material* PolyEthylen10 =
174   new G4Material("HDPE10", density= 10*g/cm3, ncomponents=2,
175                  kStateSolid, 300.0*kelvin, 1.0*atmosphere);
176 PolyEthylen10->AddElement(elementH, 0.14);
177 PolyEthylen10->AddElement(elementC, 0.86);
178
179 G4Material* PolyEthylen1_5 =
180   new G4Material("HDPE1_5", density= 1.5*g/cm3, ncomponents=2,
181                  kStateSolid, 300.0*kelvin, 1.0*atmosphere);
182 PolyEthylen1_5->AddElement(elementH, 0.14);
183 PolyEthylen1_5->AddElement(elementC, 0.86);
184
185 //--------------------------------------------------
186 //HydroCarbon (Kudryavtsev)
187 //--------------------------------------------------
188
189 G4Material* HydroCarbon =
190   new G4Material("HydroCarbon", 0.8*g/cm3, ncomponents=2,
```

```
                  kStateSolid, 300.0*kelvin, 1.0*atmosphere );
  HydroCarbon->AddElement( elementH, natoms=2);
  HydroCarbon->AddElement( elementC, natoms=1);
  //------------------------------------------------------
  //Frejus-Rock  // W. Rhode (Diss.) fractionMass // abundance
  //------------------------------------------------------
  G4Material* FrejusRock =
    new G4Material("FrejusRock", 2.74*g/cm3, 10, kStateSolid, 290.0*kelvin, 1.0*atmosphere );
  FrejusRock->AddElement(elementC,  0.065600); // 0.111175);
  FrejusRock->AddElement(elementO,  0.486849); // 0.619400);
  FrejusRock->AddElement(elementMg, 0.008856); // 0.007417);
  FrejusRock->AddElement(elementAl, 0.047732); // 0.036010);
  FrejusRock->AddElement(elementSi, 0.141776); // 0.102755);
  FrejusRock->AddElement(elementS,  0.004025); // 0.002555);
  FrejusRock->AddElement(elementK,  0.012504); // 0.006510);
  FrejusRock->AddElement(elementCa, 0.204815); // 0.104025);
  FrejusRock->AddElement(elementMn, 0.000953); // 0.000353);
  FrejusRock->AddElement(elementFe, 0.026890); // 0.009800);

  //------------------------------------------------------
  //Frejus-Rock2  // from Rachid Lemrani (17.02.05, Lyon)
  //------------------------------------------------------
  G4Material* FrejusRock2 =
    new G4Material("FrejusRock2", 2.65*g/cm3, 13, kStateSolid, 290.0*kelvin, 1.0*atmosphere );
  FrejusRock2->AddElement(elementH,  0.001250);
  FrejusRock2->AddElement(elementC,  0.020662);
  FrejusRock2->AddElement(elementO,  0.313634);
  FrejusRock2->AddElement(elementNa, 0.004047);
  FrejusRock2->AddElement(elementMg, 0.008168);
  FrejusRock2->AddElement(elementAl, 0.028065);
  FrejusRock2->AddElement(elementSi, 0.078651);
  FrejusRock2->AddElement(elementP,  0.000743);
  FrejusRock2->AddElement(elementK,  0.003285);
  FrejusRock2->AddElement(elementCa, 0.497041);
  FrejusRock2->AddElement(elementTi, 0.001340);
  FrejusRock2->AddElement(elementMn, 0.000659);
  FrejusRock2->AddElement(elementFe, 0.042455);

  //------------------------------------------------------
  //Frejus rock3  // added by Vitaly Kudryavtsev (VK), 17/06/2010, info from Rachid Lemrani,
  //            Chazal et al. Astroparticle Phys. 9 (1998) 163,
  //            Lemrani et al. NIMA 560 (2006) 454-459.
  //------------------------------------------------------
  G4Material* FrejusRock3 =
    new G4Material("FrejusRock3", density=2.65*g/cm3, ncomponents=13,
        kStateSolid, 300.0*kelvin, 1.0*atmosphere);
  FrejusRock3->AddElement(elementH, fractionmass=1*perCent);
  FrejusRock3->AddElement(elementC, fractionmass=5.94*perCent);
  FrejusRock3->AddElement(elementO, fractionmass=49.4*perCent);
  FrejusRock3->AddElement(elementNa, fractionmass=0.44*perCent);
  FrejusRock3->AddElement(elementMg, fractionmass=0.84*perCent);
  FrejusRock3->AddElement(elementAl, fractionmass=2.58*perCent);
  FrejusRock3->AddElement(elementSi, fractionmass=6.93*perCent);
  FrejusRock3->AddElement(elementP, fractionmass=0.06*perCent);
  FrejusRock3->AddElement(elementK, fractionmass=0.21*perCent);
  FrejusRock3->AddElement(elementCa, fractionmass=30.6*perCent);
  FrejusRock3->AddElement(elementTi, fractionmass=0.07*perCent);
  FrejusRock3->AddElement(elementMn, fractionmass=0.03*perCent);
  FrejusRock3->AddElement(elementFe, fractionmass=1.9*perCent);

  //------------------------------------------------------
  //LNGS-Rock
  //------------------------------------------------------
  G4Material* LNGSRock =
    new G4Material("LNGSRock", 2.71*g/cm3, 8, kStateSolid, 290.0*kelvin, 1.0*atmosphere );
  LNGSRock->AddElement(elementCa, 0.3029);
  LNGSRock->AddElement(elementC,  0.1188);
  LNGSRock->AddElement(elementO,  0.4791);
  LNGSRock->AddElement(elementMg, 0.0558);
  LNGSRock->AddElement(elementSi, 0.0127);
  LNGSRock->AddElement(elementAl, 0.0103);
  LNGSRock->AddElement(elementK,  0.0103);
  LNGSRock->AddElement(elementFe, 0.0101); //added to fill up to 100% !/mh

  //------------------------------------------------------
  //Frejus-concrete // from Rachid Lemrani (17.02.05, Lyon)
  //------------------------------------------------------

  G4Material* FrejusConcrete =
    new G4Material("FrejusConcrete", density= 2.4*g/cm3, ncomponents=7,
                  kStateSolid, 300.0*kelvin, 1.0*atmosphere);
  FrejusConcrete->AddElement(elementH,  0.001658);
  FrejusConcrete->AddElement(elementC,  0.024693);
  FrejusConcrete->AddElement(elementO,  0.342121);
  FrejusConcrete->AddElement(elementAl, 0.005547);
  FrejusConcrete->AddElement(elementSi, 0.032342);
  FrejusConcrete->AddElement(elementK,  0.000321);
  FrejusConcrete->AddElement(elementCa, 0.593318);

  //------------------------------------------------------
  //Frejus concrete 2 // added by Vitaly Kudryavtsev (VK), 17/06/2010, info from Rachid Lemrani,
  //            Chazal et al. Astroparticle Phys. 9 (1998) 163,
  //------------------------------------------------------
   G4Material* FrejusConcrete2 =
        new G4Material("FrejusConcrete2",density=2.4*g/cm3,ncomponents=13,
                  kStateSolid, 300.0*kelvin, 1.0*atmosphere);
```

```
287   FrejusConcrete2->AddElement(elementH, fractionmass=1.09*perCent);
288   FrejusConcrete2->AddElement(elementC, fractionmass=7.78*perCent);
289   FrejusConcrete2->AddElement(elementO, fractionmass=49.68*perCent);
290   FrejusConcrete2->AddElement(elementNa, fractionmass=0.01*perCent);
291   FrejusConcrete2->AddElement(elementMg, fractionmass=0.78*perCent);
292   FrejusConcrete2->AddElement(elementAl, fractionmass=0.48*perCent);
293   FrejusConcrete2->AddElement(elementSi, fractionmass=2.69*perCent);
294   FrejusConcrete2->AddElement(elementP, fractionmass=0.07*perCent);
295   FrejusConcrete2->AddElement(elementK, fractionmass=0.02*perCent);
296   FrejusConcrete2->AddElement(elementCa, fractionmass=36.78*perCent);
297   FrejusConcrete2->AddElement(elementTi, fractionmass=0.09*perCent);
298   FrejusConcrete2->AddElement(elementMn, fractionmass=0.01*perCent);
299   FrejusConcrete2->AddElement(elementFe, fractionmass=0.52*perCent);
300
301   //--------------------------------------------------
302   //LNGS concrete // s. Hesti Wulandari p.42
303   //--------------------------------------------------
304   G4Material* LNGSConcrete =
305     new G4Material("LNGSConcrete", density= 2.4*g/cm3, ncomponents=13,
306                    kStateSolid, 300.0*kelvin, 1.0*atmosphere);
307   LNGSConcrete->AddElement(elementH,  0.009009);
308   LNGSConcrete->AddElement(elementC,  0.080879);
309   LNGSConcrete->AddElement(elementO,  0.490232);
310   LNGSConcrete->AddElement(elementNa, 0.006073);
311   LNGSConcrete->AddElement(elementMg, 0.008604);
312   LNGSConcrete->AddElement(elementAl, 0.009110);
313   LNGSConcrete->AddElement(elementSi, 0.039073);
314   LNGSConcrete->AddElement(elementP,  0.000405);
315   LNGSConcrete->AddElement(elementS,  0.001620);
316   LNGSConcrete->AddElement(elementK,  0.005466);
317   LNGSConcrete->AddElement(elementCa, 0.344772);
318   LNGSConcrete->AddElement(elementTi, 0.000404);
319   LNGSConcrete->AddElement(elementFe, 0.004353);
320
321   //--------------------------------------------------
322   //PVT
323   //--------------------------------------------------
324   G4Material* PVT =
325     new G4Material("PVT",  1.032*g/cm3, ncomponents=2,
326                    kStateSolid, 290.0*kelvin, 1.0*atmosphere );
327   PVT->AddElement( elementH, natoms=21);  // resolve Ratio H:C Atoms of 1.104 (BC-412)
328   PVT->AddElement( elementC, natoms=19);
329
330
331   //--------------------------------------------------
332   // Mild (carbon) steel // inserted by VK on 17/06/2010: this is mild steel, not stainless steel
333   //--------------------------------------------------
334   G4Material* MildSteel = new G4Material("Steel", density=7.85*g/cm3, ncomponents=8);
335   MildSteel->AddElement(elementC, 0.002);
336   MildSteel->AddElement(elementFe, 0.94);
337   MildSteel->AddElement(elementCo, 0.01);
338   MildSteel->AddElement(elementMn, 0.016);
339   MildSteel->AddElement(elementCu, 0.006);
340   MildSteel->AddElement(elementSi, 0.006);
341   MildSteel->AddElement(elementCr, 0.01);
342   MildSteel->AddElement(elementNi, 0.01);
343
344   //--------------------------------------------------
345   //Stainless Steel // Added by VK, 17/06/2010 for 304L (average values)
346   //--------------------------------------------------
347
348   G4Material* StainlessSteel=new G4Material("StainlessSteel",density=8.*g/cm3,ncomponents=9);
349   StainlessSteel->AddElement(elementC, fractionmass=0.03*perCent);
350   StainlessSteel->AddElement(elementCr, fractionmass=19*perCent);
351   StainlessSteel->AddElement(elementNi, fractionmass=10*perCent);
352   StainlessSteel->AddElement(elementMn, fractionmass=2*perCent);
353   StainlessSteel->AddElement(elementFe, fractionmass=68.33*perCent);
354   StainlessSteel->AddElement(elementSi, fractionmass=0.5*perCent);
355   StainlessSteel->AddElement(elementN, fractionmass=0.1*perCent);
356   StainlessSteel->AddElement(elementP, fractionmass=0.02*perCent);
357   StainlessSteel->AddElement(elementS, fractionmass=0.02*perCent);
358
359   //--------------------------------------------------
360   // wood
361   //--------------------------------------------------
362   G4Material* wood = new G4Material("wood", density=0.9*g/cm3, ncomponents=3);
363   wood->AddElement(elementH ,natoms= 4);
364   wood->AddElement(elementO ,natoms=1);
365   wood->AddElement(elementC ,natoms=2);
366
367   //--------------------------------------------------
368   // liquid Helium
369   //--------------------------------------------------
370
371   G4Material* lHelium = new G4Material("lHelium", density=0.145*g/cm3, ncomponents=1);
372   lHelium->AddElement(elementHe, 1);
373
374   //--------------------------------------------------
375   // water
376   //--------------------------------------------------
377   G4Material* Water =
378     new G4Material("Water", density= 1.000*g/cm3, ncomponents=2);
379   Water->AddElement(elementH, natoms=2);
380   Water->AddElement(elementO, natoms=1);
381   // overwrite computed meanExcitationEnergy with ICRU recommended value
382   //Water->GetIonisation()->SetMeanExcitationEnergy(75.0*eV);
```

```
383
384   //--------------------------------------------------
385   // generic scintillator
386   //--------------------------------------------------
387   G4Material* Sci =
388     new G4Material("Scintillator", density= 1.032*g/cm3, ncomponents=2);
389   Sci->AddElement(elementC, natoms=9);
390   Sci->AddElement(elementH, natoms=10);
391
392   //--------------------------------------------------
393   // mylar
394   //--------------------------------------------------
395   G4Material* Myl =
396     new G4Material("Mylar", density= 1.397*g/cm3, ncomponents=3);
397   Myl->AddElement(elementC, natoms=10);
398   Myl->AddElement(elementH, natoms= 8);
399   Myl->AddElement(elementO, natoms= 4);
400
401   //--------------------------------------------------
402   //quartz
403   //--------------------------------------------------
404   G4Material* SiO2 =
405     new G4Material("quartz",density= 2.200*g/cm3, ncomponents=2);
406   SiO2->AddElement(elementSi, natoms=1);
407   SiO2->AddElement(elementO , natoms=2);
408
409   //--------------------------------------------------
410   // teflon
411   //--------------------------------------------------
412   G4Material*  Teflon =
413     new G4Material("Teflon",density = 2.00*g/cm3, ncomponents=2);
414   Teflon->AddElement(elementC,natoms=1);
415   Teflon->AddElement(elementF, natoms=2);
416
417
418   //--------------------------------------------------
419   // Epoxy // VK - DJ Epoxy for connectors on the crystals
420   //--------------------------------------------------
421
422   G4Material* Epoxy =
423     new G4Material("Epoxy",density = 1*g/cm3, ncomponents=4);
424   Epoxy->AddElement(elementC, natoms=12);
425   Epoxy->AddElement(elementH, natoms=14);
426   Epoxy->AddElement(elementO, natoms=2);
427   Epoxy->AddElement(elementN, natoms=4);
428
429   //------------------------------------------------------------------------
430   // define a material from elements and/or others materials (mixture of mixtures)
431   //------------------------------------------------------------------------
432   G4Material* Aerog =     new G4Material("Aerogel", density= 0.200*g/cm3, ncomponents=3);
433   Aerog->AddMaterial(SiO2    , fractionmass=62.5*perCent);
434   Aerog->AddMaterial(Water     , fractionmass=37.4*perCent);
435   Aerog->AddElement (elementC, fractionmass= 0.1*perCent);
436
437  //--------------------------------------------------
438  // Connectors 1K same volume Epoxy StainlessSteel
439  //--------------------------------------------------
440  G4Material* Connect1K =
441     new G4Material("Connect1K", density= 2.245*g/cm3, ncomponents=2);
442  Connect1K->AddMaterial(Epoxy, fractionmass=0.5);
443  Connect1K->AddElement(elementAl, fractionmass=0.5);
444  //--------------------------------------------------
445  // Connectors FETBOX 15 pins same volume Epoxy StainlessSteel
446  //--------------------------------------------------
447  G4Material* ConnectFB15 =
448     new G4Material("ConnectFB15", density= 3.42*g/cm3, ncomponents=2);
449   ConnectFB15->AddMaterial(Epoxy, fractionmass=0.5);
450   ConnectFB15->AddElement(elementAl, fractionmass=0.5);
451
452  //--------------------------------------------------
453  // Connectors FETBOX 15 pins Support  same volume Epoxy StainlessSteel
454  //--------------------------------------------------
455  G4Material* ConnectFBSup15 =
456     new G4Material("ConnectFBSup15", density= 3.46*g/cm3, ncomponents=2);
457   ConnectFBSup15->AddMaterial(Epoxy, fractionmass=0.5);
458   ConnectFBSup15->AddElement(elementAl, fractionmass=0.5);
459
460  //--------------------------------------------------
461  // Connectors FETBOX 51 pins same volume Epoxy StainlessSteel
462  //--------------------------------------------------
463  G4Material* ConnectFB51 =
464     new G4Material("ConnectFB51", density= 4.*g/cm3, ncomponents=2);
465   ConnectFB51->AddMaterial(Epoxy, fractionmass=0.5);
466   ConnectFB51->AddElement(elementAl, fractionmass=0.5);
467
468  //--------------------------------------------------
469  // Connectors FETBOX 51 pins Support  same volume Epoxy StainlessSteel
470  //--------------------------------------------------
471  G4Material* ConnectFBSup51 =
472     new G4Material("ConnectFBSup51", density= 3.84*g/cm3, ncomponents=2);
473   ConnectFBSup51->AddMaterial(Epoxy, fractionmass=0.5);
474   ConnectFBSup51->AddElement(elementAl, fractionmass=0.5);
475
476
477   //--------------------------------------------------
478   // Connectors 300K same volume Epoxy StainlessSteel
```

```
479   //--------------------------------------------------
480   G4Material* Connect300K =
481     new G4Material("Connect300K", density= 2.83*g/cm3, ncomponents=2);
482   Connect300K->AddMaterial(Epoxy, fractionmass=0.1111);
483   Connect300K->AddMaterial(StainlessSteel, fractionmass=0.8889);
484
485
486   //--------------------------------------------------
487   // examples of gas in non STP conditions
488   //--------------------------------------------------
489   G4Material* CO2 =
490     new G4Material("CarbonicGas", density= 27.*mg/cm3, ncomponents=2,
491                    kStateGas, 325.*kelvin, 50.*atmosphere);
492   CO2->AddElement(elementC, natoms=1);
493   CO2->AddElement(elementO, natoms=2);
494
495   G4Material* steam =
496     new G4Material("WaterSteam", density= 0.3*mg/cm3, ncomponents=1,
497                    kStateGas, 500.*kelvin, 2.*atmosphere);
498   steam->AddMaterial(Water, fractionmass=1.);
499
500   new G4Material("ID401Alu", 13., 26.981539*g/mole, 2.7*g/cm3);
501
502   //--------------------------------------------------
503   //Borosilicate glass (Schott BK7) (8" PMT window)
504   //--------------------------------------------------
505
506   G4Material* BorGlass =
507         new G4Material("BorGlass", 2.51 * g / cm3, 6);
508
509   BorGlass->AddElement(elementB, 0.040064);
510   BorGlass->AddElement(elementO, 0.539562);
511   BorGlass->AddElement(elementNa, 0.028191);
512   BorGlass->AddElement(elementAl, 0.011644);
513   BorGlass->AddElement(elementSi, 0.377220);
514   BorGlass->AddElement(elementK, 0.003321);
515
516
517   //--------------------------------------------------
518   //BiAlkali photocathode (NIM A567, p.222) K2CsSb;
519   //For the references for the optical properties see ../ref/ComplexRefractionSpectrum_KCSSb.pdf
520   //--------------------------------------------------
521   // exact composition of the bialkali is unknown, density is the 'realistic' guess!;
522   G4Material* BiAlkali = new G4Material("BiAlkali", 1.3 * g / cm3, 3);
523   BiAlkali->AddElement(elementK, 2);
524   BiAlkali->AddElement(elementCs, 1);
525   BiAlkali->AddElement(elementSb, 1);
526
527
528   //--------------------------------------------------
529   // PMMA (plexiglass)
530   //--------------------------------------------------
531
532   G4Material* matPMMA = new G4Material("Plexiglass", 1.19 * g / cm3, 3);
533   matPMMA->AddElement(elementH, 8);
534   matPMMA->AddElement(elementO, 2);
535   matPMMA->AddElement(elementC, 5);
536
537
538   //============================================================================
539   // BC-525 liquid scintillator; according to datasheet, elC+elH+elGd=1, elH=1.56*elC, elGd=0.002
540   //For the references for the optical properties see ../ref/EmissionSpectrum_BC-525.pdf
541   G4Element* elGd = nistMan->FindOrBuildElement("Gd");
542   G4Material* matLiqScin = new G4Material("liqScintillator", 0.88 * g / cm3, 3);
543   matLiqScin->AddElement(elementC, .8825);
544   matLiqScin->AddElement(elementH, .1155);
545   matLiqScin->AddElement(elGd, .002);
546
547
548   G4cout << *(G4Material::GetMaterialTable()) << G4endl;   // Printout materials
549 }
```

D. Uranium and Thorium Decay Chain

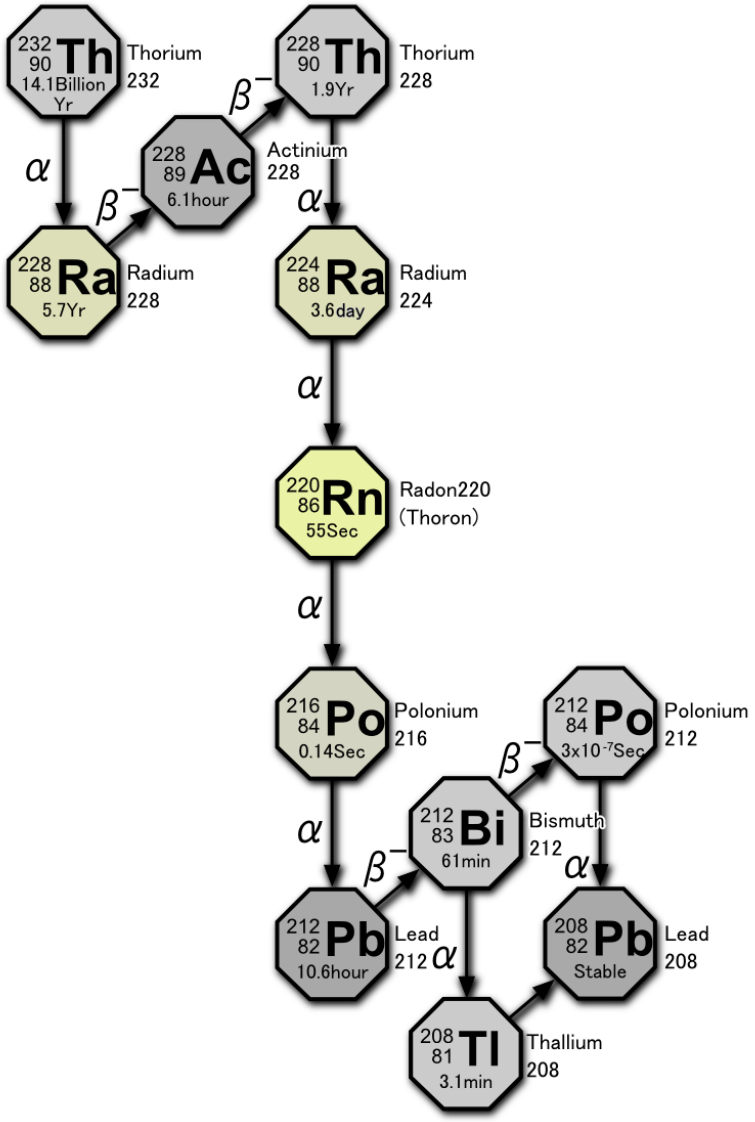

Figure D.6.: Thorium decay chain. Fig. from [168]

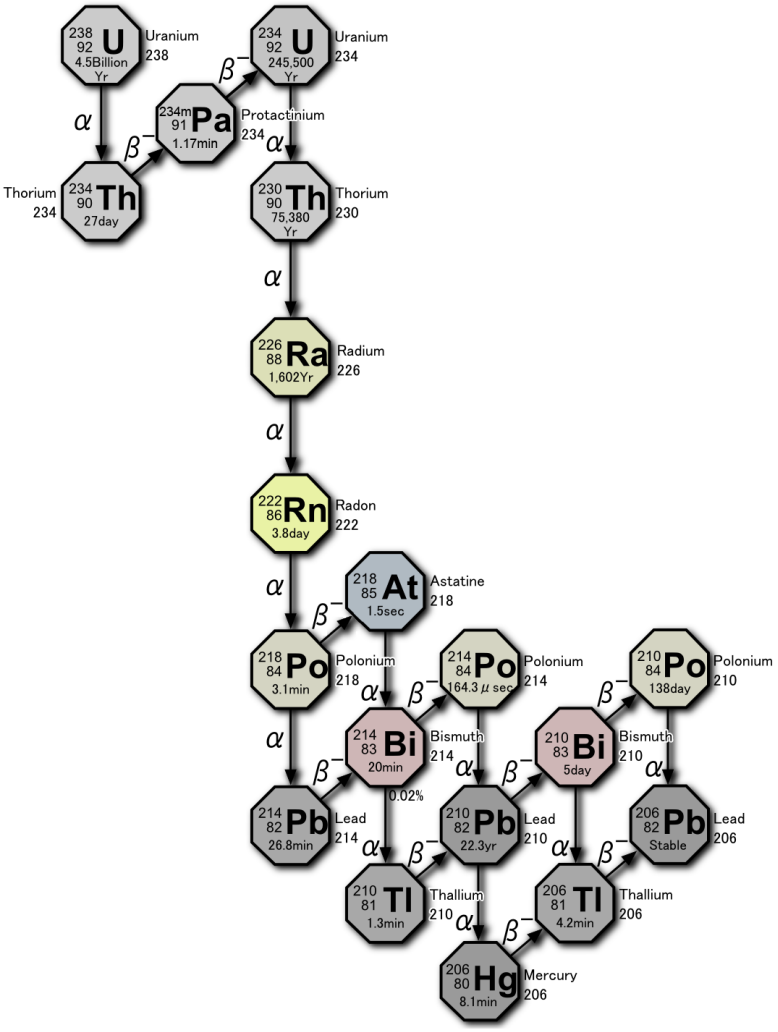

Figure D.7.: Uranium decay chain. Fig. from [169]